Real-time Energy Management System of Battery-Supercapacitor in Electric vehicles

Submitted by

Miguel Robayo

to the

University of Exeter

as a thesis for the degree of

Doctor of Philosophy in Renewable Energy

September 2022

I certify that all materials in this thesis which is not my own work has been identified and that no material has previously been submitted and approved for the award of the degree by this or any other University.

Signature:……

In appreciation of Our Heavenly Father for his loving kindness towards me and my family.

This thesis is dedicated to my dear parents, for their endless love, encouragement and continuous moral, emotional, and financial support. To my brothers and sister for supporting me throughout my studies.

I am thankful to my wife and daughter for their patience and unconditional love. This work could not have been accomplished without your sacrifices.

Acknowledgement

I would like to offer my sincerest gratitude and praise to Dr. Mohammad Abusara for giving the opportunity to come to the UK to complete my PhD at the University of Exeter. Mohammad has served as a mentor, a teacher, and a friend that constantly looked after me. Being under his guidance has made me strive to do more and acquire more skills. Thank you Mohammad for your support, for believing in me, and of course for taking me as your PhD student in the first place.

I am grateful to the Ecuadorian Secretary of Higher Education, Science, Technology and Innovation SENESCYT for providing the scholarship to study my PhD at the University of Exeter.

Abstract

This thesis presents the design, simulation and experimental validation of an Energy Management System (EMS) for a Hybrid Energy Storage System (HESS) composed of lithium ion batteries and Supercapacitors (SCs) in electric vehicles. The aim of the EMS is to split the power demand considering the weaknesses and strengths or the power sources. The HESS requires an EMS to determine power missions for the battery and SC in real time, where the SC is commanded to assist the battery during high power demand and recover the energy generated during braking. Frequency sharing techniques have been proposed by researchers to achieve this objective, including the Discrete Wavelet Transform (DWT) and conventional filtration methods (low and high pass filters). However, filtration approaches can introduce delay (milliseconds to tens of seconds) in the frequency components which undermines the hybridisation advantages. Hence, the selection of the filtration technique and filter design are crucial to the system's performance. Researchers have proposed power demand prediction methodologies to deal with time delay, however, the advantages and drawbacks of using such methods have not been investigated thoroughly, particularly whether time delay compensation and its inherent prediction error improves the system performance, efficiency, and timely SC contribution during the motoring and braking stages. This work presents a fresh perspective to this research field by introducing a novel approach that deals with delay without complicated prediction algorithms and improves the SC contribution during the motoring and braking stages while reducing energy losses in the system.

The proposed EMS allows the SC to provide timely assistance during motoring and to recover the braking energy generated. A charging strategy controls energy circulation between the battery and SC to keep the SC charge availability during the whole battery

discharge cycle. The performance and efficiency of the HESS is improved when compared to the traditional use of conventional filtration techniques and the DWT. Results show that the proposed EMS method improves the energy efficiency of the HESS. For the US06 driving cycle, the energy efficiency is 91.6%. This is superior to the efficiency obtained with an EMS based on a high pass filter (41.3%), an EMS based on DWT high frequency component (30.3%) and an EMS based on the predicted DWT high frequency component (41%).

Contents

List of Figures

List of Tables

List of Equations

Acronyms

ADAM	Adaptive moment estimation
ADC	Analogue to digital converter
API	Application programming interface
APP	Accelerator pedal position
AWD	All wheel drive
BEV	Battery electric vehicles
BMW	Bayerische Motoren Werke GmbH
BPP	Brake pedal position
BYD	Build your dreams
CALB	China aviation lithium, battery technology
CAN	Controller area network
CATL	Contemporary Amperex Technology Co. Limited
CCS	Code composer studio
CG	Centre of gravity
DSP	Digital signal processor
DWT	Discrete wavelet transform
EDLC	Electric double layer capacitor
EIA	US Energy Information Administration
EMF	Electromotive force
EMS	Energy management system
ESS	Energy storage system
EUDC	Extra Urban Driving Cycle
EV	Electric vehicle
F	Farad
FIR	Finite impulse response
FOC	Field oriented control
FPGA	Field programmable gate arrays

FTP72	Federal test procedure driving cycle
FWD	Front wheel drive
GPIO	General Purpose input/output
HESS	Hybrid energy storage system
HEV	Hybrid electric vehicle
HIL	Hardware in the loop
HPB	High power battery
HUDDS	Urban dynamometer driving schedule
HWFET	Highway fuel economy test
ICE	Internal combustion engine
IGBT	Insulated-gate bipolar transistor
IHZ	Inner Helmholtz plane
IIR	Infinite impulse response
IM240	Inspection and Maintenance Driving Schedule
JC08	Japanese chassis dynamometer test
JTAG	Joint test action group
LA92	Unified dynamometer driving schedule
LDV	Light duty vehicle
LFP	Lithium iron phosphate oxide
LIB	Lithium Ion Battery
LMO	Lithium manganese oxide
LSTM	Long short memory neural network
LTO	Lithium Titanate
MCU	Microcontroller unit
MOSFET	Metal Oxide Semiconductor field effect transistor
MSE	Mean squared error
NARNN	Non linear autoregressive neural network
NARX	Non linear autoregressive neural network with exogenous input

NCA	Nickel Cobalt Aluminium Oxide
NEDC	New European driving cycle
NMC	Nickel manganese cobalt oxide
OEM	Original equipment manufacturer
OHP	Outer Helmholtz plane
PHEV	Plug-in hybrid vehicles
PI	Proportional-integral
PIL	Processor in the loop
PMSM	Permanent magnet synchronous motor
PWM	Pulse width modulation
QEP	Quadrature encoder pulse
RAM	Random access memory
RMS	Root mean square
RMSE	Root mean squared error
RNN	Recurrent neural networks
RPM	Revolution per minute
SC	Supercapacitor
SC03	Chassis dynamometer test
SCI	Serial communication interface
SMES	Superconducting magnetic energy storage
SOC	State of charge
SOH	State of health
SPI	Serial peripheral interface
TANH	Hyperbolic tangent
UART	Universal asynchronous receiver/transmitter
UDDS	Urban dynamometer driving schedule
US06	EPA Driving Schedule for Light-Duty Vehicles and Trucks
USB	Universal serial bus

WLTP3	Worldwide Harmonized Light Vehicle Test Procedure

Publications

- M. Robayo, M. Abusara, M. Mueller and S. Sharkh, "A Smart Energy Management System for Battery-Supercapacitor in Electric Vehicles based on the Discrete Wavelet Transform and Deep Learning," 2020 IEEE 29th International Symposium on Industrial Electronics (ISIE), 2020, pp. 9-14, doi: 10.1109/ISIE45063.2020.9152559.

- M. Robayo, M. Mueller, S. Sharkh and M. Abusara, “Assessment of Supercapacitor performance in a hybrid energy storage system with an energy management based on the discrete wavelet transform,” Journal of Energy Storage, Volume 57, 106200. https://doi.org/10.1016/j.est.2022.106200

- M. Robayo and M. Abusara, “Efficient real-time energy management system for battery- supercapacitor hybrid energy storage in electric vehicles,” submitted to Journal of Energy Storage (in revision Dec-2022)

CHAPTER

1

1 INTRODUCTION

1.1 Batteries used in electric vehicles

The development of electric vehicles (EVs) is driven by technological advances in batteries. Lithium-ion batteries (LIBs) dominate in several applications including portable electronics and EVs due to their advantages over other battery systems, specifically their high energy density (250-693 Wh/L;100-265 Wh/kg), power capability (250-340 W/kg), no memory effect, excellent cycling (400-1200 cycles), little self-discharge (0.35%-2.5% per month depending on state of charge), and wide temperature operation range (5˚C-45 ˚C) [1] [2]. As LIBs have become more prevalent since their commercialisation, remarkable progress has been made towards improving their energy density, reducing their costs, and improving their performance. The global sales of EVs including Hybrid Electric Vehicles (HEVs), broke a new record of 6.6 million in 2021, according to the most recent edition of the annual Global Electric Vehicle Outlook report [3]. Two million EVs were sold globally in the first quarter of 2022; an increase of 75 percent over the same period last year despite supply chain strains. Around 16.5 million EVs were on the road by the end of 2021, triple what they were in 2018. EVs - including HEVs - accounted for roughly 1.5% of the global fleet as of mid-2022. EV sales are projected to rise from 6.6 million in 2021 to 20.6 million by 2025, according to Bloomberg NEF [4]. In 2025, EVs are forecast to raise their share of new passenger vehicle sales to 23%, up from just under 10% in 2021, being 75% of those fully electric vehicles [4].

Bloomberg's NEF long-term electric vehicle outlook estimates that electric vehicles models will account for 35% of the whole global car fleet by 2040. The U.S. Energy Information Administration (EIA) estimates that today's light duty vehicle (LDV) fleet is about 1.31 billion vehicles and this would grow up to 2.21 billion by 2050. By this time, global share of the light –duty electric vehicle fleet will grow from 0.7% to 31%, reaching 672 million EVs on the road [5].

In order for EV adoption to become sustainable, battery technology must overcome a few barriers before vehicles equipped with this type of energy storage system (ESS) can compete with internal combustion engine vehicles (ICE). Usable energy density at C/3 should be >750Wh/L at cell level and >500 Wh/L at pack level, usable specific energy at C/3 should be >350 Wh/kg at cell level and 235 Wh/kg at pack level [6] [7]. Peak specific discharge power (80% depth of discharge, 30s) should be in the order of 700 W/kg and the peak power density (80% depth of discharge, 30s) at around 1500 W/L. Cost should be less than $100/kWh [6]. Other important features include fast charge capability (0-80% in 15 minutes) [7], long life of 15 years, safety of operation, and being able to perform in a wide range of temperatures (-20˚to 60˚C) [8]. Reported energy densities of battery cells range from 83 Wh/kg for high power cells to 267 Wh/kg for high energy cells [9]. As of today, no battery meets all the requirements of an advanced high-performance battery for EV applications [6], [10].

Driving range, vehicle performance, charging time, and cost are the major concerns of customers regarding EVs. The driving range is determined by the battery energy density, which is the amount of electrical energy per unit volume (Wh/L) or per unit weight (Wh/kg) that the battery can store. With the limited space available for batteries in an EV, and the fact

that weight plays a vital role in the vehicle's performance, high energy density is a must since it results in smaller, lighter batteries that allow the vehicle to travel further.

The EV battery pack is sized to provide acceptable driving range and power output. Battery cells are arranged in a connection of series and parallel strings. Connecting the cells in series defines the total voltage of the battery pack as the voltage of each cell in the string is added. The total capacity is obtained by connecting parallel strings a shown in Fig. 1.1.

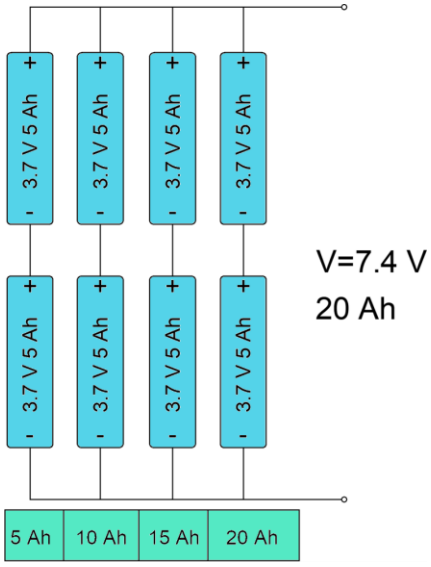

Fig 1.1 Series-parallel connection of battery cells (2 series, 4 parallel)

The cell basic structure consists of a metal oxide cathode, a graphite or graphite silicon blended anode, a separator to prevent direct contact between them and an electrolyte to help with movement of ions [11]. The cell performance is bounded by its electrochemical performance, nominal voltage, energy density, high current capability, thermal stability, cyclability, and safety.

The search for high performing cathode materials to produce batteries with high energy and high power densities resulted in two preferred cathode chemistries among vehicle manufacturers: Nickel Cobalt Aluminium Oxide (NCA) and Nickel Manganese Cobalt Oxide

(NMC). Batteries with $Li[Ni_{0.8}Co_{0.15}Al_{0.05}]O_2$ (NCA) cathodes exhibit high experimental capacity of up to 200 mAh/g compared to other cathode materials including Lithium Manganese Oxide $LiMn_2O_4$ (LMO) with 130 mAh/g [12], Lithium Iron Phosphate Oxide $LiFePO_4$ (LFP) with 120-160mAh/g [13], and Nickel Manganese Cobalt Oxide $Li[Ni_{0.33}Mn_{0.33}Co_{0.33}]O_2$ (NMC333) with 163-220 mAh/g [14]. Both NCA and NMC batteries have high specific energy and can provide satisfactory performance at high current rates [12]. NMC is the chemistry of choice by the majority of Original Equipment Manufacturers (OEMs) including BMW, General Motors, Toyota, Mitsubishi, Daimler, Renault and Nissan while NCA is mainly used by Tesla [15].

Different levels of nickel are used in batteries depending on the application. The ratio between the three metals is indicated by three numbers. For example, $LiNi_{0.333}Mn_{0.333}Co_{0.333}O_2$ is abbreviated to NMC111 or NMC333, $LiNi_{0.5}Mn_{0.3}Co_{0.2}O_2$ to NMC532 (or NCM523), $LiNi_{0.6}Mn_{0.2}Co_{0.2}O_2$ to NMC622 and $LiNi_{0.8}Mn_{0.1}Co_{0.1}O_2$ to NMC811. Due to potential issues with cobalt sourcing, there is interest in increasing the level of nickel, even though this lowers thermal stability [16].

In terms of chemistry, deployment of LFP cells amounted to 52.7 GWh (27% of total) in the first half of 2022, followed by NMC 5-series with 41.6 GWh (21%), NMC 8-series with 36.2 GWh (19%) and NCM 6-series with 12%. NCA Gen 3 made it to the top five with a share of 10% of total deployment. Seven cell suppliers, including (Contemporary Amperex Technology Co. Limited) CATL, LG Energy Solution, Panasonic, Build your dreams (BYD), SK On, Samsung SDI and China aviation lithium battery technology (CALB), are responsible for more than 82% of all battery capacity and battery metals deployed into roads globally in passenger EVs in the first half of 2022 [17]. In terms of the total battery capacity deployed in electric vehicles including battery electric vehicles (BEV), plug-in hybrid vehicles

(PHEV), and HEV, Asia Pacific dominates the global market with 113 GWh deployed compared to Europe with 48.1 GWh, Americas with 33.4 GWh, and Middle East and Africa with 1.1 GWh [17].

Vehicle performance and charging time are a direct function of the battery power capability. During power intensive events, such as acceleration, the battery should be able to discharge at high rates to meet the demand. On the other hand, the ability to accept high current rates is critical for energy recovery during regenerative braking and charging speed. The peak C-rate for charging a Tesla Model 3 with 75 kWh battery pack (2019 LR all-wheel-drive (AWD) V3 SV) is about 3.3C and the average C-rate when charging from 20% to 80% state of charge (SOC) is about 1.5 C. A comparison between 3 different models is shown in Table 1.1 [18]. The C-rate capability of the batteries installed in these vehicles allows for a charging time (20%-80% SOC) that fluctuates between 23-26 minutes. Batteries with higher C-rate capabilities are required to achieve charging time below 5 minutes.

Table 1.1. DC fast charging comparison of Tesla Model 3 vehicles with 75 kWh and 80 kWh batteries [18]

DC Fast Charging Comparison by InsideEVs						
Model [data source]	Drive / Battery (kWh)	Max Power	Avg Power (20-80%)	Max C-Rate	Avg C-Rate (20-80%)	Time (20-80%)
2019-2020 Tesla Model 3 LR [Fastned]	AWD 75 kWh	**195 kW**	**128 kW**	2.6	1.7	**23 min est.**
2021 Tesla Model 3 LR AWD (V3 SV) [Tom Moloughney]	AWD 80 kWh	**250 kW**	**106 kW**	3.1	1.3	**26 min**
2019 Tesla Model 3 LR AWD (V3 SV) [Tom Moloughney]	AWD 75 kWh	**250 kW**	**113 kW**	3.3	1.5	**24 min**

The DC fast charging rate for 3 different Tesla Model 3 vehicles is shown in Fig. 1.2.

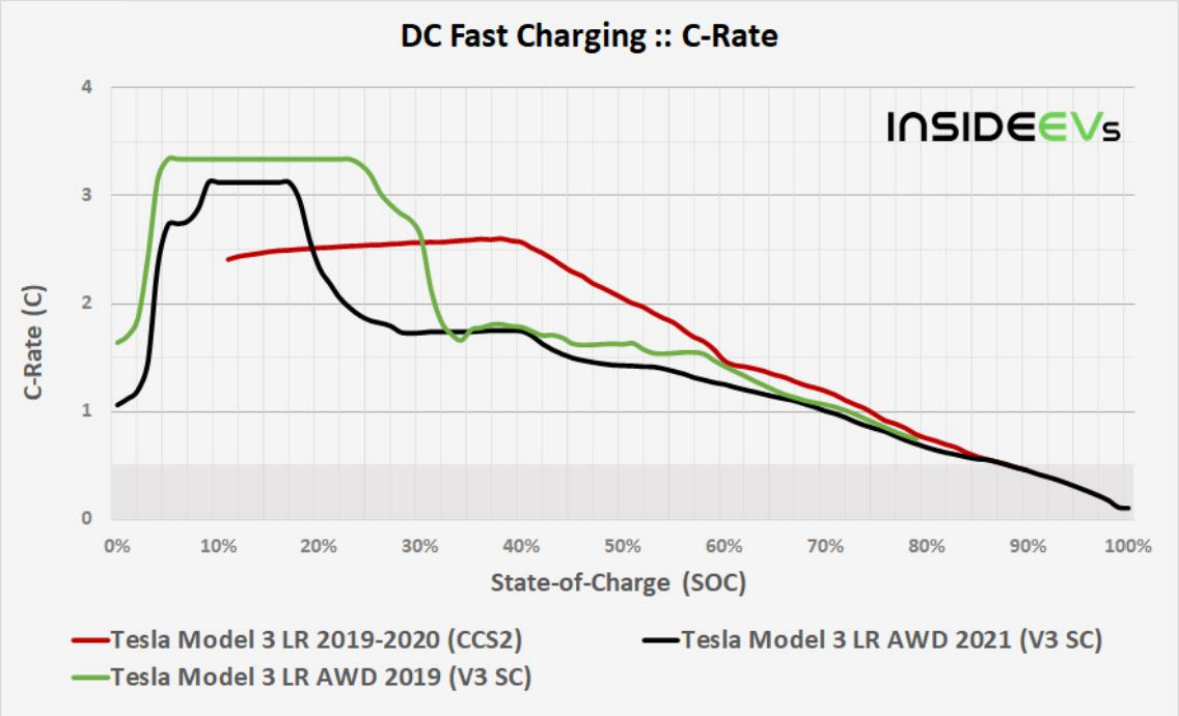

Fig.1.2 DC fast charge comparison curves for Tesla Model 3 vehicles [18]

Battery prices have declined during the last decade reaching a sales-weighted average price of USD 132/kWh [4]. However, this price must decline even further to make EVs more affordable and speed up the uptake. With the unprecedented rise in battery metal prices caused by production challenges as a result of both the coronavirus pandemic and the war in Ukraine, as well as an increase in battery demand, tighter supply chains, and increased production costs, it is estimated that battery prices will increase at least by 15% from their average in 2022 [3]. As a result, automakers will face major challenges, resulting in higher battery costs, reduced manufacturer margins, and higher prices for consumers.

1.2 Battery ageing

The capability of the battery to charge and discharge at high rates is critical for rapid charging and high power delivery. However, this is limited by the electrochemical processes occurring

in the battery including the electron transport in electrodes, ion transport both in bulk electrolyte and electrolyte-filled pores, solid-state diffusion of ions in the active materials and electrochemical reactions at the electrode/electrolyte interface [19].

One of the most challenging aspects of battery design is to increase energy density while maximising power output and battery life. Battery manufacturers use different approaches to optimise cells to achieve high energy and high power densities. Research efforts to improve energy density at cell level include the development of high capacity anode and cathode materials, improvements of electrode design and composition, and optimisation of cell architecture. In terms of rate performance, research has shown that improvements can be obtained by increasing solid-state diffusivity, electrode porosity and the optimisation of electrolyte properties including concentration and viscosity [20]. Currently, there is an inevitable trade-off between energy and power, as the requirements for maximum energy density are conflicting with those for high power density [21].

To reach peak vehicle performance while avoiding premature battery degradation, the battery pack must be able to provide/accept peak currents that lay within the manufacturer's recommended rate of charge/discharge, usually specified in terms of C-rate. Battery manufacturers often indicate the maximum continuous and pulse (<10s) charge and discharge C-rates in the battery specifications. Batteries designed for energy applications exhibit relatively low charge/discharge rates (<3C), whereas batteries designed for power applications show high rates (>3C). The C-rate is defined as the current through the battery divided by the theoretical current draw under which the battery would deliver its nominal rated capacity in one hour [22]. Certainly, the battery can discharge beyond this value for short periods of time, usually with detrimental effects on its cycle life.

Electrolytes, anodes, cathodes, and the structural components used in batteries, all undergo

irreversible changes as the battery ages. Battery performance and degradation are determined by how it is operated. In automotive applications, the following factors contribute most to degradation (not arranged in any specific order or grouping) [23]:

- Environment temperature
- Discharging current rate
- Charging current rate
- Depth of discharge
- Time intervals between full charge cycles

The internal resistance of the battery increases at low ambient temperatures because the viscosity of the electrolyte increases, aggravating the diffusion and movement of the lithium ions between the positive and negative electrodes. In simple words, chemical reactions occurring in the battery are slowed down. This leads to poor performance and accelerated battery degradation. In contrast, operating batteries in hot environments worsens the cell temperature build-up due to internal heat generation, resulting in loss of capacity from lithium loss and reduction of active materials, as well as increased internal resistance which leads to reduced power. Operating above or below the acceptable temperature range (15-35 °C) accelerates the ageing process [24].

Battery degradation is affected by the rate of charging and discharging. In EVs the discharge rate is influenced by power demand variations caused by changes on the slope of the route, the weight of the car, and the speed and acceleration of the vehicle. During braking, it is possible for the lithium-ion traction battery to be damaged by peak current recharge periods during regenerative braking [25]. To protect the battery from degradation, potential braking power is wasted by activating the friction brakes. Likewise, fast charging has shown to accelerate degradation, reducing both capacity and power capabilities [26].

Battery cells will degrade if they are operated at a rate exceeding the manufacturer's recommendation. Bryden et al. [27] confirmed this conception by carrying out an experiment where two identical Lithium-ion NMC energy cells were cycled to determine cell degradation. One of them was discharged at the manufacturer recommended discharge rate of 1C and the other at maximum discharge rate of 3C. The cell cycled at higher rate degraded faster than the cell cycled at the standard rate. After 400 cycles, the cell discharged at 3C had 81.4% of the maximum capacity while the cell discharged at 1C had 83.9%. This study also confirmed that high discharge rates increases the cell's temperature, which contributes to degradation. Degradation due to charging was not analysed in the mentioned work, however, it is worth noting that the manufacturer recommended C-rate for charging was 0.5C and the maximum 1C, so anything beyond this figures would result in accelerated degradation. It is typical of energy batteries to have specifications similar to those of the energy cells used in this study. A key observation is the relatively high current rating for discharge, but low ratings for charge. Table 1.2 shows typical charge and discharge C-rates for different battery chemistries [28].

Table 1.2. Comparison of C-rates for different battery chemistries

Battery Chemistry	**Charge C-rate**	**Discharge C-rate**
$LiFePO_4$. Lithium Iron Phosphate (LFP)	1C	1C
$LiCoO_2$. Lithium Cobalt Oxide (LCO)	0.7C-1C	1C
$LiNiMnCoO_2$. Lithium Nickel Manganese Cobalt Oxide (NMC)	0.7C-1C	1C-2C
$LiMn_2O_4$. Lithium Manganese Oxide (LMO)	0.7C-1C	1C-10C, 30C pulse
$LiNiCoAlO_2$ Lithium Nickel Cobalt Aluminium Oxide (NCA)	0.7C	1C
Li_2TiO_3 Lithium Titanate (LTO)	1C-5C	10C-30C

EV manufacturers often oversize the battery pack to achieve high energy and acceptable power density to match the desired vehicle performance, thus realising both longer range and improved power handling, but at the expense of system's weight and cost [29]- [30]. The

main objective of battery oversizing is to guarantee that the battery operates within the manufacturer's specifications when it is exposed to high current charge and discharge rates derived from demanding driving conditions. In this way the battery cycle life is not compromised by premature degradation. Batteries used in EVs have a cycle life defined as the number of full discharge-charge cycles that it takes to reduce a cell's capacity to 80% of its original value [31]. A typical battery layout and location in an EV is shown in Fig. 1.3.

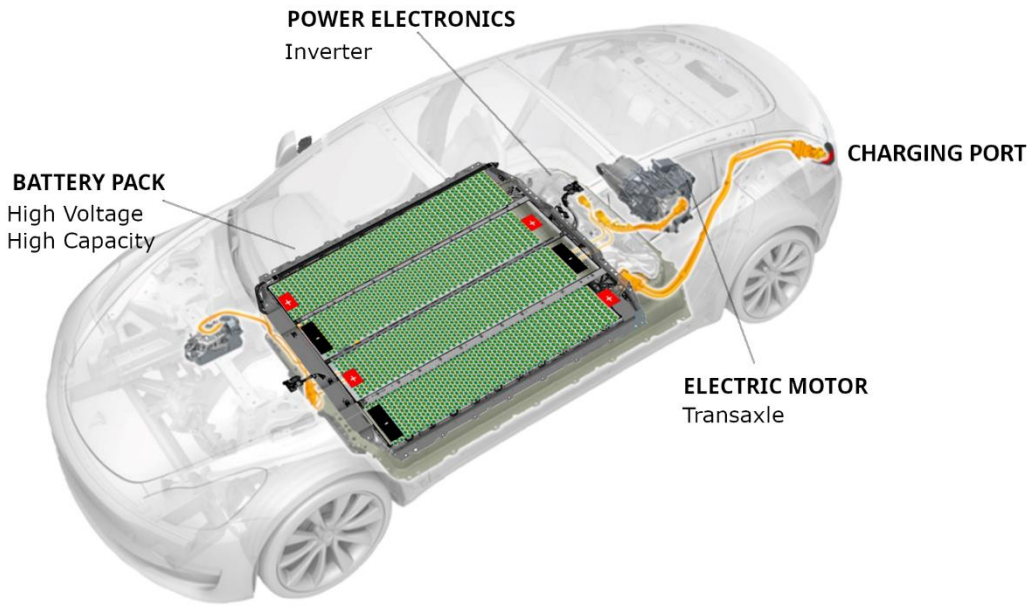

Fig. 1.3 Typical battery layout and location in an EV

1.3 Hybridisation as an alternative to boost the energy storage system power capability

Hybridising the EV ESS by complementing a battery designed for maximum specific energy with a power-dense source dedicated to delivering peak power can realise battery life improvements and enhance the ESS performance [32], [33]. The high power source provides for the rapid response to power demand, which reduces the battery charge/discharge C-rate, and recovers energy from braking, relieving the battery from the stress imposed by short time peak charging currents. The Hybrid Energy Storage System (HESS) can be designed to have

both high energy and high power capabilities. Literature suggests Supercapacitors (SCs) [34] - [35] and high power batteries [36]- [37] as feasible devices to complement the high-energy battery and achieve substantial improvements in vehicle performance, durability, and economy. SCs are attractive for this application because they have much higher power density (3000-14000 W/kg), longer cycle life (100.000-1.000.000 cycles), wider operational temperature range (-40˚C to 70˚C) [38], and smaller internal resistance than batteries (typically an order of magnitude lower than batteries) [39]. However, they lack energy density (1-10 Wh/L compared to 250-650 Wh/L of energy batteries) [39]. Therefore, with hybridisation, batteries and SCs complement each other and their combination exploits their benefits [10], [40]. Hybridisation can lead to the following scenarios:

- Battery size reduction: The capacity of the battery can be reduced (connecting less parallel strings) as the SC compensates for the reduction in the battery power output. However, this also reduces the vehicle's driving range, which is undesirable.
- Bigger powertrain: The vehicle's performance can be improved with a bigger powertrain. The higher peak power demand can be provided by the battery and SC. In this case the EV performance is improved.
- Battery peak power relief: The battery is complemented with SCs resulting in a reduction of the charge/discharge C-rate. In this case, battery cycle life is improved.

This work focuses on relieving the battery from peak power during acceleration and braking by adding SCs to the system.

1.4 Supercapacitor

SCs are high capacity capacitors, with capacitances much higher than electrolytic capacitors. It stores 10 to 100 times more energy per unit of volume or mass (higher energy density) than the latter. Its main advantage is that is able to accept and deliver charge at high rates and

tolerates many more charge and discharge cycles than other power sources such as batteries. Due to these characteristics, they are often used in applications where many rapid charge/discharge cycles are required. Unlike ordinary capacitors, SCs do not use the conventional solid dielectric, but rather, they use electrostatic double-layer capacitance and electrochemical pseudo capacitance [41]. More details regarding this technology will be introduced in later chapters.

1.5 Power split: The role of the energy management system

The design and implementation of the Energy Management System (EMS) is the most significant challenge in HESS design and control. It depends upon a number of variables including the control topology, power split strategy, driver commands, state of charge, and limitations of each power source [32]. The aim of the EMS is to determine the current references to control the battery and SC power contribution, considering the strengths and weaknesses of each power source. It also ensures that the system operates within specifications and strives to improve the overall efficiency of the system.

The main EMS task is to control the SC to assist the battery during sudden power demands caused by changes in acceleration or road grade, and recover the energy generated when braking. Different approaches have been proposed to achieve this task, which can be broadly classified into rule, frequency and optimisation based control strategies as shown in Fig. 1.4 [42].

Rule-based EMSs are suitable for implementation in real time controllers due to their simplicity and convenience. These methods are based on empiric human expertise where a set of rules are generally implemented as lookup tables or if-then expressions. However, its control performance is heavily dependent on rule-switching thresholds, which cannot always provide good results in the face of different driving conditions [43]. Rule-based strategies are

classified into deterministic approaches, fuzzy logic and feedback based approaches. Frequency based strategies are used to decompose a given signal into its high and low frequency components using techniques such as the discrete wavelet transform and conventional filtering control. Optimisation based strategies employ advanced optimisation algorithms such as dynamic programming, particle swarm optimisation, genetic algorithm, Pontryagin's minimum principle, model predictive control and optimisation of rule based control approaches to explore the potential economic performance of the HESS, minimise losses, size the HESS optimally, and reduce the current magnitude and fluctuation seen by the battery. However, their complexity results in heavy computations based on known driving cycles and power demand profiles, which result in long processing times that prevent their implementation in real-time systems. Therefore, they are usually used for benchmarking purposes. Real time implementation is possible through optimisation of a rule based strategies, model predictive control, stochastic dynamic programming, and adaptive approaches.

This thesis focuses on filtration strategies through which power demand can be decomposed into frequency components that match the dynamics of the power sources. EMS strategies based on conventional filters, i.e. low and high pass filters [44] [45] [46] [47], and the Discrete Wavelet Transform (DWT) [48] [49] [50] have been proposed to extract frequency components from the power demand. This technique is chosen as it has been widely used by researchers as the main component to build EMSs. However, some details are still missing in the literature, especially when the DWT is used to split the power in the HESS. Studying these details constitute the focus of this research, including the effects of delay, the efficacy of the SC assistance during motoring and braking, and the system's energy efficiency in light of delay.

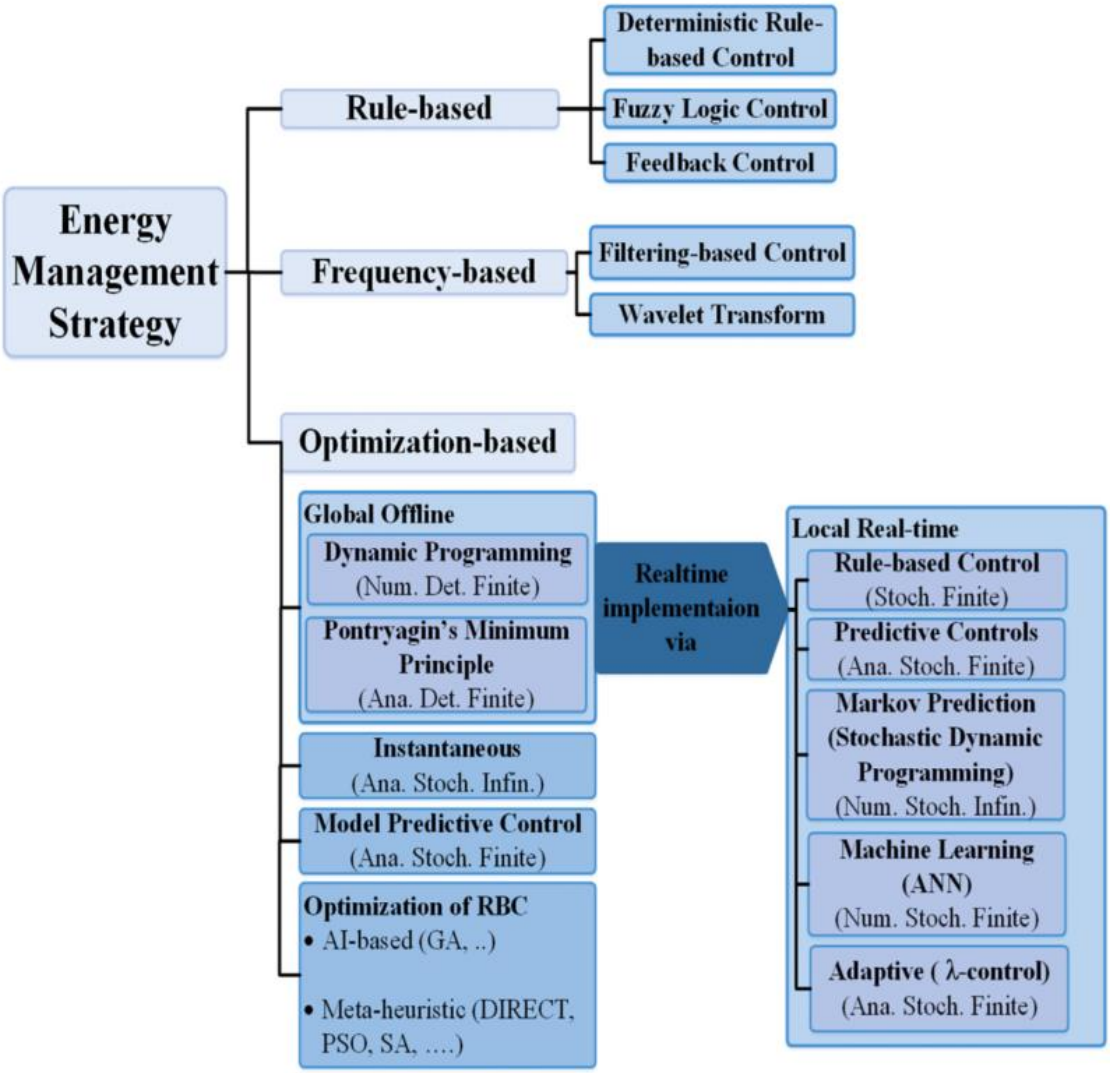

Fig. 1.4 Energy management strategy classification [42]

Based on the hybrid system topology, an energy management system coordinates the distribution of energy. There are three types of interconnection topologies: passive, semi active and active [51], [52], [53]. In passive topologies, power is distributed based on the ESS output characteristics and internal resistance, so power is naturally distributed without any control action. Active topologies use two bidirectional DC/DC converters to interface the ESS elements to the DC-bus, actively managing power flow of each ESS element. This design option compromises cost, volume and control complexity. Semi-active topologies connect one energy storage source straight to the DC-bus, while the other is connected

through a DC/DC converter. A SC semi-active topology is considered in this work, where a bidirectional DC-DC converter is used to control the power contribution of the SC with a high frequency current reference determined by the EMS. The high-energy battery is connected directly to the motor drive, defining the voltage of the DC-bus. This topology is typically chosen in automotive applications as it balances cost and control complexity [54].

1.6 Power split issues with an energy management system based on frequency sharing techniques

The selection of the filtration strategy, as well as the particular characteristics of the filter, can compromise the performance of the system and undermine the benefits of using the SC in the HESS [55]. High pass and low pass filters can introduce a phase shift in the filtered signal and thus the output of the filter can lag (low pass filter) or lead (high pass filter) the input signal. DWT based approaches can introduce long time delays in the frequency components. Using the delayed frequency components to control the SC, results in some issues such as failing to assist the battery during peak positive and negative power demand, exposing the battery to undesirable peak power, energy inefficiency, and an increase in the system energy loss due to energy circulation between the battery and SC via the DC/DC converter. The author defines energy circulation as the energy transfer (in a HESS connected in a SC semi-active topology) between the battery and SC with other purposes other than assisting the battery during positive power demand and recovering energy during braking. This uncontrolled ‘excess’ energy circulates through the DC/DC converter (which is not 100% efficient), increasing the system energy losses, compromising the system’s efficiency. Energy circulation is, of course, an inefficient process that is exacerbated by delay.

To deal with the long-time delays in the frequency components, especially with the DWT approach (from few seconds to tens of seconds), power demand prediction approaches using recurrent neural networks such as nonlinear autoregressive neural network (NARNN) [49],

nonlinear autoregressive neural network with exogenous input (NARX) [56], and Long Short Term Memory (LSTM) neural networks [57], have been proposed in the literature to compensate for the delay and enable the use of the frequency components in real time. In this work, the LSTM neural network approach is chosen, as this type of recurrent neural network has been experimentally proven to have higher prediction accuracy than the standard recurrent neural networks (RNN) [58]. However, an analysis of whether time compensation improves the system performance is missing in the literature. A thorough investigation of the effectiveness of the SC contribution with and without time delay compensation, as well as the influence of energy circulation in the system's efficiency, constitutes the purpose of the present work. Effectiveness is assessed by comparing the SC contribution during positive and negative power demand against a benchmark signal that is proportional to the rate of change of current (during positive power demand) and includes the energy generated during braking. The determination of this signal is detailed in section 3.4.4.

1.7 Research questions

This thesis examines the design, simulation and implementation of a Real Time EMS to control power flow in a HESS composed of a battery and a SC. Simulations consider Lithium –ion batteries, while the experiment includes a lead-acid battery. The latter was chosen as these batteries were readily available in the lab. However, this would not influence the result of the experimental part as the intention of this work is to demonstrate the performance on an energy efficient EMS with the capability to split the power demand in a HESS in real time. For this specific purpose, the use of a lead-acid or a lithium battery in the experimental part makes no difference. The HESS performs in an EV where highly dynamic power demands are expected.

The specific research questions motivating this work are:

1. What are the effects of time delay in power distribution and efficiency of the hybrid system?
2. Does compensating for time delay in the frequency components with a power demand prediction approach improve the performance of the system?
3. How to fairly assess the performance of the SC with different frequency sharing techniques?
4. How the performance of an EMS based on DWT does compare to one based on conventional filters?
5. How to improve the system efficiency by controlling energy circulation in the system?

1.8 Aims and objectives

The aim of this thesis is to investigate the effects of the time delay in power distribution and the system's energy efficiency when the HESS real time EMS is based on frequency sharing techniques including the DWT and conventional filters. This understanding allows for the development of a novel method to tackle the delay problem and its side effects, so the HESS can perform efficiently.

This aim will be achieved through the following objectives:

1. Build a DWT decomposition/reconstruction multiresolution tree in Simulink to assess the difference between the original signal, the sampled signal and the filtered signal for different levels of decomposition and sampling rates.
2. Build a detailed electric vehicle model in Simulink using appropriate reported methodologies to produce realistic results.
3. Compare the performance of conventional filters with different cut-off frequencies versus the DWT for different driving cycles.

4. Build a LSTM to perform power demand predictions to compensate for the DWT delay.
5. Assess the advantages and drawbacks of power demand prediction as a way to compensate delay.
6. Validate the proposed EMS experimentally by exposing the experimental rig to a varying power demand signal that includes positive (motoring) and negative (braking) power demands. The experimental results will be compared to that of a system without the proposed EMS.

1.9 Scope

The design and implementation of a real-time EMS controller based on a frequency sharing approach is the focus of this project. The development of a novel high fidelity battery, SC, DC/DC converter, motor, and motor drive models as well as the optimal sizing of the sources are beyond the scope of this investigation. The investigated ESS comprises a battery and a SC interfaced in a semi-active control topology. The architecture of the system is shown in Fig. 1.5. A driver model is used to obtain the torque demand. With this signal, the motor drive controls the torque requirements of a permanent magnet synchronous motor (PMSM) and supplies the power demand from the hybrid energy storage system connected in a SC semi-active topology. This topology uses a DC/DC converter to interface the SC to the DC-bus, while the battery is directly connected to the motor drive. The power delivered by each power source is determined in real time by an EMS that accounts for the SOC of the power sources and the real time current demand measured at the DC-bus. The scope of the EMS comprises the determination of a current reference to control the SC so it provides a portion of the total energy required during accelerations and recovers the energy generated during braking (when its SOC allows it). As the voltage of the system will be set by the battery, the DC/DC converter will be controlled in current mode. This is the reason a current reference needs to be calculated to split the power. An energy flow analysis is conducted to determine

energy losses in the system, including the losses that occur due to energy circulation influenced by delay.

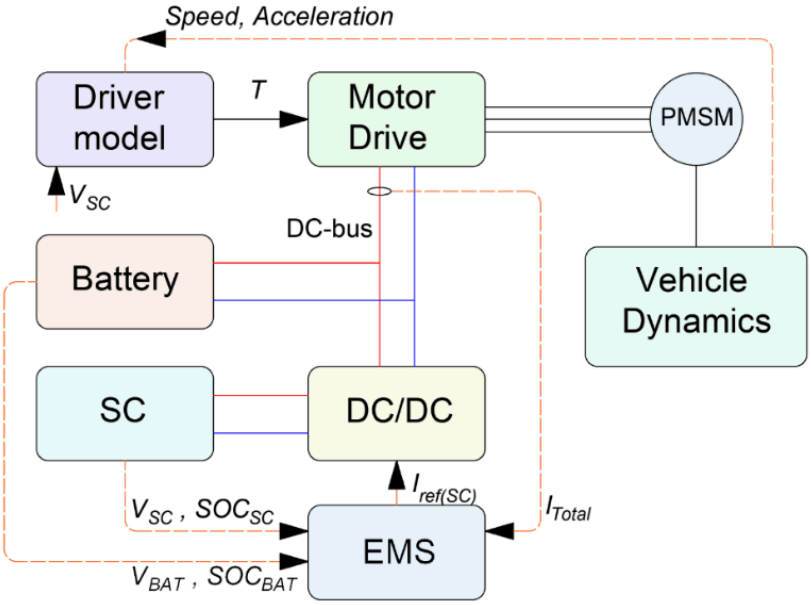

Fig. 1.5 Electric vehicle model architecture

Power demand prediction with LSTM is implemented to compensate for the delay. An analysis of advantages and disadvantages of this approach are analysed in detail to ultimately determine if compensation of delay improves the performance of the system and reduces energy losses. The vehicle's power demand considered in this study is limited to propulsion loads and additional power requirements of auxiliary loads and their associated losses are not considered. The core of the work focuses on addressing power arbitration with frequency sharing techniques whilst minimising energy losses in the system and mitigating the effects of delay including the late response of the SC, failing to relieve the battery from peak power, and uncontrolled energy circulation.

A consequence of relieving the battery from peak power during motoring and braking is the reduction of the battery temperature. As temperature is one of the main factors affecting battery lifetime, the proposed EMS is expected to improve the battery cycle life. However,

the detailed analysis of battery lifetime improvements and its relation to temperature is not within the scope of this work.

1.10 Methodology

The research begins from the general proposition of providing additional high power capability to a battery only system by installing a SC with the objective to boost the battery cycle life. Firstly, a detailed EV model comprising the vehicle dynamics, powertrain, driver model, and a battery ESS is implemented in Matlab-Simulink. The strengths and weaknesses of the battery only system in a vehicular environment are analysed and used as the benchmark. Subsequently, subsystem models and baseline design parameters of the HESS are obtained through iterative simulations and reference to relevant literature.

The research proceeds in reviewing past and current techniques to coordinate the operation of multiple power sources in EVs, with a special focus on the application of frequency sharing techniques to control power flow in a SC semi-active control topology.

An EMS based on the DWT approach to obtain the frequency components is implemented and analysed in Matlab-Simulink. The effects of long time delays (specifically a delay of 4 seconds) in power distribution and in the system's efficiency are studied in detail. A power demand prediction approach using LSTM neural networks is implemented with the purpose of compensating for the delay produced by the DWT signal decomposition process. For this purpose, a deep learning Application Programming Interface (API) written in Python known as Keras [59] is used for developing, training and testing the neural network.

As results show that prediction alone is not sufficient to bring the desired performance and fully mitigate the issues produced by delay, a novel approach to determine the SC current reference is implemented. This approach controls energy circulation in the system and allows the SC to provide assistance during motoring and recover the energy generated during

braking.

To assess the performance of the SC, an algorithm to determine a benchmark signal is developed. This benchmark allows for a fair comparison of the results obtained with different filtration approaches. A comprehensive comparison of the results obtained with EMSs based on the DWT and conventional filters is carried out to determine which technique delivers superior performance in terms of SC assistance, battery relief and reduced energy losses. Energy efficiency is calculated for each method.

A low power test rig is assembled to test the best performing EMS under dynamic power demand profiles. The ratio between the battery simulated (40.6 kWh) and the battery used in the experiment (4.22 kWh) is 96.3:1. The energy ratio between the SC simulated (430.5 Wh) to the one used in the experiment (5.07 Wh) is 85:1. The battery is connected directly to the input of the motor drive, defining the voltage of the DC-bus. The SC is interfaced to the dc-bus through a half bridge bidirectional DC-DC converter.

Two three-phase PMSM are coupled in a dyno setup. Motor 1 runs in the closed-loop speed control mode. Motor 2 runs in torque control mode and loads Motor 1 as they are mechanically coupled (back to back connection). The setting allows to use a different speed reference for Motor 1 and a different torque reference for Motor 2. Motor 1 runs at the reference speed for the load conditions provided by Motor 2.

Both motors are individually controlled with a Field Oriented Control (FOC) approach implemented using a Texas Instruments LAUNCHPADXL F28069M microcontroller and 2 BOOSTXL DRV8305EVM 3-phase motor drives. Real time data acquisition, control and monitoring is performed via Matlab and Simulink. The proposed real time EMS is implemented in a Texas Instruments LAUNCHPADXL F28027F microcontroller, which

monitors the currents measured at the DC-link, SC, and battery, as well as the voltage of the SC. The SC current reference is determined in real time based on the acquired data and used to control the bidirectional DC-DC converter.

1.11 Thesis contribution

In the literature, many authors have theoretically demonstrated how power is distributed between power sources in a HESS. Systematic procedures and complete implementation of such systems are rarely detailed in literature. It is expected that practical implementation of the systems involved will uncover significant findings that cannot be found with purely theoretical approaches. There is a wealth of research studying the implementation of SCs as part of a hybrid system, and the EMSs to determine the proportional power split. Nevertheless, a thorough investigation of the effective SC contribution with filtration approaches, with and without time delay compensation, and the effects of delay on the system's efficiency remain to be conducted. Moreover, energy circulation between the battery and SC as a consequence of delay and the effects on the system's efficiency has not been addressed before. Finally, a back-to-back comparison between results obtained with conventional filters versus those obtained with the DWT are not available in the literature. This work presents a fresh perspective to this research field by introducing a novel approach to reduce energy losses in a semi-active control topology managed with frequency sharing techniques.

The contributions of this work are summarised as follows:

1. Investigation of different real time EMS implementations based on the DWT and their performance in terms of energy circulation due to time delay, SC assistance, and energy efficiency during motoring, acceleration, and braking.
2. Design of a LSTM neural network to predict future power demand before it is fed to the

DWT to compensate for the time delay. Unlike neural networks presented in the literature, this network has been trained offline using power demand corresponding to 8 different standard driving cycles and tested using 3 driving cycles not included in the training dataset to ensure network generalisation capability.

3. Evaluation of the effectiveness of time delay compensation in improving the performance of the SC in a HESS controlled with an EMS based on the DWT.
4. Development of a novel EMS strategy that allows the SC to assist the battery during the motoring stage, recover the energy generated during braking, and improve the efficiency of the system by controlling energy circulation between the battery and SC to maintain its availability.
5. Detailed real-time implementation of the proposed EMS in a microcontroller and experimental validation with a PMSM low power test rig.

1.12 Thesis outline

This thesis is organized into 6 chapters. Each chapter starts with a brief introduction to provide an overview and highlight the main contribution and findings of the chapter.

Chapter 1 establishes the context in which the research will take place and explains why it is important. It provides a brief background about HESS comprising batteries and SCs in electric vehicles and the real time EMS necessary to control power flow. This is followed by a description of the research questions, scope of the work, methodology and contributions.

Chapter 2 presents literature review to understand state of the art EMS approaches that are based on frequency sharing techniques including the DWT and conventional filters. This chapter identifies and describes the knowledge gaps and highlights the contributions of this work.

Chapter 3 details the DWT Matlab/Simulink implementation to obtain power demand frequency components and how this process introduces delay in the filtered signals. The effects of delay in the HESS power distribution is assessed. Power demand prediction is implemented to compensate for the delay and enable the DWT to be applied in real time. The benefits of power demand prediction are investigated by comparing the performance of the HESS with and without prediction. 4 different real-time implementation for the DWT based EMS are evaluated using different metrics to assess the HESS performance.

Chapter 4 details the development of a real time EMS approach that uses first order filters to determine the SC current reference in a way that enables the SC to assist the battery during motoring, recover all the braking energy generated, and improve the system efficiency by controlling energy circulation. Simulation results obtained in this chapter are compared with those obtained in chapter 3 in order to assess the performance of the proposed method. Moreover, the results obtained with the proposed EMS are compared to those obtained with traditional filtration mechanisms as detailed in the literature, highlighting the superiority of the proposed method.

Chapter 5 reports the experimental implementation of the hardware and software required to validate the proposed real time EMS.

Chapter 6 concludes the thesis and explores suggestions for future research

CHAPTER

2

2 LITERATURE REVIEW

2.1 Improving battery lifetime and power capabilities of the energy storage system through hybridisation with SCs or high power batteries

Academic researchers studying hybridisation of the ESS for EV applications agree that the main goals of the high power source as part of the HESS is to extend battery life [60]- [61] and improve the system power capability. Hybridisation involves complementing the high energy battery with a power dense source dedicated to deliver peak power, provide rapid response to power demand (defined by the SC time constant), and recover energy from braking. In this way, the high energy battery is relieved from the stress imposed by peak power demand with a resulting improvement in lifetime. The time constant of most commercial SCs normally ranges from 0.5 to 3.6 seconds, where the time constant is defined as the product between the internal resistance and the capacitance. Smaller time constants reflect better responsiveness of the SC [62].

Several studies suggested that SCs [34]- [35] or high power batteries (HPB) [36]- [37] can complement high-energy batteries and improve vehicle performance, durability, and economy. The advantages of SCs over HPBs in this application include higher power density (SC: 3000-14000 W/Kg vs HPB=4200 W/kg), longer cycle life, wider temperature range, and lower internal resistance [63]. However, they have some disadvantages, the most important being their lack of energy density, lower nominal voltage compared to batteries, and their high deployment cost. The latter is a barrier preventing the application of SCs in EVs as their implementation is potentially more costly compared to the battery oversizing option. Battery costs have declined significantly

reaching an average of USD 132/kWh in 2022 [3] compared to more than USD 1100/kWh in 2010 [64]. This has been possible due to the continuous developments in technology and the establishment of battery mega factories that boosted economies of scale and manufacturing processes. On the other hand, SC cost per kWh remain quite high. Literature reports SC prices that vary between USD 3000/kWh [65] and 10000/kWh [66]. Clearly, SCs are not competitive on a USD/kWh basis with battery technologies. Nevertheless, they are more competitive in a USD/kW basis, with prices between USD 160/kW and 401/kW [67]. The number of SCs that must be connected in a series and parallel arrangement to match the required operational voltage range (~200V-400V) and the capacity to provide the power necessary to relief the high energy battery from power stress during a given driving cycle, yields an expensive system. In this context, batteries optimised for high power density offer an alternative. Due to the significant development of materials and components for battery manufacturing in recent years, high power density is achievable by optimising battery cell design and chemistry. The main advantages of high power batteries over SCs are their higher energy density and less voltage variation. Table 2.1 shows a side-by-side comparison between a high energy battery, a high power battery and a SC.

Table 2.1. Comparison of high energy battery, high power battery and SC

	High Energy Battery	**High Power battery**	**SC**
	Samsung INR21700-50E 5Ah [68]	Kokam SLPB11543140H5 [69]	Maxwell BCAP3400 [70]
Chemistry	NCA	NCM	-
Weight	70 gr	132 gr	496 gr
Capacity	4.9 Ah	5 Ah	3400F Capacitance
Nominal Voltage	3.6 V	3.6 V	3.0V
Continuous discharge	9.8 A (2C)	150 A (30C)	140-225 A
Maximum discharge (pulse)	14.7 A (3C)	250 A (50C)	2800 A
Charge current standard	2.45 A (0.5C)	20 A (4C)	140-225 A
Max charging current	4.9 A (1C)	20 A (4C)	140-225 A
Gravimetric Energy Wh/Kg	257	140	8.57
Gravimetric Power kW/Kg	0.77	4.2	14.5
Cycle life	500 cycles	800 cycles	1000000 cycles

The comparison between the HESS power sources reveals their strengths and weaknesses. The SC is clearly superior in terms of discharging and accepting high currents. The high power battery cell has higher nominal voltage and much higher gravimetric energy than the SC. Although the discharge current of the power battery is acceptable for hybridisation purposes, the charge current is still low (20A per string). Therefore, several parallel strings would be required to improve the charging current. In terms of size and volume, Fig. 2.1 shows a scale drawing of the three types of ESS.

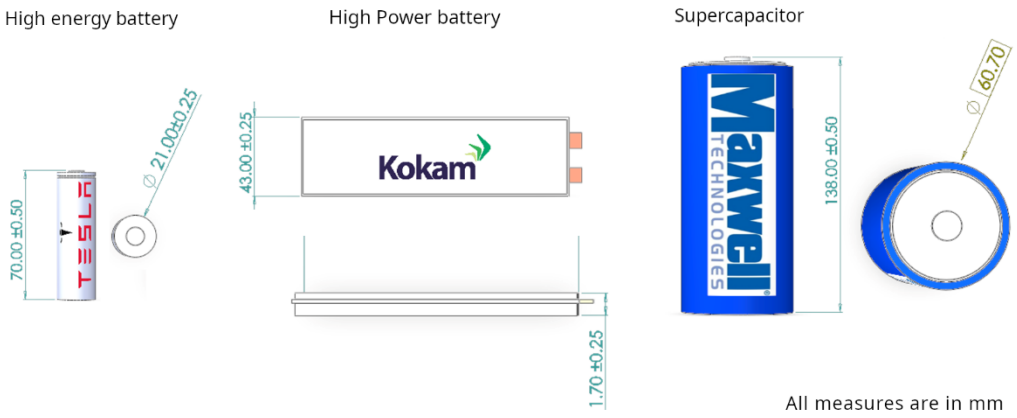

Fig. 2.1 Size and volume comparison of a 21700 cylindrical battery cell (high energy battery), prismatic high power cell, and cylindrical SC

Volume and weight are important parameters to consider when designing and sizing the HESS. The sizing and economic optimisation considering either SCs or high power batteries is an exercise that goes beyond the scope of this work. The EMS design, models and simulations performed in this thesis assume SCs as the high power source, considering the high charging and discharging currents as the main factors for choosing this technology. Nevertheless, the solution developed in this thesis still apply to high power batteries, however, in this case the EMS must impose additional charge/discharge rate limits to safeguard the lifetime of the power battery. The control principle of the HESS is to make batteries and the SC work together to meet the total power demand by allocating the battery with the average power and SC with peak and fluctuating power demand. Ideally, the SC should assist the battery to cope with sudden power demands caused by changes in acceleration and recover the energy generated when braking.

2.2 Hybrid energy system topologies

In general, HESS topologies can be classified as passive, semi-active, and fully active.

2.2.1 Passive topology

The passive topology is the simplest way to combine a battery with a SC. In this topology, the battery is connected in parallel with the SC as shown in Fig. 2.2. Power flow is naturally allocated between the battery and SC depending on their internal resistances. As the SC has lower internal resistance than the battery, it reacts faster to sudden changes in power demand, effectively acting as a low pass filter [71]. The major advantages are the simple implementation and low cost as power converters are not included. However, as the SC is directly connected to the battery, its operation voltage is limited by the battery, therefore, the energy stored in the SC cannot be fully utilised.

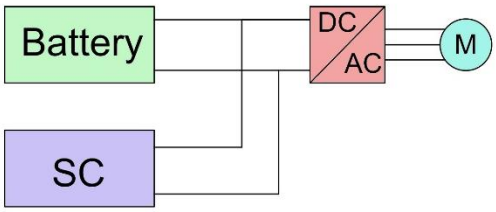

Fig. 2.2. Battery and SC interfaced directly via the DC-bus in a passive topology

2.2.2 Semi-active topology

With the semi-active topology, the power contribution of the battery or the SC can be controlled through a bidirectional DC/DC converter. With the battery semi-active topology as shown in Fig. 2.3a, the DC/DC converter is used to control the battery while the SC is connected directly to the DC-bus. In this case, the voltage of the DC-bus fluctuates according to the variation of SOC of the SC, which is the disadvantage of this approach as the SC voltage varies in a wide range. Conversely, the SC semi-active topology offers a more stable DC-bus voltage as it is set by the battery. This topology is one of the most widely used configurations [71]. In this case the SC power

contribution is controlled through the DC/DC converter. The HESS topology adopted in this thesis is the SC semi-active topology as shown in Fig. 2.3b.

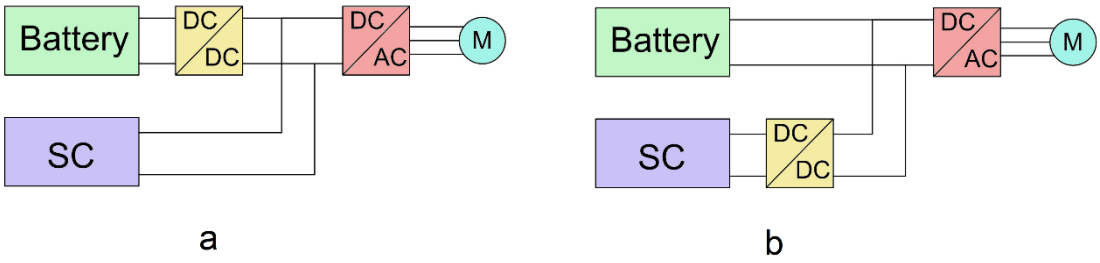

Fig. 2.3. a) Battery semi-active control topology b) SC semi-active control topology.

2.2.3 Fully active topology

The fully active topology enables full control of the power contribution of each source in the HESS. For this purpose, each source is connected to the DC-bus through a DC/DC converter. Although this increases the degrees of freedom in terms of control, it also adds complexity to the system and increases the cost. The schematic of this topology is shown in Fig. 2.4.

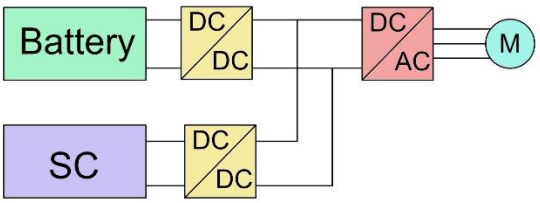

Fig.2.4. Fully active control topology

2.3 Energy management system based on frequency sharing techniques

Filtration based techniques have been widely proposed to decompose the power signal into its frequency components. The basic principle is that low frequency components are provided by the battery and high frequency components by the SC. In this way, the battery can be relieved from sudden changes in power demand during the motoring and braking stages. The high-frequency component represents sudden variations in the power demand as a result of changes in the vehicle speed due to acceleration and braking commands and is allocated to the high power density source. The low-frequency component corresponds

to the average power requirement and is allocated to the high energy density source. Some of the frequency-based methodologies proposed in the literature include first-order filters [72]- [73] (represented in continuous time), digital filters [45], [74] and filtration strategies based on the DWT multiresolution analysis [75]- [76].

Filtered signals obtained with these filtration methods are often used directly as the references to control power flow in the HESS. This can, however, negatively affect the performance of the system, mainly due to the delay introduced by signal processing, as it will be demonstrated in more detail later in the thesis.

2.4 The discrete wavelet transform (DWT)

The DWT is a technique that allows the translation of a time-domain signal into a signal localised in both the time and frequency domains with pre-specified detail resolutions. The multi-resolution decomposition obtained with the DWT offers a method for the analysis of signals that feature high-frequency components for short durations and low-frequency components for long durations [77]. Practically, the DWT is implemented by a filter bank, which is an array of low pass and high pass Finite Impulse Response (FIR) filters with filter coefficients that correspond to a particular mother wavelet. As the name indicates, the DWT requires a discrete set of samples representing the original signal. Sampling is performed according to Nyquist theorem. These samples are passed through a low pass filter resulting in the convolution of the two. At the same time, the samples are passed through a high pass filter. The filters used are related to each other and are known as quadrature mirror filters [78]. Since at each level of decomposition half of the frequencies of the signal are removed, half of the samples can be discarded by down-sampling the signal before passing it through the next level of decomposition (low pass and high pass filter). This structure decomposes the input signal into several frequency components defined by the calculated DWT coefficients, each one carrying a single frequency sub-band of the original signal. High frequency components are obtained from

the calculated DWT detail coefficients whilst the low frequency component is obtained from the DWT approximation coefficient. The decomposition process results in one approximation coefficient (lowest frequency sub-band) and a number of detail coefficients that depend on the chosen level of decomposition. The original signal (sampled version) can be perfectly reconstructed from the DWT coefficients by means of the inverse DWT. Specific frequency sub-bands can be isolated and reconstructed with this procedure. However, the DWT frequency components contain a delay that is influenced by the sampling frequency, the target low-frequency sub-band, and the chosen wavelet function.

A power spectrum analysis of power demand signals associated with driving cycles show that most of the energy of the signal is contained at low frequencies (below 500 mHz). For the Federal Test Procedure driving cycle (FTP72), which represents an urban driving cycle, the periodogram power spectral density presented in Fig. 2.5a shows that a great portion of the energy contained in the signal is concentrated at low frequencies, mostly below 500 mHz. The same occurs with the EPA Driving Schedule for Light-Duty Vehicles and Trucks (US06) and the Worldwide Harmonized Light Vehicle Test Procedure (WLTP3) driving cycle as shown in Fig. 2.5 b and Fig 2.5 c, respectively.

Considering a sampling frequency of 1Hz, the DWT is able to decompose the signal in sub-bands of 0-250 mHz for the first level of decomposition, 0-125 mHz for the second level and 0-62.5 mHz for the third level, etc., as presented in Table 2.2. With each level of decomposition the frequency is divided by two (dyadic decomposition). Intermediate frequency bands are not possible unless the sampling frequency is changed. For example, to obtain a low frequency range of 0-100 mHz, the sampling frequency should be 0.8 Hz as it produces the desired frequency range after 2 levels of decomposition. This is one of the disadvantages of the DWT in this particular application, as it doesn’t offer the same flexibility as conventional filters. The sampling frequency must be modified in order to

obtain specific frequency ranges. It is important to note that the DWT decomposes a signal into frequency sub-bands and does not filter out a specific frequency as is the case with conventional filters. Sampling at 1 Hz seems to be the preferred sampling rate among researchers using the DWT [50], [75]- [76], [79]- [80] as it is easier to implement.

The frequency sub-band chosen in this work is 0-125 mHz as this is obtained after 2 levels of decomposition with a total delay of 4 seconds. If the frequency sub-band of 0-250 mHz obtained with 1 level of decomposition and a total delay of 2 seconds would be chosen, the total energy supplied by the SC would be smaller than the supplied when the level of decomposition is 2. Therefore, the SC would be sub-utilized. This is evidenced for three driving cycles as shown in Fig. 2.5. The energy contributed by the battery and SC have been shaded with different colours, separated by a line at the 125 mHz frequency (obtained with 2 levels of decomposition and 1 HZ sampling rate). The battery provides the energy below 125 mHz (0-125mHz sub-band) and the SC all the frequency above 125 mHz. With 3 levels of decomposition two main problem arise: the total delay is 8 seconds, which is more difficult to handle, and the SC should have a bigger size to supply more energy. This corresponds to a frequency sub-band of 62.5 mHz (the red line in Fig. 2.5 would move to the left to 62.5 mHz).

Choosing low levels of decomposition e.g. level 1 (frequency range towards the right hand side of Fig.2.5), results in the battery providing for most of the power demand, while high levels of decomposition e.g. level 3 (frequency range towards the left hand side of Fig 2.5), relieves the battery from high frequency power demand as the SC takes over a greater portion of the signal energy.

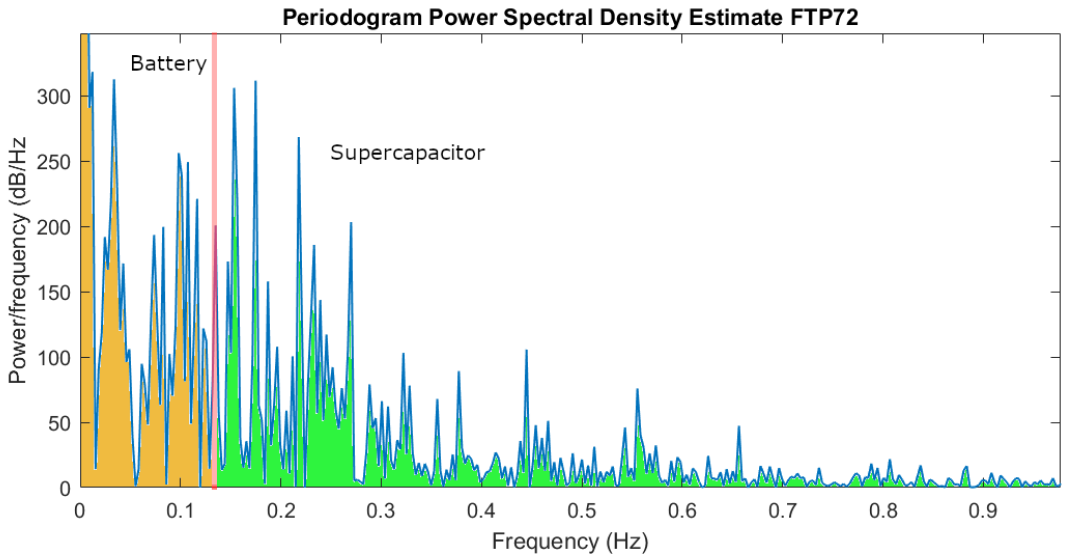

a)

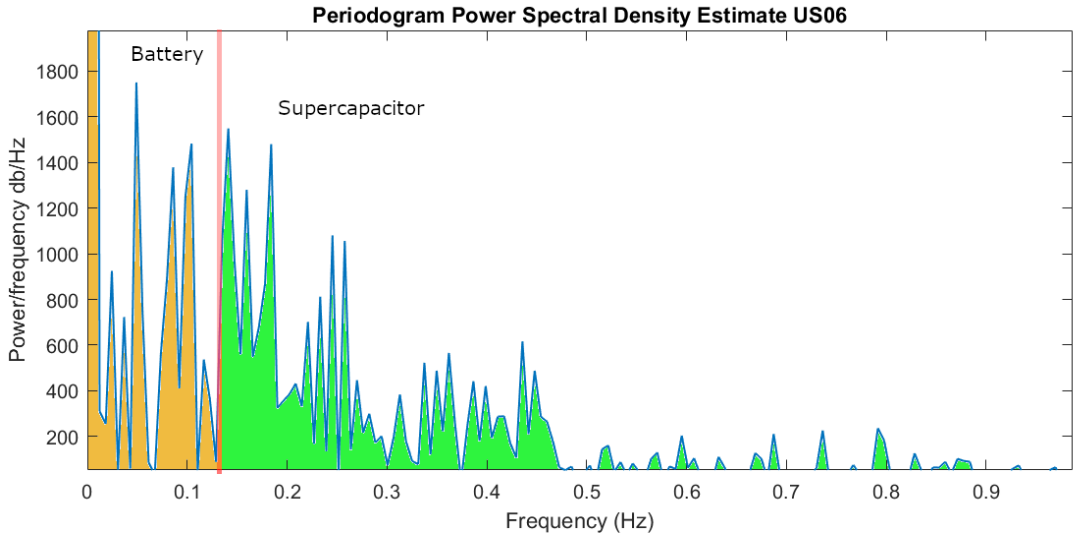

b)

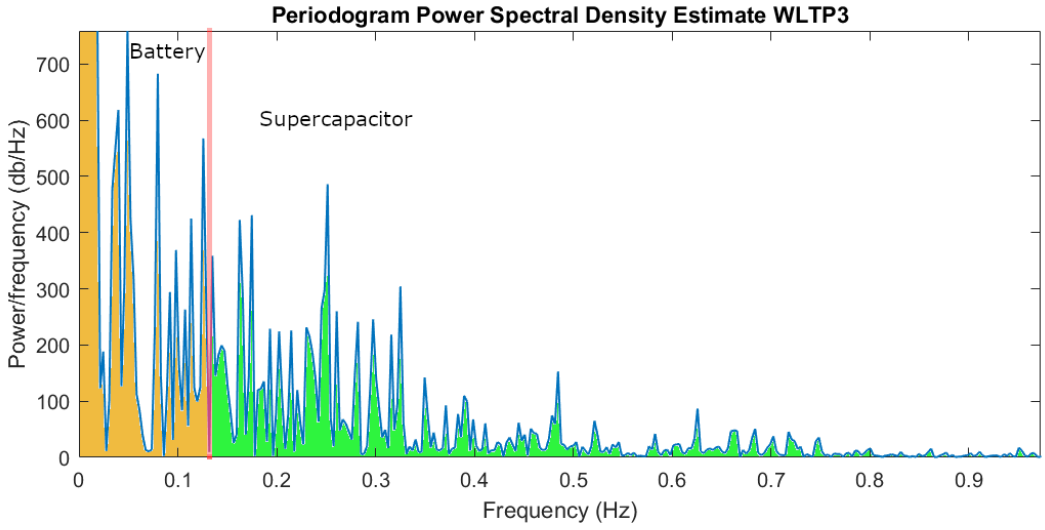

c)

Fig. 2.5.Power spectral density estimate for: a) the FTP72 driving cycle, b) the US06 driving cycle, and c) the WLTP3 driving cycle

Table 2.2. DWT decomposition sub-bands obtained with different sampling frequencies and levels of decomposition

Sampling Freq. f_s	1 Hz	2 Hz	4 Hz	8 Hz	16 Hz
Nyquist Freq (f_s/2)	0.5 Hz	1 Hz	2 Hz	4 Hz	8 Hz
Level 1	0-250 mHz	0-500 mHz	0-1 Hz	0-2 Hz	0-4 Hz
Level 2	0-125 mHz	0-250 mHz	0-500 mHz	0-1 Hz	0-2 Hz
Level 3	0-62.5 mHz	0-125 mHz	0-250 mHz	0-500 mHz	0-1 Hz
Level 4	0-31.25 mHz	0-62.5 mHz	0-125 mHz	0-250 mHz	0-500 mHz
Level 5	0-15.625 mHz	0-31.25 mHz	0-62.5 mHz	0-125 mHz	0-250 mHz
Level 6	0-7.8125 mHz	0-15.625 mHz	0-31.25 mHz	0-62.5 mHz	0-125 mHz

Obviously, sampling at higher rates e.g. 16 Hz, yields a smoother and better representation of the real time power demand than sampling at 1Hz. However, to obtain the low frequency sub-band e.g. 0-125 mHz, more levels of decomposition are necessary, specifically 6 levels. In this case, the signal is decomposed into more detailed frequency sub-bands which yields better resolution in terms of high frequency components (details), while the low frequency component (0-125 mHz) would be mostly similar to the one obtained at with a sampling rate of 1 Hz. It is important to note that increasing the sampling rate does not reduce the total delay. The higher the sampling rate, the higher the level of decomposition and the number of samples required to reach the approximation coefficient. Proof of this will be presented in Chapter III.

Other important parameter defining the performance of the DWT strategy is the chosen wavelet function. It defines the number of coefficients of the low pass and high-pass FIR filters used in the DWT decomposition and reconstruction process. Wavelet function families are designed for different purposes including feature detection (Haar, Daubechies 2 or symlet 2), signal denoising (Symlet or Daubechies), signal or image compression (Biorthogonal), etc. [81].

The Haar wavelet is the simplest possible wavelet. Its disadvantage is that is not continuous, and therefore not differentiable. This, however, is an advantage for the analysis of signals with sudden transitions [82]. The Haar wavelet has the smallest filter order (N=2) among wavelet functions. This has a direct influence on the delay produced by the DWT decomposition and reconstruction process. Higher filter orders associated with wavelet functions other than the Haar wavelet, result in longer time delays, which makes DWT implementation in real time more difficult.

Reported literature suggests that the frequency components obtained with the DWT can be used directly in real time to control the battery and SC power contribution despite the delay. Some researchers developed EMS strategies based on the Haar wavelet and 3 levels of decomposition [48], [83] [84] [85] [86] [87] [88] [89] [90], while others proposed 5 levels [61], [79]. As the level of decomposition remains unchanged during runtime, the delay caused by the DWT is fixed. Other researchers proposed adaptive methods to control the battery and SC charge/discharge rate by varying the decomposition level of the DWT depending on the driving conditions [76], and the SOC of the SC [50], [80]. In this case, however, the delay is variable.

Wang et al. [79] performed an evaluation of the performance of an EMS based on the DWT to determine the level of decomposition under the New European Driving Cycle (NEDC). The evaluation consisted of a comparison between the maximum battery and SC currents, and final SOC of the battery and SC when the power demand signal was decomposed using 2 to 5 levels. This work concluded that for a signal sampled at a rate of 1 Hz, 3 levels of decomposition (0 to 62.5 mHz) showed better performance than other decomposition levels as the SC relieves the battery more than levels 1 and 2 and avoids excessive energy losses that occur with 4 and 5 levels. In [75], the level of decomposition was selected by considering the frequency response range of the power sources. The suggested range of frequencies for the battery was 10^{-2} to 10^{2} Hz. For a battery-

ultracapacitor system, it was concluded that 2 levels (0 to 125 mHz) were appropriate while for a fuel cell-ultracapacitor system, 8 levels (0 to 1.95 mHz) were recommended. According to the analysis that will be presented in Chapter III, a delay of 8 seconds would be introduced in the frequency components with 3 levels of decomposition, the Haar wavelet, and a sampling frequency of 1Hz. Similarly, a delay of 4 seconds is associated with 2 levels of decomposition and 256 seconds with 8 levels, considering a sampling rate of 1Hz and the Haar wavelet as presented in [75]. Obviously, using the frequency components with such long delay will generate significant performance deterioration if applied in real time.

With the variation of the DWT level of decomposition in adaptive methodologies, the problem with varying delay becomes more challenging. Zhang and Deng [76], presented an adaptive multi-level Haar wavelet transform for allocating power to batteries and SCs. The level of decomposition was variable and determined according to the driving cycle which was identified using a learning vector quantisation neural network. It was concluded that a 4^{th} level of decomposition is needed for highway driving cycle, a 3^{rd} level for moderate urban cycle and a 2^{nd} level for congested urban cycle. However, the authors ignored the DWT delay and did not consider its implications in real time, especially when switching between levels of decomposition. In this particular case, the EMS would be required to jump between frequency components with different delays depending on the changes in the driving cycle, specifically 4 seconds delay (2 levels of decomposition), 8 seconds delay (3 levels of decomposition) and 16 seconds delay (4 levels of decomposition). Peng et al. [50] proposed a methodology for adaptively varying the DWT level of decomposition between 1 and 5 based on the SOC of the SC. A similar approach was proposed in [80], however this time the level of decomposition varied between 2 and 5. In [91] an adaptive wavelet transform-fuzzy logic control energy management strategy based on driving pattern recognition was proposed. The algorithm

used cluster analysis to classify driving cycles into different patterns according to the features extracted from historical driving data in real-time. After recognition results were obtained, an adaptive wavelet transform was employed to allocate the high frequency components of power demand to the SC, while the low frequency component was distributed to battery. Fuzzy logic was used to maintain the SOC of the SC within desired range. The level of decomposition was varied between 2 and 5 according to a driving pattern recognition algorithm. All the proposed methodologies presented above have been suggested for real time operation, however, the presence of significant delay in the frequency components was neglected. Moreover, the system's energy efficiency has not been analysed.

Wavelets with high filter order have also been proposed instead of the Haar wavelet to obtain frequency components to control power flow in a HESS. Shen et al. [92], proposed an EMS based on a Symlet wavelet with 3 levels of decomposition and performed an experimental test to validate the strategy. However, important information regarding the order of the Symlet wavelet, which can be between 2 and 20, and the sampling rate were not provided, which made this work difficult to replicate.

To depict the delay problem when a high order wavelet is used, let suppose that the chosen wavelet was symlet2, which has 4 filter coefficients, and the sampling rate was 1 Hz. The total delay that would be present in the frequency components after 3 levels of decomposition would be 22 seconds with respect to the real time power demand (see eq. 3.30, and 3.31 in Chapter III). Conversely, the Haar wavelet under the same conditions yields a delay of 8 seconds. Obviously, higher order wavelets results in longer time delays. Although the shortest time delay can be achieved with the Haar wavelet, dealing with the delay in real time applications remains a challenge.

Song et al. [93] proposed a Wavelet-transform-based energy management strategy using Daubechies 4 (db4) wavelet and 5 levels of decomposition. In this case, the delay

introduced by the DWT, considering that the db4 wavelet has 8 filter coefficients, is 218 samples. The sampling rate was not provided, therefore the delay in seconds and the frequency sub-bands cannot be calculated.

Several research papers include hardware in the loop (HIL) validation of the proposed 'real-time' approach based on the DWT. However, the mathematical principles behind the DWT signal decomposition considering the very low sampling frequency commonly used (1Hz), results in a considerable delay that provokes energy circulation in the system, reducing the system's efficiency. As the effects of delay have been neglected, the HESS performance and efficiency are compromised. Many of the researchers insist that the technique is able to perform in real time in this particular application, however, the detailed research work carried in this thesis shows otherwise.

2.5 Conventional filtering approach

Among the most significant benefits of the conventional filtration approach are its simplicity and low computational burden. Filters can be designed in hardware and software with specific parameters, which is the advantage of this method against the DWT. While hardware analogue filters require physical components that are not noise tolerant, software digital filters are implemented in digital controllers such as Digital Signal Processors (DSPs) or Field Programmable Gate Arrays (FPGAs), which makes them highly immune to noise.

Digital filters are categorised into Infinite Impulse Response (IIR) and FIR filters. An IIR filter can be designed in continuous time domain using established methodologies including Butterworth, Chebyshev, and Elliptic. With the bilinear transformation, which is often called the 'Tustin' method, the resulting filter transfer function can be transformed into discrete time. The main advantages of an IIR filter over an equivalent FIR filter are their efficient implementation, smaller computational burden, ability to implement prototype analogue filters, and smaller delay as a consequence of less filter

coefficients [94]. However, there are some disadvantages such as non-linear phase (frequency dependent delay), potential instability, and harder to implement using fixed-point arithmetic.

Compared to IIR filters, FIR filters offer linear phase design, meaning that all frequency components are delayed by the same amount, they are always stable, they can be implemented efficiently in hardware, and allow multi-rate computational advantages. A major disadvantage of FIR filters is that they often require much higher filter orders to achieve the same performance levels as IIR filters. As a result, the delay of these filters is often much greater than that of an IIR filter of equal performance [95].

A variety of high pass and low pass filtering strategies with fixed and variable cut-off frequency have been proposed by researchers. In [45], the battery current reference was obtained by filtering the power demand associated with urban dynamometer driving schedule (UDDS) driving cycle with 4 types of IIR low pass filters. With the help of MATLAB's filter design tool, Chebyshev type 1 and type 2 as well as Elliptic and Butterworth filters were implemented to split the power demand in a SC semi-active topology. The SC current reference (high frequency component) was determined by subtracting the real time power demand from the output of the low pass filter. This is a common approach to obtain the high frequency component when low and high frequency components are required as it avoids the use of a dedicated high pass filter. This study found that an Elliptic filter implementation delivers the best results concluding that the filtration strategy improved the battery State of Health (SOH) by 47% for the UDDS driving cycle.

Luo et al. [44] described a methodology to hybridise an energy storage system with lead-acid batteries and SCs. The results showed that a simple first-order low pass filter is an effective and reliable solution for the power filtering, performing more favourably than higher order FIR filters. Researchers in [46] proposed a HESS for railway power

applications based on Superconducting Magnetic Energy Storage (SMES) in conjunction with a battery in order to reduce pulse power fluctuation and improve power quality. Power sharing was achieved with an EMS based on a low pass filter, which was used to allocate the low frequency power component to the battery and the high frequency component to the SMES. Simulation results indicated that the proposed strategy can effectively improve power quality and achieve peak load shifting. Hussain et al. [47] proposed an energy management system for a semi-active hybrid electric vehicle using an adaptive low pass filter (varying the filter's cut-off frequency). The stress on the battery was reduced by deviating the peak power of the load to the SC. The simulation results confirmed that the proposed technique provided less variation in voltage, small increase in battery temperature, higher battery SOC, lower battery power losses, higher efficiency, reduction in the battery Root Mean Square (RMS) current, and a controlled SOC of the SC.

2.6 Effects of delay on power distribution in a SC semi-active topology

When the SC current reference to control the DC/DC converter is derived from a filtering approach that yields delayed frequency components (i.e. DWT, FIR filter, IIR filter), energy circulation between the battery and SC is observed. This results in the battery taking extra stress and a reduction on the systems' efficiency. Due to delay, the effective contribution of the SC occurs late, therefore, the SC fails to assist the battery at the right time and discharges when not required forcing the battery to absorb the excess power. Equally, when the SC is commanded to recharge, the battery provides the required power when no braking energy is being generated. In addition to the unnecessary energy circulation, the energy transfer from the battery to the SC and vice versa, uses the DC/DC converter, increasing the system losses. This thesis investigates the energy circulation to understand how battery-SC energy transfer is affected by delay as well as how the effective SC contribution and system efficiency may be impacted. With first order filters, the delay problem is less prominent, however, energy circulation still exists. Chapter III

has a section describing the matter. The energy circulation issue has not been addressed before in the literature. This thesis analyses and proposes a solution to this problem, which undermines the SC's primary purpose and the rationale for hybridisation.

2.7 Power demand prediction as a way to compensate for delay

To enable real time operation in the presence of delay, power demand prediction has been proposed in the literature as a mechanism to compensate for it. This can be achieved by implementing a prediction algorithm with the capability to predict future power demand with a time window equivalent to the total delay. A delay compensation approach was presented in [49], where a NARNN was trained to perform power demand predictions to compensate for the DWT delay (3.2s) when the power demand, sampled at 10 Hz, was decomposed into 5 levels. The predicted high frequency component was used to control the SC. The neural network consisted of one hidden layer with 10 neurons, which was trained to predict 32 future samples based on the previous 60 samples. The training dataset consisted of a power demand time series that resulted from a low speed (24 km/h peak) driving cycle with a smooth pattern that was repeated 2 times over a long-time span (13000s). The trained network was, unfortunately, exposed to the same driving pattern during testing. In addition, driving cycles representing real-world driving schedules, where power demand is highly variable, were not used to test the generalisation ability of the trained network. Furthermore, this study did not compare SC performance before and after time delay compensation, making it impossible to determine whether or not the prediction strategy had improved the system's performance.

In [56], a combination of DWT and NARX was proposed. In the first instance, the DWT was used to decompose the power demand into 3 levels using the Haar wavelet. The obtained wavelet coefficients were fed to three NARX networks (one for each coefficient) to predict 20 steps in the future. The predicted coefficients were used to reconstruct the predicted power demand with the inverse DWT transform. The researchers stated that the

purpose of the prediction in this work was to anticipate transient power and not time delay compensation. Therefore, the rationale to determine the prediction window (20 future samples) was not time delay compensation.

The work presented in [57] trained a LSTM to predict 10 seconds in the future to enable a DWT based EMS to work in real time. The chosen level of decomposition was 3 and the mother wavelet used was Daubechies 4 (db4), which filter's order is 8. As the sampling rate and the structure of the LSTM network was not provided, it was difficult to determine the actual number of samples predicted by the network. To depict the delay problem with the parameters presented in this work, let's assume the sampling rate. With a sampling rate of 1Hz, the low frequency sub-band (3 levels) would contain the frequencies from 0 to 62.5 mHz and the high frequency sub-band the frequencies between 62.5 mHz and 500 mHz. According to the calculations using equations 3.30 and 3.31 (see Chapter III), the delay that would be introduced in the frequency components with db4 wavelet is 50 samples (50 seconds at 1Hz). This means that the LSTM network should predict 50 samples in the future to compensate for the delay. The prediction window of 10 seconds proposed in this work would not be justified with the assumed parameters. With prediction methodologies, prediction errors are inevitable and increase when the prediction window in longer.

Zhang et al. [63], proposed a real time EMS for battery-SC HESS based on a combination of DWT, neural network, and fuzzy logic. A 2-level DWT was used to decompose the power demand signal associated with 9 standard driving cycles. The obtained DWT low frequency component along with the load power demand were used as inputs to train the neural network with the aim to predict the low frequency power demand. However, the chosen prediction window was not in agreement with the delay generated by the DWT.

There is a scarcity of research detailing the implementation of filtration methods and the DWT as part of a real time EV EMS in light of delay issues. Most of previous studies

suggested the direct use of the DWT high frequency component to control the SC, but there is little work done to compare this with other possible implementations such as obtaining the SC current as the difference between total current and DWT low frequency component with and without prediction. Furthermore, the analysis of whether delay compensation improves the SC performance in terms of timely assistance during acceleration and braking and its influence on energy efficiency has not been addressed. The energy efficiency problem arises from the fact that in addition to the total amount of energy supplied/recuperated by the HESS to match the load requirements during a given driving cycle, additional energy is circulated between the battery and the SC as a consequence of delay through the non-ideal DC/DC converter which results in additional power loss.

CHAPTER 3

3 SYSTEM MODELLING AND ENERGY MANAGEMENT SYSTEM BASED ON THE DISCRETE WAVELET TRANSFORM

3.1 Introduction

When battery and SC ESSs coexist in EVs, energy management is imperative to ensure efficient power distribution based on the strengths and weaknesses of each ESS. The decoupling of highly dynamic power demands into components that match the dynamic nature of each ESS is essential. The DWT has been widely recommended as a way to get frequency components and use them to allocate power in the HESS in real time. However, little focus has been put on how signal processing delays affecting the DWT frequency components undermine the benefits of hybridisation. Power demand prediction has been suggested to deal with delay and enable the DWT to work in real time. However, a thorough analysis of the benefits and drawbacks of this approach is missing in the literature. This chapter analyses the contribution of the SC to alleviate the battery when the DWT is used with and without time delay compensation using future demand prediction. 4 different real-time implementation strategies for a DWT based EMS have been evaluated using different metrics to quantify energy circulation and SC assistance during motoring, acceleration, and braking. Simulation results included in this chapter, using urban and highway driving cycles, show evidence that obtaining the SC current reference as the difference between the real time current demand and the DWT low frequency component enhances SC assistance during motoring and braking at the expense of higher energy circulation. The complexity added by future demand prediction does not reap SC performance benefits as suggested in the literature. However, in terms of energy efficiency, the prediction approach improves it (less energy circulating in the system).

An efficiency index is calculated to aid in the selection of the method that yields most benefits. For this purpose the energy efficiency and the effectiveness of the SC contribution are considered.

3.2 System modelling

To model the vehicle tractive torque, either a kinematic or quasi-static approach can be used [96]. The kinematic method calculates the vehicle speed by using simple kinematic relationships based on the wheel revolution speed and the total transmission ratio. Using the main vehicle characteristics, it is possible to calculate the tractive torque needed to drive the vehicle according to the chosen speed profile. This approach assumes that the vehicle meets the target performance and that the driving speed profile will be exactly followed. With this theoretical approach, power request is directly calculated from the speed and not checked against the actual powertrain capabilities, thus, there is no guarantee that the vehicle can meet the desired speed profile.

The quasi-static approach is based on a driver model, where the target vehicle speed is compared to the actual vehicle speed in order to generate a torque demand profile. With this approach, the vehicle performance is limited by the powertrain capabilities, which makes the model more realistic. In this work, the vehicle model is based on the quasi-static approach.

3.2.1 Vehicle and powertrain characteristics

The EV model developed in this investigation includes five important parts: the driver model, vehicle dynamics, the powertrain, the hybrid energy storage system, and the EMS. The high-level system schematic modelled in Matlab-Simulink is shown in Fig. 3.1.

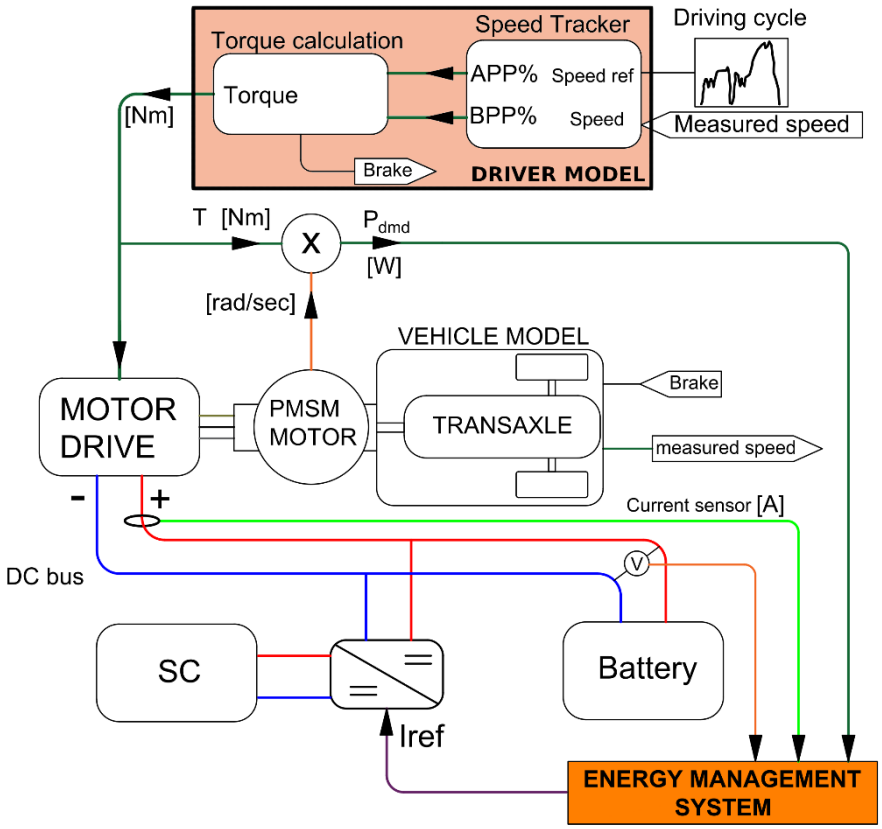

Fig. 3.1. Electric vehicle system with a HESS schematic

3.2.2 Driver model

The driver model is based on a proportional-integral (PI) longitudinal speed tracking controller that compares the reference speed from a given driving cycle with the measured speed of the vehicle [97]. The calculated error generates the accelerator pedal position (APP) and the brake pedal position (BPP) commands that are used to calculate the tractive and braking torque requirements while ensuring that these values lay within the maximum power and torque ratings of the electric motor. The Matlab-Simulink model is shown in Fig. 3.2.

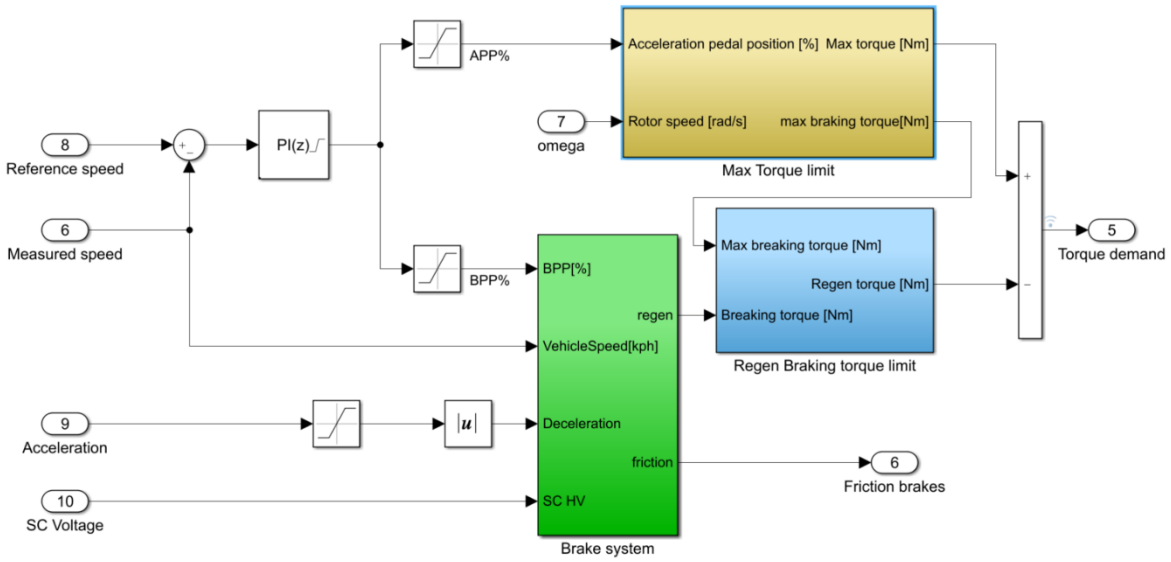

Fig. 3.2. Vehicle model driver subsystem

The torque is limited by the capability of the powertrain, which defines the operation torque envelope for the motoring and braking stages. The maximum torque limit subsystem (Max torque limit block) shown in Fig. 3.2 calculates the maximum motoring torque and the maximum braking torque based on the powertrain maximum torque and power as shown in Fig 3.3.

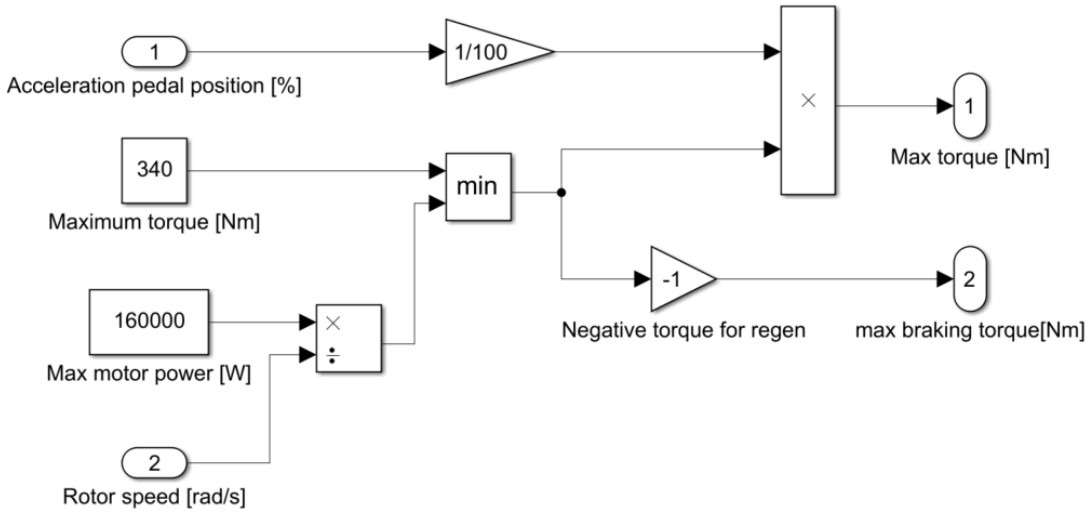

Fig. 3.3. Maximum motoring and braking torque calculation (max torque limit block)

The brake system block calculates the available regenerative braking torque as a function of the vehicle speed and the accelerator and brake pedal positions. The details of this block are discussed in section 3.2.6.

The regen torque limit block ensures that the calculated regenerative braking torque (input 2) is limited by the maximum regenerative braking torque (input 1) as shown in Fig.3.4.

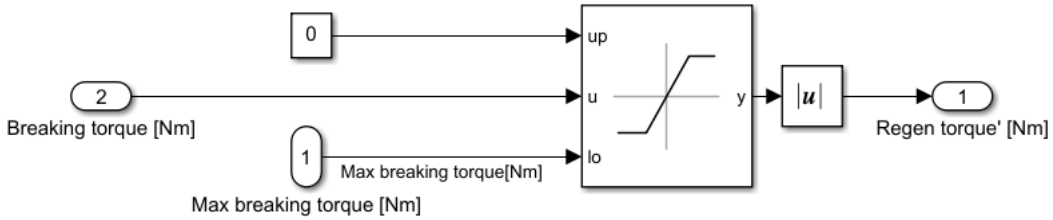

Fig. 3.4. Regenerative braking torque limiter Simulink model

The calculated torque demand (output 5 in Fig. 3.2) is supplied to a 3-phase motor drive, operating in torque control mode that drives a PMSM.

The vehicle features a front wheel drive transaxle and tires with a rolling radius of 326 mm equivalent to a standard size designation of 205/55R16. The product of the calculated torque demand T and the measured angular speed of the motor ω, yields the power demand P_{dmd} which is calculated by:

$$P_{dmd} = T\omega \tag{3.1}$$

Power demand is then used by the prediction algorithm and EMS to calculate the current reference to control the dc-dc converter commanding SC power flow.

3.2.3 Vehicle model

Dynamics is the study of the movement of objects as a result of the physical factors that affect them, such as force, mass, momentum, and energy. Two popular methodologies for formulating dynamic model of systems are the Newton-Euler and the Lagrange method. Newtonian mechanics considers the forces and torques acting on the system, while Lagrangian mechanics considers energies and generalised coordinates. Although both methods result in equivalent dynamic models, the Newton-Euler approach is adopted in this work as it is often the most common approach to analyse mechanical system and because the author is familiar with Newtonian mechanics.

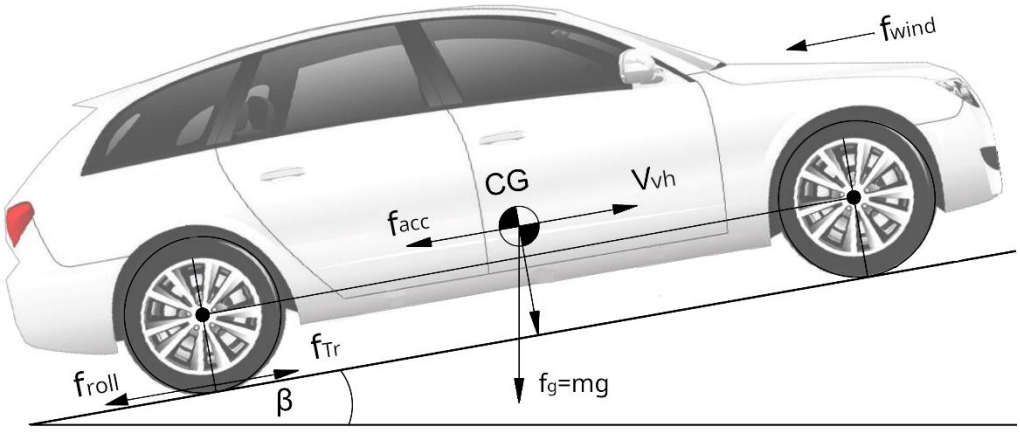

Fig. 3.5. Longitudinal vehicle dynamics schematic

The vehicle motion is a result of the net effect of all the forces and torques acting on it as shown in Fig. 3.5. The drag is assumed to act through the centre of gravity (CG). The electric motor must overcome inertial f_{acc}, gravitational f_g, rolling resistance f_{roll}, and aerodynamic f_{wind} forces acting against the movement of the vehicle. Thus, the tractive force f_{Tr} required to move the vehicle can be expressed as [98]:

$$f_{Tr} = f_{acc} + f_g + f_{roll} + f_{wind} \tag{3.2}$$

$$f_{Tr} = \underbrace{M_{vh}\dot{V}_{vh}}_{f_{acc}} + \underbrace{M_{vh} g \sin(\beta)}_{f_g} + sign(V_{vh})\underbrace{M_{vh} g \cos(\beta) C_{rr}}_{f_{roll}} + sign(V_{vh}+V_{wind})\underbrace{\frac{1}{2}\rho C_d A_{vh}(V_{vh}+V_{wind})^2}_{f_{wind}} \tag{3.3}$$

Where:

M_{vh}	[kg]	Mass of the vehicle
$g=9.81$	[m/s^2]	Free fall acceleration
β	[rad]	Road gradient angle
ρ	[kg/m^3]	Air density assumed to be that of dry air at 20°C
C_d	[-]	Aerodynamic drag coefficient
A_{vh}	[m^2]	Vehicle's frontal area
V_{vh}	[m/s]	Velocity of the vehicle
V_{wind}	[m/s]	Headwind speed

$\dot{V}_{vh}$	[m/s^2]	Vehicle acceleration
C_{rr}	[-]	Rolling resistance coefficient

The longitudinal dynamics of the vehicle are modelled with the vehicle body block available in Matlab-Simulink which is part of the Simscape Driveline library. This block represents a two-axle vehicle body in longitudinal motion. The block accounts for body mass, aerodynamic drag, and road incline. The latter is assumed to be zero (flat terrain). The vehicle and power train characteristics are presented in Table 3.1. The total weight of the vehicle has been calculated assuming:

- The vehicle body and power train without the ESS and power electronics: 1250 kg
- Battery pack: 2304 battery cells, 96 series, 24 parallel (69 gram each); 159 Kg (see table 3.2)
- SC pack: 135 cells (496 grams each): 67 kg (see table 3.3)
- ESS structure, wiring, power electronics: 106 kg
- Driver: 80 kg

Table 3.1. Vehicle and powertrain characteristics

Vehicle Characteristics		
Mass (kerb weight)	1662	kg
Aerodynamic drag	0.28	
Rolling resistance coefficient	0.012	
Front area	2.27	m^2
Air density	1.204	kg/m^3
Powertrain characteristics		
Maximum Torque	340	Nm
Maximum Power	160	kW
Max speed	11330	RPM [99]

3.2.4 Transmission

The transmission or gearbox adapts the electric motor output to a suitable speed and torque to be transferred to the wheels. The differential allows splitting the power generated by the motor between a pair of driving wheels, allowing them to rotate at

different speeds. In front-wheel drive (FWD) vehicles, the transmission, axle, and differential functions are combined in one integrated assembly known as a transaxle [100]. An important parameter affecting the vehicle's performance is the final drive ratio, which is the last set of gears that connects the vehicle's motor to the driving axle. In general, a lower final drive ratio will lead to less torque at the wheels but a higher top speed, while high final drive ratio results in more torque at the wheels at the expense of lower top speed. The schematic of the transmission system is shown in Fig. 3.6.

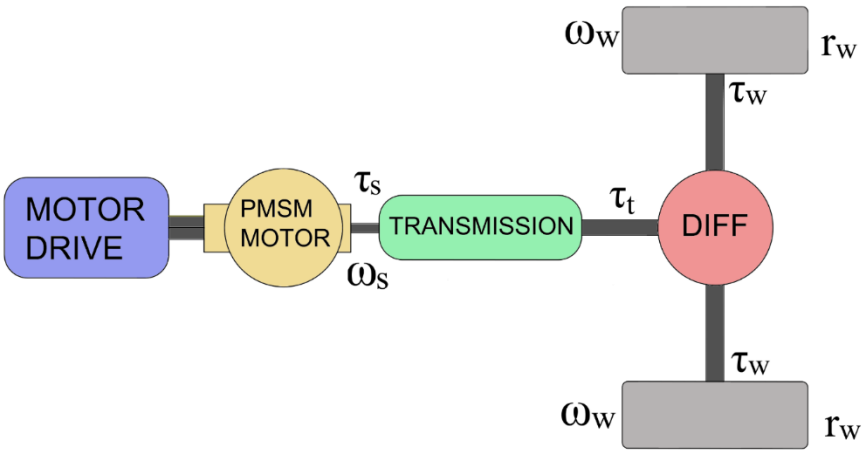

Fig 3.6. Electric vehicle transaxle system

The torque, power and angular velocities of the transmission system are given by [98] (assuming straight ahead tractive performance):

$$\tau_t = f_{Tr} r_w \tag{3.4}$$

$$\tau_w = \frac{\tau_t}{2} \tag{3.5}$$

$$\omega_w = \frac{V_{vh}}{r_w} \tag{3.6}$$

$$P_t = f_{Tr} V_{vh} \tag{3.7}$$

where:

τ_t	[Nm]	Traction torque
τ_w	[Nm]	Torque of each driving wheel
r_w	[m]	Wheel radius
ω_w	[rad/s]	Angular velocity of the wheels
P_t	[W]	Traction power

It assumed that the system has no losses due to friction and that the final drive ratio is 8.1938 (Nissan Leaf) [101]. The shaft torque, angular velocity and power of the electric machine are [98]:

$$\tau_s = \frac{\tau_t}{G} \tag{3.8}$$

$$\omega_s = G\omega_w \tag{3.9}$$

$$P_s = \tau_s \omega_s \tag{3.10}$$

where:

τ_s	[Nm]	Shaft torque of electric machine
ω_s	[rad/s]	Shaft angular velocity of electric machine
P_s	[W]	Shaft power of electric machine
G	[-]	Final drive ratio (transaxle)

3.2.5 Electric motor

PMSMs are widely used in EVs due to their high efficiency, high power factor, small volume, and wide speed range [102]. The motor is controlled by a motor drive, which receives the torque demand as commanded by the driver when the accelerator pedal is pressed/released. The PMSM motor and its drive are modelled in Matlab-Simulink using the servomotor block available in the Simscape Electrical library. This block represents a generic motor and drive operating in torque control mode, where motoring (positive

power demand) and generation (negative power demand) are supported. By using this block, system-level simulation can be performed based on the torque-speed behaviour of the combined motor and drive, thereby speeding up the simulation process. This is important considering the variable time span associated with the driving cycles used in this work. The schematic of the model is presented in Fig. 3.7.

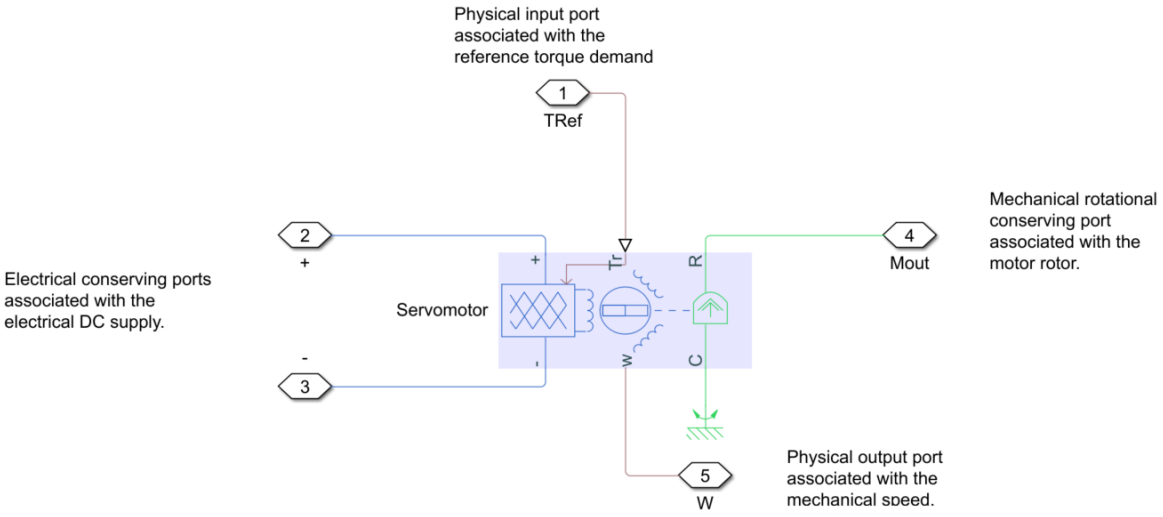

Fig.3.7. Servomotor Simulink model

This block allows only the range of torques and speeds defined by the torque-speed envelope, which can be specified as a set of speed data points with its corresponding maximum torque values. Alternatively, the speed-torque envelope profile can be determined by specifying the maximum toque and power. Fig. 3.8 depicts the typical torque-speed characteristics of an electric traction motor, showing the area of permissible steady state operation. All 4 operation quadrants (motoring, braking, and reversed operation) are constrained by this same profile.

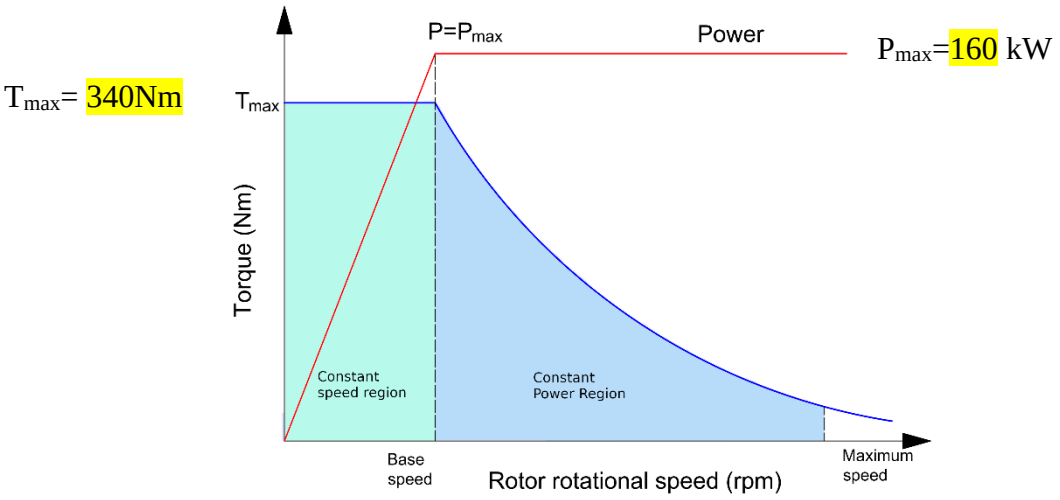

Fig. 3.8. Electric traction motor torque-speed envelope

The motor model allows simplified and tabulated definition of electrical losses. In this work the simplified model is adopted, where the losses result from the sum of the following terms [103]:

- A series resistance between the DC power supply and the motor drive
- Fixed losses independent of torque and speed, P_0, which accounts for fixed converter losses
- A torque-dependent electrical loss $k\tau^2$, where τ is the torque and k is a constant. This term represents ohmic losses in the cooper windings.
- A speed-dependent electrical loss $k_w\omega^2$, where ω is the speed and k_w is a constant. This represents iron losses due to eddy currents.

3.2.6 Braking model

The Simulink schematic of the brake system is shown in Fig. 3.9.

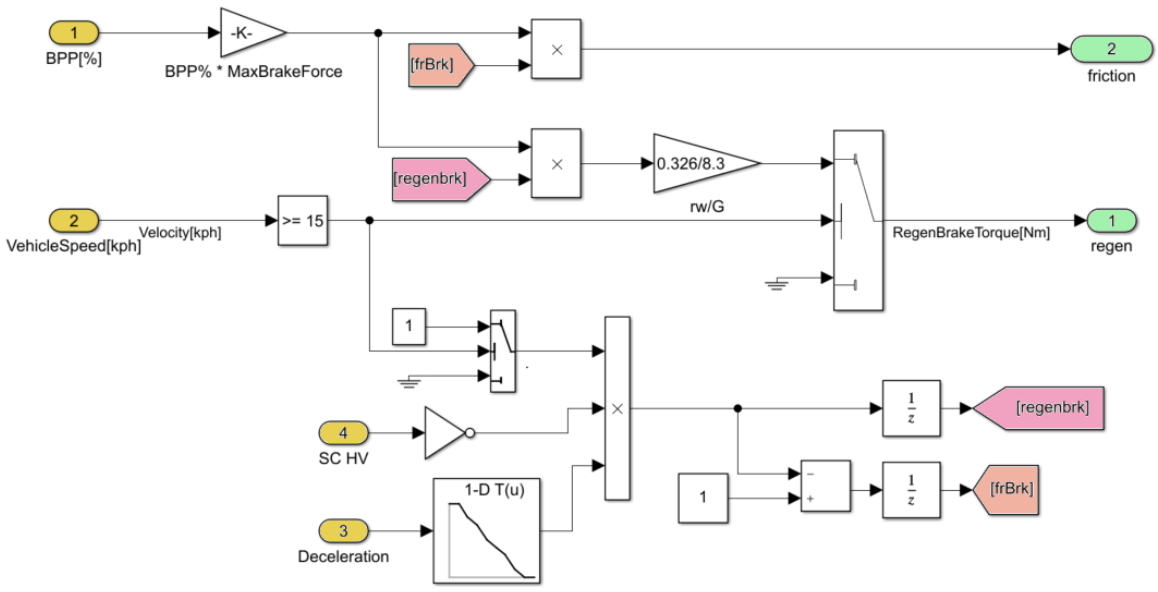

Fig. 3.9. Brake system schematic

The braking strategy is based on a fixed ratio between electric and mechanical braking forces as presented in [104]. The braking model consists of a parallel braking strategy, where the regenerative torque of the motor is exerted on the front driving axle directly in addition to the friction brake. In passenger cars with a single motor, regenerative braking is better utilised when the electric motor is installed on the front axle [104]. The mechanical brake has a fixed ratio distribution of 80% on the front and 20% on the rear brakes. The electric motor brake is controlled by the vehicle controller based on vehicle speed, brake pedal position, and the SOC of the SC. When the wheel speed is lower than 15 km/hr, due to either very low vehicle speed or wheel speed close to lock up, the electric brake produces no braking force and braking is produced only by the mechanical system. When the speed is higher than a set threshold and the SC is able to accept charge, the following braking actions are performed considering the deceleration rate:

a) When the vehicle deceleration is less than 0.15g (g = 9.81m/s^2), all the braking force is produced by electric regenerative braking and no mechanical force is

applied to the front and rear wheels, emulating the internal combustion engine retarding function.

b) When the vehicle deceleration is between 0.15g and 0.7g, 80% of the total braking force is allocated to the front axle and 20% to the rear axle. The electric and friction brakes work together to meet the required braking force on the front axle. The rear axle brake is purely mechanical. The maximum electric force is generated when the deceleration is close to 0.15g and minimum when it is close to 0.7g. The reduction in the electric braking force is linear.

c) Any deceleration above 0.7g is considered emergency braking and therefore braking is performed by the mechanical system only.

These actions are implemented with a lookup table that calculate the brake split ratio depending on the deceleration rate as shown in Fig. 3.10.

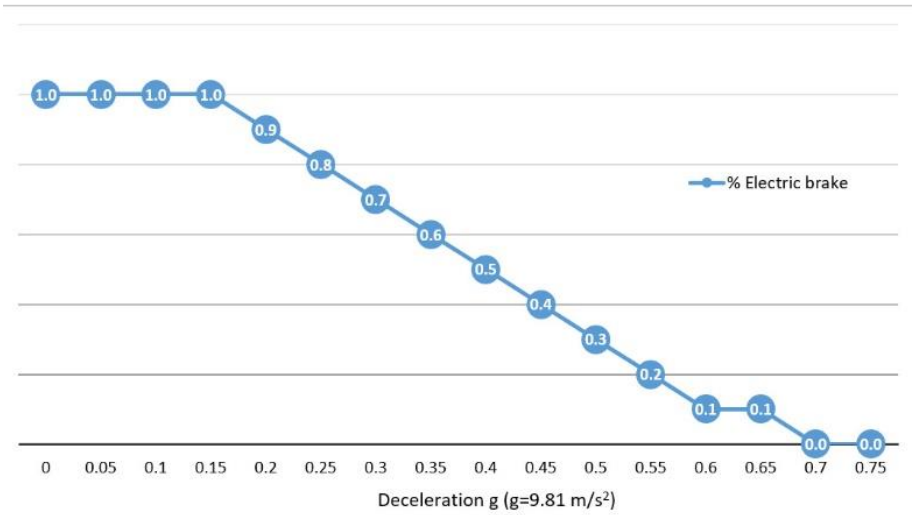

Fig. 3.10. Electric brake percentage depending on the deceleration rate

3.3 Hybrid energy storage system

3.3.1 Battery model

The battery model is based the Shepherd model, which is one of the best known mathematical models for constant current discharge [105]. A modification of this model is presented in [106], which constitutes the basis for the generic battery model readily available in Matlab-Simulink. This model represents accurately the battery voltage

dynamics in the presence of variable charging and discharging currents by considering the open circuit voltage as function of SOC. The parameters for this model can be easily extracted from the battery manufacturer's discharge curve in steady state. The model equations for a lithium-ion battery are:

Discharge:

$$V_{batt} = E_0 - R.i - \underbrace{K\frac{Q}{Q-it}it}_{Pol.Voltage} - \underbrace{K\frac{Q}{Q-it}i^*}_{Pol.Resistance} + A.\exp(-B.it) \tag{3.11}$$

Charge:

$$V_{batt} = E_0 - R.i - \underbrace{K\frac{Q}{it-0.1Q}i^*}_{Pol.Resistance} - \underbrace{K\frac{Q}{Q-it}it}_{Pol.Voltage} + A.\exp(-B.it) \tag{3.12}$$

where:

V_{batt} is the battery voltage (V)

E_0 is the open circuit voltage of a battery at full capacity(V)

K is the polarisation constant (V/Ah) or polarisation resistance coefficient (Ω)

Q is the battery capacity (Ah)

$it = \int idt$ is the removed charge (Ah)

A is the exponential zone amplitude (V) (empirical constant)

B is the exponential zone time constant inverse $(Ah)^{-1}$ (empirical constant)

R is the internal resistance (Ω)

i is the battery current (A)

i^* is the filtered current (A).

In Li-ion batteries, the voltage increases rapidly when the battery reaches the full charge. This is modelled by the polarisation resistance term in eq. 3.12. In the charge mode, the polarisation resistance increases until the battery is almost fully charged. After that, the resistance increases sharply. In theory, when the battery is fully charged (it=0), the polarisation resistance is infinite. However, in practice the contribution of the polarisation resistance is shifted by about 10% of the capacity of the battery, hence the term 0.1 in eq. 3.12.

This model offers the possibility to find all the model parameters from a typical discharge curve given by the battery manufacturer, avoiding experimental tests to obtain them.

The model is based on the following assumptions:

- The internal resistance remains constant during the charge and discharge cycle and does not vary with the amplitude of the current. This is a limitation of this model as the internal resistance varies during charge and discharge and is affected by the amplitude of the current and the temperature that builds up in the battery during operation.
- The model parameters are extracted from the discharge characteristics and used to define the charging characteristics. In the real life, charging and discharging characteristics are different.
- The model behaviour is not affected by changes in temperature. Temperature is a very important factor that affects the performance of the battery. However, this adds considerable complexity to the model.

The model has the following limitations:

- The minimum no-load battery voltage is 0V and the maximum battery voltage is 2 times the battery constant voltage (E_0). In reality, the battery voltage should not

be lower than a set voltage given by the manufacturer of the cell, usually around 3.0 V and the maximum voltage is usually 4.2 V.

- The minimum capacity of the battery is 0 Ah and the maximum capacity *Q*. Consequently, the maximum SOC cannot be greater than 100% if the battery is overcharged

The parameters for this model can be easily extracted from the battery manufacturer's discharge curve in steady state, as shown in Fig. 3.11. The fully charged voltage V_{full}, the end of the exponential zone Q_{exp} and V_{exp}, the end of the nominal zone Q_{nom} and V_{nom}, the maximum capacity Q, and the internal resistance R are the only parameters required.

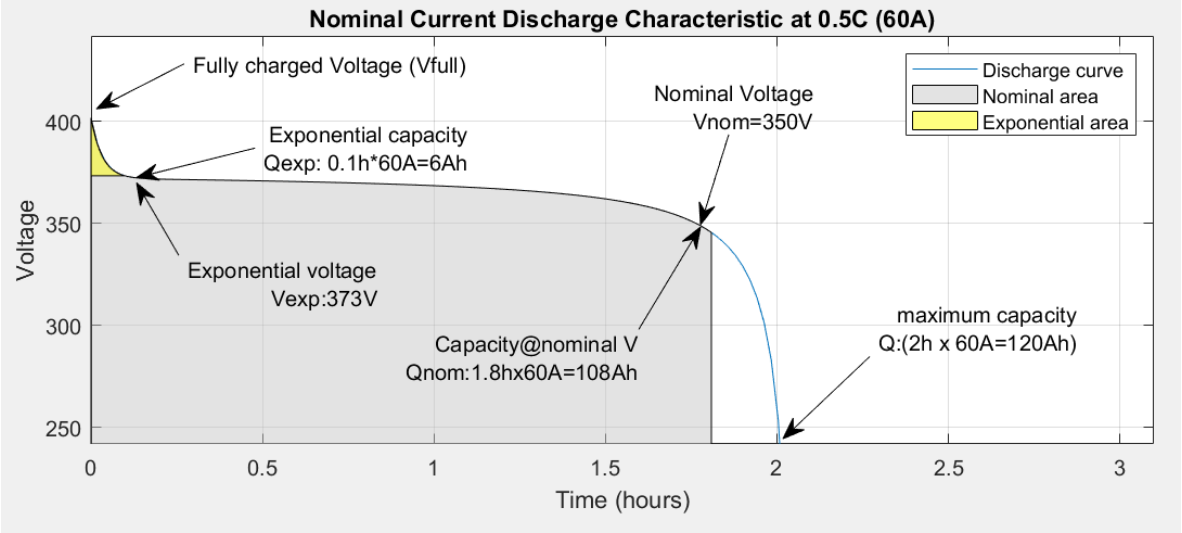

Fig. 3.11. Battery discharge curve in steady state

It is important to note that the discharge curves are obtained with a constant current discharge. When all the parameters mentioned before are extracted, eq. 3.11 can be rewritten for each of the identified characteristics resulting in a set of three equations with three unknowns: E_0, K and A [105].

When the battery is fully charged $V=V_{full}$, the extracted charge is 0, therefore the term $it=0$ and the term $i^*=0$ because the current step is about to start, yielding eq.3.13.

$$V_{full} = E_0 - R.i + A \tag{3.13}$$

The parameter *B* in eq. 3.11 represents the time constant of the exponential term and depends on the shape of the discharge curve. When the exponential term energy is small or approaches zero, the term can be approximated to $4/Q_{exp}$ as shown in Fig.3.12a. When the exponential term is predominant, the time constant B can be approximated to $2/Q_{exp}$, as shown in Fig. 3.12b.

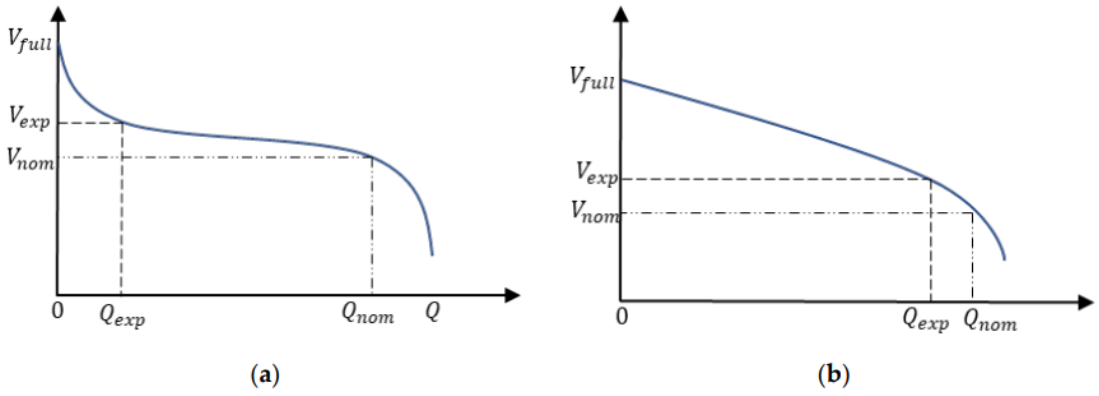

Fig. 3.12. Typical discharge curve of: a) LFP cell (small exponential zone energy), b) NMC cell (predominant exponential zone energy) [105]

Considering the discharge curve used in this work, *B* is approximated to $3/Q_{exp}$ as the energy of the exponential zone doesn't approach to zero and is not predominant. To calculate the exponential voltage (V_{exp}), the supplied charge is $it=Q_{exp}$, and the filtered current is $i^*=0$ because it is assumed that steady state has been reached. With these considerations eq. 3.11 yields:

$$V_{\exp} = E_0 - K\frac{Q}{Q - Q_{\exp}}(Q_{\exp} + i) - R.i + A.\exp\left(\frac{-3}{Q_{\exp}}.Q_{\exp}\right) \tag{3.14}$$

For the end of the nominal zone (V_{nom}) as shown in Fig. 312, the supplied charge is $it=Q_{nom}$ so eq. 3.11 gives:

$$V_{nom} = E_0 - K\frac{Q}{Q - Q_{nom}}(Q_{nom} + i) - R.i + A.\exp\left(\frac{-3}{Q_{\exp}}.Q_{nom}\right) \tag{3.15}$$

By solving eq. (3.13)-(3.15) gives the unknown model parameters, expressed as:

$$E_0 = \frac{E_{\exp} C_{nom} - E_{nom} C_{\exp}}{\left[\left(1 - e^{(-B.Q_{nom})}\right) C_{\exp} - (1 - e^{-3}) C_{nom}\right]} \tag{3.16}$$

Where:

$$C_{\exp} = \frac{Q}{Q - Q_{\exp}}\left(Q_{\exp} + i\right); \tag{3.17}$$

$$C_{nom} = \frac{Q}{Q - Q_{nom}}(Q_{nom} + i); \tag{3.18}$$

$$E_{\exp} = -V_{\exp} - Ri + (V_{full} + Ri)e^{-BQ_{\exp}}; \tag{3.19}$$

$$E_{nom} = -V_{nom} - Ri + (V_{full} + Ri)e^{-BQ_{nom}} \tag{3.20}$$

$$K = E_0\left(\frac{1 - e^{-BQ_{\exp}}}{C_{\exp}}\right) + \frac{E_{\exp}}{C_{\exp}} \tag{3.21}$$

$$A = V_{full} - E_0 + Ri \tag{3.22}$$

Experimental validation of the model shows a maximum error of 5% (when SOC is between 10% and 100%) for the charge (when the current is 0 through 2C) and discharge (when the current is 0 through 5C) dynamics [107].

The battery cell parameters used to model the battery pack in this work correspond to the Samsung INR21700-50E 5000mAh cell. A 0.2C rate (1A) is used as the curve to estimate the parameters of this battery, which are shown in Fig. 3.13 and Table 3.2.

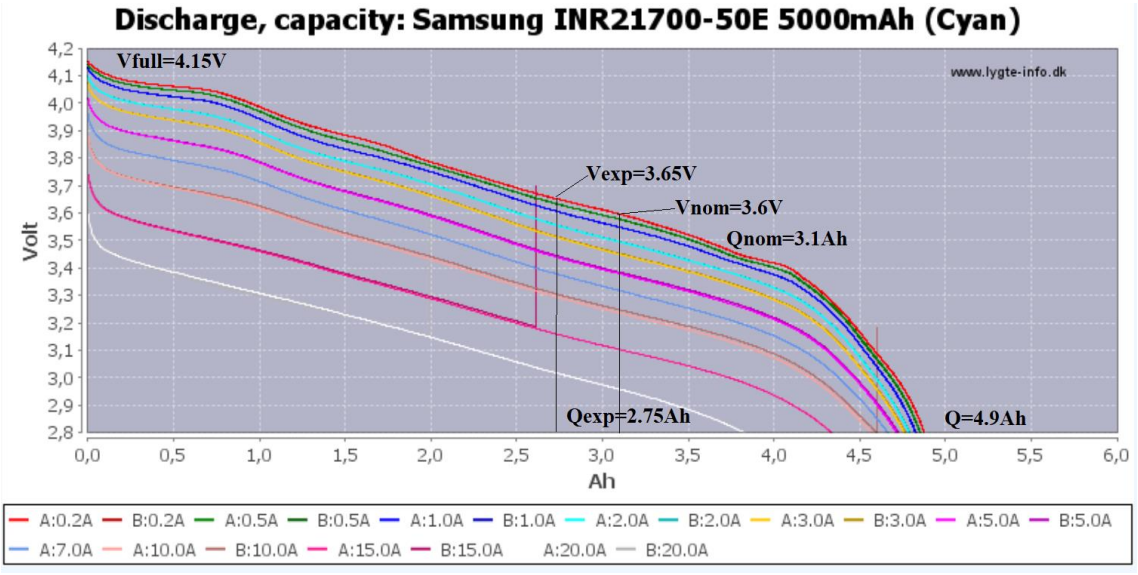

Fig. 3.13. Samsung INR21700-50E battery cell discharge curve [68].

Table 3.2. Battery parameters extracted from Fig.3.13

V_{full} (V)	Q (Ah)	V_{exp} (V)	Q_{exp} (Ah)	V_{nom} (V)	Q_{nom} (Ah)	R (ohms)
4.15	4.9	3.65	2.75	3.6	3.1	0.028

The battery parameters used in this paper are summarised in Table 3.3.

Table 3.3 Battery characteristics

Samsung INR21700-50E 5000mAh		
Cell specific energy	255.6	Wh/kg
Cell weight	69	g
Standard discharge capacity(0.2C)	4.9	Ah
Rated discharge capacity (1C)	4.753	Ah
Charge voltage	4.15	V
Nominal voltage	3.6	V
Maximum charge current	4.9	A
Maximum continuous discharge	9.8	A
Maximum pulse discharge	14.7	A
Discharge cut-off voltage	2.5	V
Internal resistance	<28	mohms
Battery pack characteristics		
Pack nominal voltage (V_{nom})	345.6	V
Pack maximum Capacity (Q)	117.6	Ah
Fully Charged voltage (V_{full})	398.4	V
Cut-off voltage	240	V
Pack configuration	96 series, 24 parallel	
Pack energy	40.6	kWh
Pack internal resistance	112	mΩ
Cont./pulse discharge C-rate (2C/3C)	235/351	A
Charge C-rate standard (0.5C)/max (1C)	58.5/117.6	A

The size of the battery modelled in this work has a capacity similar to that of a Nissan Leaf. However, some other brands produce vehicles that exhibit similar battery capacities such as Kia, Hyundai, and Fiat. Top of the range models exhibit batteries from 80 kWh, being the Mercedes EQS SUV 450 4MATIC the vehicle with the highest capacity installed (108.4 kWh). A list of EVs and their installed battery capacity is presented in Table 3.4 (the Nisan Leaf is highlighted) [107].

Table 3.4. Electric vehicle and usable battery capacity installed

Vehicle model	kWh	Vehicle model	kWh	Vehicle model	kWh
Mercedes EQS SUV 450 4MATIC	108.4	Tesla Model X Plaid	95	Porsche Taycan Turbo	83.7
Mercedes EQS SUV 580 4MATIC	108.4	Ford Mustang Mach-E ER RWD	91	Porsche Taycan 4S Plus	83.7
Mercedes EQS 450+	107.8	Ford Mustang Mach-E ER AWD	91	Porsche Taycan Plus	83.7
Mercedes EQS AMG 53 4MATIC+	107.8	Ford Mustang Mach-E GT	91	Porsche Taycan 4S Cross Turismo	83.7
Polestar 3 Long Range Dual motor	107	Mercedes EQE AMG 53 4MATIC+	90.6	Porsche Taycan Turbo Cross Turismo	83.7
Polestar 3 Long Range Performance	107	Mercedes EQE SUV 350+	90.6	Porsche Taycan Turbo S Cross Turismo	83.7
Lotus Eletre	107	Mercedes EQE SUV 350 4MATIC	90.6	Porsche Taycan GTS	83.7
Lotus Eletre R	107	Mercedes EQE SUV 500 4MATIC	90.6	Porsche Taycan GTS Sport Turismo	83.7
Volvo EX90 Twin Motor	107	Mercedes EQE SUV AMG 53 4MATIC+	90.6	Porsche Taycan Plus Sport Turismo	83.7
Volvo EX90 Twin Motor Performance	107	Mercedes EQV 300	90	Porsche Taycan 4S Plus Sport Turismo	83.7
Audi Q8 e-tron 55 quattro	106	Mercedes eVito Tourer L2 90 kWh	90	Porsche Taycan Turbo Sport Turismo	83.7
Audi Q8 e-tron Sportback 55 quattro	106	Mercedes eVito Tourer L3 90 kWh	90	Porsche Taycan Turbo S Sport Turismo	83.7
Audi SQ8 e-tron	106	Mercedes EQE 300	89	Genesis G80 Electrified Luxury	82.5
Audi SQ8 e-tron Sportback	106	Mercedes EQE 350	89	BMW i4 eDrive40	80.7
BMW iX xDrive 50	105.2	Audi Q8 e-tron 50 quattro	89	BMW i4 M50	80.7
BMW iX M60	105.2	Audi Q8 e-tron Sportback 50 quattro	89	Mercedes EQC 400 4MATIC	80
BMW i7 xDrive60	101.7	Nissan Ariya 87kWh	87	Skoda Enyaq iV 80	77
Fisker Ocean Ultra	100	Nissan Ariya e-4ORCE 87kWh	87	Skoda Enyaq iV 80x	77
Fisker Ocean Extreme	100	Nissan Ariya e-4ORCE 87kWh Performance	87	Volkswagen ID.4 Pro Performance	77
Fisker Ocean One	100	Audi e-tron GT RS	85	Volkswagen ID.4 GTX	77
Rolls-Royce Spectre	100	Audi e-tron GT quattro	85	CUPRA Born 77 kWh e-Boost	77
Tesla Model S Dual Motor	95	Jaguar I-Pace EV400	84.7	Volkswagen ID.5 Pro	77
Tesla Model S Plaid	95	Porsche Taycan Turbo S	83.7	Volkswagen ID.5 Pro Performance	77
Tesla Model X Dual Motor	95	Porsche Taycan 4 Cross Turismo	83.7	Volkswagen ID.5 GTX	77

Vehicle model	kWh	Vehicle model	kWh	Vehicle model	kWh
Volkswagen ID.4 Pro	77	Genesis GV60 Sport	74	Mercedes EQA 350 4MATIC	66.5
Skoda Enyaq Coupe iV 80	77	Genesis GV60 Sport Plus	74	Mercedes EQB 300 4MATIC	66.5
Skoda Enyaq Coupe iV 80x	77	Hyundai IONIQ 5 Long Range 2WD	74	Kia Niro EV	64.8
Skoda Enyaq Coupe iV VRS	77	Hyundai IONIQ 5 Long Range AWD	74	BMW iX1 xDrive30	64.7
Volkswagen ID. Buzz Pro	77	Hyundai IONIQ 6 Long Range 2WD	74	Hyundai Kona Electric 64 kWh	64
Audi Q4 e-tron 40	76.6	Hyundai IONIQ 6 Long Range AWD	74	Smart #1	64
Audi Q4 e-tron 50 quattro	76.6	Genesis GV70 Electrified Sport	74	Smart #1 Brabus	64
Audi Q4 Sportback e-tron 50 quattro	76.6	Toyota bZ4X FWD	71.4	Kia Soul EV 64 kWh	64
Audi Q4 Sportback e-tron 40	76.6	Toyota bZ4X AWD	71.4	Nissan Ariya 63kWh	63
Tesla Model Y Long Range Performance	75	Subaru Solterra AWD	71.4	MG MG4 EV Long Range	61.7
Volvo C40 Recharge Twin Pure Electric	75	Lexus RZ 450e	71.4	Lightyear 0	60
Polestar 2 Long Range Single Motor	75	Porsche Taycan 4S	71	Nissan Leaf e+	59
Polestar 2 Long Range Dual Motor	75	Porsche Taycan	71	Skoda Enyaq iV 60	58
Tesla Model 3 Long Range Dual Motor	75	BMW iX xDrive 40	71	CUPRA Born 58 kWh	58
Volvo XC40 Recharge Twin Pure Electric	75	Porsche Taycan Sport Turismo	71	CUPRA Born 58 kWh e-Boost	58
Tesla Model Y Long Range Dual Motor	75	Porsche Taycan 4S Sport Turismo	71	Volkswagen ID.3 Pro Performance	58
Tesla Model 3 Performance	75	Mercedes EQA 250+	70.5	Skoda Enyaq Coupe iV 60	58
Fisker Ocean Sport	75	Ford Mustang Mach-E SR RWD	70	Tesla Model 3	57.5
Polestar 2 Long Range Performance	75	Ford Mustang Mach-E GT	70	Tesla Model Y	57.5
Kia EV6 GT	74	MG ZS EV Long Range	68.3	MG MG5 EV Long Range	57
Kia EV6 Long Range 2WD	74	Volvo XC40 Recharge Pure Electric	67	Renault Megane E-Tech EV60 220hp	55
Kia EV6 Long Range AWD	74	Volvo C40 Recharge Pure Electric	67	Hyundai IONIQ 5 Standard Range 2WD	54
BMW iX3	74	Mercedes EQB 350 4MATIC	66.5	Hyundai IONIQ 6 Standard Range 2WD	54
Genesis GV60 Premium	74	Mercedes EQA 300 4MATIC	66.5	Audi Q4 e-tron 35	52

Vehicle model	kWh	Vehicle model	kWh
Renault Zoe ZE50 R135	52	Peugeot e-2008 SUV	45
Audi Q4 Sportback e-tron 35	52	Vauxhall Corsa-e	45
Volkswagen ID.4 Pure Performance	52	Vauxhall Mokka-e	45
Volkswagen ID.4 Pure	52	Citroen e-C4	45
Peugeot e-308	51	Citroen e-SpaceTourer Business M 50 kWh	45
Peugeot e-308 SW	51	Citroen e-SpaceTourer Business XL 50 kWh	45
MG MG4 EV Standard Range	50.8	Vauxhall Vivaro-e Life Combi M 50 kWh	45
MG ZS EV Standard Range	49	Vauxhall Vivaro-e Life Combi L 50 kWh	45
ORA Funky Cat First Edition	47.8	Hyundai Kona Electric 39 kWh	39.2
CUPRA Born 45 kWh	45	Kia Soul EV 39.2 kWh	39.2
Citroen e-SpaceTourer M 50 kWh	45	Nissan Leaf	39
Citroen e-SpaceTourer XL 50 kWh	45	Fiat 500e Cabrio	37.3
Vauxhall Vivaro-e Life Elite M 50 kWh	45	Fiat 500e Hatchback 42 kWh	37.3
Vauxhall Vivaro-e Life Elite L 50 kWh	45	Abarth 500e Scorpionissima	37.3
Peugeot e-Traveller Standard 50 kWh	45	Mazda MX-30	30
Peugeot e-Traveller Long 50 kWh	45	Mini Electric	28.9
Peugeot e-Rifter Standard 50 kWh	45	Honda e Advance	28.5
Peugeot e-Rifter Long 50 kWh	45	Smart EQ fortwo coupe	16.7
Vauxhall Combo-e Life 50 kWh	45	Smart EQ fortwo cabrio	16.7
Vauxhall Combo-e Life XL 50 kWh	45		
Citroen e-Berlingo M 50 kWh	45		
Citroen e-Berlingo XL 50 kWh	45		
DS 3 Crossback E-Tense	45		
Peugeot e-208	45		

3.3.2 Supercapacitor model

Electrochemical SCs are divided into three types depending on the interfacial physics and chemistry [108]:

- Electric double layer capacitors (EDLCs), built with various carbon based substances like graphene and carbon nanotubes.
- Pseudocapacitors, which are built with materials that undergo redox reactions such as conducting polymers and transition metal oxides, and
- Hybrid capacitors which have one electrode of EDLC type material and the other made up of either of materials used for pseudocapacitor electrode or materials used for the electrodes in batteries.

Energy storage in EDLCs rely on the formation of the electric double layer formed at the electrolyte-electrode interface. Energy is saved between an electrolyte/ionic liquid and a conducting electrode (semiconductor or metallic) interface by the reversible absorption of ions on the surface of the electrode holding large surface area with varied porous structure. Several models have been proposed to explain the behaviour of charges in the electrode-electrolyte interface including the Helmholtz theory, the Gouy Chapman model and the Stern theory.

The SC is based on the Stern-Tafel model which reproduces the double layer capacitance related to the nonlinear diffusion dynamics by a combination of the Helmholtz's capacitance and the Gouy-Chapman's capacitance [109]. This model is the basis of the generic SC block available in Matlab-Simulink.

3.3.2.1 The Helmholtz model

The model explains charge separation on the interface between an electrolyte solution and a metallic electrode. The electrode holds a charge density resulting from either an excess or deficiency of electrons at the electrode surface. The electrode's charge is

balanced by redistribution of ions in the electrolyte solution by an equal but opposite charged amount of ions. This results in two layers of opposite charge separated by a distance limited by the radius of the attracted ions and a single layer of solvation around each ion. The double layer capacitance per unit is given as [110].

$$C_H = \frac{\varepsilon_0 \varepsilon}{d} \tag{3.23}$$

Where ε_0 is the permittivity of vacuum (8.854×10^{-12} F/m), ε is the relative permittivity of the electrolyte material and d is the thickness of the double layer. The two layers of polarized ions formed at the electrode-electrolyte interface is shown in Fig 3.14 [108].

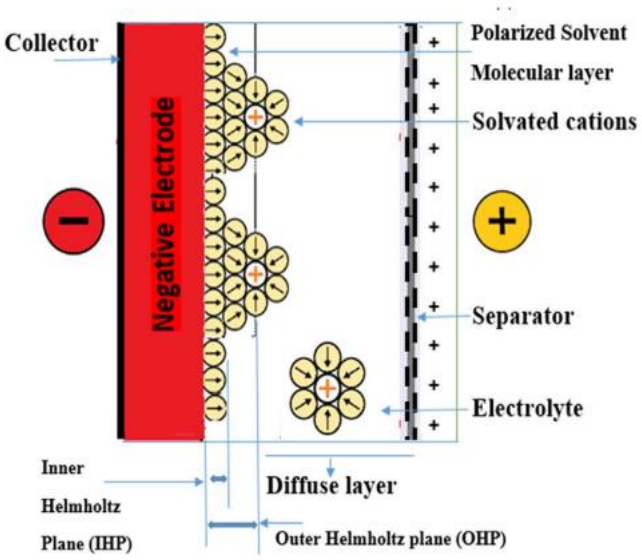

Fig.3.14. Helmholtz model of electric double layer

One layer is present at the surface of the electrode which is in contact with the electrolyte. The second layer (with opposite polarity) is formed from solvated electrolytic ions (cations) that have been attracted towards the polarized electrode. A layer of solvent molecules works as a molecular dielectric that separates the two layers of opposite polarity and is called the inner Helmholtz plane (IHP). The quantity of charge on the electrode is balanced by the opposite ions present in the outer Helmholtz plane (OHP). Depending on the strength of the voltage applied, the charge on the electric double layer

forms an electric field in the inner Helmholtz plane. The accumulated charge in the layer depends on the electrode surface area and the number of ions absorbed [108].

A SC comprises two electrodes: one for the positive terminal and one for the negative. At one electrode, the charge is opposite in polarity to that of the other electrode. Therefore, the total capacitance of an EDLC is modelled as a two capacitors in series. A drawback of the Helmholtz theory is that it is not able to explain the interactions that occur further away from the electrode (electrolyte area).

3.3.2.2 The Gouy-Chapman model

Gouy and Chapman noticed that in an electric double layer the capacitance is not constant and varies with the ionic concentration of the electrolyte as well as with the voltage applied.

This model considers the thermal motion of ions near a charged surface. The model is explained by a combination of Poisson- Boltzmann differential equation, which describes the distribution of ions considering the concentration of ions ($mol.m^{-3}$), their charge and the absolute temperature. With these parameters, the model defines the total charge density per unit volume for all ionic species. The model assumes point-like ions in thermodynamic equilibrium and neglects statistical correlations. For low concentration electrolytes, the model has been successful in predicting ionic profiles. However, it is known to overestimate ionic concentrations close to charged surfaces [110]. The differential capacitance is given by:

$$C_{GC} = \left(\frac{2z^2 e^2 n_i^0 \varepsilon\varepsilon_0}{kT} \right)^{1/2} \cosh\left(\frac{ze\varphi_0}{2kT} \right) \tag{3.24}$$

where:

C_{GC} is the Gouy-Chapman capacitance

z is the charge on the ion

e is the unit charge

n_i^0 is the concentration of ion *I* in the bulk

k is the Boltzmann constant=1.380649x10^{-23} J/K

T is the absolute temperature

φ_0 is the potential at the electrode

3.3.2.3 Stern model

Otto Stern proposed to combine the Helmholtz and Gouy-Chapman models to explain the electric double layer. In this model, the inner layer is called the Stern layer and agrees with the Helmholtz model in that ions stick to the electrode. The other layer of ions received the name of Gouy Chapman diffuse layer. The differential capacitance of the double layer C_s is equivalent to two capacitors in series as [110]:

$$\frac{1}{C_s} = \frac{1}{C_H} + \frac{1}{C_{GC}} \tag{3.25}$$

Where

C_s is the Stern capacitance

C_H is the Helmholtz capacitance

C_{GC} is the Gouy-Chapman capacitance

The Stern layer considers the impact of the finite size of the ions and thus suggested that the value of the closest ionic approach to the electrode should be approximately equal to the radius of the ion [108]. The model assumes that the fluid viscosity lies in a constant plane and the permittivity remains constant through the electric double layer. In addition, the model assumes that the inner activities taking place in the Guoy Chapman layer are

coulombic in nature. These assumptions are considered the limitations of this model. The location of the Stern layers in shown in Fig.3.15.

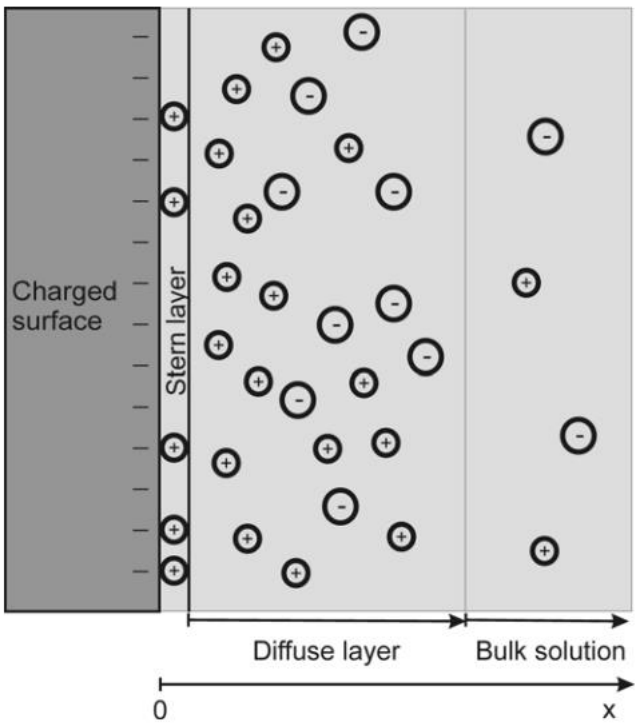

Fig.3.15. Representation of the Stern model of electric double layer [111].

3.3.2.4 The Stern-Tafel model

The model schematic is shown in Fig. 3.16.

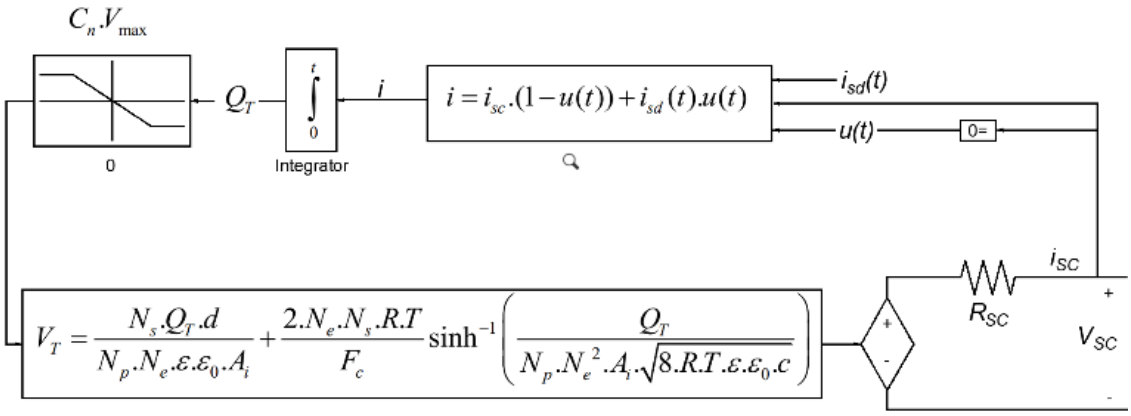

Fig. 3.16 Stern Tafel SC model schematic [109]

C_n is the nominal capacitance (F) and $V_{\max}$ is the maximum SC voltage (V). The SC voltage V_{sc} is given by the difference between the total voltage V_T and the product between the internal resistance R_{sc} and the SC current i_{sc}, such as [109]:

$$V_{sc} = \underbrace{\frac{N_s.Q_T.d}{N_p.N_e.\varepsilon.\varepsilon_0.A_i} + \frac{2.N_e.N_s.R.T}{F_c}\sinh^{-1}\left(\frac{Q_T}{N_p.N_e^{\,2}.A_i\sqrt{8.R.T.\varepsilon.\varepsilon_0.c}}\right)}_{V_T} - R_{sc}.i_{sc} \tag{3.26}$$

Where N_p is the number of parallel SC cells, N_s is the number of series connected SC cells, N_e is the number of layers of electrodes, A_i is the interfacial area between electrode and electrolyte (m^2), R is the ideal gas constant ((J/(K.mol)), T is the operating temperature (°K), F_c is the Faraday constant (C/mol), d is the ion molecular radius (m), c is the molar concentration ($mol.m^{-3}$) and Q_T is the electric charge given by:

$$Q_T = \int i_{sc}\,dt \tag{3.27}$$

The model accounts for self-discharge phenomena by modifying the electric charge when the SC current $i_{sc} = 0$ by:

$$Q_T = \int i_{sd}\,dt \tag{3.28}$$

where, i_{sd} is the self-discharge current and is determined by the Tafel equation as follows:

$$i_{sd}(t) = N_e I_f e^{\left(\frac{\alpha F_c\left(\frac{V_{init}}{N_s} - \frac{V_{\max}}{N_s} - \Delta V\right)}{RT}\right.} \tag{3.29}$$

Where I_f is the leakage current (A), V_{init} is the initial voltage (V), α is the charge transfer coefficient and ΔV is the over-potential (V).

Simulink default parameters for the Stern equation including the number of layers (default=1), molecular radius (default=1e-9), and permittivity of electrolyte material (default=6.0208e-10) are selected along with the characteristics shown in Table 3.5.

Simulink default parameters have been determined from experimental tests and validated showing a maximum error of 2% for charge and discharge [112].

Table 3.5 Supercapacitor characteristics

Maxwell BCAP 3400 [70]		
Cell capacity	3400	F
Cell Equivalent DC series resistance	0.15	mΩ
Cell Rated voltage	3	V
Cell specific power	14.5	kW/kg
Cell weight	496	g
Pack configuration	135 series, 1 parallel	
Pack Voltage (max)	405	V
Pack capacity	25.2	F
Pack resistance	20	mΩ
Pack Specific Energy	5.36	Wh/kg
Maximum continuous current (15°C)	140	A
Maximum continuous current (40°C)	225	A
Maximum energy stored	574	Wh
Usable energy (min V=202.5V)	430.5	Wh

The usable energy shown in Table 3.5 is calculated according to:

$$E = \frac{1}{2} C(V_{initial}^2 - V_{final}^2) \tag{3.30}$$

Where $V_{initial}$ is the voltage of the SC at the start of the discharge and V_{final} is the voltage at the end of the discharge. To calculate the usable energy, it is assumed that SC discharges from the fully charged state (405 V) to half its voltage (202.5V). In this way, 75% of the total energy stored in the SC is used [113].

The model assumes the following:

- The internal resistance remains constant during the charge and the discharge cycles
- Temperature effect on the electrolyte material is not considered
- Ageing effect is not considered
- Charge redistribution is the same for all values of voltage
- Cell balancing is not considered
- The current through the SC is assumed to be continuous.

In reality, the SC internal resistance varies during charge and discharge cycles affected by the temperature of operation. The increase in the internal resistance is an indication of SC degradation.

In the simulations, charge and discharge currents are continuous either in the positive (discharge) and negative (charge) cycles. However, there are some periods of time where the SC is at rest or is not providing nor receiving power. This can be interpreted as a discontinuous operation mode as the current flowing through the capacitor changes from a continuous positive or negative value to zero. During these periods of time, the model can implement self-discharge, however this option is not implemented in the present work and therefore the SC is assumed to remain idle when the current is zero.

The battery to SC energy ratio 95:1 considering the battery capacity of 40.6 kWh and 430.5 Wh of the SC. The power ratio is 1:11.9 considering the battery capability at 2C at nominal voltage (81285 W) and the SC 970 kW.

3.3.3 DC/DC converter

DC/DC converters are high frequency conversion circuits that use high frequency switches, inductors and capacitors to smooth out switching noise into regulated DC voltages.

The DC/DC converter has been modelled considering the following assumptions:

- The time to simulate the whole system for each full driving cycle and each EMS variant analysed should be within a reasonable time frame (minutes), which is not possible when accurate DC/DC converter models simulating high frequency switching are used (several hours).
- The model does not include losses, therefore the conversion process is lossless.

The model consists of two controlled current sources receiving the same current command. The first controlled current source is connected to the SC model and the second to the DC-bus. The schematic is shown in Fig. 3.17.

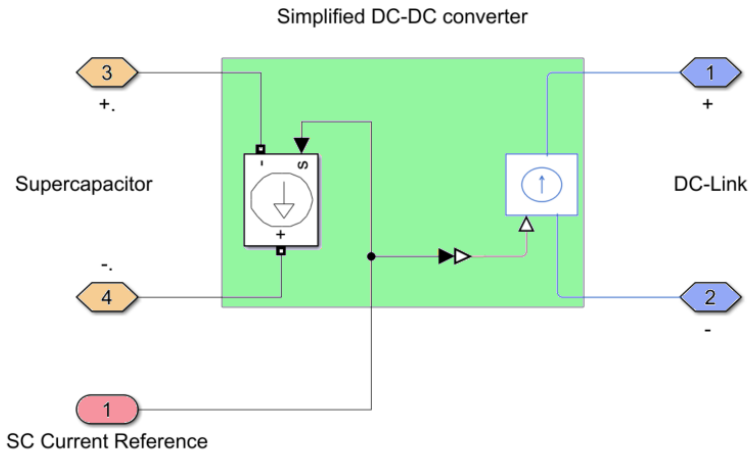

Fig. 3.17. Simplified bidirectional DC/DC converter for system level simulation

In this work, the focus is on the energy inefficiency caused by energy circulation. The lossless DC/DC converter makes this analysis easier to understand.

3.4 Energy management system

3.4.1 The discrete wavelet transform

The DWT is given by the series:

$$f(t) = \sum_{j,k} a_{j,k} \psi_{j,k} \tag{3.31}$$

where the set of coefficients $a_{j,k}$, are called the discrete wavelet transform of $f(t)$, and $\Psi(t)$ is the orthonormal wavelet basis or mother wavelet, j and k are the level of the dyadic decomposition and the displacement factor, respectively [114]. $\Psi_{j,k}$ is given by:

$$\psi_{j,k}(t) = 2^{-j/2} \psi(2^{-j} t - k) \tag{3.32}$$

The original signal can be reconstructed from the wavelet coefficients $a_{j,k}$ and the orthonormal wavelet basis $\Psi(t)$ by means of the inverse DWT. The DWT process involves a signal decomposition stage known as analysis, and a signal reconstruction phase known

as synthesis. This is performed with a filter bank, as shown in Fig. 3.18, which is a collection of conjugate mirror filters [115]. The analysis stage decomposes the signal into low and high frequency components by passing the discrete input signal through high pass $H(z)$ and low pass $L(z)$ filters simultaneously. At the first level of decomposition, the $H(z)$ and $L(z)$ filter output signals each contain half the frequency content and the same number of samples as the input. Decimation by a factor of two is applied to discard half of the samples on each signal without loss of information, according to the Shannon-Nyquist sampling theorem. This process is called down-sampling. At the next level of decomposition, only the low frequency component is decomposed into low and high frequencies and decimated again. In Fig. 3.18, the DWT decomposition and reconstruction (inverse DWT) schematic is shown. The approximation coefficient (A2) represents the low frequency sub-band component, while details (D1, D2) characterise high frequency sub-band components.

In this example, a signal with 4 samples is passed through a high and low pass filter simultaneously, so at the output of each filter the number of samples is 4. This duplicates the number the total number of samples. A down-sampling operator reduces the number of samples by a factor of 2 according to the Nyquist sampling theorem. The output of the low frequency component is passed through a set of high and low pass filters again and down-sampled. This process results in a set of coefficients with a total number of samples that equals the input. These coefficients are enough to perfectly reconstruct the original signal by means of the inverse DWT. The inverse DWT process involves up-sampling the coefficients by a factor of 2 and then passing the resulting samples through a set of conjugate mirror low and high pass filters. When the inverse DWT is calculated to reconstruct the original signal from the DWT coefficients, the up-sampling operator fills with zeroes the gaps created by the down sampling during the DWT decomposition, so the number of total samples correspond to those of the original signal.

The low frequency coefficient (A2) is up-sampled and passed through a low pass filter. The high frequency component (D2) is up-sampled and then passed through a high pass filter. The output of both filters is added and the result up-sampled again. The same process is carried out until all the coefficients are added. This process reconstructs the original signal perfectly. It is worth noting that the frequency corresponding to the approximation coefficient (lowest frequency sub-band) can be found by:

$$f_{Approx} = \frac{f_{nyquist}}{2^j} \tag{3.33}$$

where f_{Approx} is the low frequency sub-band, j is the level of decomposition and $f_{nyquist}$ is the Nyquist frequency which is defined as half the sampling frequency [116]:

$$f_{nyquist} = \frac{f_s}{2} \tag{3.34}$$

The sampling frequency, f_s, at which the signal can be perfectly reconstructed from its samples without loss of information is defined as the Nyquist sampling rate, which must satisfy:

$$f_s > 2 f_{\max} \tag{3.35}$$

where f_{max} is the highest frequency present in a band limited signal.

Although the original signal is perfectly reconstructed, this signal is delayed due to signal processing. The reconstructed DWT frequency components carry a delay that is influenced by the sampling frequency, the target level of decomposition, and the chosen wavelet function. This delay makes the direct use of the DWT frequency components troublesome in real time controllers.

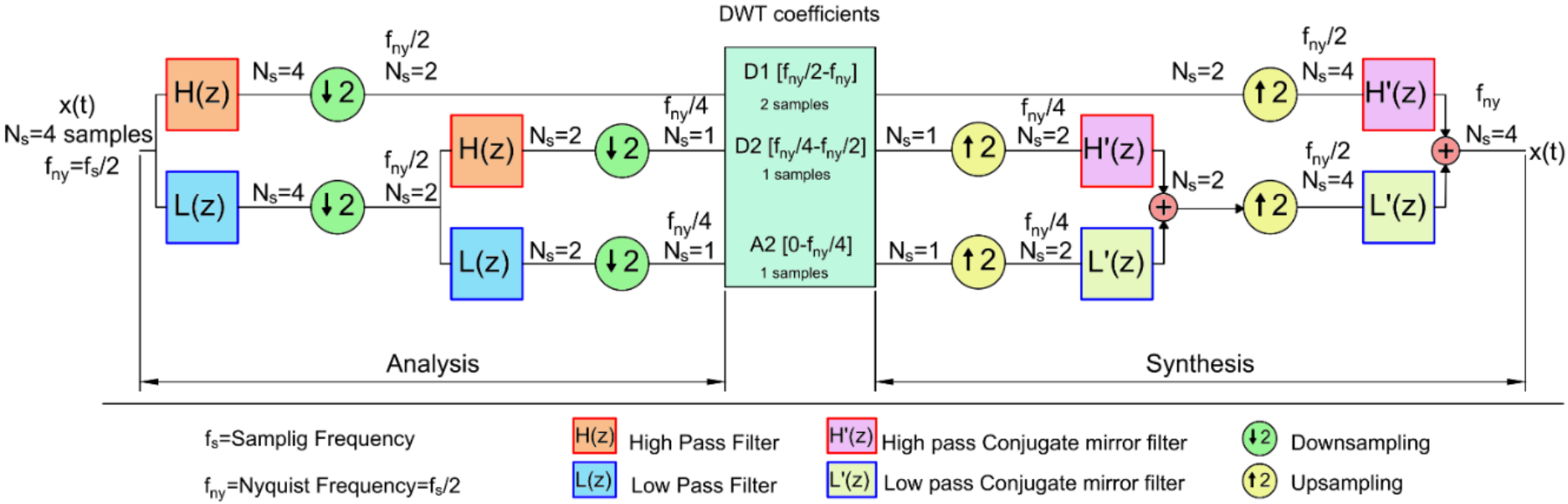

Fig. 3.18. 2 level discrete wavelet transform dyadic signal decomposition tree

The delay results from adding the current sample time period (T_s) to the product between T_s and number of previous samples N_s required to perform a given level of decomposition. The delay (T_d) is given by:

$$T_d = T_s \times (1 + N_s) \tag{3.36}$$

where N_s can be calculated according to [117] such as:

$$N_S = \sum_{i=1}^{j} (N_f - 1)2^{i-1} \tag{3.37}$$

N_f is the order of the filter, characterised by the number of coefficients associated with the chosen orthogonal wavelet base, i is the current level of decomposition and j is the final level of decomposition. The number of samples grow exponentially with the increase of the levels of decomposition. The delay is exacerbated as the order of the filter increases when using different wavelet bases other than the Haar wavelet. Haar is the simplest wavelet with the smallest filter order ($N_f = 2$).

The Haar wavelet has good time localisation, but low frequency resolution. It is better suited for edge detection and sharp signal transitions [115] due to its square shaped waveform as shown in Fig 3.19. It is expressed as [114]:

$$\psi(t) = \begin{cases} 1, & i < t < 1/2; \\ -1, & 1/2 \le t < 1; \\ 0, & \text{otherwise} \end{cases} \tag{3.38}$$

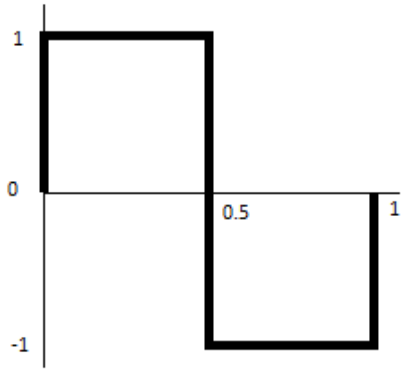

Fig.3.19 Haar wavelet waveform

In Table 3.6, the low frequency sub-bands achieved with several levels of decomposition using the Haar wavelet and different sampling rates are presented. It is important to note that increasing the sampling rate does not reduce the total delay. The higher the sampling rate, the higher the level of decomposition needed to achieve the same low frequency sub-band. This will also increase the number of samples. The delay in seconds of the reconstructed signal with respect to the original signal for different sampling rates and levels of decomposition with the Haar wavelet is presented in Table 3.7.

Table 3.6. Low frequency sub-bands and number of samples required for several levels of decomposition and sampling frequencies using the Haar wavelet

Number of previous samples N_s	Sampling Freq. f_s	1 Hz	2 Hz	4 Hz	8 Hz	16 Hz	32 Hz
Haar Wavelet	Nyquist Freq (f_s/2)	0.5 Hz	1 Hz	2 Hz	4 Hz	8 Hz	16 Hz
1	Level 1	0-250 mHz	0-500 mHz	0-1 Hz	0-2 Hz	0-4 Hz	0-8 Hz
3	Level 2	0-125 mHz	0-250 mHz	0-500 mHz	0-1 Hz	0-2 Hz	0-4 Hz
7	Level 3	0-62.5 mHz	0-125 mHz	0-250 mHz	0-500 mHz	0-1 Hz	0-2 Hz
15	Level 4	0-31.25 mHz	0-62.5 mHz	0-125 mHz	0-250 mHz	0-500 mHz	0-1 Hz
31	Level 5	0-15.62 mHz	0-31.25 mHz	0-62.5 mHz	0-125 mHz	0-250 mHz	0-500 mHz
63	Level 6	0-7.81 mHz	0-15.62 mHz	0-31.25 mHz	0-62.5 mHz	0-125 mHz	0-250 mHz
127	Level 7	0-3.90 mHz	0-7.81 mHz	0-15.62 mHz	0-31.25 mHz	0-62.5 mHz	0-125 mHz
255	Level 8	0-1.95 mHz	0-3.90 mHz	0-7.81 mHz	0-15.62 mHz	0-31.25 mHz	0-62.5 mHz
511	Level 9	0-0.97 mHz	0-1.95 mHz	0-3.90 mHz	0-7.81 mHz	0-15.62 mHz	0-31.25 mHz

Table 3.7. Levels of decomposition and time delay relationship when using the Haar wavelet

		Delay in samples Eq.3.30 and delay in seconds Eq.3.29 according to sampling rate					
Level of decomposition	Delay in samples (Haar) (Eq. 3.30)	1 Hz	2 Hz	4 Hz	8 Hz	16 Hz	32 Hz
Level 1	1	2 sec	1 sec	0.5 sec	0.25 sec	0.125 sec	0.0625 sec
Level 2	3	4 sec	2 sec	1 sec	0.5 sec	0.25 sec	0.125 sec
Level 3	7	8 sec	4 sec	2 sec	1 sec	0.5 sec	0.25 sec
Level 4	15	16 sec	8 sec	4 sec	2 sec	1 sec	0.5 sec
Level 5	31	32 sec	16 sec	8 sec	4 sec	2 sec	1 sec
Level 6	63	64 sec	32 sec	16 sec	8 sec	4 sec	2 sec
Level 7	127	128 sec	64 sec	32 sec	16 sec	8 sec	4 sec
Level 8	255	256 sec	128 sec	64 sec	32 sec	16 ec	8 sec

The decomposition of a chirp signal with 5 levels of decomposition using the sym5 wavelet is shown in Fig 3.19. Notice that the detail coefficients for each level of decomposition hold the high frequency sub-bands of the chirp signal, where the highest frequency sub-band is obtained at level 1, while the approximation coefficients hold the low frequency components, where the lowest frequency sub-band is obtained at the last level of decomposition (level 5).

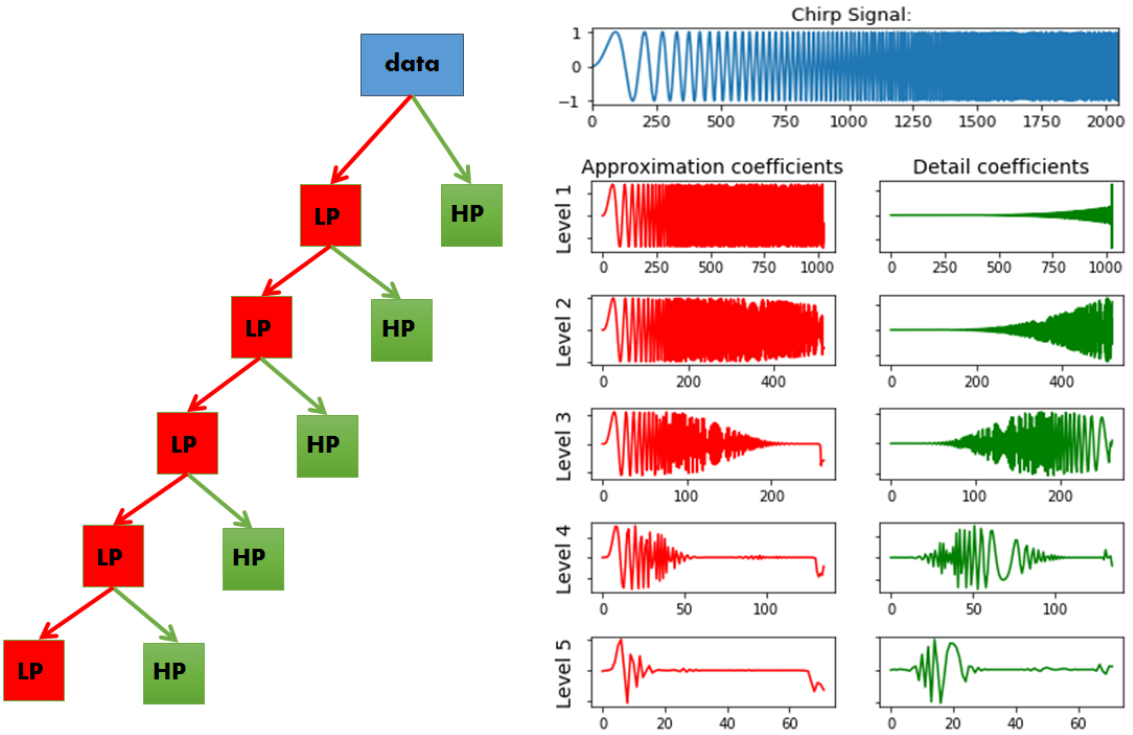

Fig. 3.20 The approximation and detail coefficients of the sym5 wavelet (level 1 to 5) applied on a chirp signal. On the left, a schematic representation of the high pass and low pass filters applied on the signal at each level is shown [118].

Fig.3.21 depicts the DWT decomposition and reconstruction process for the power demand signal corresponding to 120 seconds of the FTP72 driving cycle. The signal is first sampled at a given sampling rate (1 Hz in this example), then passed through the DWT process with 2 levels of decomposition. The DWT outputs 3 frequency components. Adding the frequency components results in a perfectly reconstructed signal that is delayed (4 seconds) with respected to the original signal.

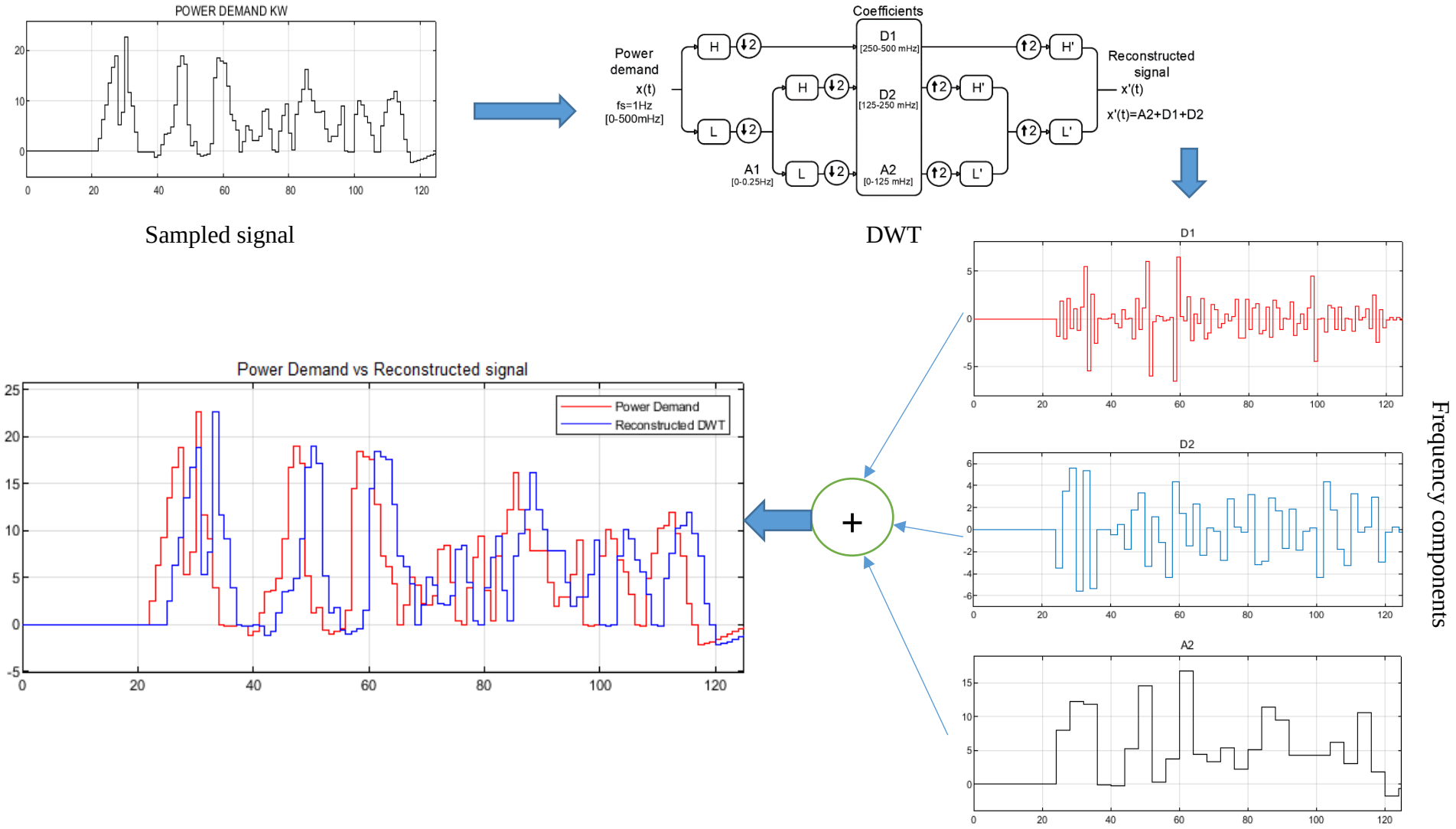

Fig.3.21. Decomposition of power demand signal (FTP72 driving cycle) into 3 levels

3.4.2 Discrete wavelet transform multiresolution simulink model

The Simulink model for the DWT decomposition (analysis) and reconstruction (synthesis) processes is shown in Fig. 3.22. The DWT decomposes the sampled input signal into high and low frequency sub-bands, each with half the bandwidth and half the sample rate of the input. In the analysis filter bank, the signal is simultaneously filtered with a high pass and a low pass FIR filters. The result of these filters is down sampled by 2. The Simulink block implements the FIR filtering and down sampling steps together using a polyphase filter structure [119]. To configure this block, a vector with the filter coefficients defined by a given wavelet are calculated for the high pass and low pass FIR filters. The filter coefficients for the Haar wavelet can be obtained with the following Matlab code:

```
[LoD,HiD,LoR,HiR] = wfilters('db1')
```

where ‘db1’ refers to the Haar wavelet, which represents the same wavelet as Daubechies db1, LoD and HiD are the decomposition low pass and high pass filter coefficients, respectively, and LoR and HiR are the reconstruction low pass and high pass filter coefficients, respectively. The resulting coefficients for the filters are shown in Table 3.8.

Table 3.8. Haar wavelet FIR low pass and high filter coefficients for decomposition and reconstruction

	Low pass filter	High pass filter
Decomposition coefficients	$1/\sqrt{2}$, $1/\sqrt{2}$	$-1/\sqrt{2}$,$1/\sqrt{2}$
Reconstruction coefficients	$1/\sqrt{2}$,$1/\sqrt{2}$	$1/\sqrt{2}$,$-1/\sqrt{2}$

The synthesis filter bank is divided in two branches as shown in Fig. 3.22. One is used to calculate the high frequency components (details) by zeroing the low pass filter input, and the other is used to calculate the low frequency component (approximation) by zeroing the high pass filter input.

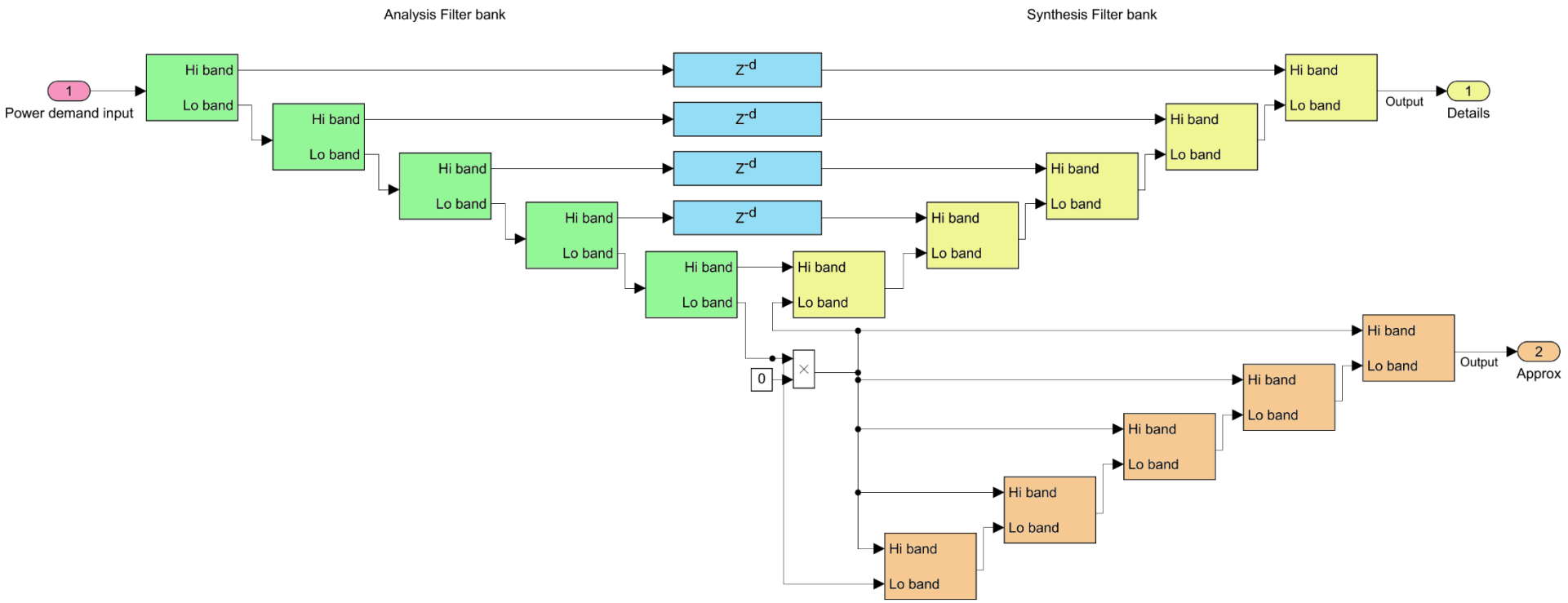

Fig. 3.22. 5 level Discrete wavelet transform Simulink model

3.4.3 Discrete wavelet transform in energy management systems, energy circulation and supercapacitor assistance

To illustrate energy circulation between the battery and SC in a semi-active topology, the SC current reference is first obtained with a conventional first order high pass filter. This will enable the observation of the exacerbated energy circulation when the SC current reference is obtained later with the DWT. At a certain frequency range, the output of the high pass filter has a response that is proportional to the time derivative of the input. Thus, when the slope of the current demand signal (measured at the DC-bus) changes from positive to negative, the output of the high pass filter will also change from positive to negative. For example, when the driving cycle demands a reduction in acceleration i.e. from acceleration to cruising, the current demand declines but remains positive. However, this drop in current demand can appear as a negative signal at the output of the filter even though there is no braking command requested. Fig. 3.23 illustrates this event with a conventional first order high pass filter with a cut-off frequency of 125 mHz. The current demand and the vehicle speed from t=20 seconds to t=37 seconds of FTP72 driving cycle are displayed. At time t = 26 seconds the slope of the current demand changes from positive to negative because of the drop in the power demand caused by an adjustment in speed. Although speed keeps rising from 26 km/h at t = 26 seconds to 28 km/h at t = 27.6 seconds (i.e. no braking command), the high pass filter output becomes negative. As the SC is controlled with the output of the high pass filter, energy circulation occurs as the SC is commanded to recharge (negative current command represented as green shades) even when no braking power is generated. The SC is recharged from the battery (orange shades), which transfers power to the SC through the DC/DC converter. The areas shaded in light blue represent the effective contribution of the SC during motoring and braking.

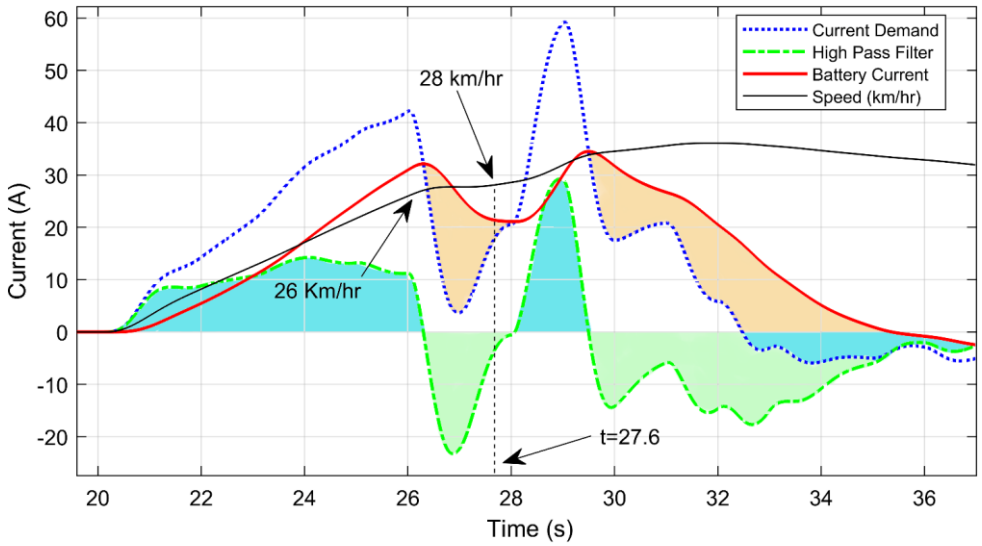

Fig. 3.23. Energy circulation with 1st order High Pass Filter 125 mHz

Energy circulation is exacerbated when the DWT is used, as the high frequency component is delayed with respect to the real time demand. In Fig. 3.24, the SC follows the high frequency component current reference obtained with the DWT. The current demand is sampled at 1 Hz and then decomposed into 2 levels to obtain a frequency sub-band of 125-500 mHz. The drop in the current demand that starts at t = 26 seconds results in a delayed drop in the DWT high frequency component that starts at t = 30 seconds (delay = 4 seconds). Thus, the use of the DWT high frequency component results in the SC recharging when there is no braking power (green shaded areas), forcing the battery to provide power to keep the system's balance (orange shaded areas). Consequently, more stress is imposed on the battery rather than alleviating it, and poor SC contribution is observed during motoring and braking (light blue shaded areas). Moreover, efficiency decreases as energy is circulated without controlling its occurrence.

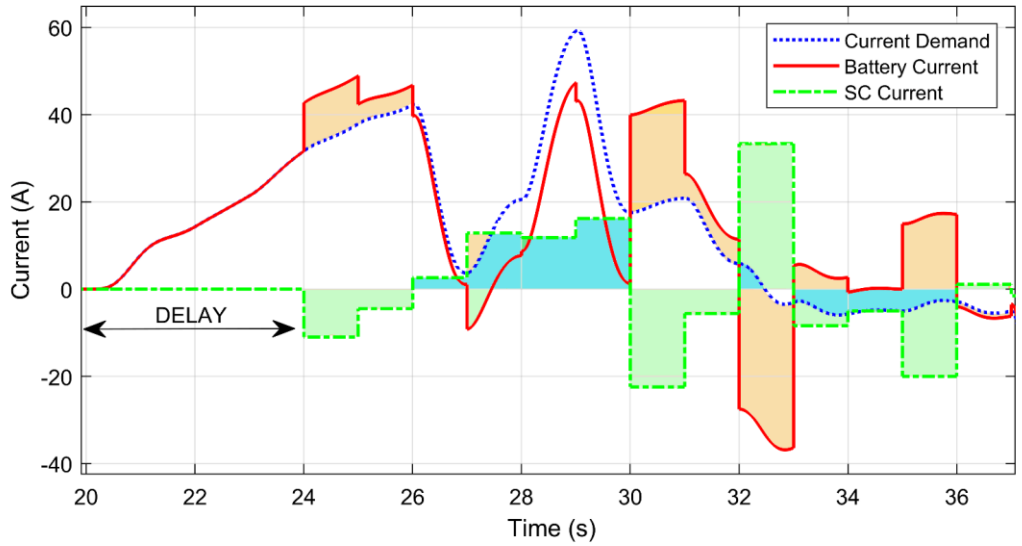

Fig. 3.24. SC current reference following the DWT high frequency component, sampling=1Hz

DWT high frequency components with more details (smoother signal) can be generated with higher sampling rates and adequate levels of decomposition. In Fig. 3.25, sampling rate of 32 Hz and 7 levels of decomposition result in frequency sub-band of 0.125 Hz-16 Hz. The delay remains unchanged (4 seconds).

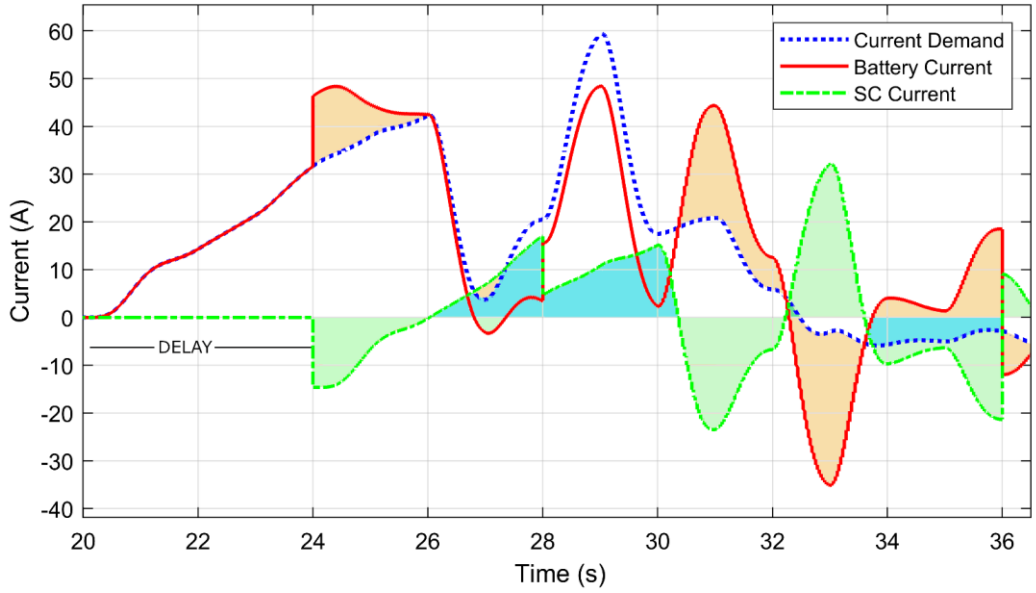

Fig. 3.25. SC current reference following the DWT high frequency component, sampling =32 Hz.

Both Fig. 3.24 and 3.25 show that the SC is not assisting the battery during acceleration and is partially recovering power generated during braking. This is evident between t=20 and t=26, and between t=33 and t=36, respectively.

The sharp transitions in the signal i.e. t=24 in Fig 3.24 and Fig 3.25 is a consequence of using the Haar wavelet as it has a squared shape signal. The sharp changes are more notorious when the sampling rate is 1 Hz as in Fig 3.24.

3.4.4 Defining a benchmark to assess SC performance in a HESS

To quantify the effectiveness of the SC assistance during motoring and braking a comparison with a benchmark reference is necessary. To determine this reference, the following factors have been considered:

1. The first derivative of the positive current demand is calculated to define time windows that correspond to positive current demand changes. Only positive values are considered. Time windows are shown in Fig. 3.26 for t=19 seconds to t=42 seconds of the FTP72 driving cycle.
2. During positive current rate, the benchmark current reference is set to match the first derivative of the current as long as the derivative is less than the total current demand, otherwise it is set to match the total current demand. This makes the benchmark reference proportional to the rate of change of current but without exceeding the total current demand. This defines the areas where SC assistance would be most beneficial.
3. During braking, all the generated energy should be absorbed by the SC if its SOC allows it. Otherwise, it will be allocated to the battery observing the maximum charging C-rate. This area is given by the negative current demand.

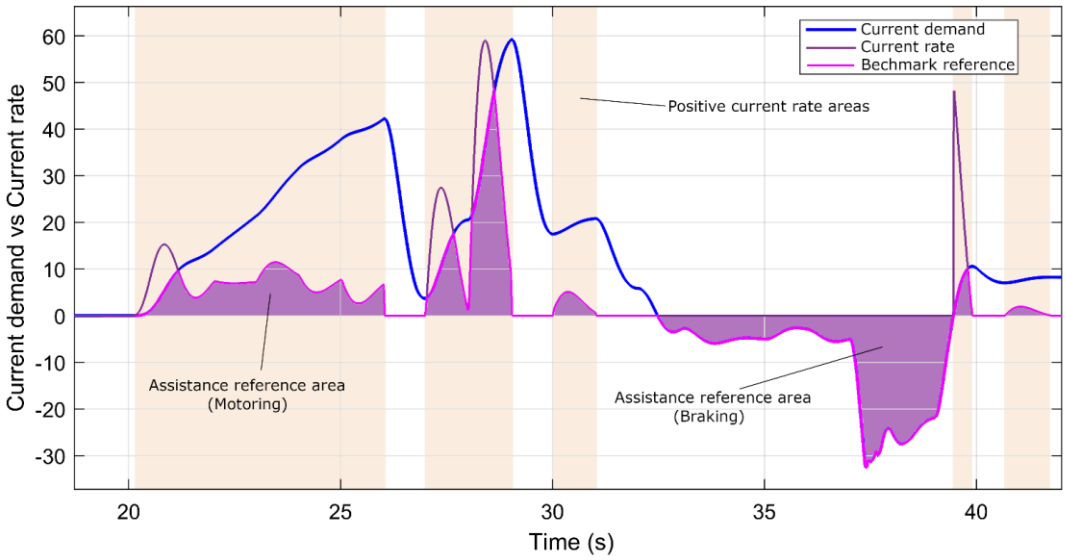

Fig. 3.26. Reference signal to assess SC performance (FTP72 case)

The effectiveness of SC assistance with different EMS approaches can be assessed by comparing the energy provided by the SC against the energy of the benchmark reference area. The energy E in Wh is calculated as follows:

$$E = \frac{1}{3600}\int_0^t I_X \times V_{DC-bus}\,dt \tag{3.39}$$

where I_X is the current of the variable being analysed i.e. total current, battery current, and SC current. V_{DC-bus} is the voltage of the DC-bus. The result of the integral is divided by 3600 to convert seconds to hours. Positive current demand is used to calculate motoring energy and negative current demand to calculate braking energy. For each EMS strategy presented in this chapter, the areas shown in Fig. 3.27 are calculated. The orange shading represents the circulation energy (unit is Ah) supplied by the battery and received by the SC (green shading), or vice versa. The blue shaded areas represent the SC effective contribution during the motoring and braking stage. The purple area represents the current reference based on the current rate of change. These areas are used to quantify the SC assistance during motoring, acceleration, braking and total energy circulation for different EMS strategies.

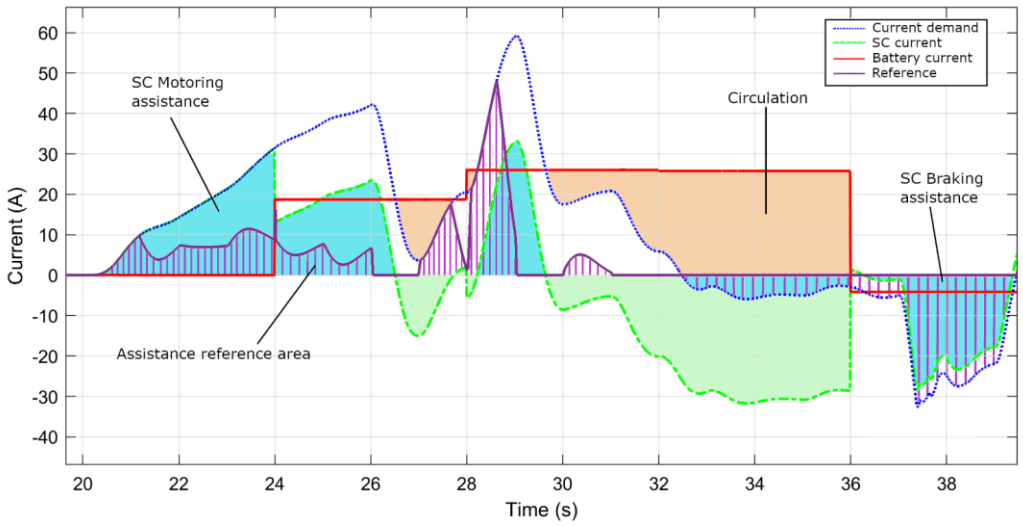

Fig. 3.27. Calculated areas to compare the performance of the SC with different EMS strategies

3.4.5 Long-short term memory neural network

Power demand prediction has been proposed in the literature as a way to mitigate delay and enable the DWT to work in real time. LSTM neural networks are a type of RNNs that perform well when learning long term temporal dependencies. RNNs carry out prediction of future steps by considering previous data. The internal structure of the network learns from earlier stages and uses this previous data along with new data to forecast future steps. However, typical generic RNNs can remember only a few previous steps in the sequence and therefore fail to remember long sequences of data [120]. On the other hand, long term memory is possible by using LSTM networks, which are designed to capture and store data. The LSTM cell behaves like a memory with the ability to write, read and delete data according to the decisions stipulated by its input, output, and forget gates. The structure of a LSTM cell with its inner operations is shown in Fig. 3.28.

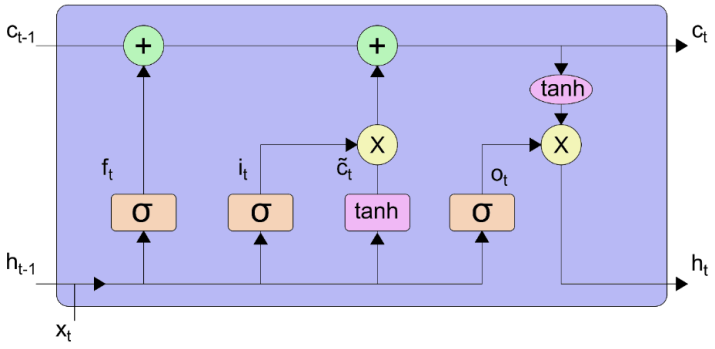

Fig. 3.28. LSTM cell structure

The forget gate output f_t is calculated from the previous output h_{t-1}, the input vector x_t, the weight matrix associated with this gate $[W_{xf}, W_{hf}]$ and a bias b_f. The input gate output i_t is calculated in similar way but using a different weight matrix $[W_{xi}, W_{hi}]$ and bias b_i. The cell state c_t is calculated from addition of the forget gate f_t and the previous cell state c_{t-1}. The result is added to the product between the input gate i_t and the cell state update $\tilde{c}_t$, the weight matrix and the bias. The output gate o_t results from the previous output h_{t-1}, the input vector x_t, the weight matrix associated with this gate $[W_{xo}, W_{ho}]$ and a bias b_o. The current output h_t results from the product between the output gate o_t and the hyperbolic tangent of the current cell state c_t. The cell equations are [121]:

$$\begin{aligned} i_t &= \sigma(W_{xi}x_t + W_{hi}h_{t-1} + b_i) \\ f_t &= \sigma(W_{xf}x_t + W_{hf}h_{t-1} + b_f) \\ o_t &= \sigma(W_{xo}x_t + W_{ho}h_{t-1} + b_o) \\ \tilde{c}_t &= \tanh(W_{xc}x_t + W_{hc}h_{t-1} + b_c) \\ c_t &= f_t \odot c_{t-1} + i_t \odot \tilde{c}_t \\ h_t &= \tanh(o_t \odot c_t) \end{aligned} \tag{3.40}$$

Where σ is the logistic sigmoid function and $\odot$ is the element wise product. A sigmoid function is a mathematical function having a characteristic “S” shaped curve or sigmoid curve. The logistic sigmoid function is shown in Fig.3.29 [122].

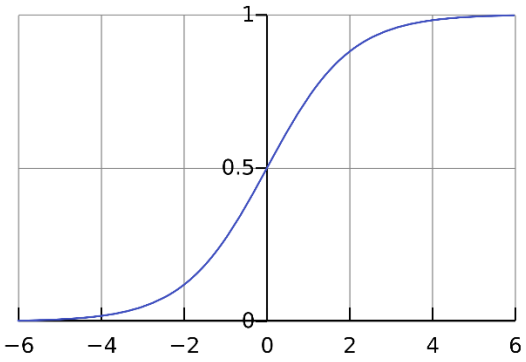

Fig. 3.29 Logistic sigmoid function

The logistic sigmoid curve is defined by the formula:

$$f(x) = \frac{1}{1+e^{-x}} \tag{3.41}$$

In this work, the hyper-parameters of the LSTM network were determined by testing several architectures and comparing their prediction Mean Squared Error (MSE) as shown in Table 3.9. A good fit learning curve is identified when the training and validation loss decrease to a point of stability with a minimal gap between the two final loss values [123] as shown in Fig. 3.30.

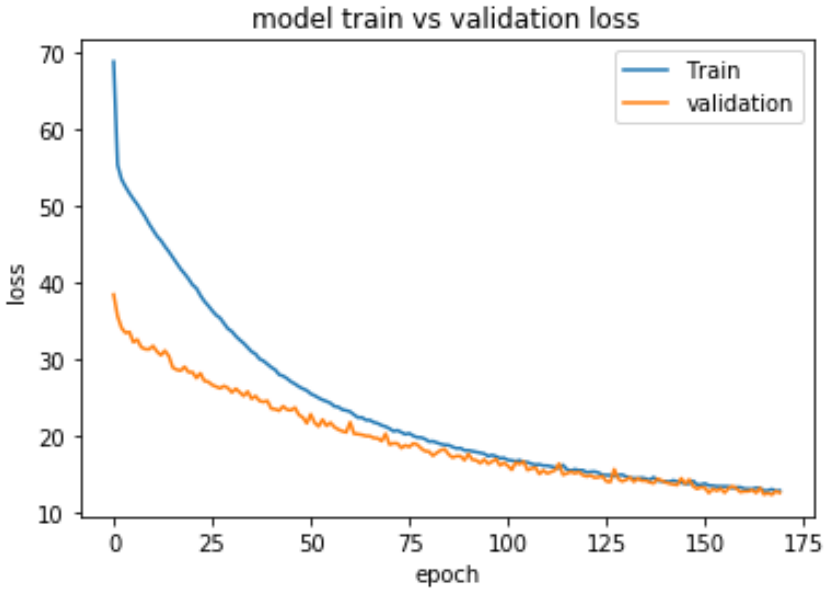

Fig. 3.30. LSTM network training vs validation loss

The mean squared error loss is calculated as the average of the squared differences between the predicted and actual values. The results is always positive regardless of the sign of the predicted and actual values. The lower the loss, the better a model. The loss is calculated on training and validation datasets and is interpreted as how well the model is doing for these two sets. Unlike accuracy, loss is not a percentage. It is a summation of the errors made for each example in training or validation sets. Naturally, the main objective in a learning model is to reduce (minimize) the loss function's value with respect

to the model's parameters by changing the weight vector values through different optimization methods. Loss value implies how well or poorly a certain model behaves after each iteration of optimization. Ideally, one would expect the reduction of loss after each, or several, iterations and reach zero.

Table 3.9 LSTM network architectures training loss and validation loss

LSTM Structure	Layers and Neurons	Epochs	Training Loss MSE	Validation Loss MSE
1	1x10	10	59.16	29.65
2	1x10	50	51.71	32.64
3	2x10	50	55.44	28.18
4	1x50	100	37.57	30.03
5	2x50	100	22.01	41.62
6	2x50	150	13.89	14.78
7	2x50	170	12.78	12.50
8	3x50	150	20.23	15.16
9	1x60	100	34.61	32.71
10	1x100	100	25.59	34.31
11	1x600	50	19.24	12.46
12	1x800	50	17.29	9.56
13	1x1000	50	21.49	14.50
14	1x1100	50	17.91	11.66
15	1x1500	50	24.34	11.30

LSTM structure 7 from Table 3.9 is chosen as the training and validation losses reached the minimum among the tested neural network structures and hyperparameters. The selected hyper-parameters correspond to those where the training and validation losses converged and reached a minimum, 12.78 and 12.50, respectively. This was achieved using the stochastic gradient descend optimisation algorithm ADAM (this term is not an acronym and is derived from ‘Adaptive Moment Estimation’), a learning rate of 0.001, and hyperbolic tangent (TANH) activation. The neural network structure consists of a sequence input layer receiving 8 samples, 2 fully connected hidden layers with 50 LSTM units each, and a regression layer with 5 outputs, corresponding to the number of predicted samples. The network was trained with 90% of the dataset and tested with 10%.

Machine learning algorithms can be evaluated using the train-test split technique, which

is used for classification and regression problems. Essentially, the procedure involves subdividing a dataset into two parts. The first subset is used to fit the model and is referred to as the training dataset. The second subset is not used to train the model; instead, the input element of the dataset is provided to the model, then predictions are made and compared to the expected values. This second dataset is referred to as the test dataset [124]. The main purpose of splitting the dataset is to estimate the performance of the machine learning model on new data: data not used to train the model. The train-test procedure is appropriate when there is a sufficiently large dataset available. As the dataset used in this work is not big (8465 samples), the split proportion was chosen to be 90% for training and 10% for testing. The Python program to train and test the neural network is presented in appendix A at the end of this thesis.

The model's hyper-parameters were tuned to achieve good performance considering the following conditions:

a) The network must predict from the measured real time raw data, as there is no time to perform data pre-processing such as de-noising, normalisation, and standardisation, which would introduce more delay.
b) The network must be able to perform the prediction with minimum delay. The ideal would be zero delay, however, the delay depends on the computing capability of the machine used to perform the predictions.
c) Prediction error must be minimal for any driving condition. A prediction error approaching zero would be ideal. However, the error depends on several factors and can be high especially with highly stochastic datasets.

Forecasting based on raw data has some limitations and drawbacks, such as computationally demanding training phases, the need for a big dataset, a large number of hyper-parameters, and sensitivity to measurement noise. The LSTM neural network was created and trained in Keras, a deep learning API written in Python, using a dataset

(duration=8465s) containing the power demand obtained by simulating the vehicle with a battery only ESS with the following 8 driving cycles (in order):

1. Artemis Urban
2. Urban Dynamometer Driving Schedule (HUDDS)
3. Highway Fuel Economy Test (HWFET)
4. JC08 Japanese Chassis Dynamometer Test
5. Unified Dynamometer Driving Schedule LA92
6. Chassis Dynamometer Test SC03
7. EPA Driving Schedule for Light-Duty Vehicles and Trucks (US06)
8. Worldwide Harmonized Light Vehicle Test Procedure (WLTP3). (The 10% of the dataset used for testing corresponds to a portion of this driving test)

The speed vs time schedule for each driving cycle is shown in Fig. 3.31.

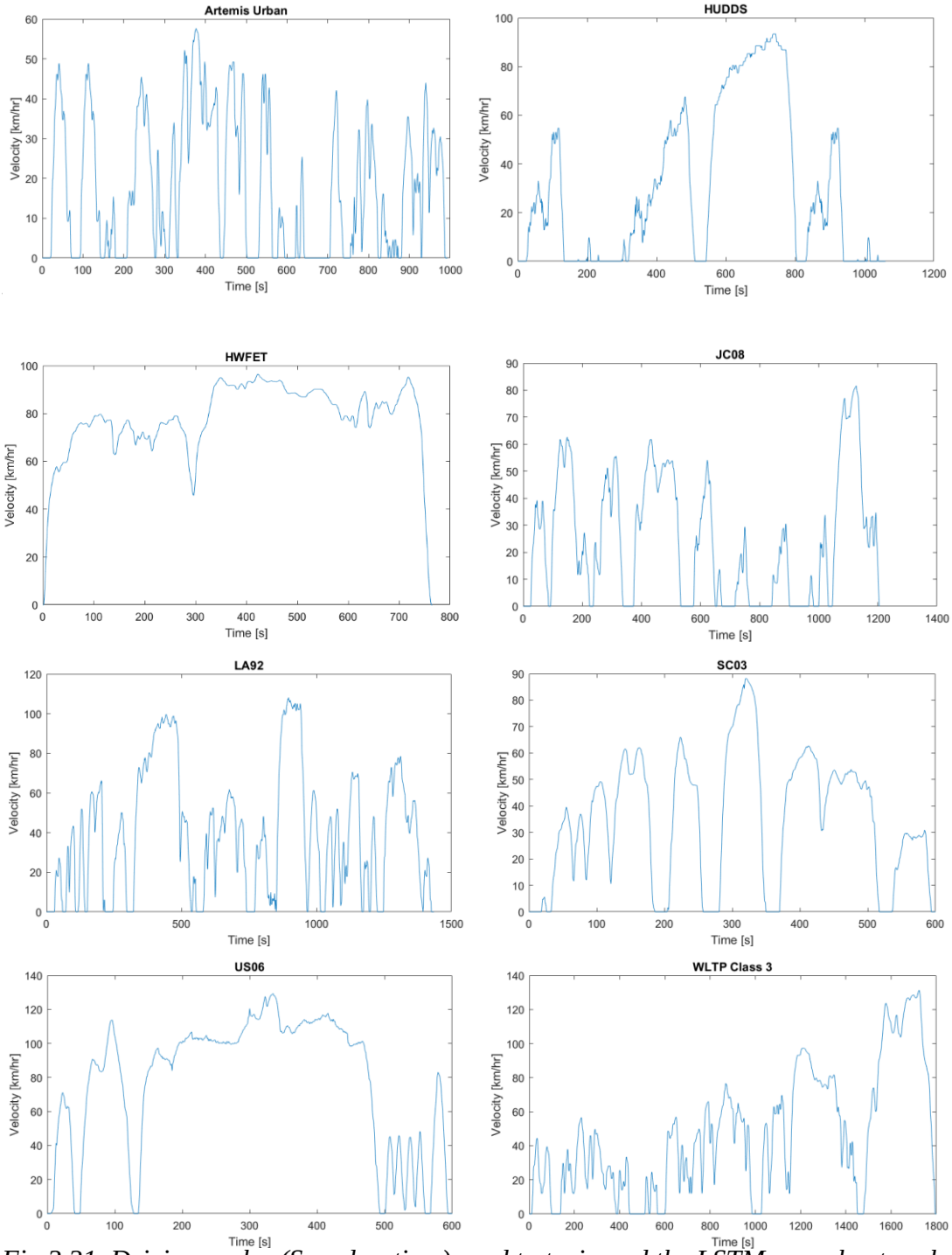

Fig 3.31. Driving cycles (Speed vs time) used to train and the LSTM neural network

The power demand associated with any driving cycle depends on several factors including driving style, road condition, road gradient, weather, traffic conditions, etc. This makes accurate prediction difficult. Due to the complex non-linearity of the power demand associated with driving, prediction errors are inevitable, especially with multi-step time

series forecasting. The generalisation capability of the trained network is tested with 4 driving cycles not seen by the network during training, obtaining a prediction Root Mean Squared Error (RMSE) of 8.91 kW for the FTP72, 5.75 kW for the Inspection and Maintenance Driving Schedule (IM240), 3.31 kW for the Extra Urban Driving Cycle (EUDC), and 16.19 kW for the Artemis Motorway 130 km/hr, when predicting 5 future samples. Additionally, the prediction RMSE for the US06 driving cycle is 11.79 kW and 3.59 kW for the WLTP3 driving cycle, which were used during the training stage. Predictions were executed in a machine with an 8th generation Intel Core i5, 32 GB RAM, 1.9 GHz 8th generation processor. On average, the network took 0.9s to execute the predictions. This extra delay is variable and is highly dependent on the performance of the computer used. This delay was around 2s with a computer with an Intel core i5, 8 GB RAM and 2.3 GHz Sandy Bridge processor. This extra delay is added to the DWT delay yielding a total of ~4.9s. Power demand is sampled at 1 Hz, hence the prediction window of 5 samples. Fig.3.32 presents the driving cycles used for testing the trained neural network.

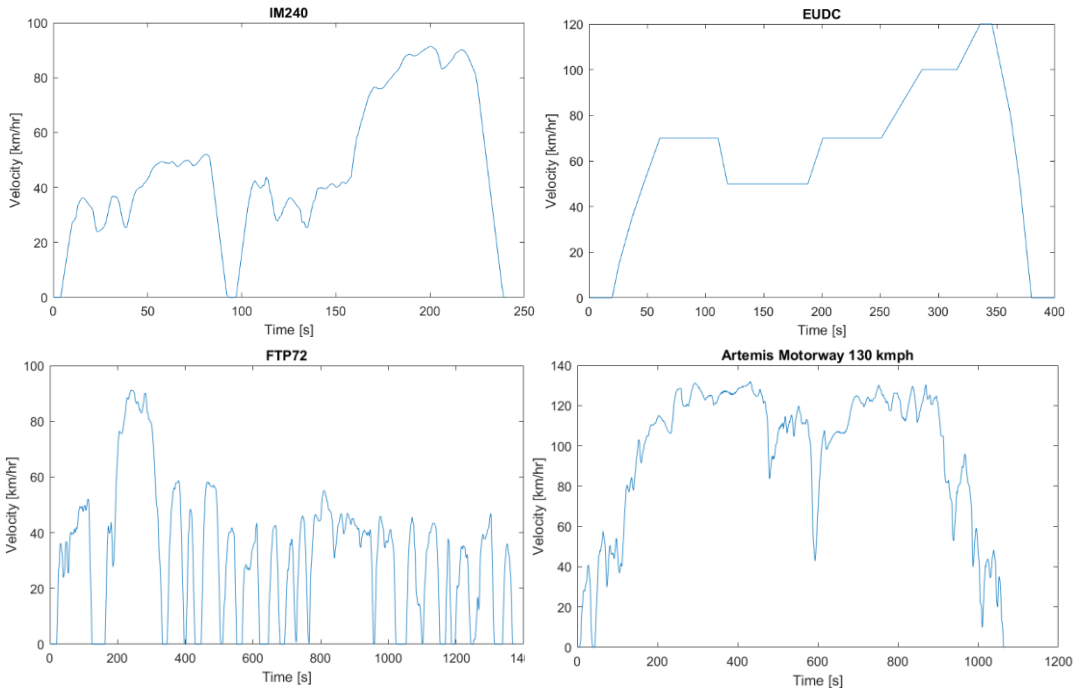

Fig. 3.32. Driving cycles used to test the trained neural network

3.5 Energy management system performance evaluation

In this section, 4 different real-time implementation strategies for the DWT are evaluated in terms of SC assistance during motoring, peak assistance, braking energy recuperation, energy circulation, and energy efficiency. The 4 strategies depend on how the SC reference current $I_{ref(SC)}$ is determined:

A. DWT high frequency component
B. Predicted DWT high frequency component
C. Difference between the real-time current demand and the DWT low frequency component
D. Difference between the real-time current demand and the predicted DWT low frequency component

A schematic of these 4 strategies is shown in Fig. 3.33. The detailed EV model is implemented in Matlab-Simulink along with the DWT strategies and tested using a variety of driving cycles representing real-world loading conditions including urban and highway scenarios. The battery and SC initial SOC is set to 80% for simulations. The sampling frequency is 1Hz and the DWT level of decomposition is 2, which produces a delay of 4 seconds. The sampling rate of 1Hz is chosen considering that the frequencies of interest associated with the power demand obtained for different driving cycles lays below 0.5 Hz. Another reason is to limit the number of samples to be predicted by the neural network. Higher sampling rates require to predict more samples and that would increase the complexity of the neural network as well as the computational burden during training and testing.

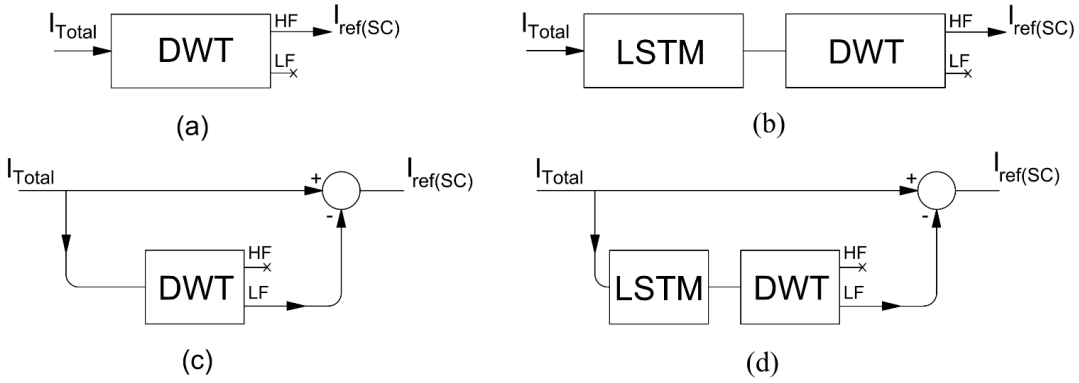

Fig. 3.33. SC current reference calculation. a) Direct DWT high frequency component, b) Predicted DWT high frequency component, c) Difference between current demand and DWT low frequency component, d) Difference between current demand and predicted DWT low frequency component

3.5.1 Direct discrete wavelet transform high frequency component (strategy A)

The current demand associated with the FTP72 driving cycle (duration of 1372 seconds) is sampled at 1Hz and decomposed into 2 levels. The DWT high frequency component (125mhz -500mhz) is used directly to control the SC power flow. As the control signal is delayed, energy is circulated between the battery and the SC, putting greater stress on the battery as it supplies more power to recharge the SC while receiving minimal assistance during the periods of positive changes in current demand. This is evident in Fig. 3.34, where at t = 57 seconds, the current demand is 41A, but the battery supplies 68A as the SC is commanded to recharge. In addition, the SC does not provide assistance during the initial acceleration (t=20 seconds to t=26 seconds) and fails to recuperate braking power, which is mostly absorbed by the battery. SC assistance during motoring and braking is represented by the shaded areas to highlight the effective contribution of the SC.

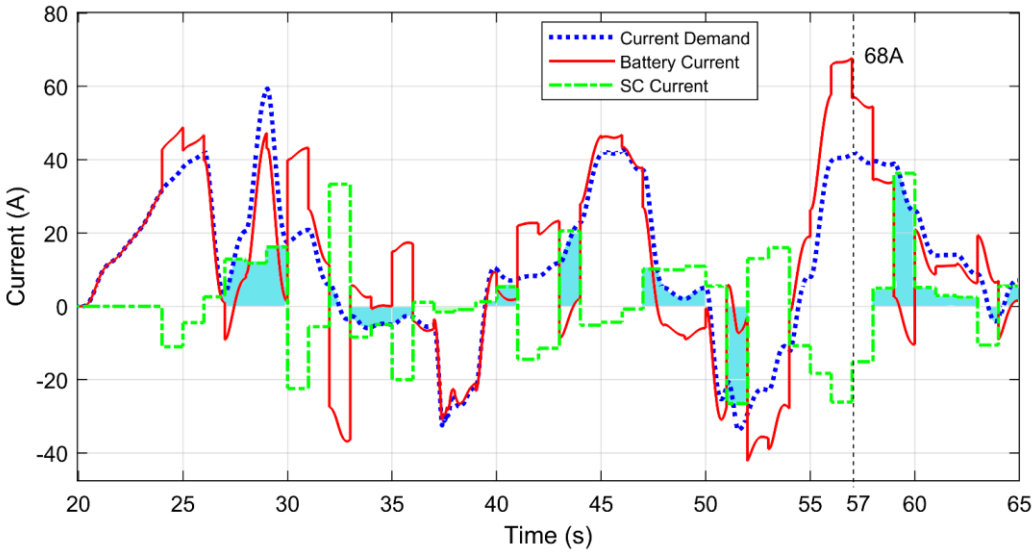

Fig. 3.34. DWT high frequency component allocated to the SC for the FTP72 driving cycle (shown from 20 seconds to 65 seconds)

Fig. 3.35 and Fig. 3.37 shows the energy balance for the motoring and braking stages, respectively. The total energy required by the EV during motoring is 1668Wh and the energy produced during braking is 470.8Wh. This is calculated according to (eq. 3.39) using the current demand. The same procedure is used to calculate the battery and SC energies using the battery and SC current, respectively. The battery provides a total of 1765Wh during motoring and recovers a total of 569.4Wh during braking. The SC provides 413.7 Wh during motoring and recovers 412.1 Wh during braking.

The battery and the SC provided a total of 2178.7 Wh (1765Wh+413.7Wh) of motoring energy (Fig. 3.35) which is equivalent to 30.6% (510.7Wh) more energy than the required (1668Wh) during the driving cycle. From the 413.7Wh provided by the SC during the motoring stage, 227.4Wh are effectively contributed to motoring. The remaining 186.3 Wh are transferred to the battery. On the other hand, from the 1765Wh provided by the battery, 1440.6Wh are effectively contributing towards motoring while 324.4 Wh are transferred to the SC through the DC/DC converter. The total energy circulating between the battery and SC is 510.7 Wh (186.3 Wh+324.4 Wh).

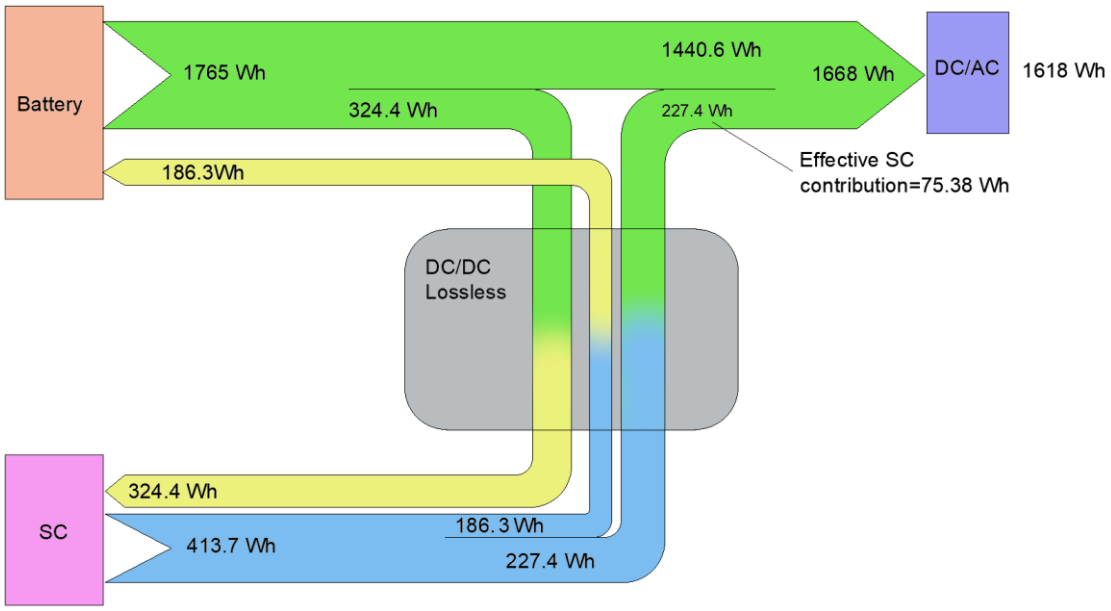

Fig. 3.35. Motoring stage energy balance

The SC provides a total of 227.4Wh of effective assistance during the motoring stage, which correspond to the positive blue shaded areas in Fig. 3.34. However, only 75.38Wh corresponds to assistance during positive changes in the current rate. This is shown as the positive blue shaded areas in Fig. 3.36, which depicts the overlap between the SC current and the benchmark reference (see Fig. 3.26).

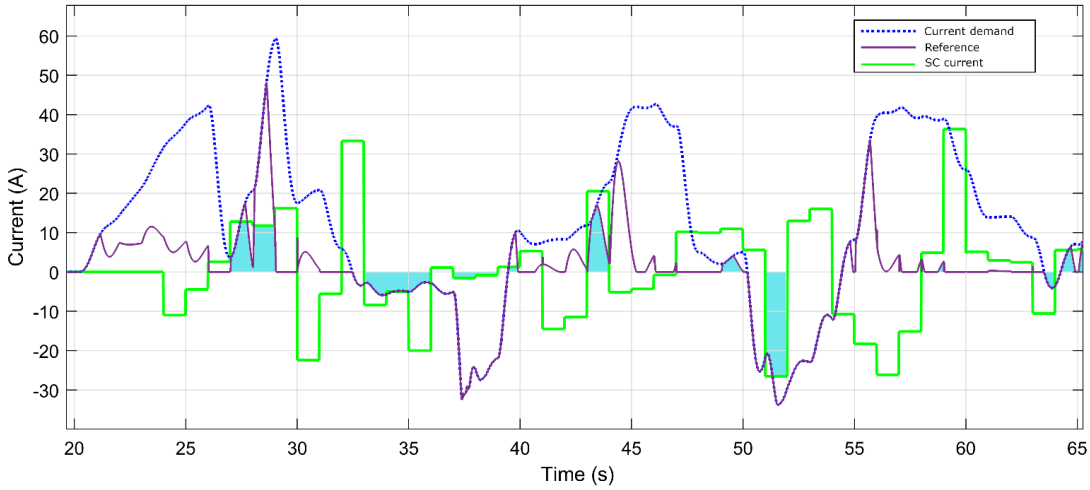

Fig. 3.36. Assessment of SC effective contribution during changes in the acceleration rate. Comparison between the SC current and current rate reference

The energy balance for the braking stage is shown in Fig. 3.37.

The SC recovers only 87.5Wh of the 470.8Wh generated during braking (negative blue shaded areas in Fig. 3.36). The battery absorbs the remaining 383.3Wh. In total the HESS

recovered 981.5 Wh that results from adding the energy recovered by the battery (569.4 Wh) and energy recoverd by the SC (412.1 Wh). The energy circulating in the system is 510.7 Wh (186.1 Wh+ 324.6 Wh).

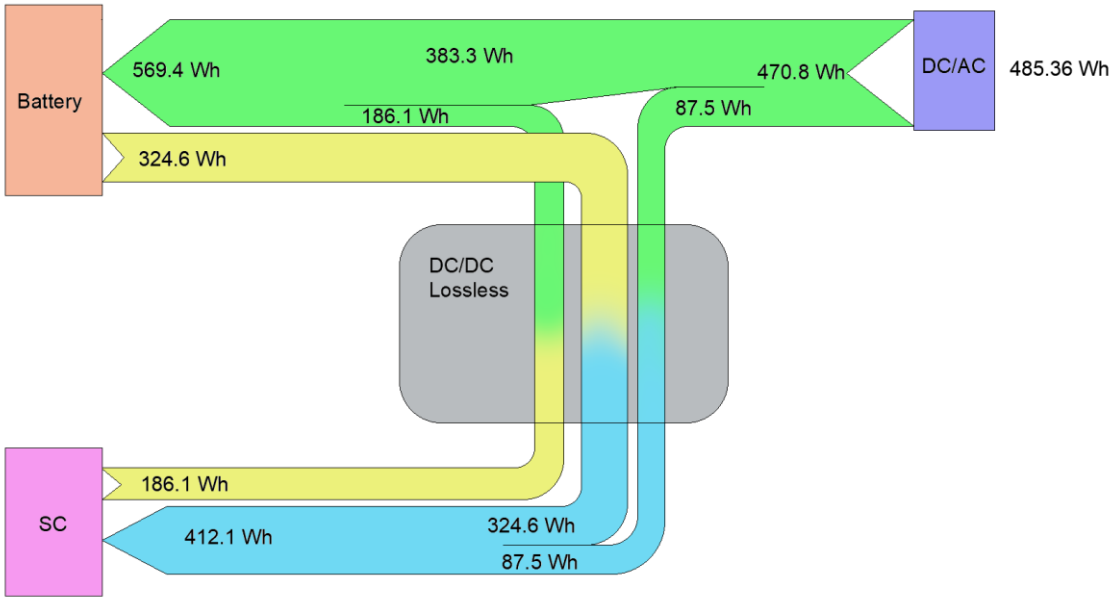

Fig. 3.37. Braking stage energy balance

In an ideal scenario, the excess energy circulating between the battery and SC should be controlled and minimized to the magnitudes necessary to maintain the SOC of the SC, therefore improving the system efficiency. The system efficiency would be improved when the battery discharges additional power (on top of the power demand) only with the purpose to maintain the SOC of the SC at operational levels. This does not occur with the strategy discussed herein. The previous analysis considers a lossless DC/DC converter. In a practical scenario, the DC/DC efficiency can fluctuate between 75% and 98% [125], so higher energy circulation translates to higher energy losses in the system and therefore a reduction in the overall efficiency. It is important to note that energy circulation by itself is an inefficient process, so by reducing its magnitude, the system efficiency can be improved.

The system's energy efficiency is calculated by considering the energy efficiency during the motoring and braking stages. The motoring stage efficiency results from the division between the total energy demand during motoring and the total energy supplied by the

HESS (battery+SC). The braking stage efficiency is calculated as the division between the total energy generated during braking and the total energy recovered by the HESS. These efficiencies are calculated as follow:

$$E_{T_m} = E_{Batt_m} + E_{SC_m} \tag{3.42}$$

$$E_{T_{br}} = E_{Batt_{br}} + E_{SC_{br}} \tag{3.43}$$

$$eff_m = \frac{E_{T_{demand}}}{E_{T_m}} x100 \tag{3.44}$$

$$eff_{br} = \frac{E_{T_{braking}}}{E_{T_{br}}} \tag{3.45}$$

where:

E_{T_m} Total energy supplied by the HESS during motoring (Wh)

E_{Batt_m} Energy supplied by the battery during motoring (Wh)

E_{SC_m} Energy supplied by the SC during motoring (Wh)

$E_{T_{br}}$ Total energy recovered by the HESS during braking (Wh)

$E_{Batt_{br}}$ Energy recovered by the battery during braking (Wh)

$E_{SC_{br}}$ Energy recovered by the SC during braking (Wh)

eff_m Motoring energy efficiency (%)

$E_{T_{demand}}$ Total energy demand during motoring (Wh)

eff_{br} Braking energy efficiency (%)

$E_{T_{braking}}$ Total energy generated during braking (Wh)

The product between the motoring energy efficiency and the braking energy efficiency yields the efficiency of the system eff_{sys}:

$$eff_{sys} = eff_m \times eff_{br} \tag{3.46}$$

Calculations of efficiency for the strategy presented herein considering the FTP72 driving cycle are presented in Table 3.10.

Table 3.10. Energy efficiency calculation for the FTP72 driving cycle and EMS strategy A.

	Motoring FTP72	**A**
a	Total energy demand Wh	1668
b	Total battery Energy supplied Wh	1765
c	Total SC energy supplied Wh	413.7
d	Energy circulation Wh (b+c-a)	510.7
	Braking FTP72	
e	Total energy generated braking Wh	470.8
f	Total energy absorbed by SC Wh	412.1
g	Total energy absorbed Battery Wh	569.4
h	Energy circulation Wh (f+g-e)	510.7
	Energy balance	
i	Total energy motoring HESS Wh (b+c)	2178.7
j	Total energy recovered HESS (f+g)	981.5
	Net energy Wh (i-j)	1197.2
	Net energy demand Wh (a-e)	1197.2
	Efficiency	
k	Energy efficiency motoring (%) (a/i*100)	76.6%
l	Energy efficiency braking (%) (e/j*100)	48.0%
	System efficiency (%) (K*L)	**36.7%**

The total energy demand during the motoring stage is 1668 Wh, however, the HESS supplied a total of 2178.7 Wh (battery=1765 Wh; SC=413.7 Wh). The motoring efficiency is therefore 76.6% according to eq. 3.44. During braking, the total energy generated is 470.8 Wh, however, the HESS recovered a total of 981.5 Wh. The excess energy circulating in the system is 510.7 Wh. The efficiency during braking is therefore 48% according to eq. 3.45. The system's efficiency is 36.7% according to eq.3.46.

It is worth noting that the net energy demand (motoring energy – braking energy) is equal to the net energy provided by the HESS, indicating that the energy system is balanced.

3.5.2 Predicted discrete wavelet transform high frequency component (strategy B)

In Fig. 3.38, the predicted DWT high frequency component is allocated to the SC according to the strategy presented in Fig. 3.33b, relieving the battery from excessive

energy circulation when compared to approach A (see Fig. 3.34) as a consequence of delay compensation. However, the battery still lacks SC assistance during acceleration and braking. With the predicted DWT approach, the battery recoups most of the generated braking power. Delay compensation with the prediction approach reduces energy circulation but it is still not sufficient to fulfil the objective of the SC in the HESS as it doesn't assist the battery during acceleration and fails to recover braking energy. The effective contribution of the SC is represented by the shaded areas.

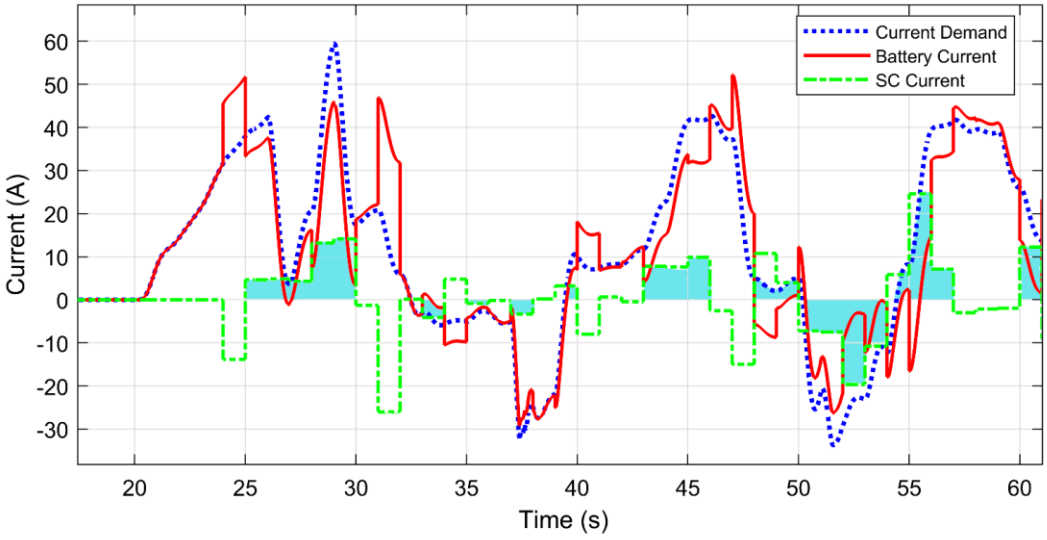

Fig. 3.38. Predicted DWT high frequency component allocated to the SC for the FTP72 driving cycle

The energy balance of the motoring stage is presented in Fig. 3.39. Assuming a lossless DC/DC converter, the SC provides a total of 301.1 Wh from which 87.8 Wh are circulated though the DC/DC converter and transferred to the battery. The SC provides a total of 213.3 Wh (12.8%) of effective assistance during the motoring stage. From this effective assistance, 62.83 Wh are provided by the SC during positive changes in the current rate, which results by calculating the area of the overlap between the SC current and the benchmark reference. On the other hand, the total energy provided by the battery is 1684 Wh, from which 1454.7 Wh are contributed to motoring and 229.3 Wh are transferred to the SC. A total of 317.1 Wh (229.3 Wh+87.8 Wh) are circulated between the battery and SC.

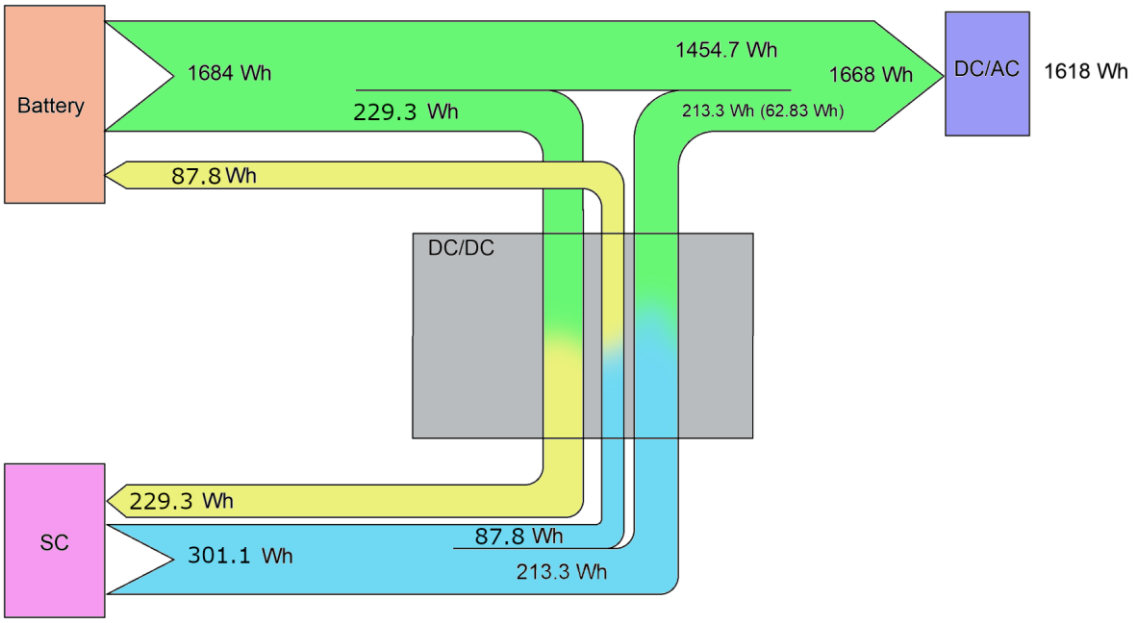

Fig.3.39. Energy balance of the motoring stage with EMS strategy B

Compared to strategy A, energy circulation is reduced from 510.7 Wh to 317.1 Wh as a consequence of time delay compensation. Although energy circulation is lower than strategy A, the effective contribution of the SC during motoring is lower (strategy A: 75.38Wh vs strategy B: 62.83Wh). As a consequence, the power demand prediction did not improve the SC performance in terms of effective assistance but reduced the energy circulation in the system.

During the braking stage (Fig 3.40), the battery recovered 487.3 Wh and the SC 300.6 Wh for a total of 787.9 Wh. However, only 470.8 Wh were generated during braking.

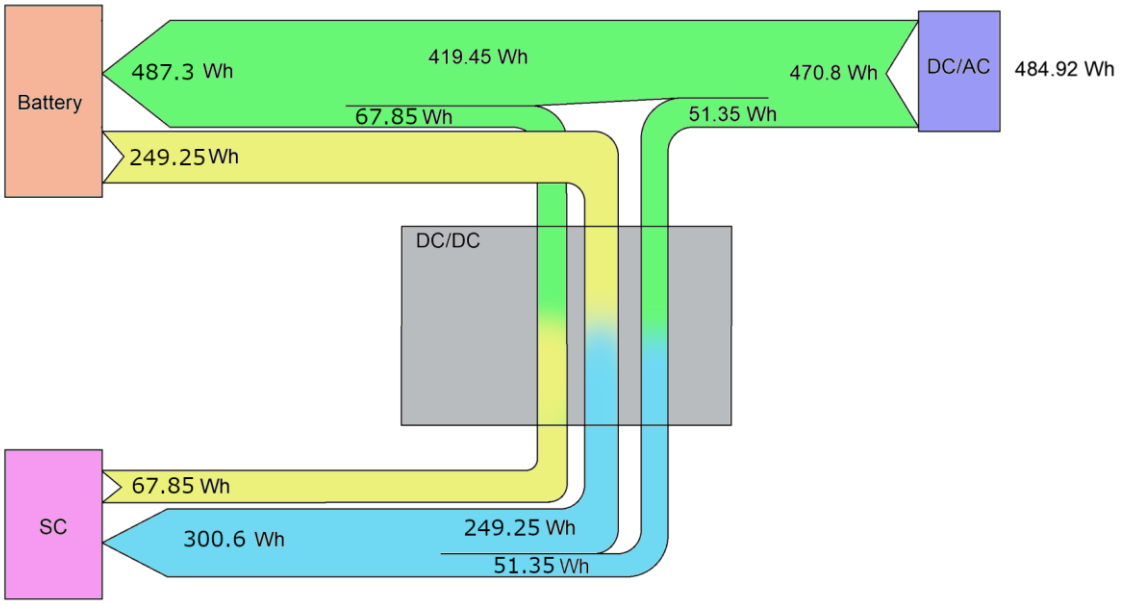

Fig. 3.40. Energy balance during the braking stage with EMS strategy B

The motoring efficiency is 84%. The total energy supplied by the HESS during motoring is 1985.1 Wh (battery :1684 Wh+ SC:301.1 Wh) while the total demand during motoring is 1668 Wh.

The system's efficiency is 50.2%. Calculations are shown in Table 3.11.

Table 3.11. Energy efficiency calculation for the FTP72 driving cycle and EMS strategy B

	Motoring FTP72	**B**
a	Total energy demand Wh	1668
b	Total battery Energy supplied Wh	1684
c	Total SC energy supplied Wh	301.1
d	Energy circulation Wh (b+c-a)	317.1
	Braking FTP72	
e	Total energy generated braking Wh	470.8
f	Total energy absorbed by SC Wh	300.6
g	Total energy absorbed Battery Wh	487.3
h	Energy circulation Wh (f+g-e)	317.1
	Energy balance	
i	Total energy motoring HESS Wh (b+c)	1985.1
j	Total energy recovered HESS (f+g)	787.9
	Net energy Wh (i-j)	1197.2
	Net energy demand Wh (a-e)	1197.2
	Efficiency	
k	Energy efficiency motoring (%) (a/i*100)	84.0%
l	Energy efficiency braking (%) (e/j*100)	59.8%
	System efficiency (%) (K*L)	**50.2%**

3.5.3 High frequency derived as the difference between the real-time current demand and the discrete wavelet transform low frequency component (strategy C)

Current demand (I_{Total}) is decomposed (2 levels) with the DWT into low and high frequencies. The low frequency component is subtracted from the current demand (I_{Total}) to obtain the SC current reference according to Fig. 3.33c. The SC assists the battery during acceleration and peak demand during motoring (positive current demand) and recuperates most of the braking current generated as shown in Fig. 3.41. However, energy circulation increases between the battery and SC, for example between t=30 seconds to t=36 seconds. With this approach, the SC provides higher energy to assist the battery during motoring and further relieves the battery from braking compared to strategies A and B.

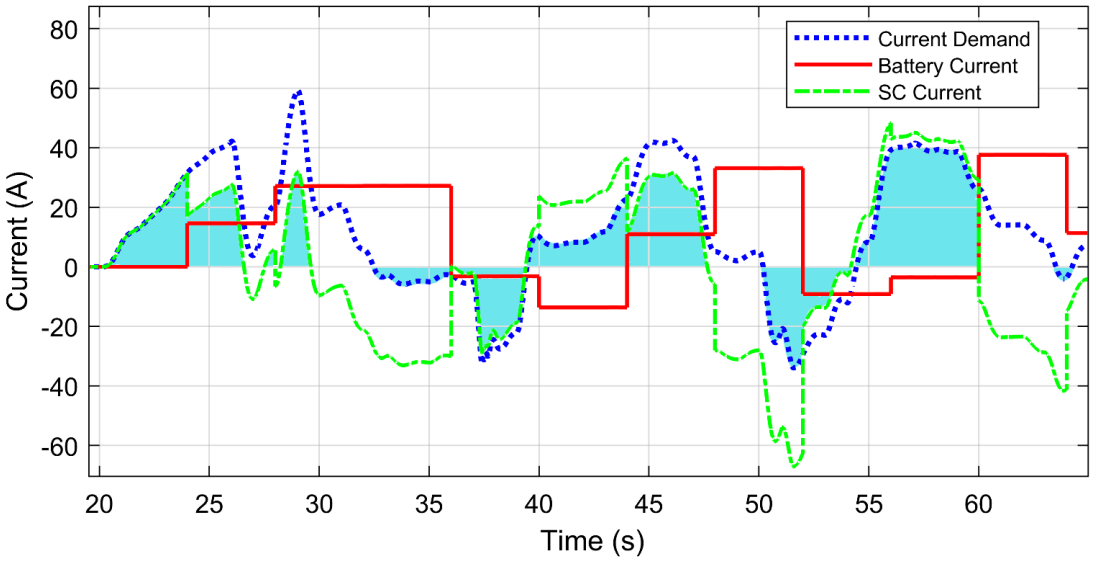

Fig. 3.41. Current distribution when the SC reference current is derived as the difference between the real time current demand and the DWT low frequency component

The energy balance of the motoring stage is shown in Fig.3.42. The battery and SC provided a total of 2401.2 Wh (1609Wh+792.2 Wh), from which 733.2 Wh are circulating between the battery and SC. The excess energy produced by the battery is 519.9 Wh, which is allocated to the SC. On the other hand, the SC produces an excess energy of 213.3 Wh, which are absorbed by the battery.

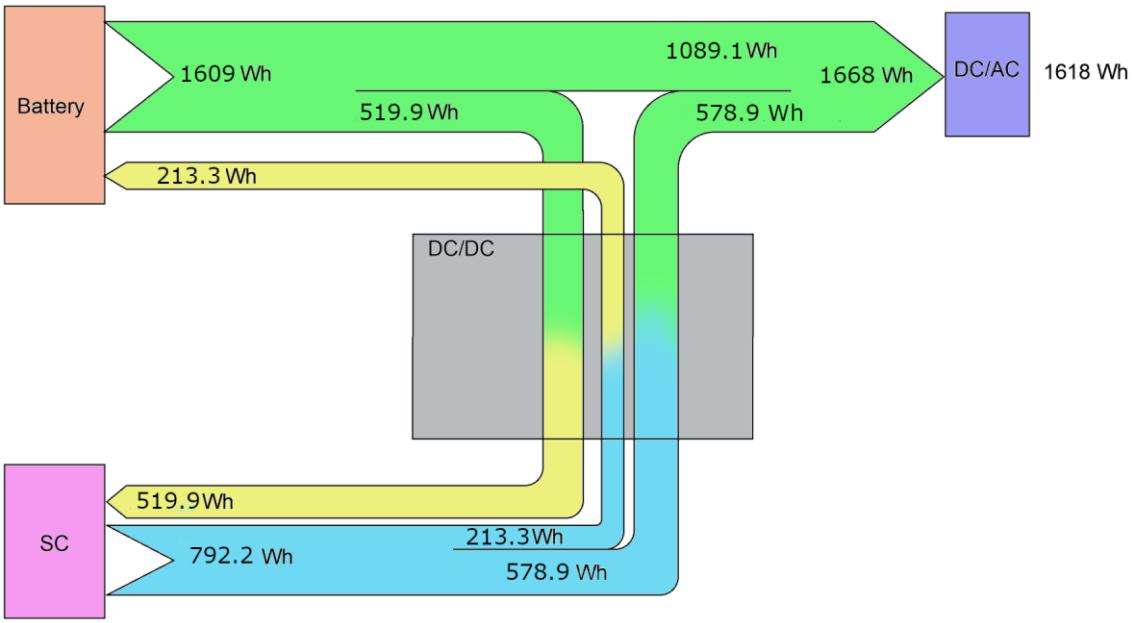

Fig.3.42. Energy balance of the motoring stage with EMS strategy C

The braking stage energy balance is shown in Fig.3.43. From the 470.8 Wh generated during braking, 299 Wh are absorbed by the SC and 171.8 Wh by the battery. However, due to energy circulating in the system (733.2 Wh), the battery receives a total of 385 Wh and the SC a total of 819 Wh.

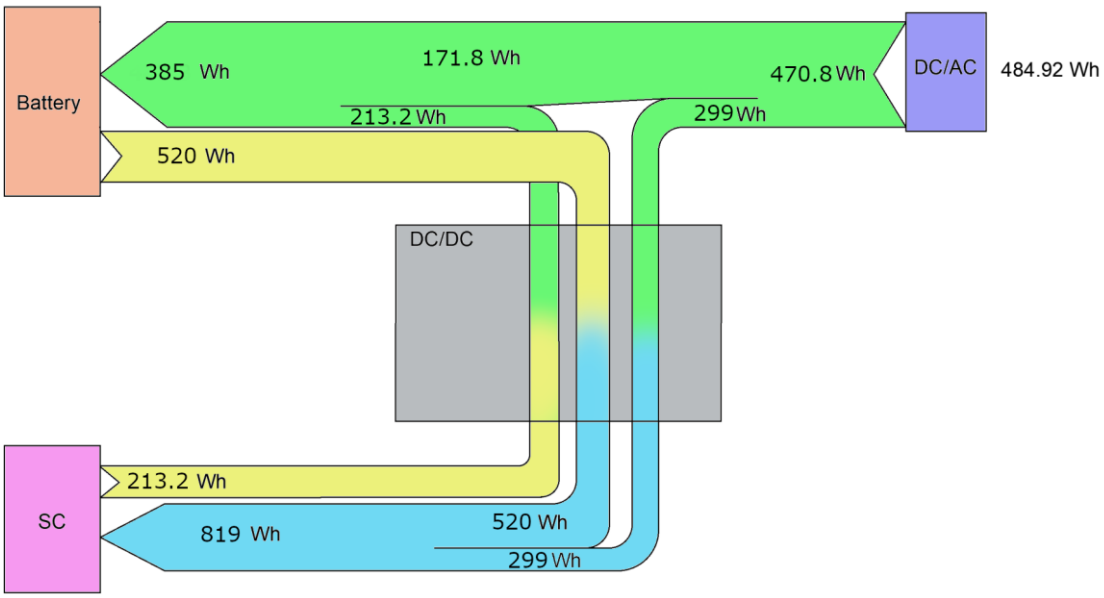

Fig.3.43. Energy balance of the braking stage with EMS strategy C

The energy efficiency of this strategy is 27.2%, which is lower than strategy A (36.7%) and strategy B (50.2%). The lower energy efficiency is influenced by the higher energy circulation achieved with this strategy. Efficiency calculations are shown in Table 3.12.

Table 3.12. Energy efficiency calculation for the FTP72 driving cycle and EMS strategy C

	Motoring FTP72	**C**
a	Total energy demand Wh	1668
b	Total battery Energy supplied Wh	1609
c	Total SC energy supplied Wh	792.2
d	Energy circulation Wh (b+c-a)	733.2
	Braking FTP72	
e	Total energy generated braking Wh	470.8
f	Total energy absorbed by SC Wh	819
g	Total energy absorbed Battery Wh	385
h	Energy circulation Wh (f+g-e)	733.2
	Energy balance	
i	Total energy motoring HESS Wh (b+c)	2401.2
j	Total energy recovered HESS (f+g)	1204
	Net energy Wh (i-j)	1197.2
	Net energy demand Wh (a-e)	1197.2
	Efficiency	
k	Energy efficiency motoring (%) (a/i*100)	69.5%
l	Energy efficiency braking (%) (e/j*100)	39.1%
	System efficiency (%) (K*L)	**27.2%**

For this specific strategy, lower energy efficiency does not mean that the system's performance of the system is worse. With this strategy, the effective SC motoring assistance (34.7%) was higher than strategy A (13.6%) and B (12.8%), as shown in Table 3.14. In terms of assistance during positive current rate changes, strategy C (59.8%) showed to be superior to strategy A (22%) and strategy B (18.5%). This trend was maintained for SC performance during braking, being strategy C the higher performing strategy as it achieved 63.4% of braking recovery against 18% achieved with strategy A and 10.9% with strategy B.

3.5.4 High frequency derived as the difference between the real-time current demand and the predicted discrete wavelet transform low frequency component (strategy D)

Using the difference between the current demand and the predicted DWT low frequency component (Fig. 3.33d) results in the SC providing assistance during peak demand which is evident between t=20 seconds to t=25 seconds, t=40 seconds to t=45 seconds and from t=54 seconds to t=56 seconds in Fig. 3.44.

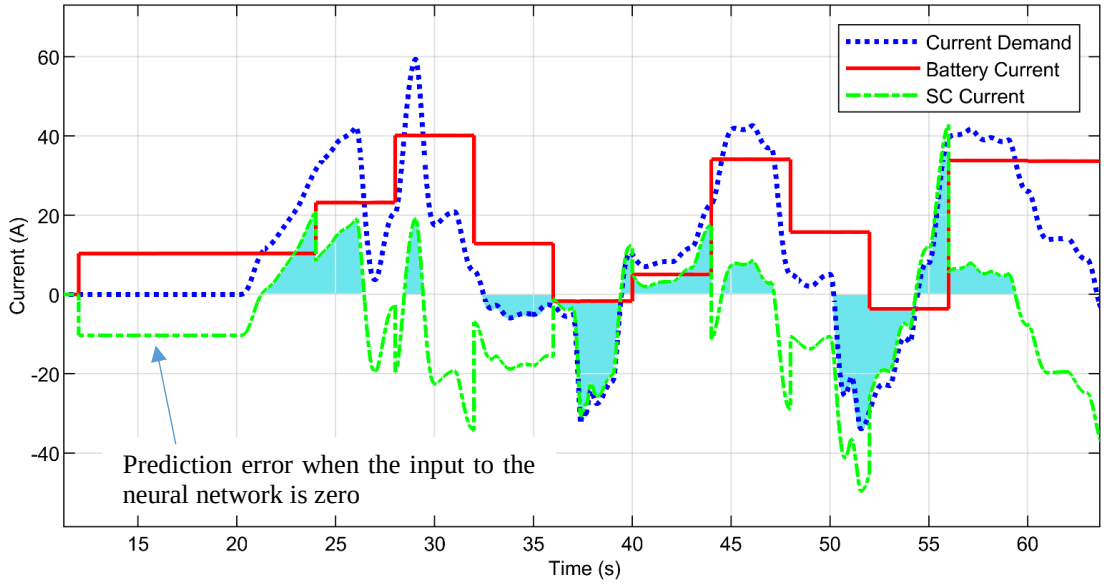

Fig. 3.44. Current distribution when the SC current reference is derived as the difference between the real time current demand and the predicted DWT low frequency component

Additionally, the SC recovers most of the power generated during braking. Shaded areas depict the SC effective contribution.

The energy balance for the motoring stage (Fig 3.45) shows that a total of 2250.5 Wh (1845 Wh+ 405.5 Wh) are provided by the battery and SC, from which 565.5 Wh are circulating (73.1 wh + 492.4 Wh) between the battery and SC. The SC provides and effective contribution of 332.4 Wh during motoring.

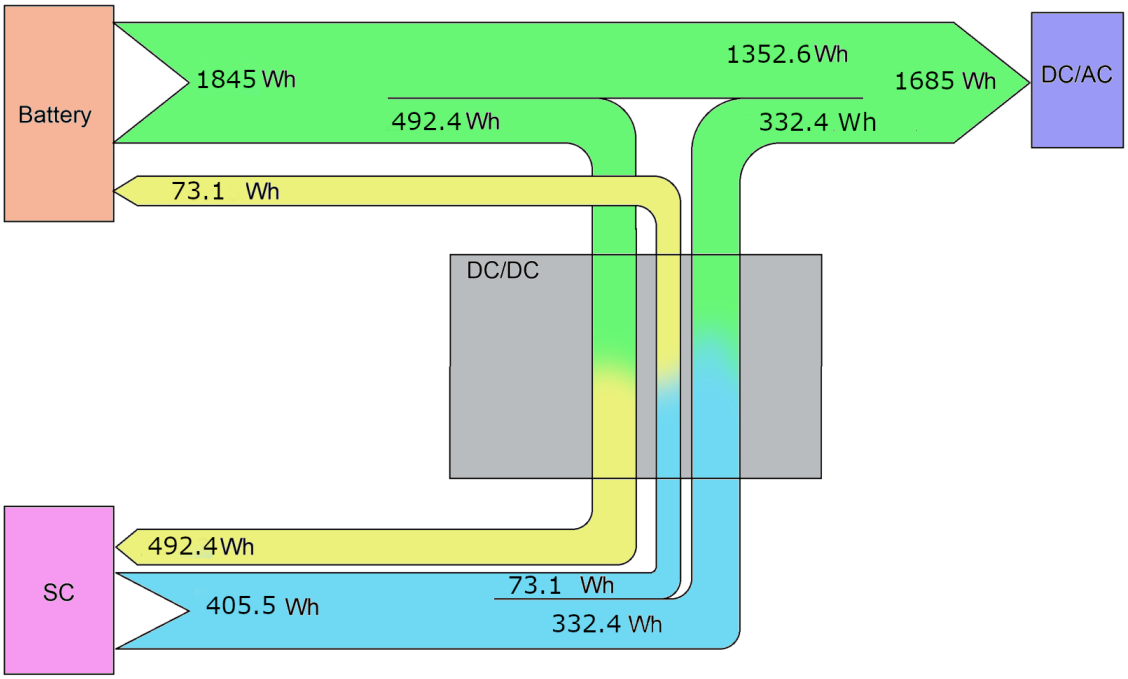

Fig.3.45. Energy balance of the motoring stage with EMS strategy D

The energy balance for the braking stage (Fig. 3.46) shows that from the 117.2 Wh generated, 105.8 Wh are recovered by the SC and 11.4 Wh by the battery. The total energy recovered by the SC is 598.1 Wh as the battery supplies an excess of 492.3 Wh to the SC. The total energy absorbed by the SC is 84.45 Wh as the SC supplies an extra 73.05 Wh. The total recuperated braking energy is lower than with strategy A, B, and C because the SOC of the SC is high and therefore it cannot take more charge. The EMS limits the regenerative braking depending on the SOC of the SC.

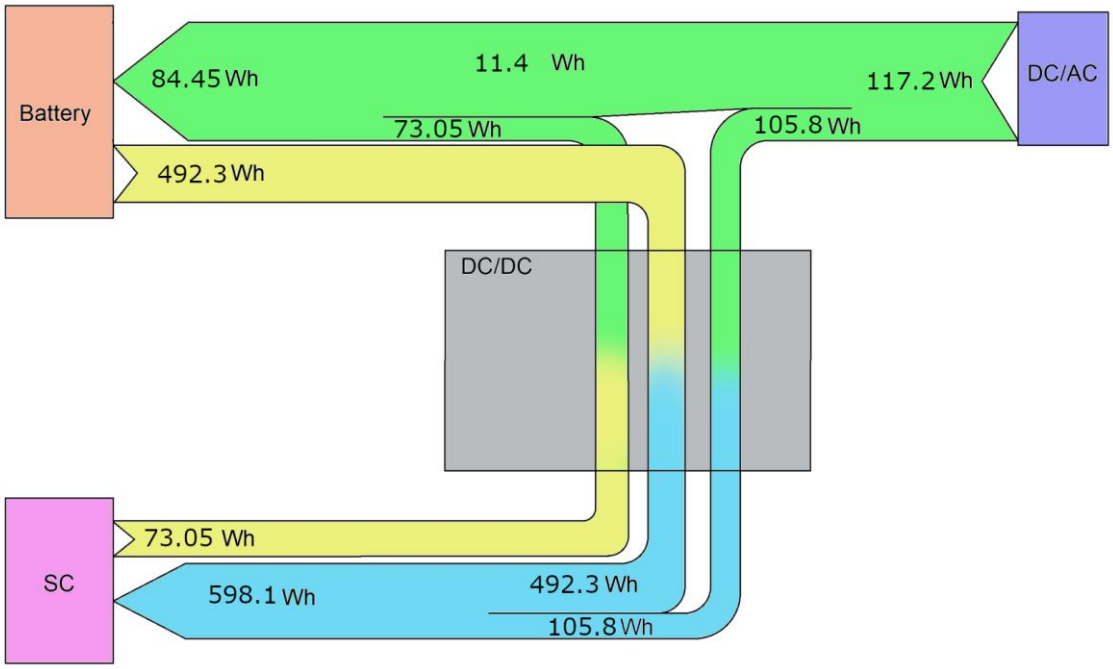

Fig.3.46. Energy balance of the braking stage with EMS strategy D

The efficiency during motoring is 74.9% which is higher than strategy C (69.5%) and lower than strategy A (76.6%) and strategy B (84%). The overall efficiency achieved by this strategy drops to 12.9% because the energy efficiency during braking is low at 17.2% as shown in Table 3.14.

Energy efficiency calculations for this strategy are presented in Table 3.13.

Table 3.13. Energy efficiency calculation for the FTP72 driving cycle and EMS strategy D

	Motoring FTP72	D
a	Total energy demand Wh	1685
b	Total battery Energy supplied Wh	1845
c	Total SC energy supplied Wh	405.5
d	Energy circulation Wh (b+c-a)	565.5
	Braking FTP72	
e	Total energy generated braking Wh	117.2
f	Total energy absorbed by SC Wh	598.1
g	Total energy absorbed Battery Wh	84.6
h	Energy circulation Wh (f+g-e)	565.5
	Energy balance	
i	Total energy motoring HESS Wh (b+c)	2250.5
j	Total energy recovered HESS (f+g)	682.7
	Net energy Wh (i-j)	1567.8
	Net energy demand Wh (a-e)	1567.8
	Efficiency	
k	Energy efficiency motoring (%) (a/i*100)	74.9%
l	Energy efficiency braking (%) (e/j*100)	17.2%
	System efficiency (%) (K*L)	**12.9%**

3.6 Performance comparison and discussion

It is obvious that strategies C and D offer the best results in terms of SC assistance during motoring and braking. However, a meaningful comparison requires an analysis of the effective contribution of the SC, especially the assistance given during positive current rate, and braking. These are referred as SC performance. Table 3.14 shows the results for the EMS strategies presented in this paper with four different driving cycles.

Table 3.14. SC performance and efficiency comparison

Driving cycle	**Strategy (ranking)**	**Energy Circulation (Wh): Lower is best** (Additional Energy on top of: FTP72=1668Wh, US06=2601Wh, WLTP3=3616Wh Artemis=5525Wh)	**SC Effective motoring assistance (Wh): Higher is best** (FTP72 Max=1668Wh) (US06 Max=2601Wh) (WLTP3 Max=3616Wh) (Artemis=5525Wh)	**SC Assistance during positive current rate (Wh): Higher is best** (FTP72 Max=306.6Wh) (US06 Max=587.4Wh) (WLTP3 Max=366.2Wh) (Artemis=979.6Wh)	**SC braking recovery (Wh): Higher is best** (FTP72 Max=470.8Wh) (US06 Max=452.9Wh) (WLTP3 Max=755.7Wh) (Artemis=565Wh)	**Energy Efficiency (%) Higher is best**	**Overall System Efficiency index(%) Higher is best** Product of performance indexes excluding Energy circulation
FTP72 (Urban)	**A**(3)	31.4%	13.6%	22.0%	18.0%	36.7%	0.2%
	B(4)	19.0%	12.8%	18.5%	10.9%	50.2%	0.13%
	C(1)	44.0%	34.7%	59.8%	63.4%	27.20%	3.58%
	D(2)	33.9%	19.9%	41.1%	22.5%	12.9%	0.24%
WLTP3 (Mixed)	**A**(4)	17.4%	8.1%	21.9%	15.0%	46.5%	0.12%
	B(3)	16.5%	9.9%	23.3%	13.1%	47.9%	0.14%
	C(1)	33.0%	26.0%	76.7%	57.0%	29.1%	3.31%
	D(2)	20.6%	17.4%	55.3%	24.5%	17.6%	0.41%
US06 (Motorway)	**A**(3)	27.6%	15.7%	17.0%	22.1%	30.3%	0.18%
	B(4)	18.5%	9.6%	8.8%	11.4%	41%	0.04%
	C(2)	34.6%	32.5%	44.0%	57.0%	24.9%	2.03%
	D(1)	33.3%	44.3%	73.5%	95.4%	25.4%	7.89%
Artemis Motorway	**A**(3)	20.5%	12.2%	20.5%	16.6%	27.6%	0.11%
	B(4)	14.2%	9.4%	19.1%	16.7%	36.7%	0.11%
	C(2)	24.7%	23.9%	42.0%	70.1%	23.5%	1.65%
	D(1)	14.7%	51.2%	70.2%	97.7%	35.8%	12.57%

3.6.1 Direct discrete wavelet transform high frequency component (strategy A) vs predicted discrete wavelet transformhigh frequency component (strategy B)

The direct use of the DWT high frequency component to obtain the SC current reference (strategy A) results in low SC effective assistance caused by a delayed response of the SC with respect to the real time demand. The percentage of SC effective motoring assistance is calculated as the ratio between the SC positive energy contribution to the total positive energy demand (FTP72=13.6%, WLTP3=8.1%, US06=15.7%, Artemis=12.2%). Prediticting the DWT high frequency component (strategy B) results in a reduction of the SC performance influenced by the prediction error. The SC performance during motoring and braking is reduced for the FTP72, US06 and Artemis driving cycles which have RMSE of 8.91 kW, 11.79 kW and 16.19 kW, respectively. For the FTP72 the SC effective contribution is reduced from 13.6% to 12.8%, for the US06 it is reduced from 15.7% to 9.6%, and for the Artemis motorway it is reduced from 12.2% to 9.4%, as shown in Table 3.14. The smaller prediction error obtained for the WLTP3 driving cycle (RMSE=3.59 kW) results in a marginal improvement in the SC effective contribution, as it rises from 8.1% to 9.9%. However, SC performance during braking is reduced from 15% to 13.1%.

With regards to energy circulation, predicting the power demand to compensate for the DWT high frequency component delay (Strategy B) leads to an expected reduction when compared to direct use of the DWT high frequency component (Strategy A). This is observed for each driving cycle. As less energy is circulating between the battery and SC, energy efficiency is improved. Results show that the complexity added by predicting the DWT high frequency component does not reap benefits in terms of SC performance. However, in terms of energy efficiency, strategy B shows a significant improvement as the energy circulating in the system is lower at 317.1 Wh against 510.7 Wh. Additionally,

the energy efficiency during braking is higher at 59.8% as shown in Table 3.14. Strategy B outperforms other strategies in terms of energy efficiency, but does not perform as good in terms of SC performance compared to other strategies.

Accounting for the SC performance indexes and the energy efficiency, the efficiency index of the strategy is calculated. The energy circulation index is not considered in the calculation as it has been already accounted for in the energy efficiency calculation. Considering the efficiency index, strategy B does not improve the system performance, therefore, power demand prediction in this case is not beneficial.

3.6.2 Difference between the real-time current demand and the discrete wavelet transform low frequency component (strategy C) vs difference between the real-time current demand and the predicted discrete wavelet transform low frequency component (strategy D)

With strategy C, the SC supplies the current demand during the delay, consequently improving the SC assistance performance. A significant improvement of SC effective assistance during motoring, positive current rate, and braking is observed when comparing strategies C and D with strategies A and B for each driving cycle, as shown in Fig. 3.47. However, this improvement comes at the cost of higher energy circulation between the battery and SC, which increases energy losses due to DC/DC conversion.

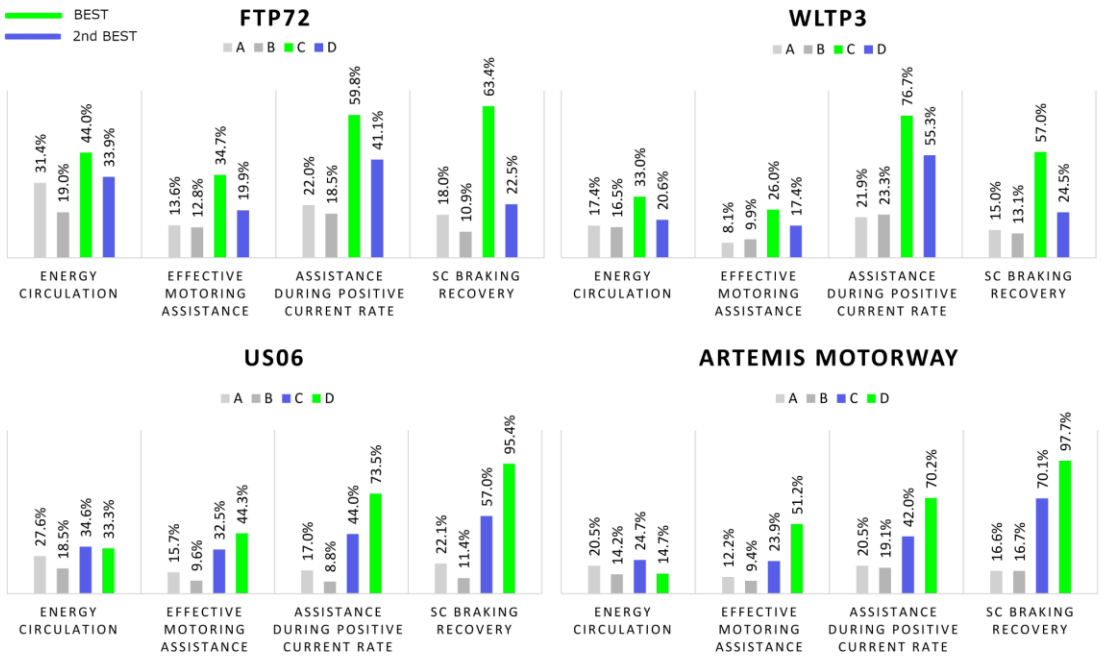

Fig 3.47. SC performance results comparison

With strategy D, energy circulation and its associated energy losses are reduced as a consequence of delay compensation, when compared with strategy C. Meanwhile, SC performance does not improve for urban or mixed driving cycles (FTP72, WLTP3), but it does for highway driving cycles (US06 and Artemis Motorway). Strategy D provides good results over strategies A and B, however, its implementation in real time is complex. Furthermore, the variable prediction error obtained for different driving cycles as well the variable time required for the prediction algorithm excecution influence SC performance. Considering that the role of the SC is to assist the battery to cope with sudden power change and recover regenerative braking, strategy C provides the best option as it improves the SC performance in all driving conditions and it is easier to implement in real time. This, however, comes at a relatively higher energy circulation which increases the system energy loss and a reduction in the system's energy efficiency.

Results show that obtaining the SC current reference as the difference between the real time current demand and the DWT low frequency component (strategy C) improves the SC assistance during motoring and braking when compared to the prediction based method in all driving conditions. Prediction proves to compensate for the delay and

reduce energy circulation but it does not improve the SC performance. With aggressive driving cycles such as the US06 and Artemis motorway, the best results are obtained with a current reference calculated as the difference between the real time current demand and the predicted DWT low frequency component (strategy D). Real time implementation is, however, more difficult. The overall efficiency index shown in Table 3.14, shows that strategy C outperforms the others, therefore, strategy C is recommended as the best control strategy in terms of SC performance and overall efficiency as it enables a DWT based EMS with 4 second delay frequency components to perform in real time.

3.7 System efficiency with additional driving cycles

Energy efficiency simply means using less energy to perform the same task, thus eliminating energy waste. The energy efficiency analysis was carried out for 4 different driving cycles: FTP72, US06, Artemis, and WLTP3. In all cases, strategy B (prediction of the DWT HF component) yields the best energy efficiency. The results are shown in Table 3.15.

Table 3.15 EMS strategies efficiency comparison for the FTP72, US06, Artemis, and WLTP3 driving cycles

	Motoring FTP72	**A**	**B**	**C**	**D**
a	Total energy demand Wh	1668	1668	1668	1685
b	Total battery Energy supplied Wh	1765	1684	1609	1845
c	Total SC energy supplied Wh	413.7	301.1	792.2	405.5
d	Energy circulation Wh (b+c-a)	510.7	317.1	733.2	565.5
	Braking FTP72				
e	Total energy generated braking Wh	470.8	470.8	470.8	117.2
f	Total energy absorbed by SC Wh	412.1	300.6	819	598.1
g	Total energy absorbed Battery Wh	569.4	487.3	385	84.6
h	Energy circulation Wh (f+g-e)	510.7	317.1	733.2	565.5
	Energy balance				
i	Total energy motoring HESS Wh (b+c)	2178.7	1985.1	2401.2	2250.5
j	Total energy recovered HESS (f+g)	981.5	787.9	1204	682.7
	Net energy Wh (i-j)	1197.2	1197.2	1197.2	1567.8
	Net energy demand Wh (a-e)	1197.2	1197.2	1197.2	1567.8
	Efficiency				
k	Energy efficiency motoring (%) (a/i*100)	76.6%	84.0%	69.5%	74.9%
l	Energy efficiency braking (%) (e/j*100)	48.0%	59.8%	39.1%	17.2%
	System efficiency (%) (K*L)	**36.7%**	**50.2%**	**27.2%**	**12.9%**

	Motoring US06	A	B	C	D
a	Total energy demand Wh	2601	2601	2601	2611
b	Total battery Energy supplied Wh	2703	2682	2502	2316
c	Total SC energy supplied Wh	616.3	399.3	997.7	1161
d	Energy circulation Wh (b+c-a)	718.3	480.3	898.7	866
	Braking US06				
e	Total energy generated braking Wh	452.9	452.9	452.9	442.4
f	Total energy absorbed by SC Wh	609.7	396.6	1005.5	1289
g	Total energy absorbed Battery Wh	561.5	536.6	346.1	19.4
h	Energy circulation Wh (f+g-e)	718.3	480.3	898.7	866
	Energy balance				
i	Total energy motoring HESS Wh (b+c)	3319.3	3081.3	3499.7	3477
j	Total energy recovered HESS (f+g)	1171.2	933.2	1351.6	1308.4
	Net energy Wh (i-j)	2148.1	2148.1	2148.1	2168.6
	Net energy demand Wh (a-e)	2148.1	2148.1	2148.1	2168.6
	Efficiency				
k	Energy efficiency motoring (%) (a/i*100)	78.4%	84.4%	74.3%	75.1%
l	Energy efficiency braking (%) (e/j*100)	38.7%	48.5%	33.5%	33.8%
	System efficiency (%) (K*L)	**30.3%**	**41.0%**	**24.9%**	**25.4%**

	Motoring Artemis	A	B	C	D
a	Total energy demand Wh	5525	5525	5525	5525
b	Total battery Energy supplied Wh	5704	5607	5341	3490
c	Total SC energy supplied Wh	954	701	1550	2846
d	Energy circulation Wh (b+c-a)	1133	783	1366	811
	Braking Artemis				
e	Total energy generated braking Wh	565	565	565	565
f	Total energy absorbed by SC Wh	945.7	696.9	1534	1345
g	Total energy absorbed Battery Wh	752.3	651.1	397	31
h	Energy circulation Wh (f+g-e)	1133	783	1366	811
	Energy balance				
i	Total energy motoring HESS Wh (b+c)	6658	6308	6891	6336
j	Total energy recovered HESS (f+g)	1698	1348	1931	1376
	Net energy Wh (i-j)	4960	4960	4960	4960
	Net energy demand Wh (a-e)	4960	4960	4960	4960
	Efficiency				
k	Energy efficiency motoring (%) (a/i*100)	83.0%	87.6%	80.2%	87.2%
l	Energy efficiency braking (%) (e/j*100)	33.3%	41.9%	29.3%	41.1%
	System efficiency (%) (K*L)	**27.6%**	**36.7%**	**23.5%**	**35.8%**

	Motoring WLTP3	A	B	C	D
a	Total energy demand Wh	3616	3616	3616	3649
b	Total battery Energy supplied Wh	3726	3674	3538	3708
c	Total SC energy supplied Wh	518.3	540.3	1272	684.3
d	Energy circulation Wh (b+c-a)	628.3	598.3	1194	743.3
	Braking WLTP3				
e	Total energy generated braking Wh	755.7	755.7	755.7	199.3
f	Total energy absorbed by SC Wh	516.9	539	1292.7	872.2
g	Total energy absorbed Battery Wh	867.1	815	657	70.4
h	Energy circulation Wh (f+g-e)	628.3	598.3	1194	743.3
	Energy balance				
i	Total energy motoring HESS Wh (b+c)	4244.3	4214.3	4810	4392.3
j	Total energy recovered HESS (f+g)	1384	1354	1949.7	942.6
	Net energy Wh (i-j)	2860.3	2860.3	2860.3	3449.7
	Net energy demand Wh (a-e)	2860.3	2860.3	2860.3	3449.7
	Efficiency				
k	Energy efficiency motoring (%) (a/i*100)	85.2%	85.8%	75.2%	83.1%
l	Energy efficiency braking (%) (e/j*100)	54.6%	55.8%	38.8%	21.1%
	System efficiency (%) (K*L)	**46.5%**	**47.9%**	**29.1%**	**17.6%**

In chapter 4, a novel real time EMS that outperforms the 4 strategies discussed above will be proposed.

CHAPTER 4

4 PROPOSED REAL TIME ENERGY MANAGEMENT SYSTEM WITH THE DWT AND CONVENTIONAL FILTERS

4.1. Introduction

This chapter details the development of a simple yet efficient EMS that deals with time delays so that the SC provides timely assistance during motoring and recovers the braking energy generated. The energy circulation between the battery and SC can be controlled to keep the SC charge availability during the driving cycle. When the SC charge is high, the generated braking energy is allocated to the battery observing the recommended charging C-rate. This approach is tested with the DWT, where a delay of up to 4 seconds can be managed without the need for any complicated prediction strategy. With the sampling rate of 1Hz, higher levels of DWT decomposition, i.e. 3, would yield longer time delays, i.e. 8 seconds, which are more difficult to manage. In those cases prediction can be considered a viable solution. Testing is also performed with first order filters. Detailed simulation results show that the proposed method eliminates undesirable power circulation allowing the SC to assist the battery throughout the full battery discharge cycle. The performance of the HESS is improved when compared to the traditional use of conventional filtration techniques and the DWT. The superiority of the proposed strategy is demonstrated with a detailed comparison using US06 and FTP72 driving cycles.

4.2. Background

In chapter III, the DWT frequency decoupling approach was presented. The effects of the delay introduced by the decomposition process in the frequency components were analysed, finding that the SC was not assisting the battery at the right time nor recovering

braking energy. The delayed response of the SC produced energy circulation between the battery and SC, allowing for an inefficient use of energy. Several researchers suggested power demand prediction to solve the time delay problem and enable the DWT to work in real time. DWT delay compensation with prediction reduces energy circulation in the system but it doesn't achieve significant improvements in terms of SC assistance, so its complexity does not bring enough benefits to justify its implementation.

In this chapter a novel EMS is proposed, where the SC provides a portion of the required power during motoring (positive power demand) and recovers the generated braking power (negative power demand). The method derives the high frequency reference signal as the difference between the real-time current demand measured in the DC-bus and the low-frequency component of the current demand obtained with a low pass filter. The positive part of this signal is used as the SC motoring current reference, which is then combined with the signal representing the generated braking power (negative power demand). To ensure the SC is always available to assist the battery, the SC is recharged from the battery (in addition to braking power) with predetermined current values that depend on the voltage of the SC and the current demand. In consequence, the battery is effectively relieved from the peak and braking power as the SC can assist the battery during the whole battery discharge cycle.

To assess the performance of the proposed EMS in the presence of delay, the low-frequency component of the current demand is obtained with different methods including a first-order low pass filter, DWT, and DWT with prediction. Results show that the proposed EMS can be adapted to any filtering technique where delay or phase shift issues are present, eliminating unnecessary energy circulation between the battery and SC and maintaining the SC voltage within operational limits throughout the full battery discharge cycle.

4.3 Energy management system

A high-level schematic of the proposed EMS is presented in Fig. 4.1. The SC reference current $I_{ref(SC)}$ is obtained from the summation of the motoring current I_m, braking current I_{br}, and charging current I_{ch}. The motoring current I_m determines the positive contribution of the SC to the system. To calculate this current, the low-frequency component of the current demand is used. This can be obtained with a conventional low pass filter or the DWT. The positive part of the filtered signal (output of saturation 2 block) is subtracted from the positive part of the current demand (output of saturation 1 block) yielding the high-frequency component. The positive part of the resulting signal is used as the motoring reference current I_m while the negative part is discarded by saturation 3 block.

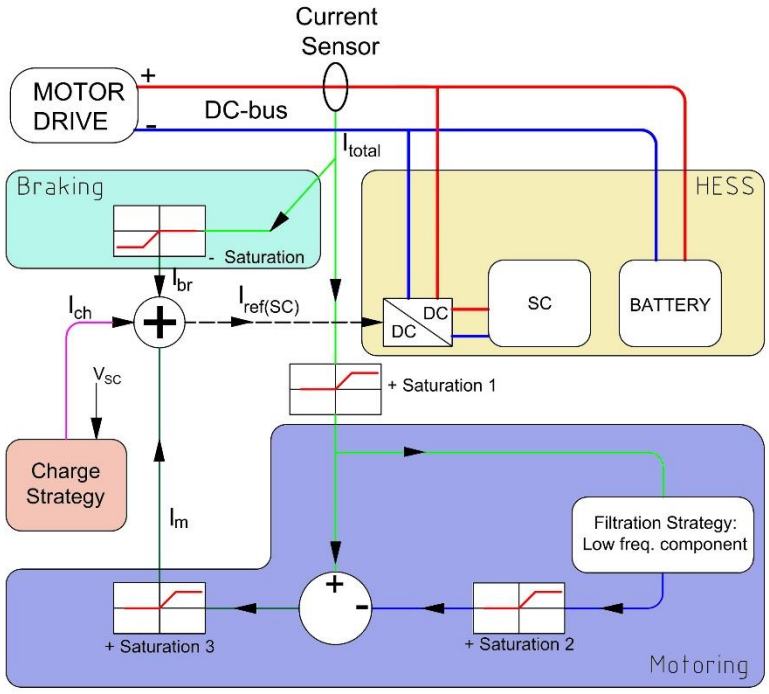

Fig 4.1. Proposed EMS high-level schematic

A comparison of I_m with and without saturation blocks 1, 2 and 3 is shown in Fig. 4.2. Saturation blocks ensure that the SC positive contribution lays within the current demand envelope at all times. The pink shaded areas in Fig. 4.2a are discarded by the saturation blocks so that only yellow shaded areas are kept as shown in Fig. 4.2b. Notice that any positive signal outside the current demand envelope is discarded (compare Fig. 4.2a at

t=40 seconds vs Fig 4.2b at t=40 seconds) as well as all negative signals shaded in pink. Therefore, only the positive output of the low pass filter that rests within the current demand envelope is considered. This eliminates energy circulation during motoring.

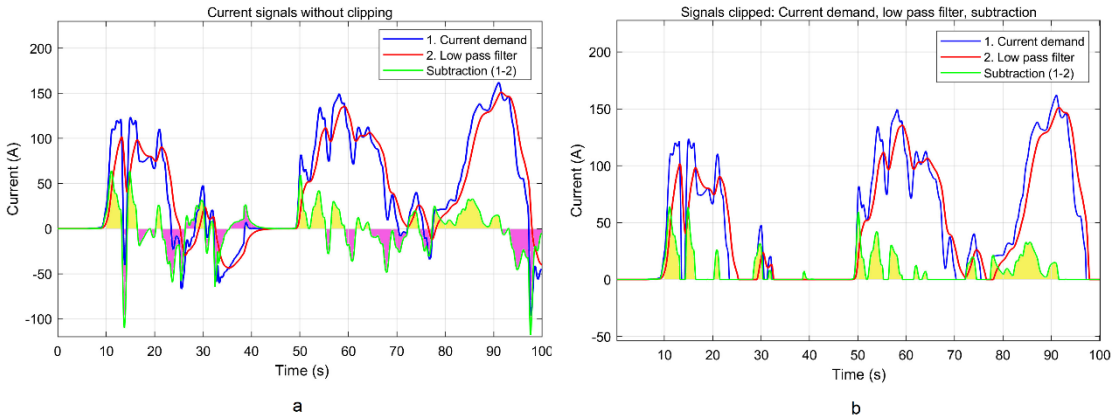

Fig. 4.2. SC motoring Current I_m. a) SC current demand without clipping (includes negative currents) b) SC current demand with clipping (negative currents are eliminated)

The braking current reference I_{br} corresponds to the negative current demand i.e. the generated braking power. Using the sum of I_m and I_{br} as the SC current reference results in a signal that eliminates power circulation. The SC is commanded to assist the battery during positive power demand and to recover all the power generated during braking as shown in Fig. 4.3.

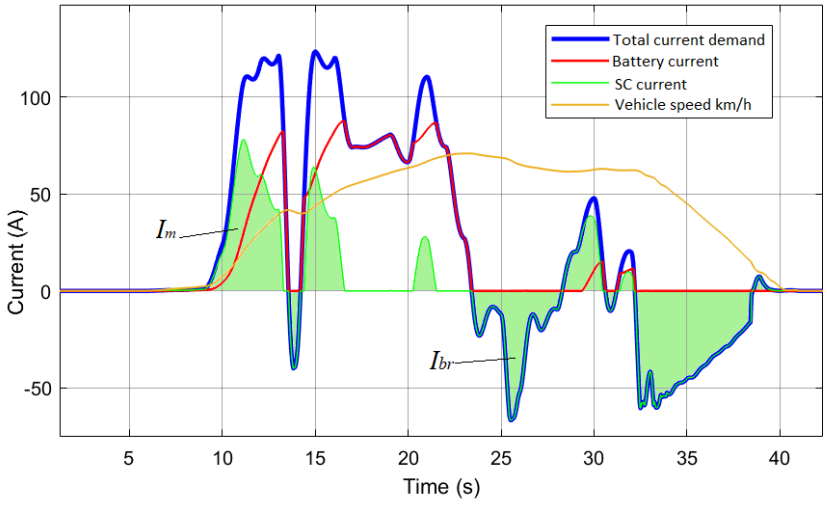

Fig. 4.3. Current distribution in the HESS for the US06 driving cycle with the proposed method with a first order low pass filter with cut-off frequency of 125 mHz

Obtaining I_m by using a high pass filter or with a low pass filter without clipping (saturation blocks 1, 2 and 3), would result in a SC current reference signal that occasionally leads the real-time demand due to the filter's phase shift at high frequencies, producing power circulation between the battery and SC.

To depict the difference between the motoring signals I_m obtained with these approaches, the output of a first-order high pass filter with a time constant τ=1.27 s (cut-off frequency=125 mHz) is compared to the output obtained with the proposed method using a low pass filter with the same time constant. The comparison of the currents obtained with these methods is shown in Fig. 4.4. The difference between the resulting signals (red shade in Fig. 4.4) is caused by the high pass filter phase shift. The red shade shows the areas when the SC provides more current than what is drawn by the motor drive meaning that the SC charges the battery unnecessarily. This causes energy circulation during the motoring stage.

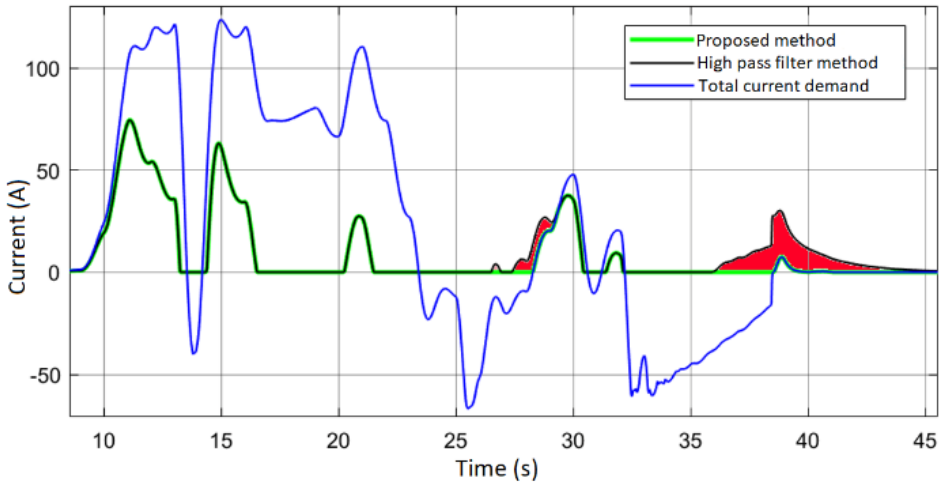

Fig. 4.4. Difference between high pass filter output and the high frequency obtained with the proposed method

As the SC recharges only from the generated braking power I_{br}, its voltage will reach the minimum limit (V_{SCmin}) long before the battery reaches its minimum charge at the end of its discharge cycle. Thus, there is a risk of leaving the battery as the sole provider of power for a relatively long period due to SC downtime [4]. To address this problem, the

proposed EMS adds a pre-set current value I_{ch}, allowing SC to be charged from the battery (controlled energy circulation). The magnitude of the pre-set current value depends on the magnitude of the current demand and the SC voltage as presented in Table 4.1.

Table 4.1. Charging current pre-set values

SC Voltage (V)/current demand (A)	Charging current pre-set values (A)
$V_{SC}>0.7V_{SCmax}$	0
$0.6V_{SCmax} < V_{SC} <0.7V_{SCmax}$ AND $I_{total} <=20A$	-20
$V_{SCmin} < V_{SC} <0.6V_{SCmax}$ AND $I_{total} <=40A$	-40

When the SC voltage is above $0.7V_{SCmax}$, the charging current is set to zero. When the SC voltage drops below $0.7V_{SCmax}$ and the current demand is below 20 A (17% of rated discharge current of the battery as presented in Table 3.3), a constant value of -20A is added to the SC current reference. When the voltage of the SC drops between V_{SCmin} and $0.6V_{SCmax}$ and the current demand is below 40A (34% of rated discharge current of the battery), -40A is added to the SC current reference. The current demand threshold values of 17% and 34% and the corresponding values added to the SC current reference (-20 and -40) have been chosen to test the strategy. These values have been chosen arbitrarily, however, they can be subject to optimization, which is not carried out in the present work. Higher current demand thresholds and constant values can be used to speed up the charging process. However, it is recommended to observe the rated discharge characteristics of the battery, so they are not overpassed and also to observe the maximum currents generated during braking so when the constant is added to the SC reference, the resulting current does not go beyond the limits of the DC/DC converter and the recommended continuous current accepted by the SC as shown in Table 3.5. In Fig.4.5, the charging strategy is depicted with a fraction of the US06 driving cycle.

The red shades in Fig. 4.5 represents the current discharged by the battery to recharge the SC (controlled energy circulation). This occurs when the SC voltage drops below 283.5

V and when the total current demand is below 20A. The green areas correspond to the energy received by the SC from the battery. When the total current demand is above 20 A, the charging strategy is disabled. This protects the battery from stress during peak current demand (motoring stage). The grey areas show that although the SC voltage drops below 283.5V (70% V_{SCmax}), the SC is not recharged from the battery as the total current demand is above 20A.

|With this charging strategy, the SC charge is maintained within operational limits without imposing stress on the battery, ensuring the availability of the SC throughout the battery discharge cycle. Only 40 seconds are shown in Fig. 4.5 to show detailed signals and improve visualization. In the results section, final SC SOC and energy circulation values are presented as indicators of the charging strategy performance.

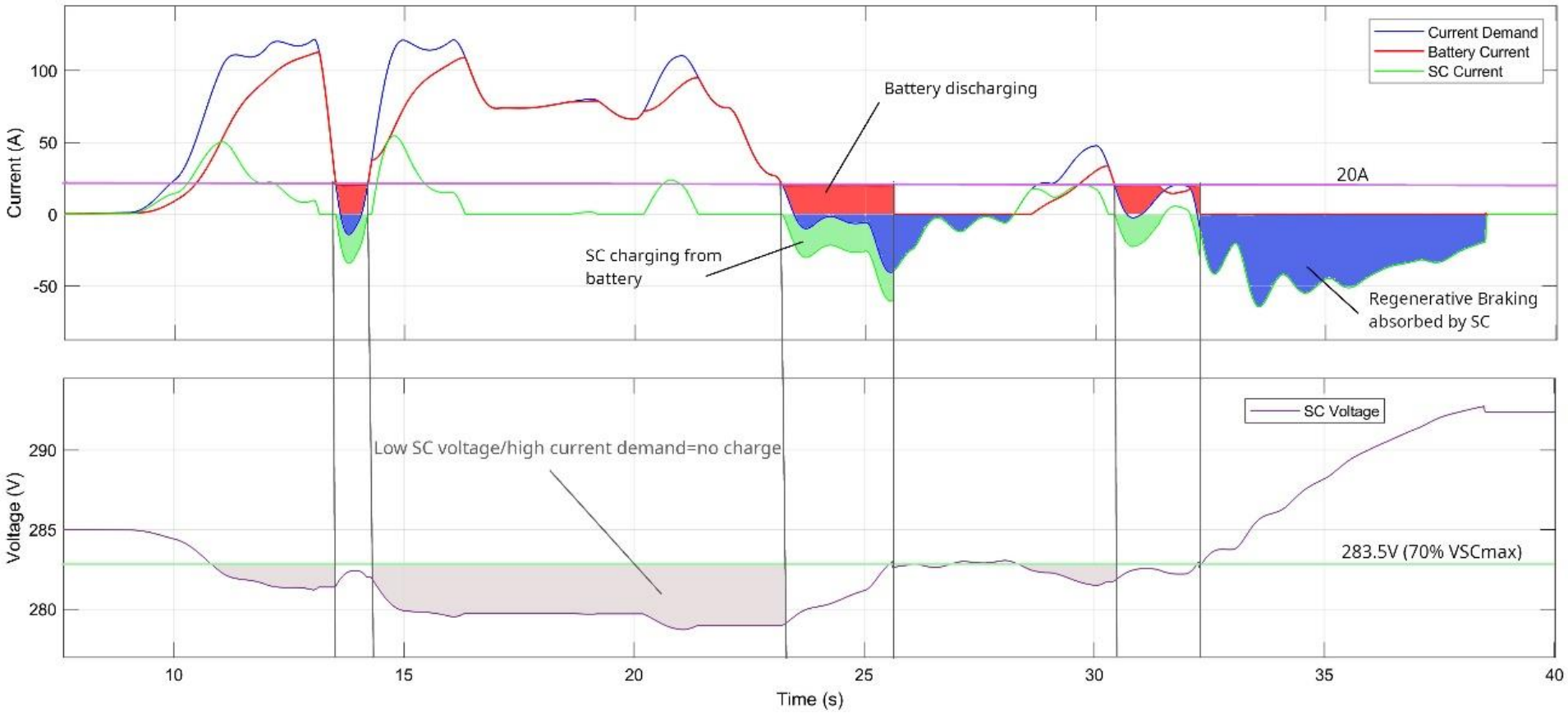

Fig. 4.5. Controlled energy circulation to charge the SC from battery

4.4. Supercapacitor sizing.

The SC in this work has been sized by considering the SC pack voltage, volume, weight and cost. The SC voltage fluctuates between 405V and 202.5V. There are SC cells with 2.7V and 3.0 V. Using the latter requires less SCs to reach the voltage range. In terms of capacitance, three different capacitors are considered: Skeleton 5000F, Maxwell 3400F and Maxwell 3000F. These SCs are discharged from 80% SOC (352 V) with 3 driving cycles: FTP72, US06 and WLTP3 using the proposed method shown in Fig.4.1 but with the charging strategy disabled. The purpose of disabling the charging strategy is to see how these 3 SCs discharge when only the braking energy is recovered (no energy circulation to keep the SC recharged). When the SCs voltage drops below 50% V_{max}, the SC does not supply energy until it is recharged to a voltage above this threshold. The time span that the SC stops supplying energy is referred as 'downtime'.

Three different SC sizes has been simulated to assess its discharge behaviour during a whole drive cycle when only braking energy is used to recharge them. The highest capacitance SC pack has 37.03 F, obtained with 135 SCs with capacitance of 5000F [126] (SkelCap 5000F, 3V, 28.4 kW/kg) connected in series. The second SC simulated has a capacitance of 25.2 F, which corresponds to the SC presented in Table 3.5. This SC (3400 F, 3V) has been used for all the simulations in this work. The third SC has a capacitance of 22.2F obtained with 135 SCs with capacitance of 3000F [127] (Maxwell 3000F, 3V, 18.1 kW/Kg).

For the FTP72 urban driving cycle shown in Fig. 4.6, SC downtime is not reached (SC voltage dropping below 202.5V). The SC with the lowest capacitance would require recharging from the battery to maintain it above 70% V_{max}.

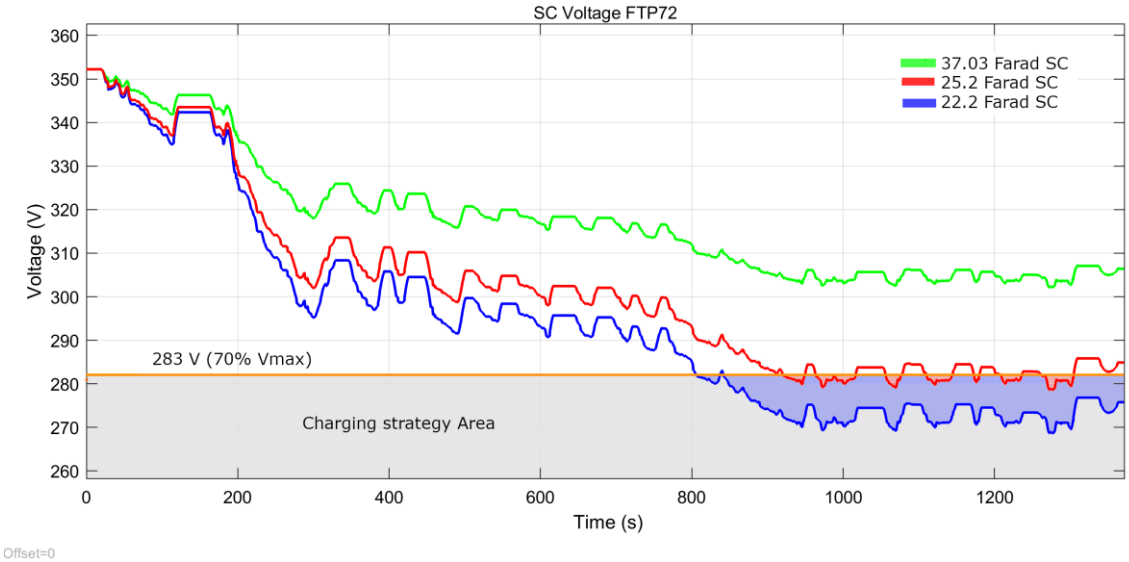

Fig 4.6. Comparison of three SC sizes for the FTP72 driving cycle.

In Fig. 4.7, only the SC with the lowest capacitance (22.2F) reaches the lowest voltage threshold, meaning that it would cease to operate until it is recharged from the available braking energy. The downtime of this SC is 69 seconds. The other two SCs do not reach the lowest voltage, however, they would require energy from the battery to maintain the SC voltage above 70% V_{max}.

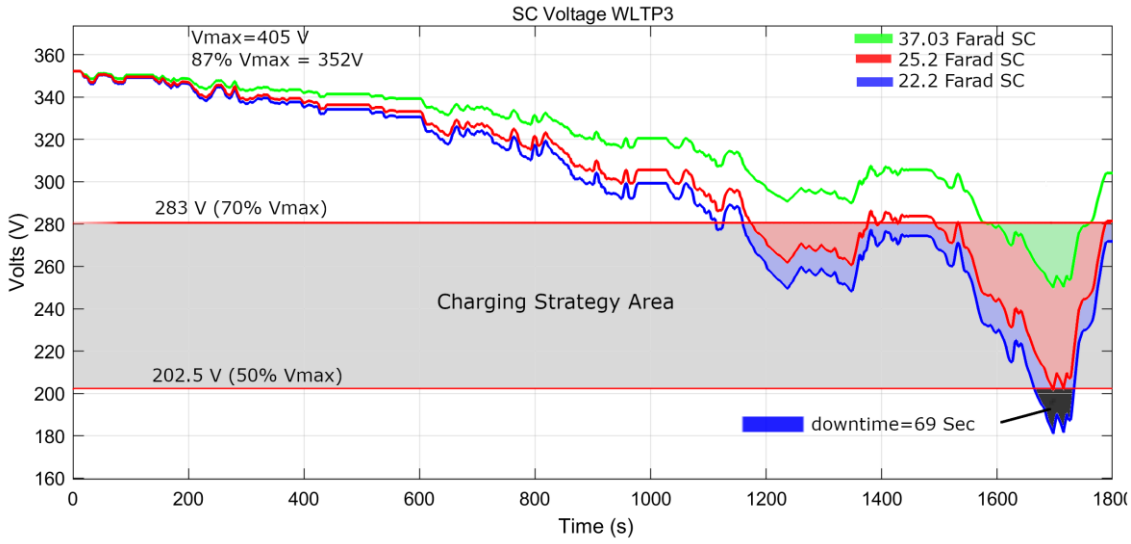

Fig 4.7. Comparison of three SC sizes for the WLTP3 driving cycle.

For the highway US06 driving cycle, the 22.2F SC discharges faster and reaches the low voltage threshold, producing a total downtime of 89 seconds. The discharge cycle is shown in Fig. 4.8. An SC with higher capacitance is desirable as it can supply energy for longer periods, however, this can come with a penalty in cost, weight, and/or volume. In Table 4.2, a comparison of these parameters is shown.

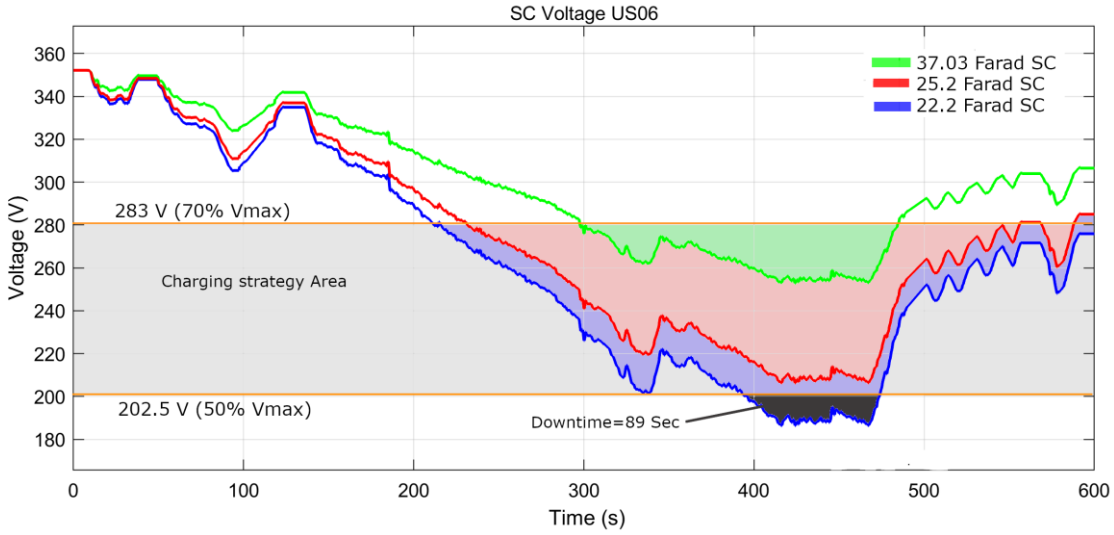

Fig 4.8. Comparison of three SC sizes for the US06 driving cycle.

Table 4.2. Comparison of 3 SCs in terms of cost, volume, and weight

	Rated Voltage (V)	Rated Capacitance (Farad)	Mass (gram)	Specific power (kW/kg)	Gravimetric energy (Wh/kg)	Volume (Litre)	Approx cost (USD/unit)
Maxwell BCAP 3400	3	3400	490	17	9.1	0.48	51.48 [128]
Maxwell BCAP 3000	3	3000	460	18.1	8.5	0.48	49.8 [129]
SkelCap 5000 F	3	5000	565	28.4	11.1	0.39	~75 [130]

4.5. Simulation results

In this section, the battery and SC energy distribution, energy circulation, and their final SOCs during the US06 and FTP72 driving cycles are compared when the following strategies are used to obtain the reference current for the SC:

a) First order high pass filter with fc=125 mHz

b) Proposed method with a first-order low pass filter with fc=125 mHz

c) Direct DWT high frequency component (125 mHz-500 mHz)

d) Proposed method with the DWT low-frequency component (0-125 mHz)

e) Predicted (LSTM) DWT high-frequency component (125 mHz-500 mHz)

f) Proposed method with the predicted DWT low-frequency component (0-125 mHz)

The schematics of these strategies are shown in Fig. 4.9. The initial SOC for the battery and SC are both set to 80% for the simulations.

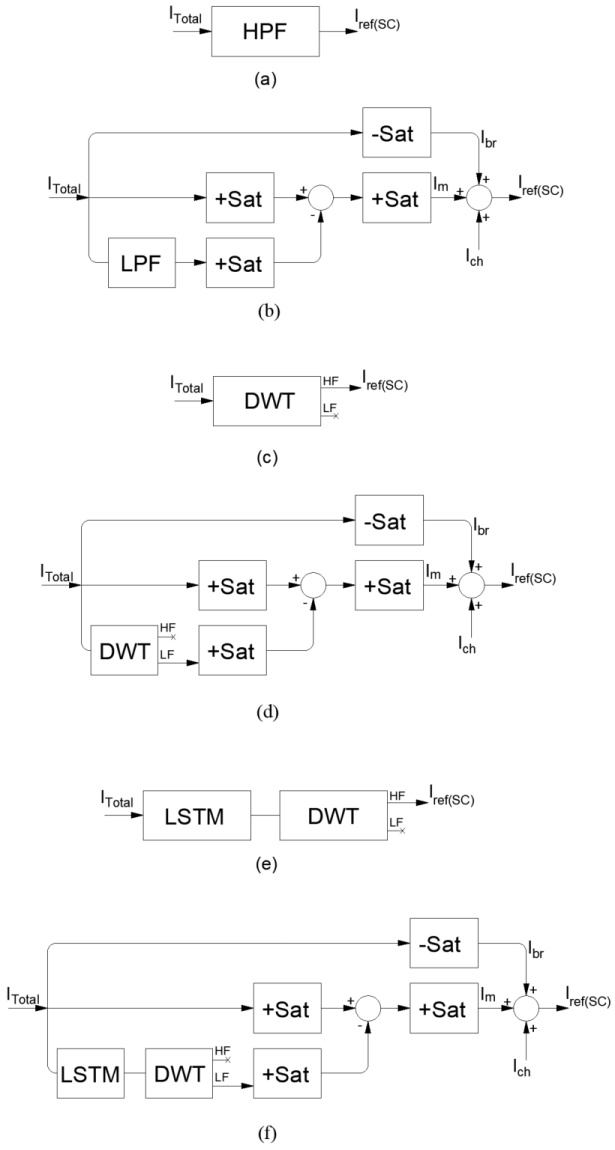

Fig. 4.9. Filtration strategies. (a) High pass filter. (b) Proposed method with low pass filter. (c) Direct DWT high-frequency method. (d) Proposed method with the DWT low-frequency component. (e) Predicted DWT high-frequency component method. (f) Proposed method with the predicted DWT low-frequency component

To determine the performance of the EMS strategies, the following areas (signal energy) are calculated with:

$$E = \frac{1}{3600}\int_{0}^{t} I_X \times V_{DC-link}\, dt \tag{4.1}$$

- Motoring energy demand (Wh): The area defined by the positive current demand. Red areas in Fig 4.10.
- Braking energy demand (Wh): The area defined by the negative part of the current demand. Orange areas in Fig. 4.10.

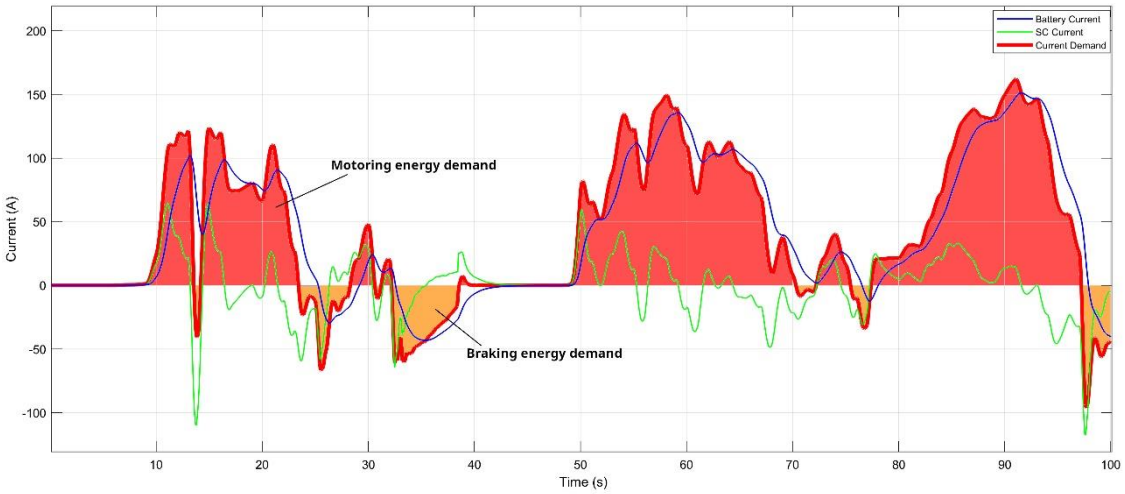

Fig 4.10. Positive and negative energy demand

- Battery motoring energy (Wh): The area defined by the positive battery current. Blue area in Fig.4.11.
- Battery braking energy (Wh): The area of the negative part of the battery current. Yellow area in Fig.4.11.

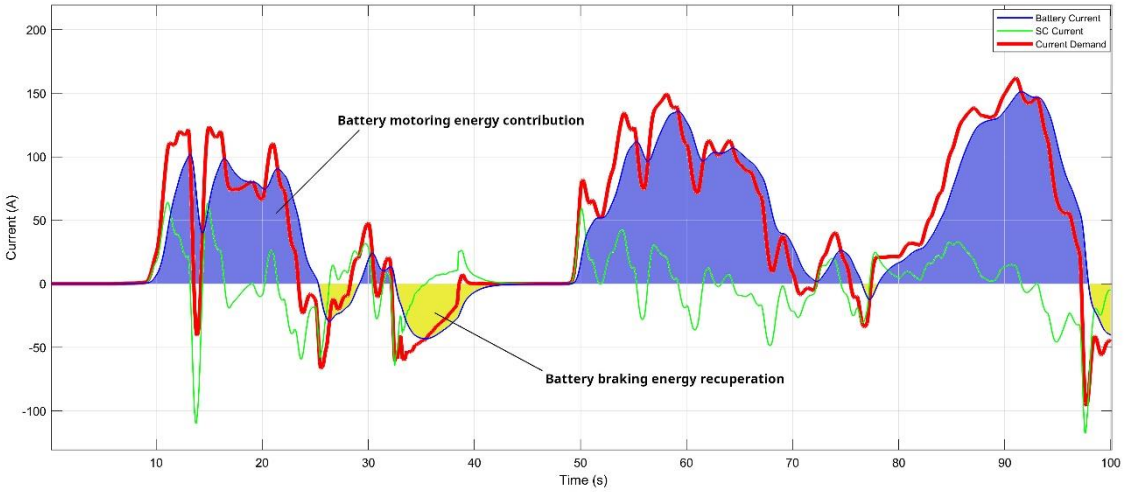

Fig. 4.11. Positive and negative battery energy contribution

- SC motoring energy (Wh): The area defined by the positive SC current. Green area in Fig. 4.12.
- SC braking energy (Wh): The area of the negative part of the SC current. Pink area in Fig. 4.12.

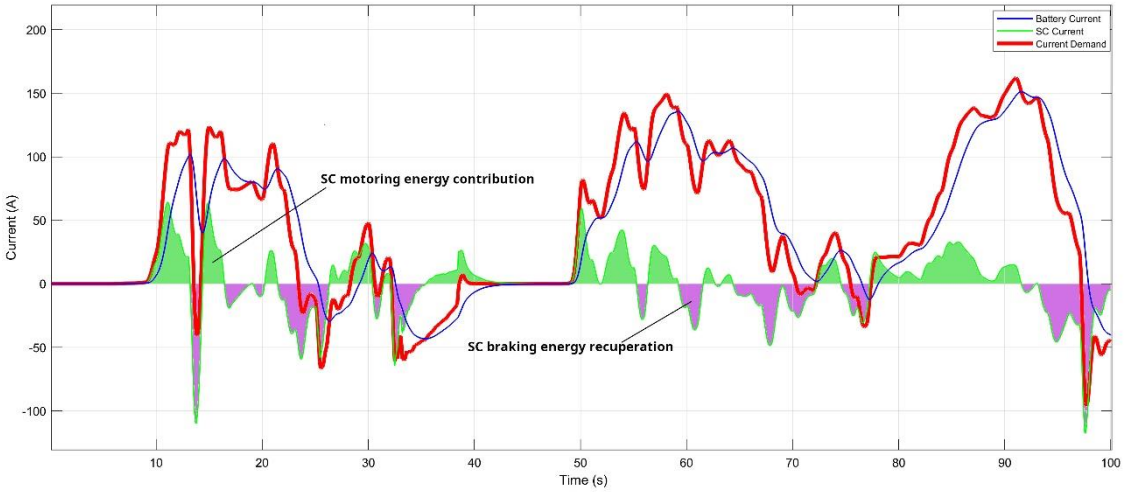

Fig. 4.12. Positive and negative SC energy contribution

4.5.1 A) First order high pass filter with fc=125 mHz

The literature suggests the use of high pass filters to determine the SC power contribution in the HESS [45], [131]. The current distribution when the SC current reference is obtained with a first-order high pass filter during the US06 driving cycle is shown in Fig. 4.13.

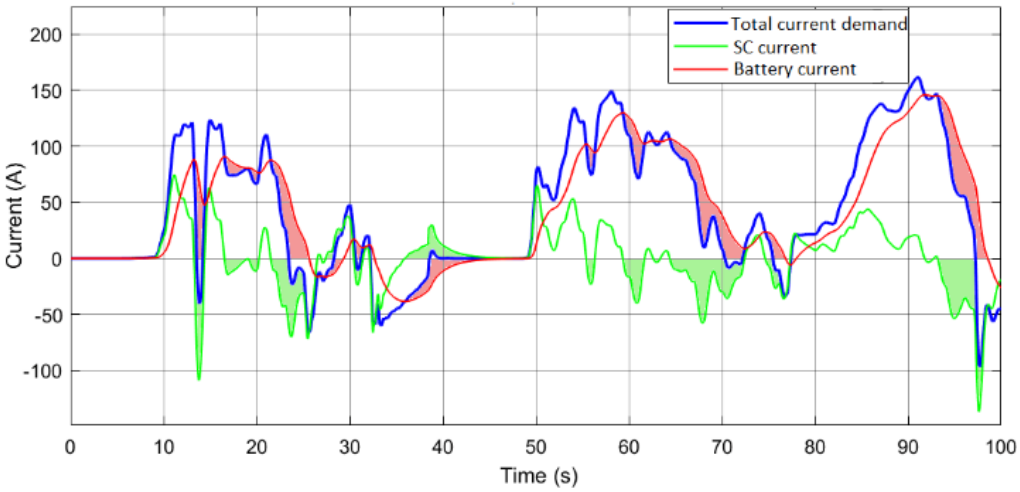

Fig. 4.13. HESS current distribution when the SC current reference is obtained with a first-order high pass filter fc=125 mHz.

The SC provides the peak power, relieving the battery from stress, especially during accelerations. However, the recuperation of the generated braking power is shared between the battery and SC. The SC recharges the battery between t=35 seconds to t=45 seconds. This occurs when braking energy is available, which is distributed between the battery and the SC. In this conditions, it would be beneficial for the battery lifetime to command the SC to absorb all the braking power. When the SC is commanded to recharge (green shades), the battery provides the necessary current to maintain the system in balance (red shades).

According to the results presented in Table 4.3, for the US06 driving cycle, the battery supplies 2467 Wh and the SC 608.9 Wh during the motoring stage when a first-order high pass filter with fc=125 mHz is used. During braking, the battery recovers 319.6 Wh and the SC 607.7 Wh. Considering that the energy demand during motoring is 2601 Wh, an excess of 479.9 Wh is circulated between the battery and SC. At the end of the US06 cycle, the final SOC of the SC is 80.01% and the battery SOC is 75.16% (the initial SOC conditions for the battery and SC were set to 80%).

4.5.2. B) Proposed method with a first-order low pass filter with fc=125 mHz.

Fig. 4.14 shows the results with the proposed method. The SC contribution during motoring is determined by the positive output of the filtration strategy that consists of the difference between the current demand and the output of a low pass filter with fc=125mHz.

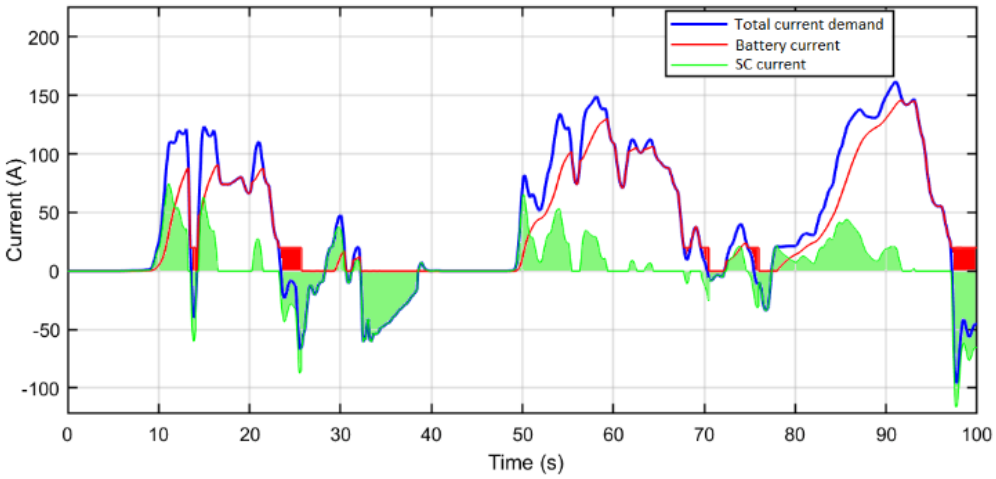

Fig. 4.14. Battery-SC current distribution with the proposed method. SC contribution (green shade). Charging strategy (red shade)

The SC absorbs all the generated braking energy and also receives charge from the battery when the SC voltage falls below $0.7V_{max}$ (red shades). The battery is effectively relieved from stress during motoring and braking, and the uncontrolled power circulation is eliminated. With this strategy, the battery provides 2098 Wh and the SC 537.9 Wh for a total of 2635.9 Wh.

Total energy circulated between the battery and SC to maintain the SC charge within operational levels ($>0.5V_{max}$) is 34.9Wh. A reduction of 92.6% in power circulation (from 474.9 Wh to 34.9 Wh) is achieved when compared to the high pass filter method. The final SOC of the SC is 74.91% and the battery SOC is 75.29%.

For the FTP72 driving cycle, power circulation is reduced by 100% with the proposed method (from 371 Wh to 0 Wh) with respect to the high pass filter method. The final SOC of the SC increased from 80% to 90.82%.

Table 4.3. Comparison of results obtained with the proposed method vs methods that use the high-frequency component directly for the US06 and FTP72 driving cycles

		HPF fc=125 mHz	Proposed method LPF fc=125 mHz	DWT high freq fc=(125-500)mHz	Proposed method DWT low freq fc=0-125 mHz	Predicted DWT high freq fc=(125-500) mHz	Proposed method with predicted DWT low freq fc=(0-125) mHz
US06 Driving cycle (12.81 km)	Motoring energy demand Wh	2601	2601	2601	2601	2601	2601
	Braking energy demand Wh	452.9	452.9	452.9	452.9	452.9	452.9
	Battery motoring energy Wh	2467	2098	2703	2049	2682	2043
	Battery braking energy (recovery) Wh	319.6	0	561.5	0	536.6	0
	SC Motoring energy Wh	608.9	537.9	616.3	832.7	399.3	969.6
	SC braking energy (recovery) Wh	607.7	487.6	609.7	733.2	396.6	864.2
	Final SOC Battery %	75.16%	75.29%	75.03%	75.40%	75.08%	75.42%
	Final SOC SC %	80.01%	74.91%	79.00%	69.64%	79.70%	69.18%
	Energy circulation Wh	**474.9**	**34.9**	**718.3**	**280.7**	**480.3**	**411.6**
FTP72 Driving cycle (11.93 km)	Motoring energy demand Wh	1668	1668	1668	1668	1668	1668
	Braking energy demand Wh	470.8	470.8	470.8	470.8	470.8	470.8
	Battery motoring energy Wh	1585	1313	1765	1119	1684	1128
	Battery braking energy (recovery) Wh	388.6	0	569.4	0	487.3	0
	SC Motoring energy Wh	454	355	413.7	577.3	301.1	576.4
	SC braking energy (recovery) Wh	453.6	470.8	412.1	499.4	300.6	506.9
	Final SOC Battery %	77.32%	77.07%	77.31%	77.50%	77.31%	77.48%
	Final SOC SC %	79.90%	90.82%	79.90%	72.60%	79.90%	73.36%
	Energy circulation Wh	**371**	**0**	**510.7**	**28.3**	**317.1**	**36.4**

During the FTP72 urban driving cycle, braking power alone maintains the charge of the SC, therefore there is no need to transfer energy from the battery. However, the SC appears underutilised as the SC receives more charge (470.8 Wh) than it is commanded to deliver (355 Wh). This is one of the disadvantages of using a fixed cut-off frequency as the SC would be able to discharge more to support the battery. Nevertheless, the HESS achieves the objective of relieving the battery from stress. A battery only system would consume 1668 Wh, while with the HESS the battery consumes 1338 Wh and the SC 335 Wh.

A comparison of the energy circulation obtained with the approaches presented in Table 4.3 for the US06 and FTP72 driving cycles is shown in Fig. 4.15 and 4.16, respectively.

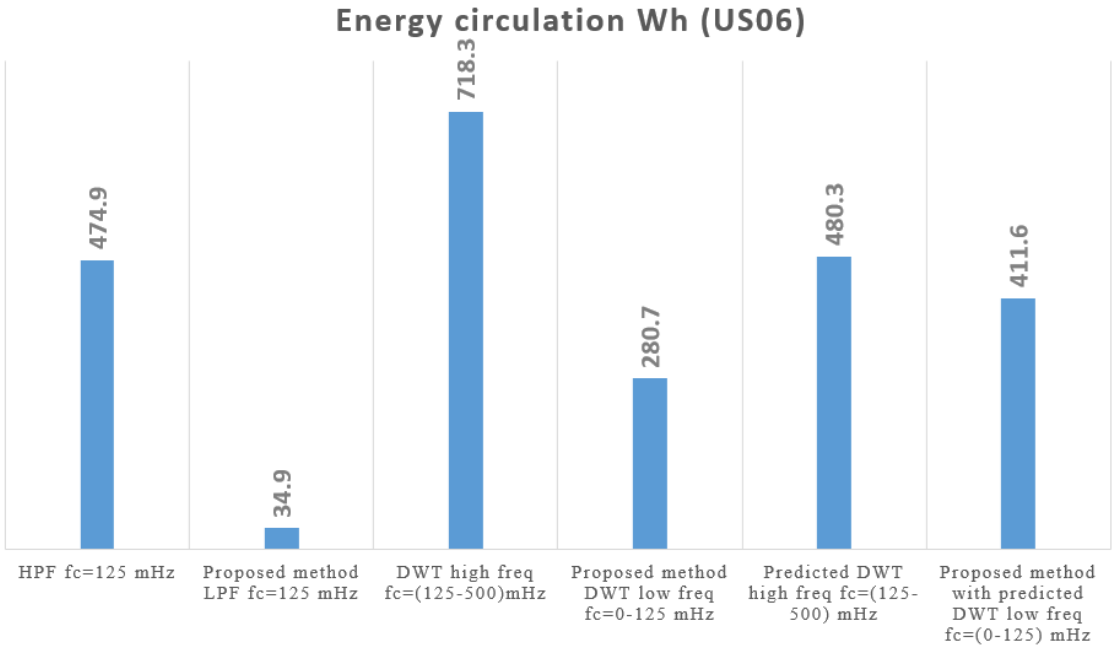

Fig.4.15. Energy circulation comparison for the US06 driving cycle for different EMS approaches

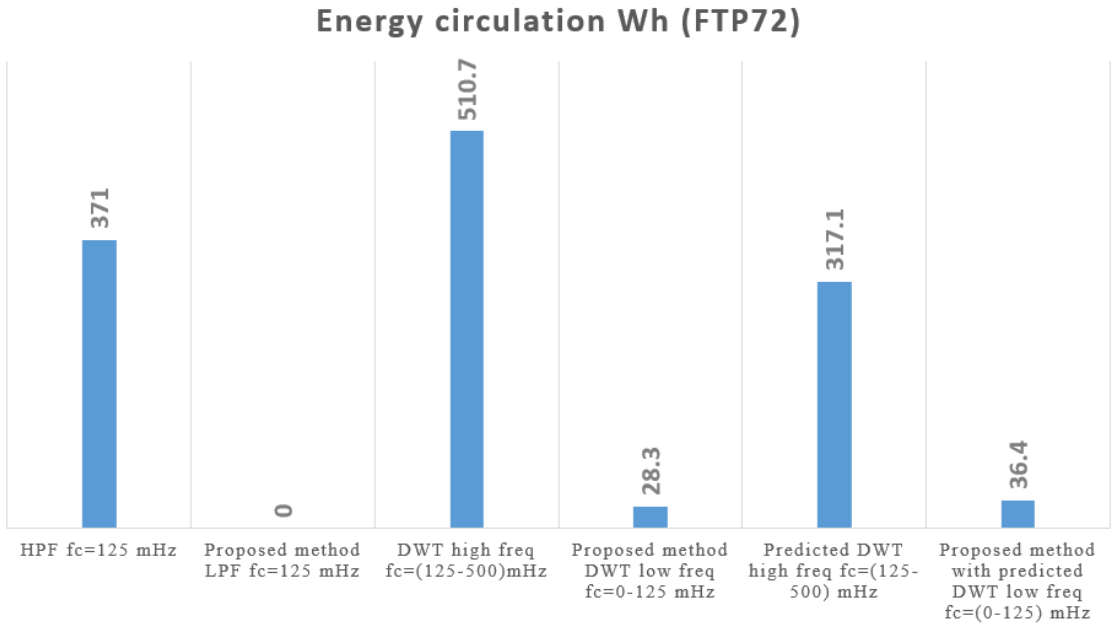

Fig.4.16. Energy circulation comparison for the FTP72 driving cycle for different EMS approaches

4.5.3. C) Direct discrete wavelet transform high-frequency component (125-500) mHz

The DWT high-frequency component has been normally used to control the SC power flow in HESS [50], [80], [132] . The total current demand signal is sampled at 1 Hz and then decomposed into 2 levels with the DWT using the Haar wavelet. The frequency sub-bands obtained with the decomposition are 0-125 mHz and 125-500 mHz for the low and high-frequency components, respectively. These frequency components are delayed 4 seconds with respect to the real-time demand. The result of this strategy during the first 100 seconds of the US06 driving cycle is shown in Fig. 4.17. The DWT introduces a delay in the filtered signal that exacerbates the power circulation between the battery and SC, as the SC is commanded to perform charge and discharge actions that are not aligned with the real-time demand. As shown in Table 4.3, using the DWT high-frequency component directly as the SC current reference results in the battery providing 2703Wh and the SC delivering 616.3 Wh. During braking, the battery recovers 561.5 Wh and the SC 609.7 Wh. A total of 718.3 Wh is circulated between the battery and SC during the US06 driving cycle. The final SOC of the SC is 79% and the battery SOC is 75.03%.

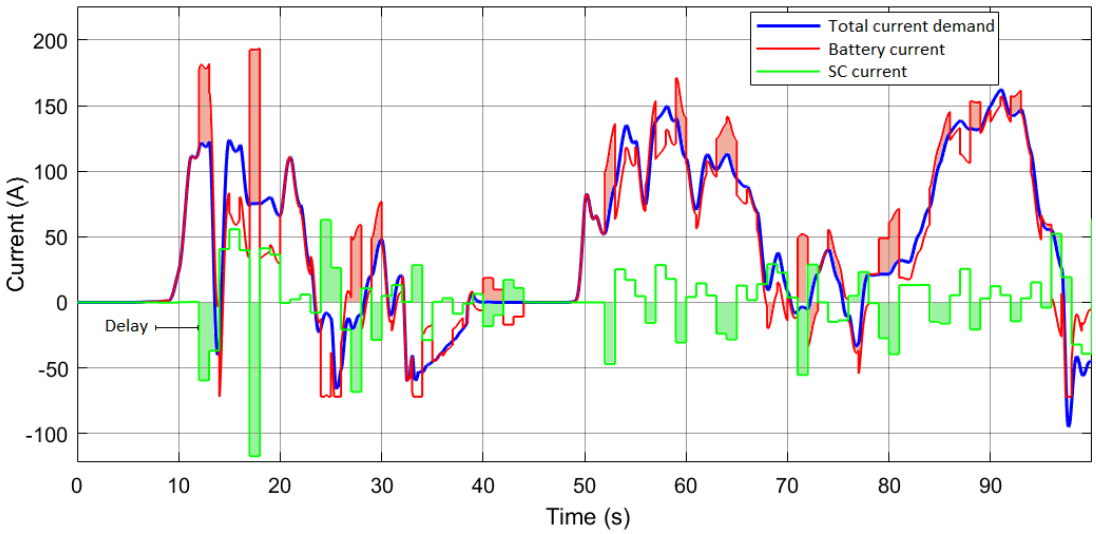

Fig. 4.17. HESS current distribution when the DWT high-frequency component is used as the SC current reference

4.5.4. D) Proposed method with the discrete wavelet transform low-frequency component (0-125 mHz)

Fig. 4.18 shows the result when the proposed method is used along with the DWT low-frequency component. Energy circulation is reduced from 718.3 Wh (direct DWT high frequency component) to 280.7 Wh (see Table 4.2). The SC recovers all the energy generated during braking, relieving the battery from it completely. The SC voltage is maintained above V_{SCmin} as the EMS allows the battery to transfer 280.7 Wh to the SC (red shades). The SOC of the SC at the end of the driving cycle is 69.64% and the battery 75.4%.

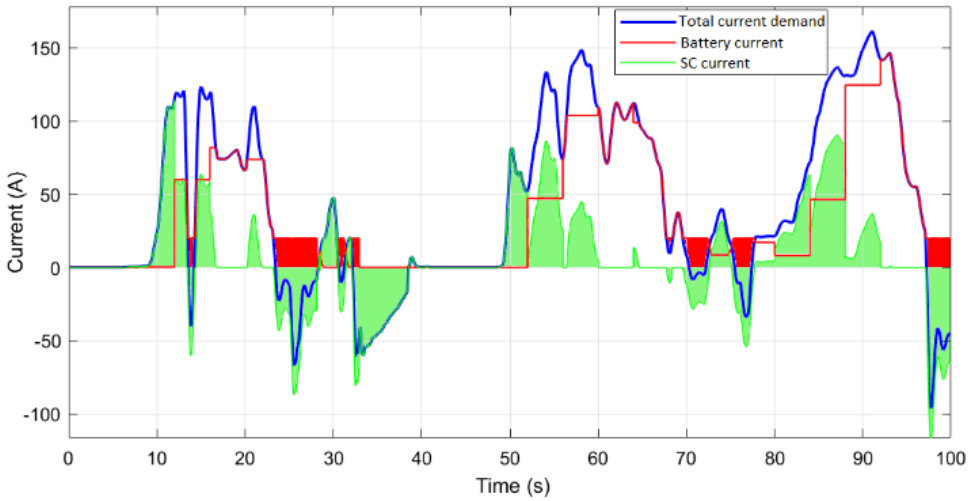

Fig. 4.18. Proposed method using the DWT low-frequency component

As shown in Table 4.3, with the urban FTP72 driving cycle, a total of 1668 Wh are required during the motoring stage and 470.8 Wh are generated during braking. Using the DWT high-frequency component directly results in the battery providing 1765 Wh and the SC 413.7 Wh for a total of 2178.7 Wh during the motoring stage. In this case, 510.7 Wh is circulated between the battery and SC. The battery recovers a total of 569.4 Wh and the SC 412.1Wh. The final SOC of the SC is 79.9%. With the proposed method, the battery provides 1119 Wh, and the SC assists with 577.3Wh reducing circulation to only 28.3Wh. The final value of the SOC of the SC is 72.6%.

4.5.5. E) Predicted discrete wavelet transform high frequency component (125 mHz-500 mHz)

The delay caused by the DWT can be compensated for by using a LSTM to predict the power demand, so the predicted demand can be fed to the DWT rather than the actual demand. Compensating for the delay can reduce energy circulation in the HESS. As shown in Table 4.3, energy circulation is reduced from 718.3 Wh (direct DWT high frequency component) to 480.3 Wh (predicted DWT high frequency component) during the US06 driving cycle and from 510.7 Wh to 317.1 Wh during the FTP72 driving cycle. This reduction in energy circulation has little effect on the final SOC of the SC. The direct use of the DWT high-frequency component results in a final SOC of the SC of 79% and 79.9% for the US06 and FTP72, respectively. When the predicted DWT high frequency is used, the SOC of the SC remains high at 79.7% and 79.9 % for the US06 and FTP72, respectively. The HESS current distribution when the predicted DWT high-frequency component is used is presented in Fig.4.19. With this approach, the battery still receives a substantial portion of the energy generated during braking (shaded areas).

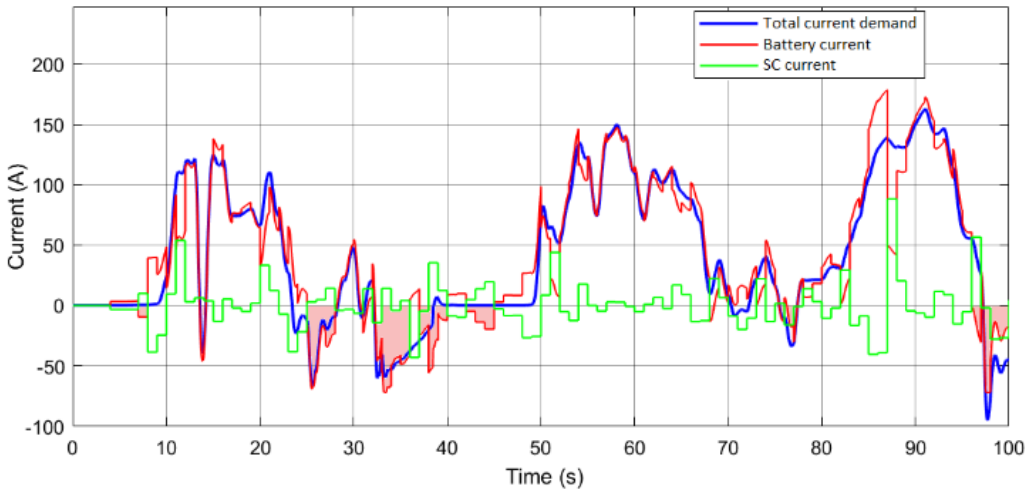

Fig. 4.19. HESS current distribution with the predicted DWT high-frequency component as the SC current reference.

4.5.6. F) Proposed method with the predicted discrete wavelet transform low-frequency component (0-125 mHz)

When the proposed method is used along with the predicted DWT low-frequency component, the battery is completely relieved from braking power as shown in Fig. 4.20. Energy circulation is further reduced to 411.6 Wh for the US06 driving cycle and to 36.4Wh for the FTP72 driving cycle (with respect to the use of the predicted DWT high frequency component). The SC voltage is maintained above V_{SCmin} and the final SOC of the SC is 69.18% and 73.36% for the US06 and FTP72, respectively.

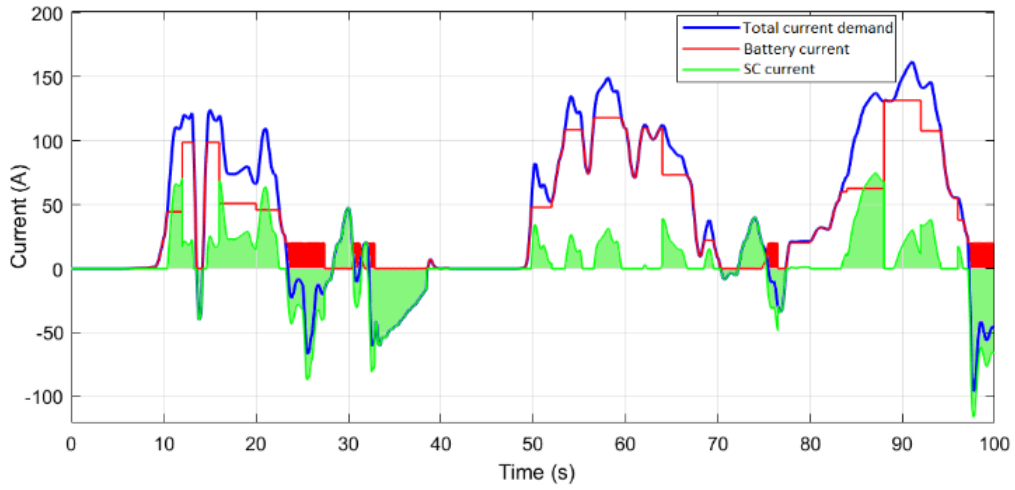

Fig. 4.20. HESS current circulation with the proposed method and the predicted low-frequency component.

Comparing the results compiled in Table 4.3 shows that when using the DWT, better results are obtained when the proposed method is used along with the DWT low-frequency component instead of the predicted DWT low-frequency component, suggesting that a prediction-based strategy is not necessary. Energy circulation is 280.7 Wh with the direct DWT low-frequency component and 411.6 Wh with the predicted DWT low-frequency component during the US06 driving cycle. The same occurs during the FTP72 driving cycle with an energy circulation of 28.3 Wh and 36.4 Wh, respectively. Overall, the best results are obtained when a simple first-order low pass filter is used along with the proposed method. Energy circulation for the US06 and FTP72 driving cycles are the lowest among the tested strategies with 34.9 Wh and 0 Wh, respectively.

4.5.7. Charging strategy simulation

To test the charging strategy along with the proposed first-order low pass filter method, the SC and battery SOCs are both set to 100%, then the US06 driving cycle is repeated until the battery is discharged. In Fig. 4.21, the SOC of the SC is recorded at the end of each US06 driving cycle (cycle duration 600 seconds) with and without the charging strategy for a total of 21 cycles (12600 seconds).

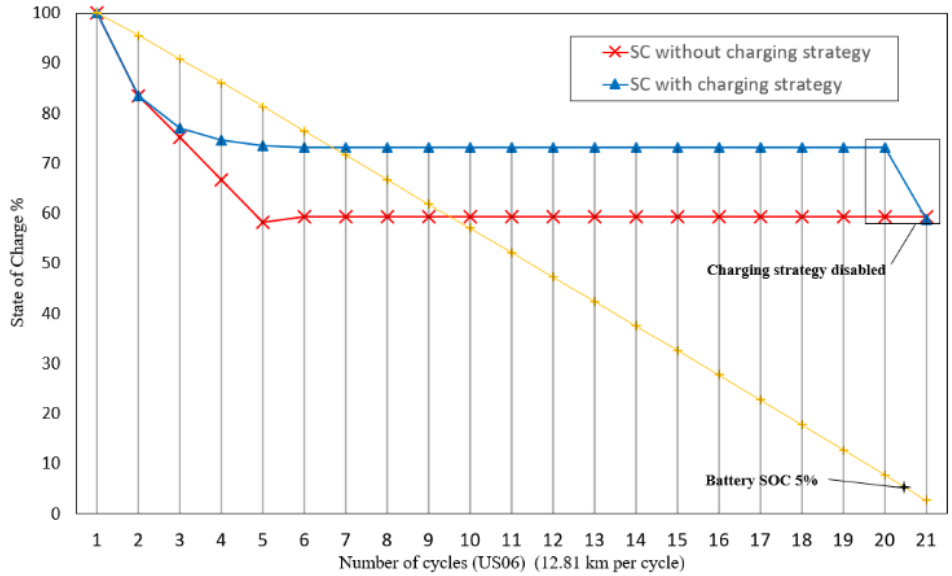

Fig. 4.21. Supercapacitor state of charge during a full discharge cycle (US06) with and without charging strategy

Without the charging strategy, the SC gives full assistance to the battery during the first 5 cycles (64.4 km). From the 5th cycle, the SC assists the battery as long as the SC voltage is higher than V_{SCmin}. However, when the SC charge is depleted the SC stops assisting the battery and only accepts charge from braking power and resumes assistance once its voltage rises above up to a set threshold, which has been set to V_{SCmin} +15 V in this test. A higher voltage threshold allows the SC to build up more charge, however, this will increase the SC downtime. When the battery SOC reaches 5% (between cycle 20 and 21), the SC charging strategy is disabled to relieve the battery from recharging the SC. The SOC of the SC at the end of the battery discharge cycle (cycle 21) is 58.77%. The total energy transferred from the battery to the SC throughout the full battery discharge cycle is 1466.7 Wh.

In terms of driving range, the EV modelled in this work with the HESS and the proposed low pass filter EMS would run for 275 Km on a single charge for the US06 driving cycle. In contrast, the same EV would run for 269 km with a battery only system. Hybridising the battery with a SC doesn't add significant driving range to the vehicle, but relieves the battery from stress and therefore improves its lifetime. This method can be implemented easily by monitoring the SC voltage and setting the rules to check the voltage thresholds.

When the same test is performed with a high pass filter without the proposed EMS strategy, the total energy circulation between the battery and SC at the end of 21 US06 driving cycles is 7860 Wh. A reduction of 81.3% in energy circulation (from 7860 Wh to 1466.7 Wh) is achieved with the proposed method while effectively assisting the battery during the motoring stage, recovering all the braking energy and managing the charge of the SC.

4.6 Energy efficiency

The energy efficiency obtained with the proposed method is calculated in Table 4.4 for the US06 driving cycle and Table 4.5 for the FTP72 driving cycle, assuming a lossless DC/DC converter. In these tables, a comparison with the other strategies analysed in this chapter show the superiority of the proposed method. The highest efficiencies obtained with the proposed method respond to an effective energy distribution where energy circulation is controlled, the braking energy generated is allocated to the SC and the battery is relived from peak power. For the US06 driving cycle, the energy efficiency during motoring is 98.7 %, meaning that only a small percentage of energy is circulating in the system with the purpose to maintain the SC charge. During braking, the efficiency is 92.8%. The overall efficiency is 91.6% which is greater than any of the other strategies.

In the case of the FTP72 driving cycle, the efficiency is 100% (considering lossless DC/DC converter) as there is no energy circulation. During motoring, the SC and the battery contribute just the necessary energy to match the demand. During braking, the SC recovers the braking energy, relieving the battery from negative power demand.

Table 4.4. Energy efficiency calculation for the US06 driving cycle and 6 different EMS strategies

	Motoring US06	**HPF fc=125 mHz**	**Proposed method LPF fc=125 mHz**	**DWT high freq. fc=(125-500) mHz**	**Proposed method DWT low freq. fc=0-125 mHz**	**Predicted DWT high freq. fc=(125-500) mHz**	**Proposed method with predicted DWT low freq. fc=(0-125) mHz**
a	Total energy demand Wh	2601	2601	2601	2601	2601	2601
b	Total battery Energy supplied Wh	2467	2098	2703	2049	2682	2043
c	Total SC energy supplied Wh	608.9	537.9	616.3	832.7	399.3	969.6
d	Energy circulation Wh (b+c-a)	474.9	34.9	718.3	280.7	480.3	411.6
	Braking US06						
e	Total energy generated braking Wh	452.9	452.9	452.9	452.9	452.9	452.9
f	Total energy absorbed by SC Wh	607.9	487.8	609.7	733.6	396.6	864.5
g	Total energy absorbed Battery Wh	319.9	0	561.5	0	536.6	0
h	Energy circulation Wh (f+g-e)	474.9	34.9	718.3	280.7	480.3	411.6
	Energy balance						
i	Total energy motoring HESS Wh (b+c)	3075.9	2635.9	3319.3	2881.7	3081.3	3012.6
j	Total energy recovered HESS (f+g)	927.8	487.8	1171.2	733.6	933.2	864.5
	Net energy Wh (i-j)	2148.1	2148.1	2148.1	2148.1	2148.1	2148.1
	Net energy demand Wh (a-e)	2148.1	2148.1	2148.1	2148.1	2148.1	2148.1
	Efficiency						
k	Energy efficiency motoring (%) (a/i*100)	84.6%	98.7%	78.4%	90.3%	84.4%	86.3%
l	Energy efficiency braking (%) (e/j*100)	48.8%	92.8%	38.7%	61.7%	48.5%	52.4%
	System efficiency (%) (K*L)	41.3%	91.6%	30.3%	55.7%	41.0%	45.2%

Table 4.5. Energy efficiency calculation for the FTP72 driving cycle and 6 different EMS strategies

	Motoring FTP72	HPF fc=125 mHz	Proposed method LPF fc=125 mHz	DWT high freq. fc=(125-500) mHz	Proposed method DWT low freq. fc=0-125 mHz	Predicted DWT high freq. fc=(125-500) mHz	Proposed method with predicted DWT low freq. fc=(0-125) mHz
a	Total energy demand Wh	1668	1668	1668	1668	1668	1668
b	Total battery Energy supplied Wh	1585	1313	1765	1119	1684	1128
c	Total SC energy supplied Wh	454	355	413.7	577.3	301.1	576.4
d	Energy circulation Wh (b+c-a)	371	0	510.7	28.3	317.1	36.4
	Braking FTP72						
e	Total energy generated braking Wh	470.8	470.8	470.8	470.8	470.8	470.8
f	Total energy absorbed by SC Wh	453.3	470.8	412.1	499.1	300.6	507.2
g	Total energy absorbed Battery Wh	388.5	0	569.4	0	487.3	0
h	Energy circulation Wh (f+g-e)	371	0	510.7	28.3	317.1	36.4
	Energy balance						
i	Total energy motoring HESS Wh (b+c)	2039	1668	2178.7	1696.3	1985.1	1704.4
j	Total energy recovered HESS (f+g)	841.8	470.8	981.5	499.1	787.9	507.2
	Net energy Wh (i-j)	1197.2	1197.2	1197.2	1197.2	1197.2	1197.2
	Net energy demand Wh (a-e)	1197.2	1197.2	1197.2	1197.2	1197.2	1197.2
	Efficiency						
k	Energy efficiency motoring (%) (a/i*100)	81.8%	100.0%	76.6%	98.3%	84.0%	97.9%
l	Energy efficiency braking (%) (e/j*100)	55.9%	100.0%	48.0%	94.3%	59.8%	92.8%
	System efficiency (%) (K*L)	45.8%	100.0%	36.7%	92.8%	50.2%	90.8%

CHAPTER 5

5 EXPERIMENTAL IMPLEMENTATION OF THE PROPOSED ENERGY MANAGEMENT SYSTEM

5.1. Introduction

This chapter details the implementation of the proposed EMS strategy along with a real time test platform that includes a dual motor kit powered by a battery-SC HESS. The algorithm to control the dual motor setup is based on a FOC approach where the first motor is controlled in speed mode and the second motor (acting as a generator) in torque mode. As both machines are mechanically coupled, the second motor can be controlled to test the first motor in different load conditions. The FOC control algorithm for the dual motor setup is implemented on a Texas Instruments C2000 Piccolo LAUNCHPAD F28069M, which allows simultaneous control of two motors through two BOOSTXL 8305EVM 3 phase motor drives. The EMS is implemented in a LAUNCHPADXL F28027F. Both, the EMS and the test platforms are developed in a rapid prototyping approach using Matlab/Simulink code generation and real time processor in the loop (PIL). The advantage of using Matlab/Simulink support for C2000 microcontrollers is that coding is efficiently generated, so manual coding in Code Composer Studio (CCS) is avoided. With Matlab's embedded code generation, the complete Simulink model is translated to C code and specifically adapted for its deployment in the selected embedded target hardware. Simulink blocks interface with the different microcontroller's modules, such as analogue to digital converter (ADC) and pulse width modulation (PWM), allowing easy and rapid configuration. The measured DC-bus current is used by the EMS algorithm to determine the current split. DC-bus current is acquired with a LEM LA-55P hall-effect current transducer with 1:1000 conversion factor (turns ratio) and a primary

current measurement range of ±70 A. As the output of this sensor is a current value, a series resistor is used to transform this signal into a voltage value, as this is the type of input accepted by the ADC. Signal conditioning with an operational amplifier is implemented to shift the output voltages of the transducer to the voltages accepted by the ADC (0-3.3V). This chapter presents the results obtained with the proposed EMS and compares them to a current distribution obtained with simple filtration. The superiority of the proposed real-time method is experimentally validated and the feasibility of implementation confirmed.

5.2. Test platform hardware

5.2.1. Texas Instruments LAUNCHPADXL F28069M

The C2000 Piccolo LAUNCHPADXL-F28069M is a low cost development board that offers an on board Joint Test Action Group (JTAG) emulation tool that allows direct interface to a PC for easy programing, debugging, and evaluation. Additional to JTAG emulation, the USB interface provides universal asynchronous receiver/transmitter (UART) serial connection to the host PC. This development board can be complemented with add-on boards called BoosterPacks. These additional boards can access all the LAUNCHPAD General Purpose Input/Outputs (GPIO) and analogue signals. One of the main applications of this LAUNCHPAD is motor control. This particular board can host 2 inverter BoosterPacks allowing for the control of two 3-phase permanent magnet servo motors. This is beneficial when prototyping a variety of applications including robotics, CNC, assembly/manufacturing, traction drives, personal transport, small-task oriented vehicles, drones, etc.

The purpose of this board in the test platform is to perform FOC control of the motor under test and the motor acting as an active load (generator).

The main specifications of Launchpadxl F28069M are listed in Table 5.1 [133] and depicted in Fig. 5.1.

Table 5.1. LAUNCHPADXL F28069M specifications

Microcontroller unit (MCU) clock frequency	90 MHz
Pulse Width Modulation (PWM) channels	16
High-resolution PWM channels	8
Quadrature Encoder Pulse modules (QEP)	2
Analog to Digital converter	12 bit, 16 channels
CAN (Controller area network)	1
SPI (Serial peripheral interface)	2
SCI/UART (serial communications interface/ Universal asynchronous receiver-transmitter)	2
USB (Universal serial bus)	1
I/O pins (digital/analogue)	54/6
Supply Voltage	3.3V

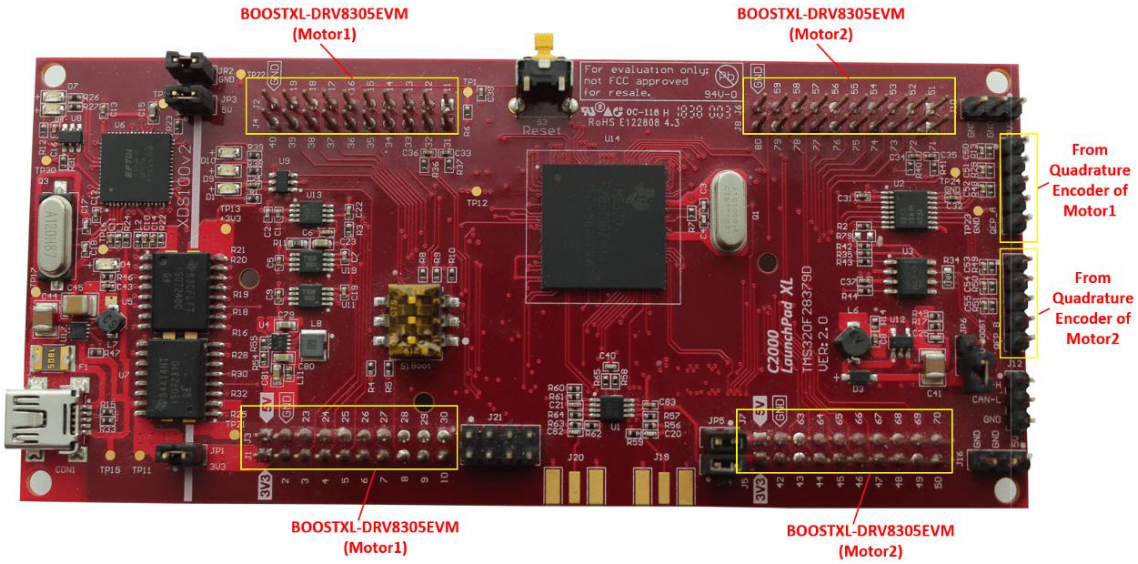

Fig. 5.1 Texas Instruments LAUNCHPADXL F28069M development board [134]

5.2.2. Texas Instruments LAUNCHPADXL F28027F

The C2000 Piccolo LAUNCHPADXL-F28027F has an on board JTAG emulation tool allowing direct interface to a PC and a USB interface provides UART serial connection to the host PC. In the test platform, this microcontroller measures DC-bus current, DC/DC inductor current, and SC voltage to supply the real-time EMS algorithm, so the SC current reference can be obtained and used to drive the DC/DC converter. For this purpose, ADC inputs are used to acquire sensor data, and PWM outputs are used to control DC/DC

converter switches. A picture of LAUNCHPADXL-F28027F is shown in Fig 5.2 and its specifications are summarised in Table 5.2.

Table 5.2 LAUNCHADXL F28027F specifications

MCU clock frequency	60 MHz
PWM channels	8
High-resolution PWM channels	4
Analog to Digital converter	12 bit, 7 channels
SPI	1
SCI/UART	1
I/O pins (digital/analogue)	20/6
Supply Voltage	3.3V

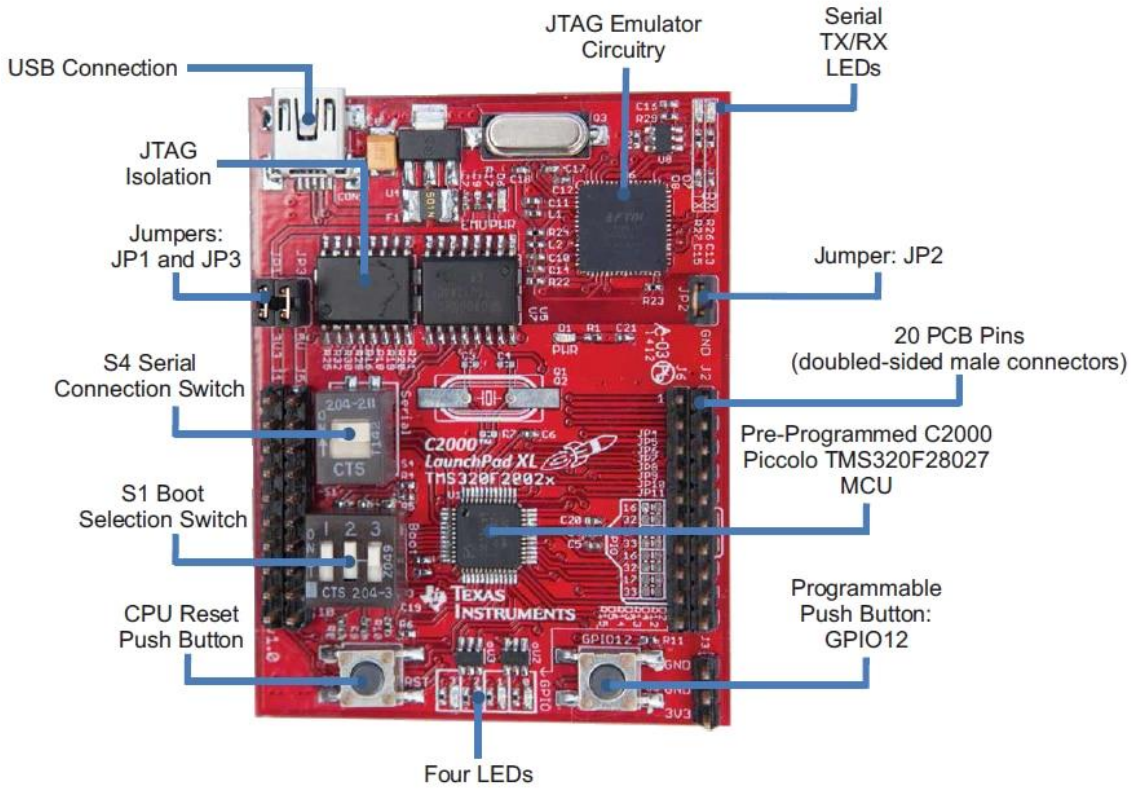

Fig. 5.2 Texas Instruments LAUNCHPADXL F28027F development board

This additional board is used because the LAUNCHPAD XL F28069M PWM ports were used up by the inverters, so there were not enough PWM ports to control the DC/DC converter.

5.2.3. BOOSTXL DRV8305EVM motor drive

The BOOSTXL-DRV8305EVM is a 15A, 3-phase brushless DC drive. It is based on the DRV8305 motor gate driver and CSD18540Q5B NexFET power MOSFET. The main characteristics are summarised in Table 5.3 [135].

Table 5.3 BOOSTXL DRV8305EVM 3-phase motor drive

Voltage Supply	4.4V to 45 V
Drive current	Up to 15A RMS (20A peak)
Operating supply current	150 mA
Operating temperature	125°C
MOSFET	6 x CSD18540Q5B N-channel NexFET Power MOSFET (1.8 mOhm)

The inverter configuration, operating parameters, and diagnostic information are communicated to the LAUNCHPADXL F28069M through SPI. A picture of the assembly including the LaunchpadXL F28069M and two Boostxl DRV8305EVM inverters is shown in Fig. 5.3.

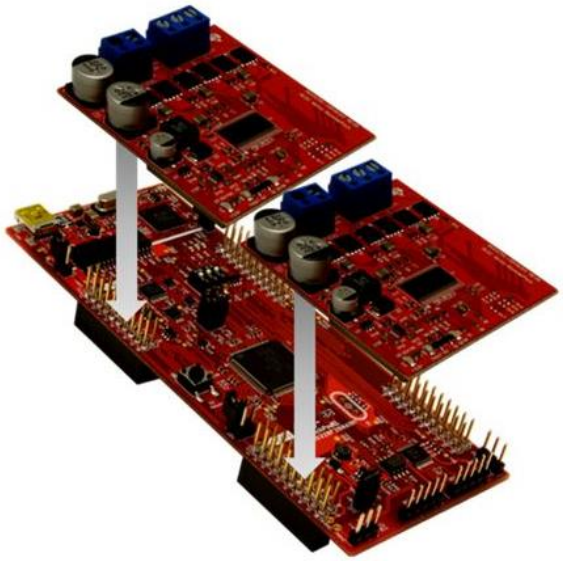

Fig. 5.3. LAUNCHPDXL F28069M + 2 BOOSTXL DRV8305EVM inverters

5.2.4. SEMIKRON Semiteach Insulated-gate bipolar transistor (IGBT) inverter stack

The Semikron Semiteach IGBT stack is a multifunction IGBT converter that allows for experimenting with typical converter configurations including 3-phase inverter + brake chopper, buck-boost converter, single phase inverters, and single or 3-phase rectifiers. This unit is used for the development of the bidirectional DC/DC converter interfacing the SC pack to the DC-bus. The schematic of the bidirectional DC/DC converter is shown in Fig 5.4.

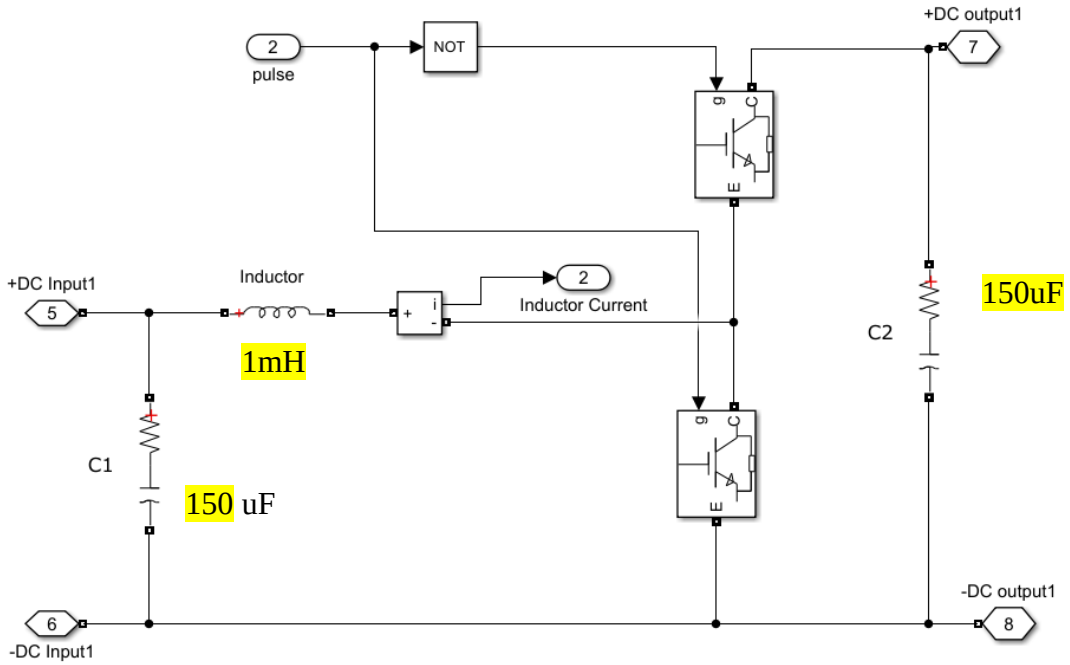

Fig. 5.4. Bidirectional DC/DC converter schematic

The specifications are summarised in Table 5.4 [136].

Table 5.4. Semicron Semiteach specifications

Maximum permanent output current	30 A_{RMS}
Maximum permanent input current	30 A_{RMS}
Maximum output voltage	400 VAC
Maximum DC-bus voltage	750 VDC
Maximum switching frequency	50 kHz
Driver supply voltage	14.4<15<15.6 VDC

A 1mH inductor and two 150uF capacitors (C1, C2) are used in the bidirectional DC/DC converter. A picture of the inverter stack is shown in Fig.5.5.

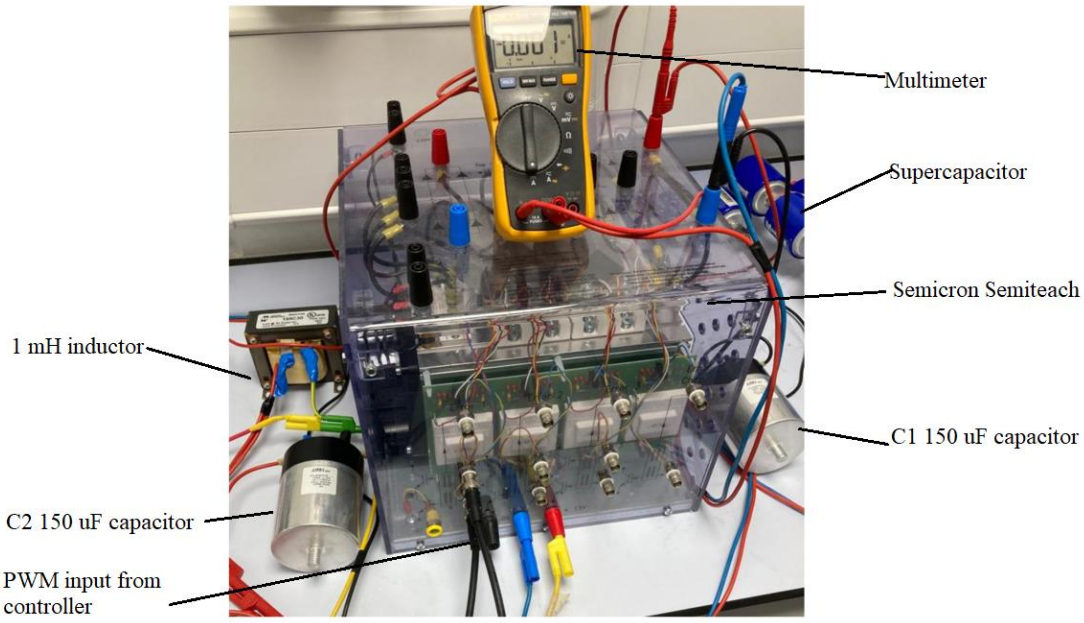

Fig. 5.5. Bidirectional DC/DC converter with the Semicron Semiteach inverter stack

5.2.5. Battery

Due to availability of Lead acid batteries in the laboratory, the battery used in the experiment is a Valve Regulated Lead Acid (VRLA) battery with Absorbent Glass Mat (AGM) technology, which are suitable for short time delivery of high currents. Although the battery used has a different chemistry and different performance than a Lithium battery, the EMS performance remains the same. The battery characteristics are listed in Table 5.5 and its picture is shown in Fig. 5.6.

Table 5.5. Battery characteristics

Victron Energy sealed VRLA AGM		
Rated capacity	110	Ah
Nominal voltage	12.8	V
Maximum charge current (0.2C)	22	A
Maximum pulse discharge (8C, 5 seconds)	800	A
Discharge cut-off voltage	10.8	V
Battery pack characteristics		
Pack nominal voltage (V_{nom})	38.4	V
Pack maximum Capacity (Q)	110	Ah
Fully Charged voltage (V_{full})	39.6	V
Cut-off voltage	32.4	V
Pack configuration	3 series, 1 parallel	
Pack energy	4.22	kWh

The ratio between the battery simulated (40.6 kWh) and the battery used in the experiment (4.22 kWh) is 96.3:1.

Fig. 5.6. Battery Pack used in the experiment

5.2.6. Supercapacitor

The SC used in the HESS test platform is produced by Maxwell Technologies. The specific model is the BCAP1200 P270, which is commonly used in applications such as automotive subsystems, back-up power, grid stabilisation, hybrid drive trains, rail system power, transportation and utility vehicles. Its main specifications are listed in Table 5.6 [137], and its picture in Fig. 5.7.

Table 5.6. BCAP1200 P270 specifications

Nominal Capacitance	1200F
Rated voltage	2.7 VDC
Surge Voltage	2.85 VDC
Equivalent series resistance	0.58 mohm
Operating temperature	-40°C to +65°C
Power density	5800 W/kg
Pmax	15900 W/kg
Energy density	4.67 Wh/kg
Maximum Continuous Current	81 A
Maximum peak current, 1 sec	955 A
Leakage current	2.7 mA
Weight	0.26 kg
Short circuit current	4650 A
Volume	0,295 L
Dimensions	74x60.4x60.7 mm
Supercapacitor Pack Specifications	
SC Pack fully charged Voltage (5 SC in series)	14.25V
Rated Capacitance	240 F
Equivalent DC series resistance	0.0029 ohms
Usable energy (100%-50%SOC)	5.07 Wh

The energy ratio between the SC simulated (430.5 Wh) to the one used in the experiment (5.07 Wh) is 85:1.

Fig.5.7. BCAP1200 P270 supercapacitor

5.2.7. Low voltage permanent magnet synchronous machine dyno kit

The kit includes two 60Vdc synchronous 3-phase sinusoidal back EMF PMSM, shaft coupling, and aluminium frame mount for the intention to run one motor under test with the other acting as an active load. The Teknic motor part number is M-2310P-LN-04K and the kit part number is 2mtr-dyno. The kit parts are shown in Fig.5.8

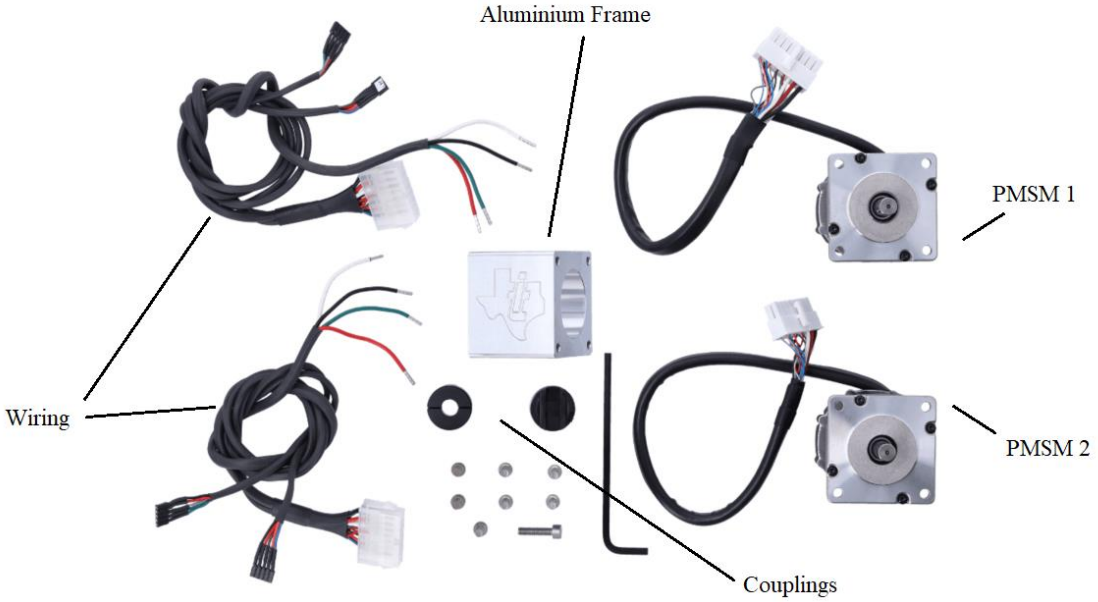

Fig. 5.8. Motor-dyno kit parts

Each motor has the characteristics shown in Table 5.7 [138]:

Table 5.7. Teknic M-2310P-LN-04K motor specifications

Resistance, phase to phase [ohms]	0.72
Inductance, phase to phase [mH]	0.40
Electrical Time Constant [mS]	0.56
Back EMS (Ke) [Vpeak/kRPM]	4.64
Continuous Torque [oz-in]	38.8
Continuous Torque [Nm]	0.274
Continuous current [A]	7.1
Maximum RPM	6000
Back EMF constant	4
Encoder density [counts/revolution]	4000
Encoder type	Line driven single-ended TTL Floating optical disk
Commutation type:	120° spaced, optical commutation sensors. Sinusoidal

5.2.8. Permanent magnet synchronous motor

The PMSM is an AC synchronous motor whose field excitation is provided by permanent magnets embedded in the rotor. The stator is made of windings which are connected to an AC supply to produce a rotating magnetic field. This type of motor produces sinusoidal back EMF, similar to its induction motor counterpart. Control is achieved through a digitally controlled inverter. This control is based on vector control techniques such as FOC and direct torque control. The basic idea of the vector control algorithm is to decompose a stator current into a magnetic field generating part and a torque generating part. Both components can be controlled separately after decomposition. Maximum torque is reached when the current and the magnetic field are orthogonal between them. Hence the goal of the control algorithm is to keep the current flowing in the windings orthogonal to the magnetic field of the rotor.

5.3. Field oriented control

Field oriented control is a method whose purpose is decoupling the torque and flux producing components of the stator current. This decomposition allows the control of 3 phase motors in the same fashion as simple DC motors with separate excitation. In this way, the flux generation is controlled by the excitation current and the torque generation is controlled by the armature current.

In Surface Mounted Permanent Magnet type motors, the d-axis (direct axis) current reference of the stator (i_d^*) is usually set to zero in order to maximise the torque production [139]. The magnets in the rotor produce the rotor flux linkages needed to generate the magnetising current. The rotor flux linkages are generated by the permanent magnets and the stator flux linkages are generated by the stator current. The d-axis current may be set to a non-zero reference when using a flux optimisation technique. For example, field weakening techniques reduce the stator flux on the d-axis in order to operate above the nominal speed.

The FOC method can be implemented using speed sensors and without them. However, where precision is important, sensored control provides better performance than sensorless. The sensor provides precise information of the rotor position and the mechanical speed of the rotor. The F28069M microcontroller performing the FOC control has two QEP rotary encoder inputs to determine the precise rotor position of the two motors, so the sensored control approach is adopted.

The control method can be summarised as follows [140]:

1. The three-phase stator currents are measured. Only two currents will suffice if the motor has balanced three phase windings. The third current is calculated as $i_a + i_b + i_c = 0$
2. The three phase currents are converted to a stationary two axis system with the Clarke transform. This transformation calculates the variables i_α and i_β, which are the time-varying quadrature current values viewed from the perspective of the stator. These variables are obtained from the measured i_a, i_b, i_c values.
3. The stationary two-axis coordinate system is rotated to align with the rotor flux using the Park transform. This transform provides the i_d, i_q, which are the quadrature currents transformed to the rotating coordinate system. These variables are calculated from i_α and i_β. For steady state conditions, i_d, i_q are constant.
4. The i_d reference current controls rotor magnetizing flux. The i_q reference current controls the torque output of the motor.
5. The i_d^* reference set point is compared to i_d, and the i_q^* reference set point is compared to i_q. The error signals are fed to PI controllers and the output of the

controllers provide v_d^*, v_q^* which are voltage vectors that will be applied to the motor.

6. The encoder pulses provides a new transformation angle that guides the FOC algorithm as to where to place the next voltage vector.
7. The v_d^*, v_q^* output values from the PI controllers are rotated back to the stationary reference frame using the new angle. For this purpose the inverse Park transform is used. This calculation provides the next quadrature voltage values v_α^*, v_β^*.
8. The v_α^*, v_β^* values are used to calculate the new PWM duty cycle values which will generate the desired voltage vector.
9. The mechanical speed (ω) is calculated after every discrete PWM cycle

In Fig. 5.9, the diagram of the FOC control of the dual motor setup is shown. The motor simulating the vehicle motor has an additional speed control loop where the angular speed measured by the sensor is compared to the desired speed. On the other hand, the load motor is controlled in torque mode, therefore, i_q^* is used to set the reference current to control the torque.

The vehicle motor drive is powered by a HESS composed by a 38.4V battery and a 14.25V SC HESS, which is interfaced to the DC-bus through a bidirectional DC/DC converter. The load motor drive is powered independently by a 38.4 V battery. A picture of the motor and controller kit is shown in Fig. 5.10.

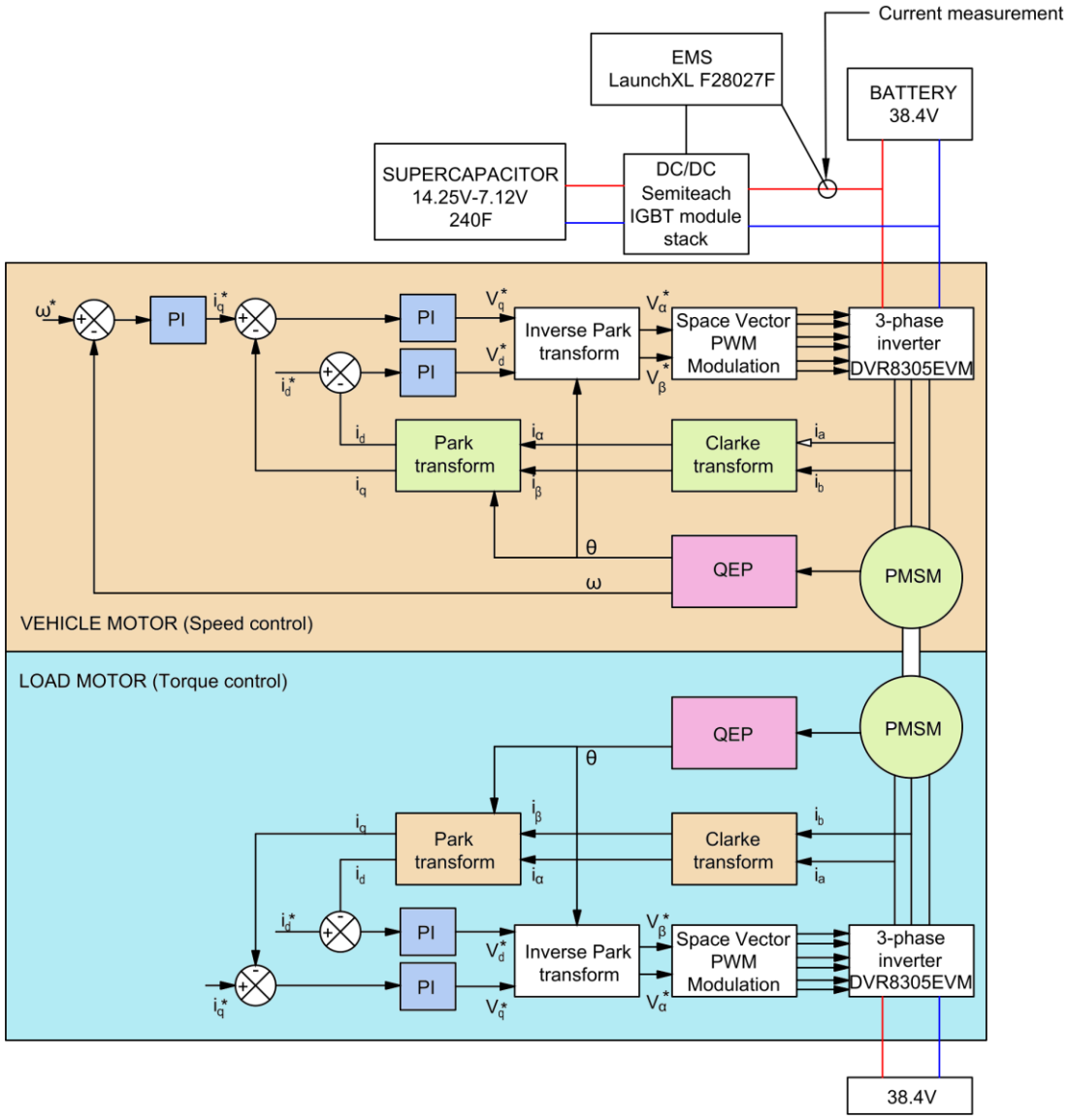

Fig. 5.9. Dual motor FOC control schematic

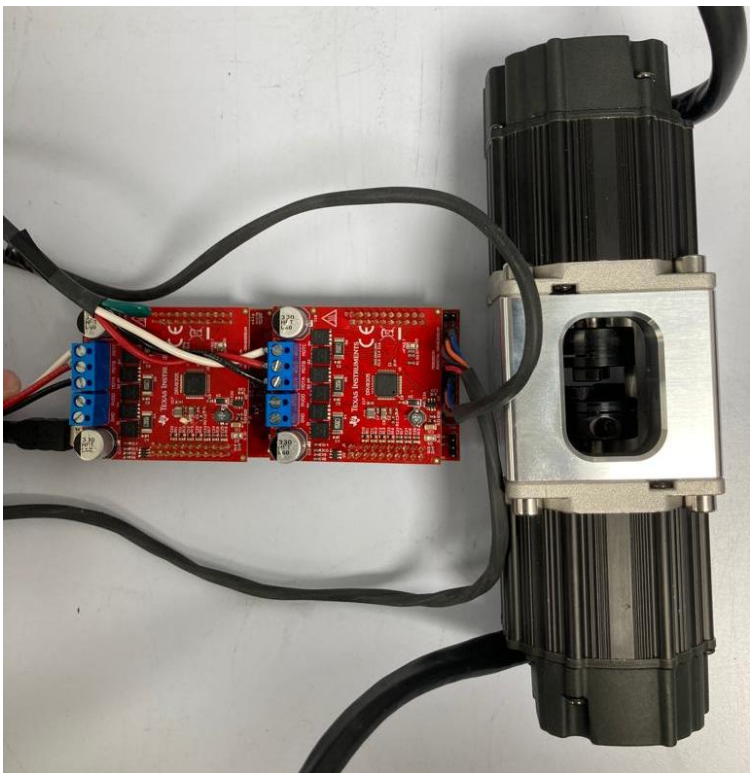

Fig.5.10. Dual motor coupling and LAUNCHPADXL controller

5.4. Model to control a dual permanent magnet synchronous motor (dyno) using C2000 processors

The dual motor FOC control model is available as a fully functional example in Matlab [141]. The model is compatible with Matlab R2014a to R2022a. For the implementation, Matlab R2021b has been used. The additional MathWorks products to simulate, generate code and deploy the model on the target hardware are:

- Motor Control Blockset
- Embedded Coder
- Embedded Coder Support Package for Texas Instruments™ C2000™ Processors
- Fixed-Point Designer
- Simulink

The Embedded Coder Support Package allows users to create real-time executable code of a Simulink model and deploy it on Texas Instruments C2000 microcontrollers. All the

algorithms and device driver blocks contained in the Simulink model are converted to C code, which is generated automatically and run directly on the target hardware. The support package allows access to the device driver blocks for ADC, PWM, SPI, I2C, serial, CAN, interruptions, DAC, etc., giving the flexibility to for rapid prototyping and production workflows for different control applications. One of the main advantages of using Simulink along with TI C2000 processors is the verification capability through Processor in the Loop (PIL), Monitor and Tune (External mode), and SD card Logging and Real-time profiling. By installing this software, it is possible to set up the Simulink model to communicate with the target hardware. Installation of the support package software and third-party software, such as Texas Instruments Code Composer Studio is part of the setup and configuration process.

Once the model is configured, the code generated is uploaded to the microcontroller. To send the speed and torque (I_q current) set points to the microcontroller a host model is used. This host model establishes a serial communication link with the microcontroller. Current loops in Motor 1 and Motor 2 control algorithms are offset by $T_s/2$, where T_s is the control loop execution rate. To access the model to control this kit, the following command must be inserted in Matlab command prompt:

```
Open_system('mcb_pmsm_foc_qep_dyno_f28069m')
```

5.5. Energy management system implementation

5.5.1. IIR filter implementation

IIR Digital filters are implemented based on the difference equation, which determines how the output signal relate to the input signal. The difference equation is given by [142]:

$$y(n) = \sum_{k=0}^{q} b_k x(n-k) - \sum_{k=1}^{p} a_k y(n-k) \tag{5.1}$$

The transfer function of the IIR filter is given by:

$$H(z) = \frac{\sum_{k=0}^{q} b_k z^{-k}}{1 + \sum_{k=1}^{N} a_k z^{-k}} \tag{5.2}$$

Where a_k are the feedback filter coefficients and b_k are the feedforward filter coefficients. Designing an IIR filter usually involves finding a transfer function H(z) in the form of eq. 5.1 such that its magnitude response, phase response, and the group delay approximate the specified magnitude response in terms of a certain criterion.

Practical implementation of an IIR filter is usually based upon analogue equivalents, where methods such as Butterworth, Chebyshev, Elliptic, and least squares are used to find the continuous time filter transfer functions that approximate the specifications given in the frequency domain. It is also possible to design bespoke filters without any reference to analogue designs. The analogue filter prototype is transformed to its digital equivalent with the bilinear transform. This digitalisation technique is the most popular for designing IIR filters, since there is a vast amount of theory on standard analogue filter design. The design process is depicted in the schematic presented in Fig 5.11.

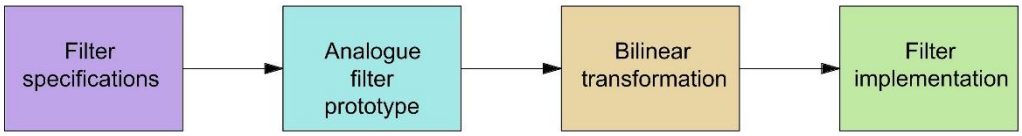

Fig 5.11. IIR filter design steps

As the bilinear transform maps the left half-plane of the s-plane into the unit circle of the z-plane, the infinitely long analogue frequency axis $j\omega$ becomes the finite-length circle. The bilinear transform mapping is illustrated in Fig 5.12.

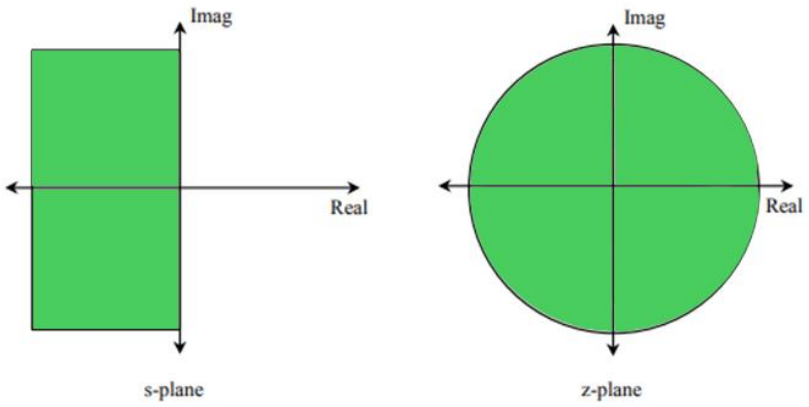

Fig. 5.12. Illustration of s-plane to z-plane mapping using the bilinear z-transform.

This is known as frequency warping, where equal increments along the unit circle in the z-plane correspond to larger bandwidths along the s-plane. This means that all the values of the frequency response of the analogue filter are compressed into the range $0 \le \omega_d T_s \le \pi$, resulting in a nonlinear compression of the frequency scale. To overcome the warping effect introduced by the transform, it is common practice to pre-warp the specification of the analogue filter, so that after warping the cut-off frequency is located at the desired place.

Once the filter has been designed, the transfer function is converted with the bilinear transform using the substitution [143]:

$$s = \frac{2}{T_s}\left(\frac{1-z^{-1}}{1+z^{-1}}\right) \tag{5.3}$$

where T_s is the sampling time.

In this thesis, the proposed filtration strategy is based on a first order low pass filter, for which its continuous time transfer function is given by:

$$H(s) = \frac{k\omega}{s+\omega} \tag{5.4}$$

where *k* is the pass-band filter gain and ω is the desired angular frequency which is given by:

$$\omega = 2\pi f_c \tag{5.5}$$

where f_c is the cut off frequency of the filter. The desired cut-off frequency is f_c=125 mHz, the filter gain is 0.8, and the sampling frequency is f_s=1 kHz. With these parameters the angular frequency of the digital filter is $\omega=2\pi$ x $125e^{-3}$ = 0.785 rad/s By substituting (5.2) in (5.3), the discrete transfer function $H(z)$ is obtained as:

$$H(z) = \frac{0.8\omega}{\frac{2}{T_s}\left(\frac{1-z^{-1}}{1+z^{-1}}\right)+\omega} \tag{5.6}$$

$$H(z) = \frac{0.8\left(\frac{\omega T_s}{\omega T_s+2}\right)+0.8\left(\frac{\omega T_s z^{-1}}{\omega T_s+2}\right)}{z^{-1}\left(\frac{\omega T_s-2}{\omega T_s+2}\right)+1} \tag{5.7}$$

Substituting the filter cut-off frequency and sampling time in (5.6) yields the filter's discrete transfer function:

$$H(z) = \frac{0.8(0.000392z+0.000392)}{z-0.9992} \tag{5.8}$$

5.5.2. Effect of filter pass-band gain on the supercapacitor current reference

Different pass-band filter gains were used to modify the SC current reference, so it approaches to the benchmark signal as calculated in Chapter III section 3.4.4. To obtain the results shown in Fig. 5.13, a low pass filter with a gain of *k=1* was used. Comparing this result to those obtained when the pass-band gain of the low pass filter was changed to 0.8 shows that with a gain lower than 1, the high frequency component signal is amplified as the low frequency component is attenuated. The results are shown in Fig. 5.14.

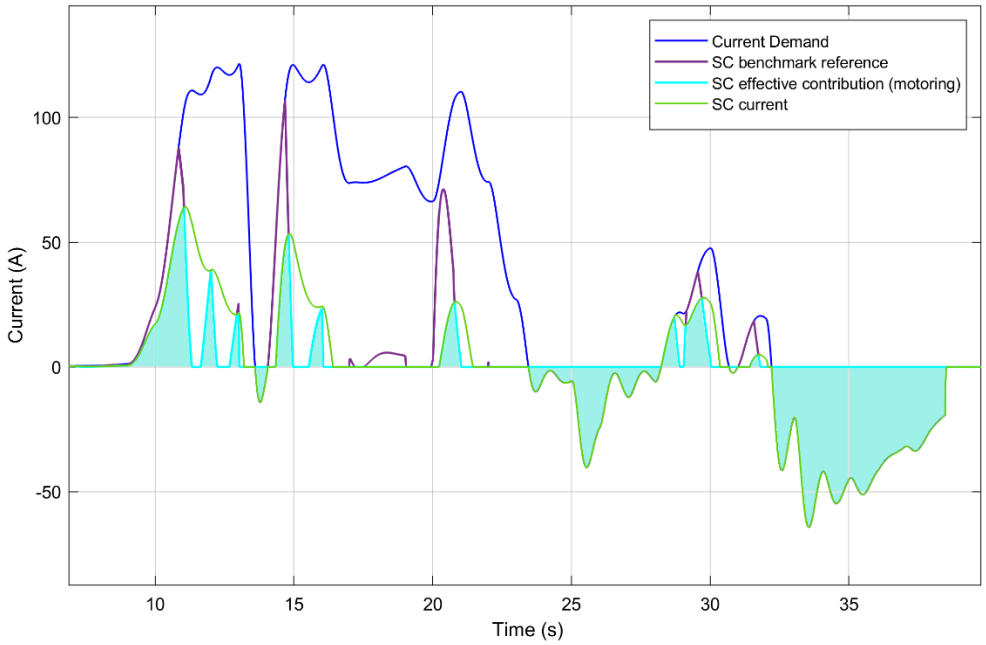

Fig.5.13. SC current reference (green) vs SC effective contribution during demand set by changes in the acceleration rate (light blue) with a filter with fc=125mHz and pass-band gain of 1.

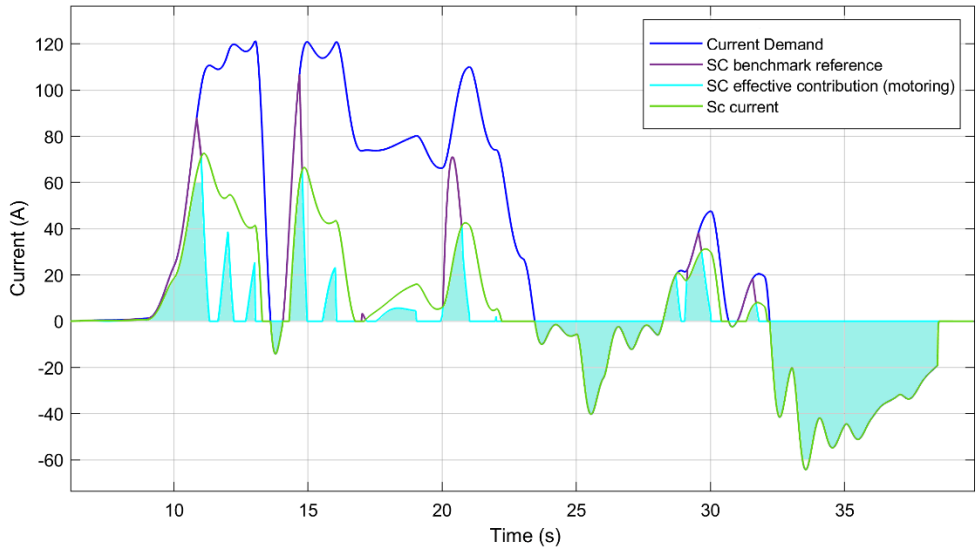

Fig.5.14. SC current reference (green) vs SC effective contribution during demand set by changes in the acceleration rate (light blue) with a filter with fc=125mHz and pass-band gain of 0.8.

These results show that varying the pass-band gain of the filter modifies the amount of energy contained in the signal, which can be used to adaptively change the contribution of the SC considering factors such as the SOC of the SC, SOC of the battery, vehicle loading, type of driving cycle, changes in acceleration, etc. In the literature, adaptive

methodologies using filters commonly change the cut-off frequency with methods such as fuzzy logic [47], leaving the gain constant. Adaptive methodologies by changing the filter pass-gain have not been reported.

5.5.3. Implementation of the proposed energy management system on the Texas Instruments C2000 Piccolo MCU F28027F Launchpad

Texas Instruments 32-bit C2000 microcontrollers can be programmed and debugged using Mathworks Embedded Coder Support Package. This enables real time closed loop control of applications such as motor control in a model-based design workflow. To implement the proposed EMS, the current measured at the DC-bus is measured with a hall-effect current transducer. As the current in the DC-bus can take positive values during the motoring stage and negative values during regenerative braking, a signal conditioning circuit is required to ensure that the range measured by the transducer is converted to a range accepted by the microcontroller. In this particular case, the LEM La-55-P transducer is able to measure DC currents within -50A and 50A in the primary. The output of the transducer is a current signal that has a proportion of 1:1000 with respect to the measured current in the primary, so for a current of 50A, the output is 50 mA. The current at the output of the sensor must be converted to voltage before it can be fed to the microcontroller ADC. A resistor of 100 ohm is connected in series with the output of the sensor to convert the current output into a voltage between -5V to 5V. The sensor connection schematic is shown in Fig. 5.15

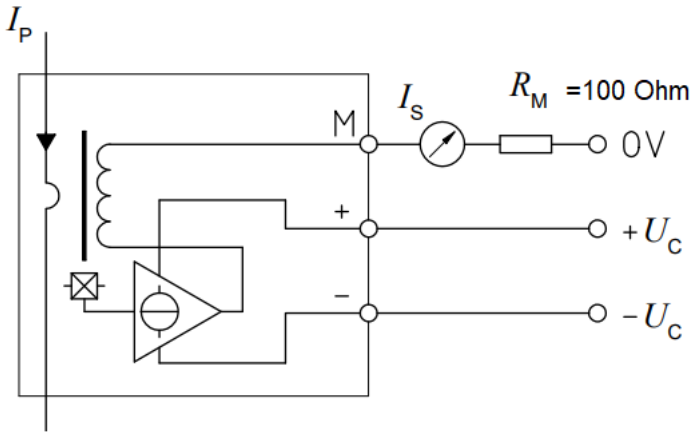

Fig. 5.15. Current sensor schematic

The F28027F microcontroller is able to accept positive voltages within 0V to 3.3V. As the output of the current sensor can vary between -5V and 5V, an operational amplifier is required to perform signal conditioning. The conditioning schematic is shown in Fig. 5.16 and is known as a level shifter.

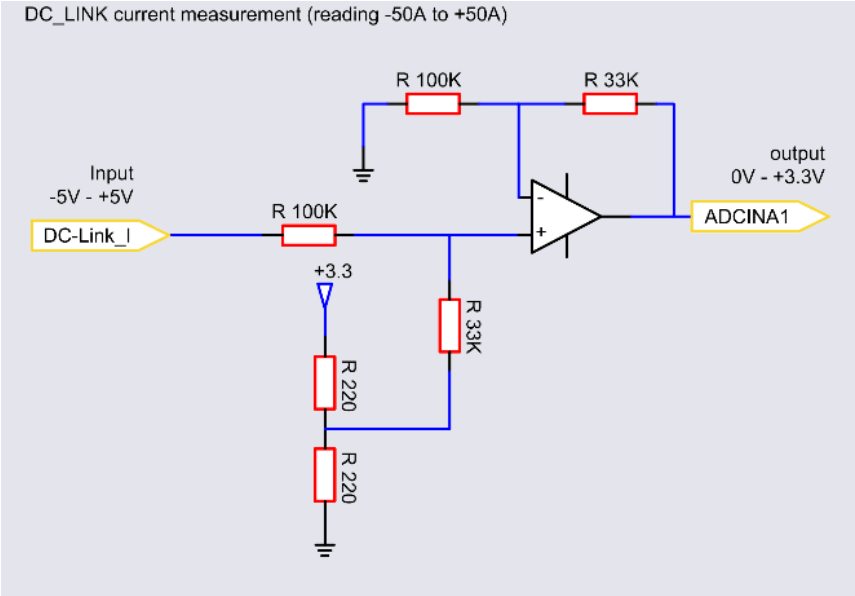

Fig. 5.16. Current sensor to ADC signal conditioning

With Simulink C2000 support package, an ADC block can be configured to read the voltage provided by the signal conditioning operational amplifier. This block interfaces

the physical microcontroller with Matlab environment, allowing for real time data acquisition and monitoring.

The proposed EMS requires the calculation of 3 currents: Motoring, braking and charging currents. To determine these currents, the measured DC-bus current is filtered from high frequency noise with a low pass filter with a cut-off frequency of 100 mHz as shown in Fig. 5.17.

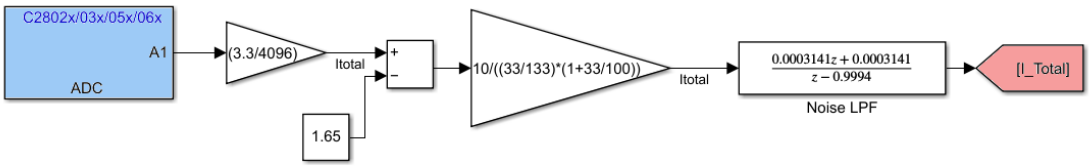

(a)

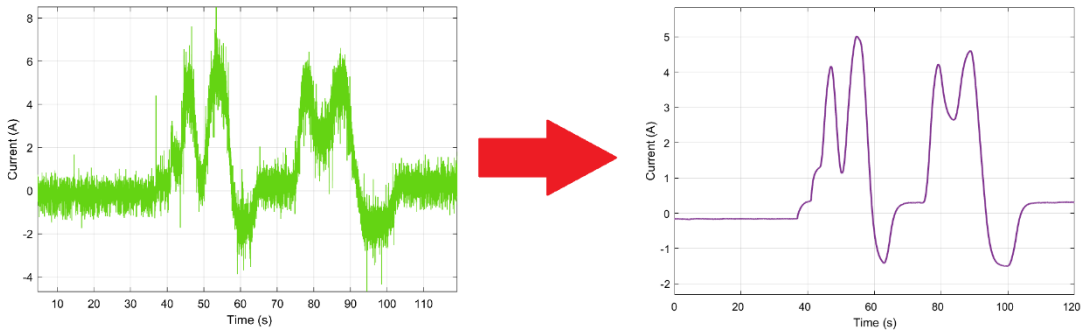

(b)

Fig. 5.17. DC-bus current measured. (a) Simulink DC-bus data acquisition model. b) (Left) Raw signal obtained at the output of the current sensor. (Right) DC-bus current after filtering

The motoring current reference I_m (see Fig.4.1) is obtained with the Simulink model presented shown in Fig. 5.18, where the current measured at the DC-link is filtered with the IIR low pass filter designed previously. The positive part of the filtered signal is subtracted from the positive part of the measured current demand. Finally, the motoring current reference corresponds to the positive part of the resulting signal.

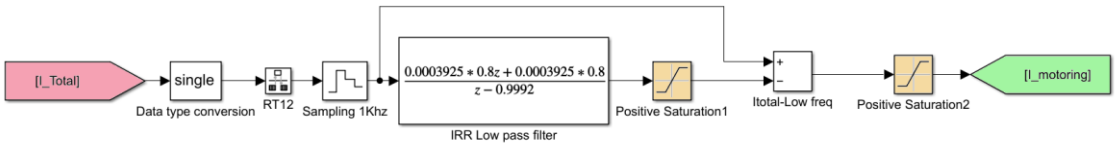

Fig. 5.18. SC motoring current calculation

By letting the negative part of the measured current pass through, the braking current I_{br} is calculated. The Simulink model is shown in Fig. 5.19.

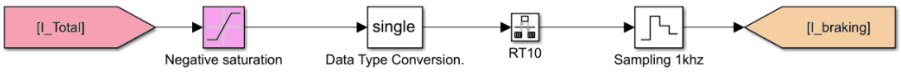

Fig. 5.19. Calculation of SC negative current

The rate transition blocks in fig 5.18 (RT12) and 5.19 (RT10) are used to transfer data from the output of a block operating at one rate to the input of a block operating at a different rate. This block ensures data integrity and deterministic data transfer. The behaviour of the rate transition block depends on the sample times of the ports to which the block connects [144].

The final component of the SC current reference is the charging current I_{ch}. For this purpose, the voltage of the SC is measured with a voltage transducer, where a current proportional to the measured voltage is passed through an external resistor as shown in Fig 5.20.

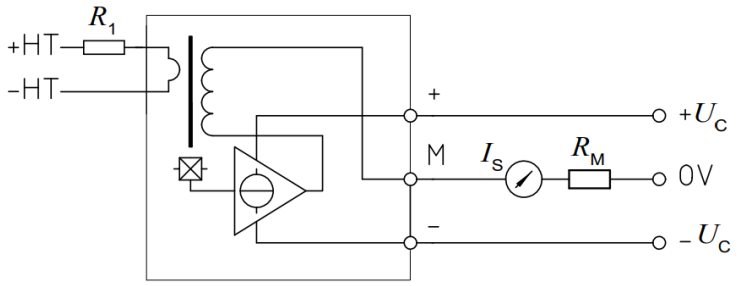

Fig. 5.20. Voltage transducer schematic

The measured voltage is checked against the voltage threshold of 10 V, so when the SC voltage is below this value and the current demand is zero, a constant current of 1.5A is

subtracted from the SC current demand. The Simulink model to obtain the charging current is presented in Fig 5.21.

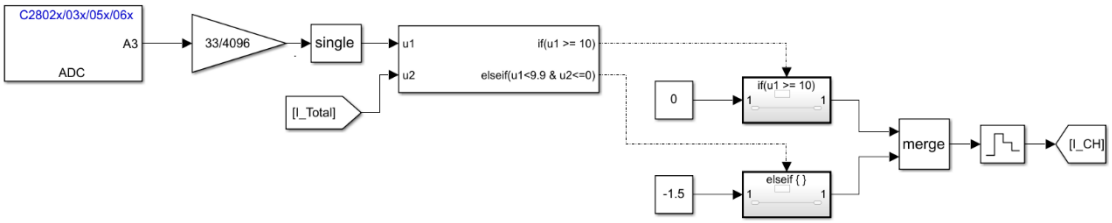

Fig. 5.21. Charging current model

The SC current reference is calculated by adding the motoring, braking and charging currents. The SC current reference is then compared to the DC/DC converter inductor current, which is measured with a LEM LA-55-P current transducer and its output signal conditioned with a similar circuit as presented in Fig. 5.16.

Once the Simulink model is completed the code generation function provided by MATLAB Coder™, Simulink Coder™, and Embedded Coder® generate ANSI/ISO C/C++ code that can be compiled and executed on Texas Instruments® processors. The generated code is uploaded to the microcontroller and monitored in real time by using Simulink external mode.

5.6. Experiment setting

The motor simulating the vehicle is controlled in speed control and set to run at a constant speed of 4000 rpm. The second motor I_q current, proportional to torque, is varied according to the reference shown in Fig. 5.22.

Fig. 5.22. Current reference schedule (Iq) to control the loading motor torque

The loading motor (dynamometer) follows the current reference shown in Fig.5.22. This loads the motor under test (running at constant 4000 RPM), producing the current demand shown in Fig.5.25 after noise filtration. This is the current used by the EMS to perform the power split between the battery and SC. Once the code is generated in Matlab, it is transferred to the target hardware (Launchpad Microcontroller). For the FOC control of the dyno, a host model is used to pass the control signals from a Simulink model to the microcontroller. This is done by using UART serial communications. In Fig 5.23, the FOC Simulink model to control both PMSMs is shown. This model is converted to C-code and uploaded to the microcontroller. The experiment complete layout and microcontroller pin assignments is presented in appendix B at the end of this thesis.

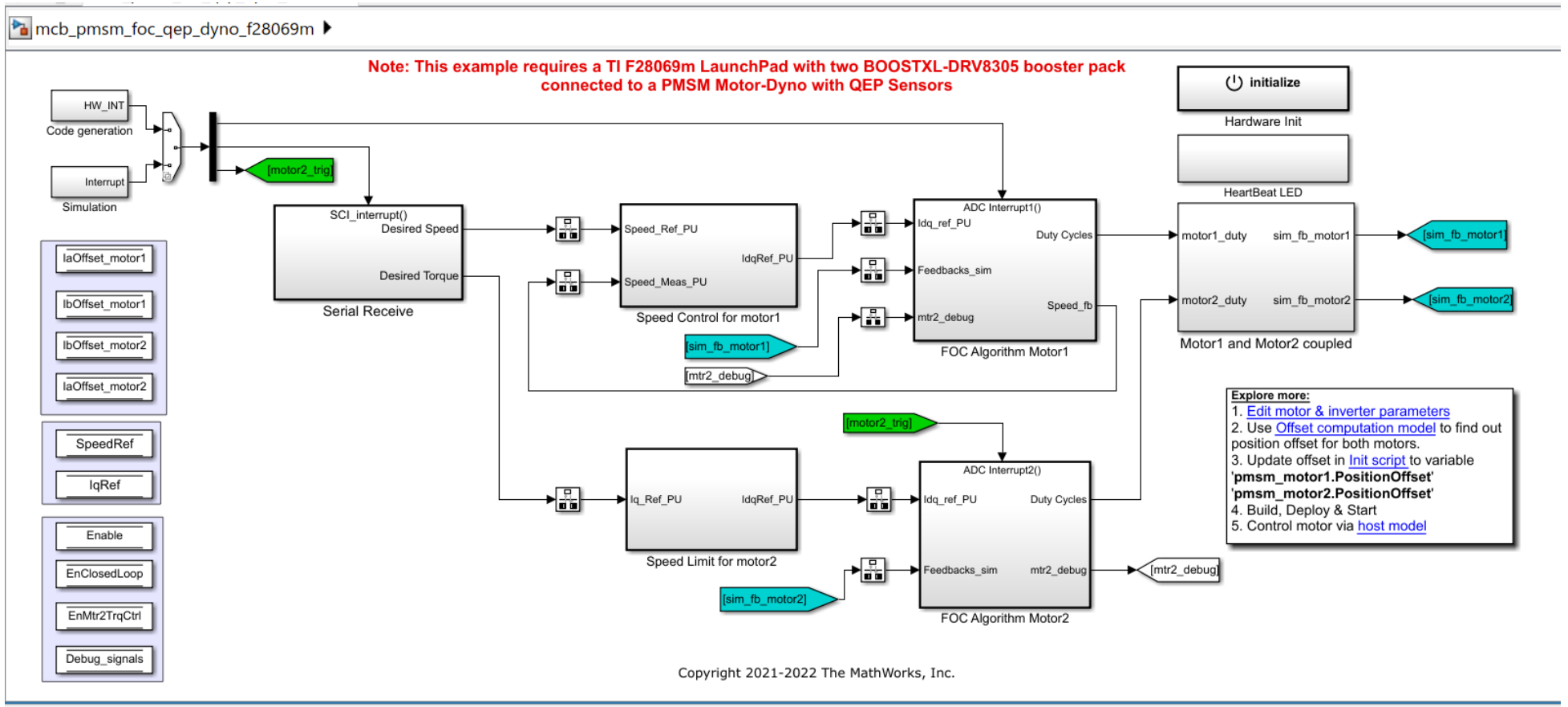

Fig.5.23. FOC control Simulink model

To interact with the model shown in Fig. 5.23, a host model is necessary. This model allos the user to send the current commands to the microcontroller, so the motors can react to these control signals. For the motor under test, the speed command is set to 4000 RPM. The second motor (loading motor) receives the current reference to control de torque of the motor. This torque can be either positive (to load the motor) or negative to simulate regenerative braking. The Host model is shown in Fig. 5.24.

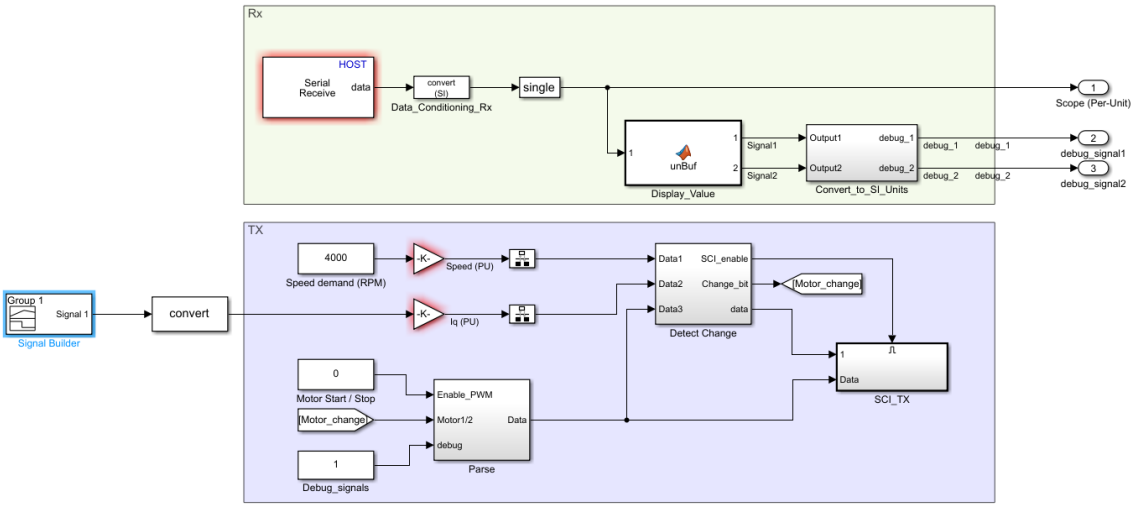

Fig.5.24. Simulink Host model to control the dyno rig

Once the current reference to control the loading motor is passed to the microcontroller, the torque of this motor will vary according to the current schedule shown in Fig, 5.22. As a response, the current of the motor running at 4000 RPM will change according to the loading torque. The current demand resulting from this is shown in Fig.5.25.

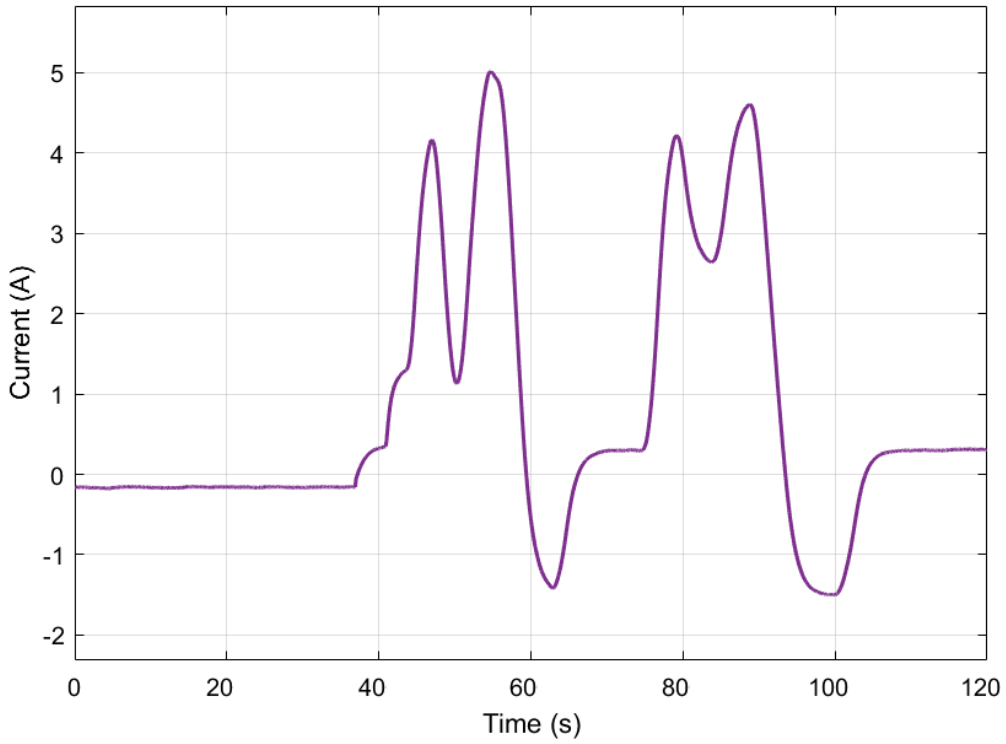

.

Fig. 5.25. Total current demand required by the motor under test

5.7. Results

The results of the experiments with and without the proposed EMS are presented in Table 5.8, and the energy efficiency calculations are presented in Table 5.9.

Table 5.8. Comparison of results obtained with and without the proposed EMS

	Without EMS		With EMS and no charging strategy		With proposed EMS and charging strategy	
	motoring	braking	motoring	braking	motoring	braking
Total demand (Wh)	11.4	1.73	11.4	1.73	11.4	1.73
Battery (Wh)	8.47	1.20	8.08	0	9.42	0
SC (Wh)	3.46	1.06	3.32	1.73	3.32	3.07
Total energy HESS (Wh)	11.93	2.26	11.4	1.73	12.74	3.07
Energy circulation (Wh)	0.53	0.53	0	0	1.34	1.34
SC effective contribution (Wh)	3.32	0.53	3.32	1.73	3.32	1.73
SC initial voltage (V)	10.2		10.2		10.2	
SC final voltage (V)	9.18		9.53		10.1	

Table 5.9. Energy efficiency calculations for the case without the proposed EMS, with the proposed EMS and no charging strategy enabled, and for the proposed EMS with charging enabled.

	Motoring	**Without EMS**	**With EMS (no charging strategy)**	**With EMS (with charging strategy)**
a	Total energy demand Wh	11.4	11.4	11.4
b	Total battery Energy supplied Wh	8.47	8.08	9.42
c	Total SC energy supplied Wh	3.46	3.32	3.32
d	Energy circulation Wh (b+c-a)	0.53	0	1.34
	Braking			
e	Total energy generated braking Wh	1.73	1.73	1.73
f	Total energy absorbed by SC Wh	1.06	1.73	3.07
g	Total energy absorbed Battery Wh	1.20	0	0
h	Energy circulation Wh (f+g-e)	0.53	0	1.34
	Energy balance			
i	Total energy motoring HESS Wh (b+c)	11.93	11.4	12.74
j	Total energy recovered HESS (f+g)	2.26	1.73	3.07
	Net energy Wh (i-j)	9.67	9.67	9.67
	Net energy demand Wh (a-e)	9.67	9.67	9.67
	Efficiency			
k	Energy efficiency motoring (%) (a/i*100)	95.5%	100%	89.48%
l	Energy efficiency braking (%) (e/j*100)	76.5%	100%	56.35%
	System efficiency (%) (K*L)	73.05%	100%	50.42%

5.7.1 Energy distribution without energy management system

The SC is commanded to follow the current reference obtained as the difference between the current demand and a low pass filter. The total energy available for recovery is absorbed mostly by the battery (1.20 Wh, 70%), while the SC effectively absorbs 30% (0.53 Wh). The total energy provided by the SC during motoring is 3.46 Wh and the total energy recovered is 1.06 Wh, which includes 0.53 Wh from braking and 0.53 Wh from energy circulation. As the energy recovered is lower than the energy provided, the SC voltage drops from 10.2V to 9.18 V. During the motoring stage, the SC relieves the battery by providing 29% (3.32 Wh) of the total energy demand (effective contribution). The main issue with this approach is the sub-utilisation of the SC during the braking stage and the energy circulation that naturally occurs as a consequence of the filter dynamics. The efficiency of the motoring stage

is 95.5% and the efficiency of the braking stage is 76.5%. The overall energy efficiency with this strategy is 73.5%. Calculation are presented in Table 5.9. The experimental data depicting the current contribution of the HESS and the SC voltage is shown in Fig.5.26. The shaded areas show energy circulation and the amount of energy recovered by the SC. It is important to note that the battery and SC recover energy.

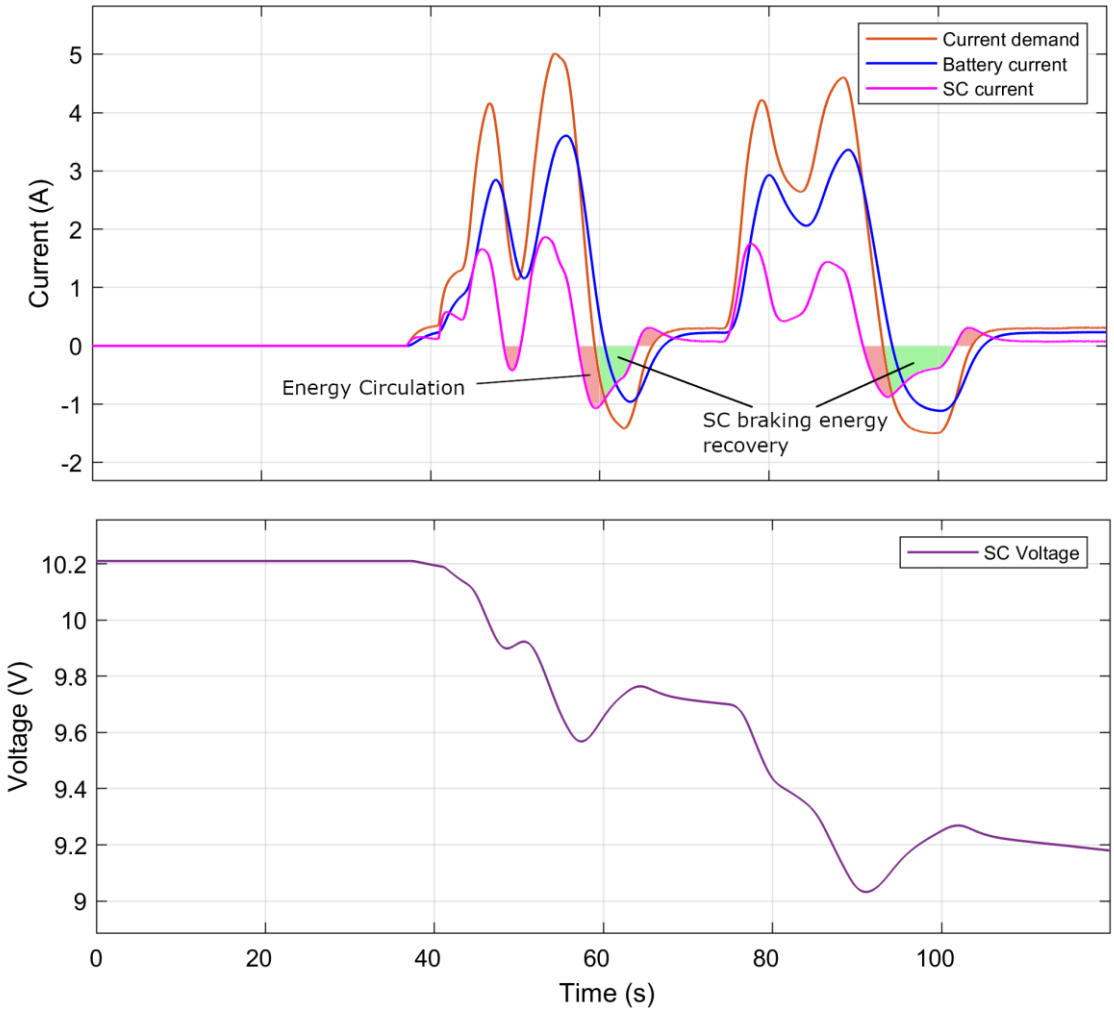

Fig. 5.26. HESS current distribution and SC voltage without EMS

5.7.2 Energy distribution with the proposed energy management system and no charging strategy

With the proposed method and no charging strategy, the SC recovers the braking energy generated (1.73 Wh). The battery is relieved from braking energy. For the motoring stage,

the battery and SC provides the required 11.4 Wh (battery 8.08 Wh and SC 3.32 Wh), so no excess energy is circulating in the system. The initial SC voltage is 10.2 V and the final voltage is 9.53. As energy is not circulating in the system, the efficiency is 100% (considering a lossless DC/DC converter and neglecting parasitic losses). Compared to the previous strategy, the final SC voltage is higher at 9.53V (vs 9.18V). This result shows that the proposed EMS is superior as it improves the energy efficiency in terms of energy distribution and ends the cycle with higher SC voltage. As the charge strategy is disabled, there is no energy circulation in the system, improving the overall energy efficiency. In other words, the same cycle is performed using less energy. The current distribution is shown in Fig. 5.27.

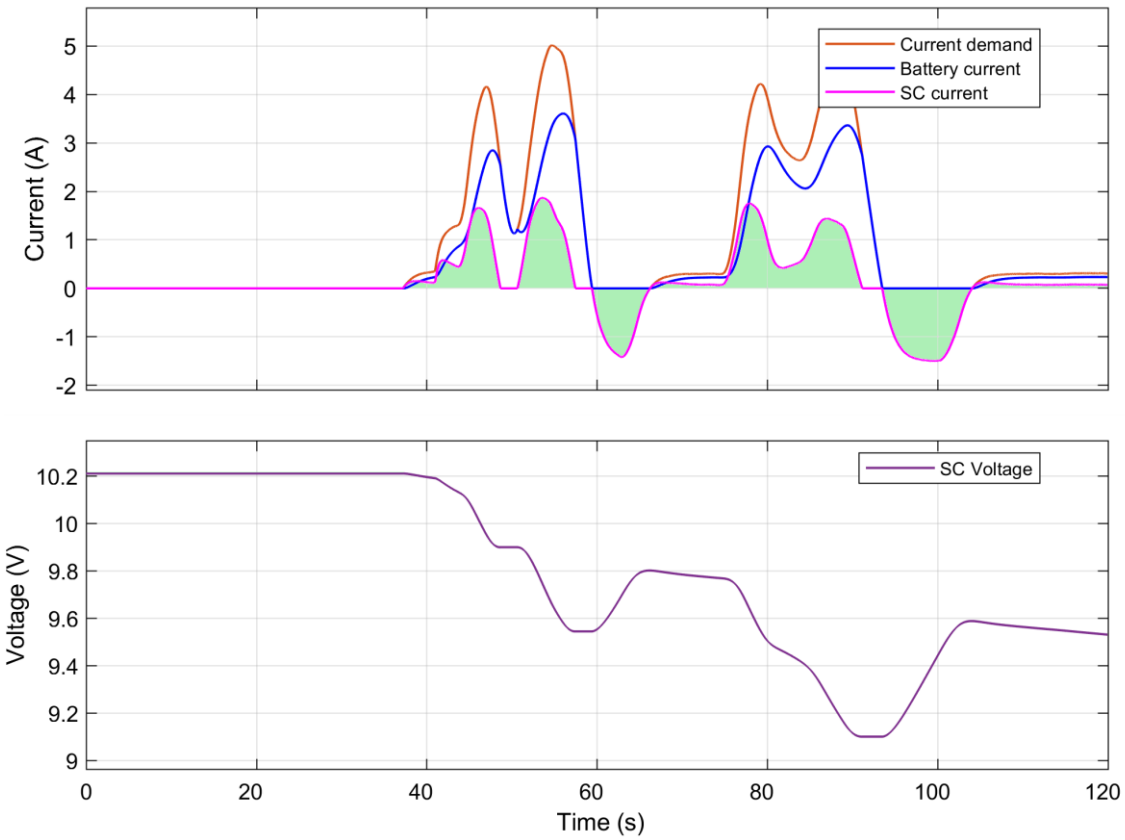

Fig. 5.27. Current distribution and SC voltage with the proposed EMS and no charge strategy

5.7.3 Energy distribution with the proposed energy management system and charging strategy

With the proposed EMS, energy circulation during the motoring stage is eliminated and is allowed only during the braking stage. The results of the experiment are presented in Table 5.8 and the current distribution in Fig. 5.28. The SC assists the battery by contributing 29% (3.32 Wh) of the total energy demand and recovers the braking energy (1.73 Wh). In addition to the braking energy, a total of 1.34 Wh are transferred from the battery to the SC to raise the voltage above 10 V. The charging strategy adds an additional 1.5 A to the braking current when two conditions are met: the current demand must be less or equal to zero, and the SC voltage should be less than 10 V. The SC voltage is not maintained above 10 V at all times as the charging strategy allows energy circulation only when braking and not during motoring. In this way, the battery is relieved from peak power that may occur when the SC voltage is low and the power demand is high during the motoring stage (charging may occur at peak time). The lowest SC voltage during the experiment is 9.34V at time t=92 seconds and the final SC voltage is 10.1 V. In terms of efficiency, the system is 56.8% as shown in Table 5.9. The lower energy efficiency is caused by the higher energy circulating in the system to maintain the SC voltage above 10V. Although the efficiency is lower due to energy circulation, the battery is completely relived from peak power during motoring and braking, energy circulation is controlled, and the objective to keep the SC charged is met.

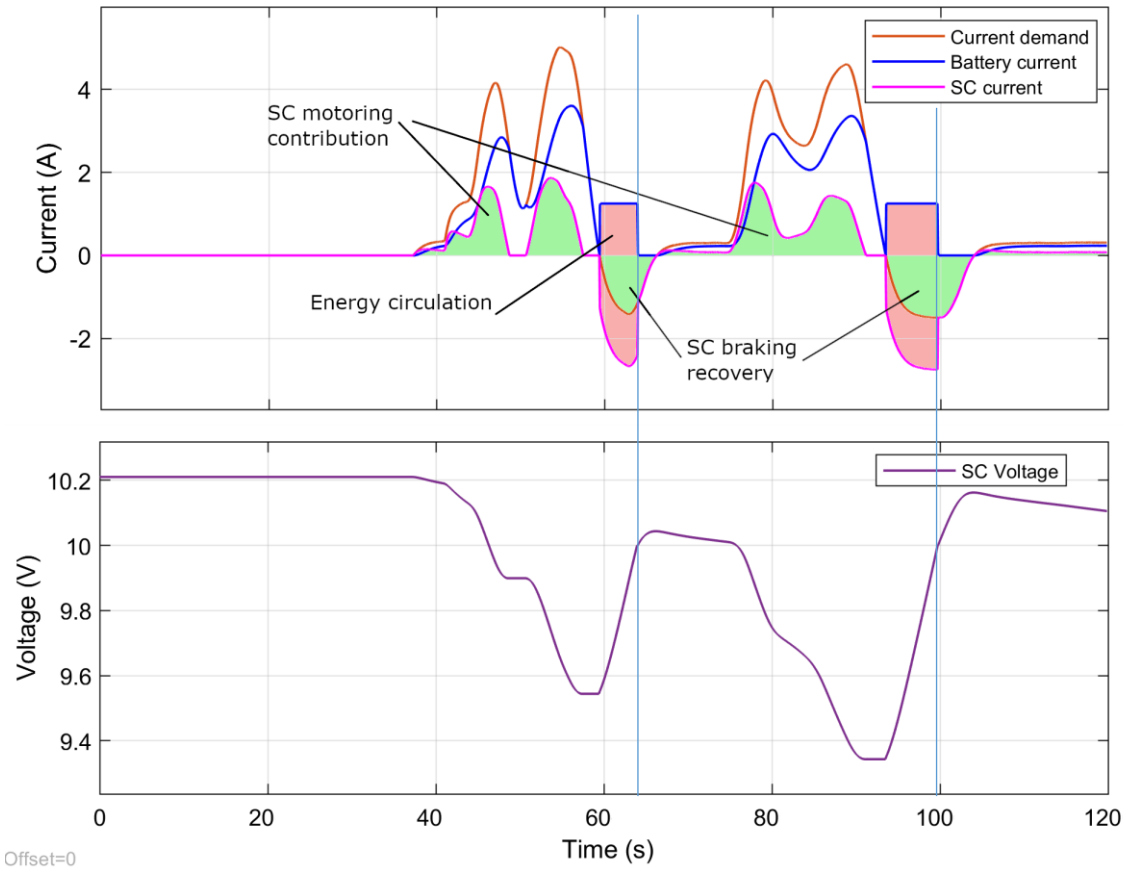

Fig. 5.28. HESS current distribution and SC voltage with EMS and charging strategy

The proposed EMS performance is assessed by repeating the cycle 6 times for a total of 800 seconds. This is performed twice with different SC voltage starting points. The first experiment starts with the SC voltage at 10.2 V as shown in Fig. 5.29. The SC voltage is boosted by the charging strategy without imposing extra stress on the battery, especially during peak power demand as the SC is not recharged when the current demand is positive. For this reason, it is observed that the voltage drops below 10V in several occasions, however, it is boosted by braking energy and energy circulating from the battery. As result, the SC voltage is maintained within operational levels (>7.12V) at all times.

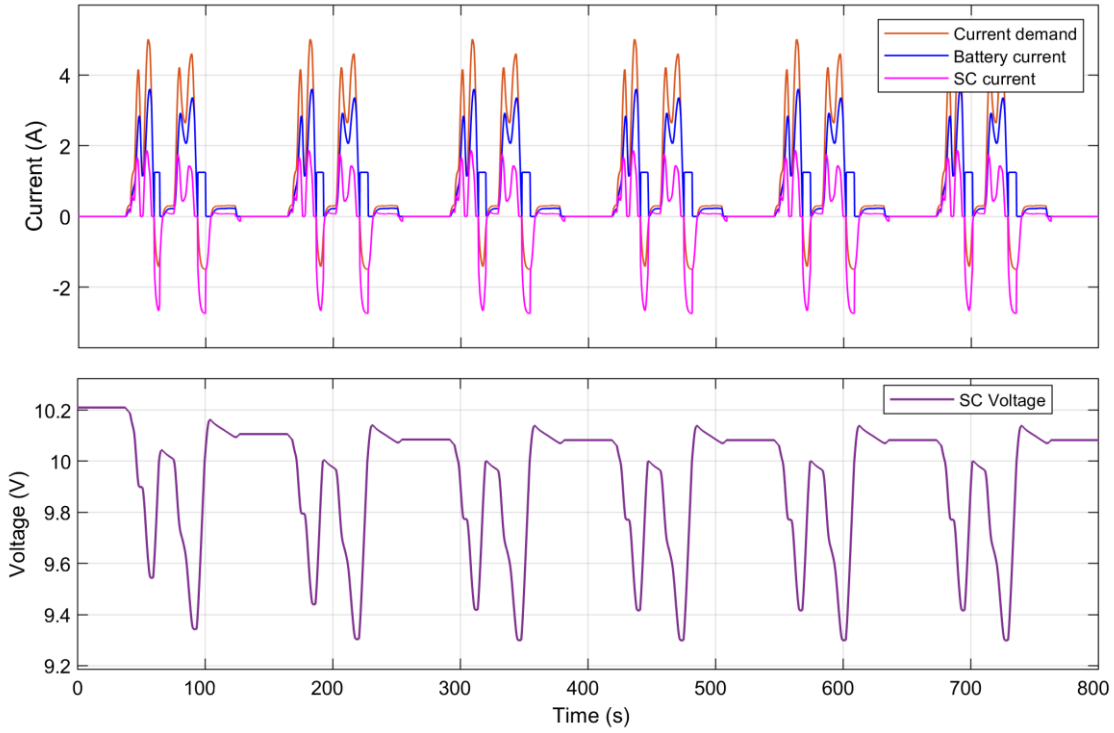

Fig. 5.29 Assessment of the proposed EMS with a repetitive current demand cycle. SC voltage starting point of 10.2V

The second experiment starts with the SC voltage at 9 V as shown in Fig 5.30. As the SC voltage is lower than the 10V threshold, the charging strategy recharges the SC from the beginning of the cycle. The battery transfers a constant 1.5 A to the SC until 10V are reached. The current demand cycle is repeated for a total duration of 800 seconds, showing that the SC voltage is maintained within operational levels (above 50% SOC or 7.12V) at all times.

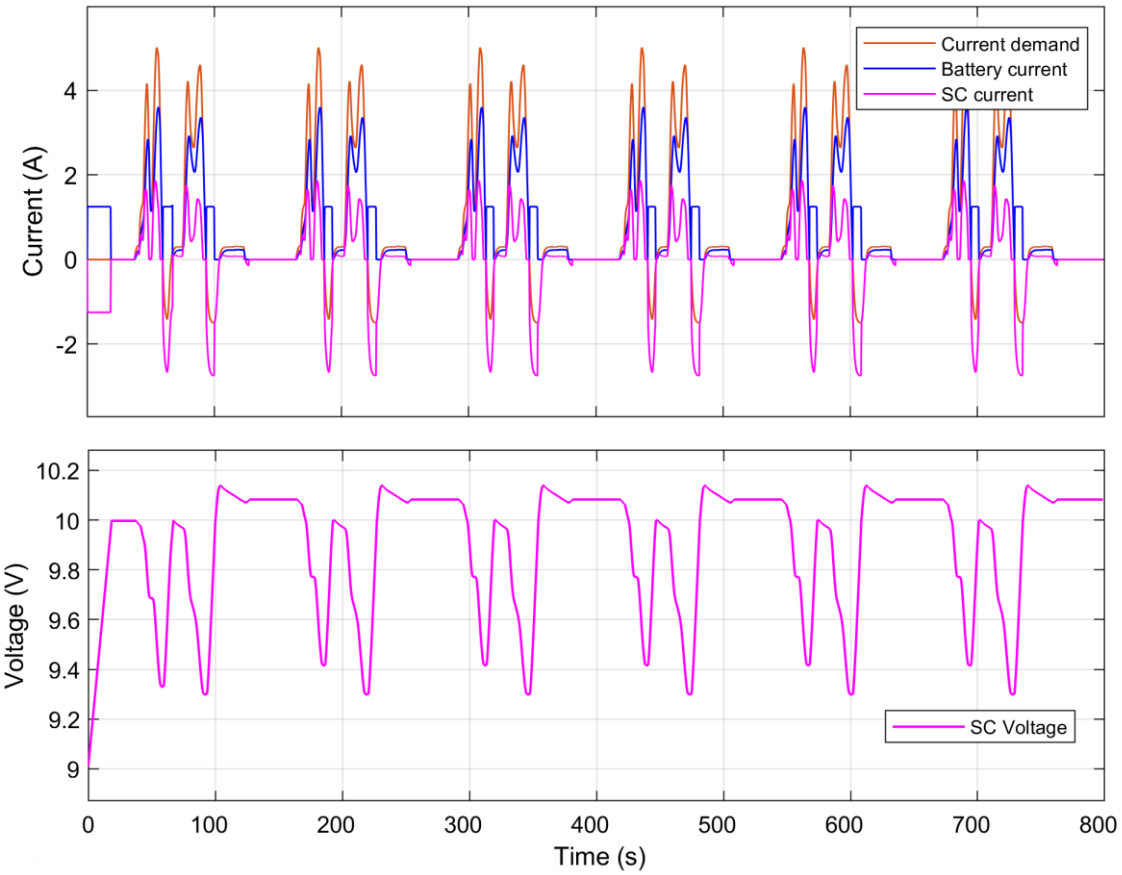

Fig. 5.30 Assessment of the proposed EMS with a repetitive current demand cycle. SC voltage starting point of 9V

The energy efficiency calculation for these two cases is presented in Table. 5.10. The energy efficiency obtained with the two scenarios described before, show that efficiency is affected by energy circulation. However, as energy circulation is necessary to maintain the SC voltage within operational level, it must be controlled to improve the system efficiency. When the starting voltage of the SC is 9V, more energy is necessary to recharge it, therefore the energy efficiency is lower at 39.9%. When the SC starts at 10.2V, the efficiency is 47.2%, as less energy is circulating.

Table 5.10. Energy efficiency calculations for repetitive driving cycle (800 sec) for different SC voltage starting points

	Motoring	**With SC starting at 10.2V**	**With SC starting at 9 V**
a	Total energy demand Wh	69.08	69.08
b	Total battery Energy supplied Wh	58.22	61.01
c	Total SC energy supplied Wh	20.06	20.05
d	Energy circulation Wh (b+c-a)	9.2	11.98
	Braking		
e	Total energy generated braking Wh	10.56	10.56
f	Total energy absorbed by SC Wh	19.76	22.54
g	Total energy absorbed Battery Wh	0	0
h	Energy circulation Wh (f+g-e)	9.2	11.98
	Energy balance		
i	Total energy motoring HESS Wh (b+c)	78.28	81.06
j	Total energy recovered HESS (f+g)	19.76	22.54
	Net energy Wh (i-j)	58.52	58.52
	Net energy demand Wh (a-e)	58.52	58.52
	Efficiency		
k	Energy efficiency motoring (%) (a/i*100)	88.2%	85.2%
l	Energy efficiency braking (%) (e/j*100)	53.4%	46.9%
	System efficiency (%) (K*L)	47.2%	39.9%

CHAPTER

6

6 CONCLUSIONS AND FURTHER WORK

In this chapter a summary of the research conducted, its outcome and further work is presented.

6.1. Addressed thesis objectives

Considering the purpose of hybridisation and the specific role of the EMS to control the function of the SC as part of the HESS, the following research questions motivating this thesis have been addressed:

1. Developed understanding of the effects of the time delay in power distribution and the system's energy efficiency when the real time EMS is based on frequency sharing techniques including the DWT and conventional filters. Commanding the SC with a delayed current reference produces unnecessary energy circulation in the system which increases the system losses. The SC fails to meet the objective of hybridisation: To relieve the battery from peak power during the motoring and braking stages.
2. Time delay compensation with prediction has been proposed in the literature to solve the delay problem. Replication of such work showed that some improvements are achieved, but the SC still fails to relieve the battery from peak power during motoring and braking. The system's performance is marginally improved so the author feels the complexity of the approach outweighs the benefits.
3. The assessment of the SC performance with EMS based on different frequency sharing techniques was achieved by developing an algorithm to generate a

benchmark reference signal. The algorithm involved calculating the first derivative of the positive current demand to define time windows that correspond to positive current demand changes. This signal defined the areas where SC assistance would be most beneficial. These areas are used to quantify the SC assistance during motoring, acceleration, braking and total energy circulation for different EMS strategies.

4. The DWT is a powerful method for decomposing signals into frequency components. However, it has limitations when applied in real time. The results obtained in this research show that an EMS based on conventional filters is superior to an EMS based on DWT. Conventional filters are easy to design and implement in real time. With the DWT it is difficult to get specific frequency sub-bands unless sampling frequency is changed. This is a consequence of the dyadic decomposition of the signal with the filter bank.
5. Energy circulation is necessary to maintain the SC charge availability during the whole battery discharge cycle. Previous methodologies based on filtration techniques used the output of the filters as the references to control power flow. However, this signal generated uncontrolled energy circulation between the battery and SC, increasing the system's energy losses. Rapid changes in the signal are processed by the filter, producing changes in the slope of the filtered signal. In many cases, this results in the SC being commanded to recharge when no braking is being generated, forcing the battery to meet the demand. With the proposed methodology, the occurrence of the energy circulation is effectively controlled, keeping the SC within its operational limits with a fraction of the energy circulation achieved with traditional methodologies.
6. By controlling the occurrence of energy circulation, the efficiency of the system has been improved. At the same time, the SC performance has been significantly

enhanced with the proposed EMS strategy, considering that it discharges when the battery needs it the most and recovers all the braking energy available. The proposed EMS truly relieves the battery from stress.

7. The ability of the SC to charge and discharge at high rates complements the battery high energy, equipping the HESS with both energy and power capabilities. Comparing a HESS against an oversized battery shows that significant performance improvements can be achieved with both options. However, with the current market prices and the small size of high energy batteries compared to high capacitance SC, an oversized battery might still be easier to implement and relatively cheaper to build.
8. Complementing the battery with a SC managed with an effective EMS, relieves the former from peak power during motoring and braking. As a consequence, the battery charge and discharge C-rate is reduced. This reduction in the current rate reduces the temperature, which is one of the main factors affecting the battery cycle life. However, it is important to emphasise the role of the EMS in achieving this objective, as a poor design approach would prevent the HESS to achieve its full potential.
9. By relieving the battery from peak power during motoring and braking, it is expected that the temperature of the battery will lower. As temperature is one of the main factors affecting battery lifetime, the proposed EMS would improve the battery cycle life. However, the detailed analysis of battery lifetime improvements is not within the scope of this work.

Results show that obtaining the SC current reference as the difference between the real time current demand and the DWT low frequency component (strategy C) improves the SC assistance during motoring and braking when compared to the prediction based method in all driving conditions. Prediction proves to compensate for the delay and

reduce energy circulation but it does not improve the SC performance. With aggressive driving cycles such as the US06 and Artemis motorway, the best results are obtained with a current reference calculated as the difference between the real time current demand and the predicted DWT low frequency component (strategy D). Real time implementation is, however, more difficult. The overall efficiency results, which include energy efficiency and SC perfromance shows that strategy C outperforms the other strategies, therefore, strategy C is recommended as the best control strategy in terms of SC performance and overall efficiency as it enables a DWT based EMS with 4 second delay frequency components to perform in real time.

6.2. Research contributions

The literature review showed the wealth of research studying the implementation of SCs as part of a HESS, and multiple approaches to design and implement the EMSs to determine the current references to control the power sources. After carrying out a comprehensive review of the literature related to the design of EMSs based on frequency sharing techniques, a clear gap in knowledge was identified: The effective SC contribution in the HESS has never been used as a metric to validate the performance of the EMS. This led to a thorough investigation of the effective SC contribution with filtration approaches, with and without time delay compensation, and the effects of delay on the system's efficiency, which constitutes the main contribution of this thesis.

This work presents a fresh perspective to this research field by introducing an effective approach to improve the SC contribution in the HESS while reducing energy losses in a semi-active control topology managed with frequency sharing techniques. The real time implementation of the EMS to operate a HESS powering the test platform developed for this purpose, has shown the applicability of the approach and provided reassurance that the EMS excels at splitting power in real time.

6.3. Final remarks

An efficient EMS for HESS has been proposed. The main merits of the proposed EMS are its simplicity and effectiveness in dealing with filter phase shift and time delays so that unnecessary energy circulation between the battery and SC is eliminated. The proposed method has been tested with different filtration techniques including a first-order filter and a DWT-based filtration strategy with and without time delay compensation. Results show that different filtration techniques can be implemented with the proposed EMS method as it allows the SC to assist the battery during positive power demand (acceleration) and completely relieve the battery from negative power demand (braking) independently of the filtration technique and its associated delay or/phase shift.

As the generated braking power is often not enough to maintain the SC charge, the proposed charging strategy has been shown to be effective in maintaining the SC availability throughout the battery discharge cycle, avoiding SC downtime. As the SC effectively reduces the battery burden during motoring and recovers all the generated braking power, the battery life can be prolonged.

A comparison of the proposed EMS method against EMS strategies where the high-frequency component of the current demand is allocated to the SC directly, show that the best results are obtained when the proposed method is used along with a first-order low pass filter. Although the fixed cutoff frequency of 125 mHz works well for the US06 driving cycle, it doesn't do the same for the FTP72 driving cycle resulting in the SC being underutilised. Literature suggests changing the cut-off dynamically as a function of the driving cycle. However, a simpler and more efficient way would be to vary the filter gain while keeping the cut-off frequency fixed.

Suggestions for further work include researching the difference between varying the cut-off frequency of the filter against varying the gain of the filter. An effective method to vary the cut-off frequency or the filter gain adaptively remains a challenge. The SC can

be replaced by other high power sources such as batteries designed for high power applications. In this specific case, high power batteries should exhibit high charge (>4C-rate) and discharge (>4C-rate) capability. Although these batteries are able to discharge at high rates, their charging rate is still inferior compared with SCs. Using these batteries as the high power source would require some modifications of the charging strategy including the limitation of the maximum currents the battery can receive and the allocation of excess recovered energy between the energy and power batteries. A thorough comparison between a HESS including a SC pack and a HESS with a high power battery is missing in the literature, especially in terms of weight and volume.

Temperature analysis of the battery with and without the proposed EMS would help in the determination of battery cycle life improvements.

Management of the SC self-discharge has not been included in the present work. Further investigation is required to assess the effects of the SC self-discharge, especially when the HESS is in idle state for prolonged periods of time. In this scenario, would a high power battery provide better performance?

A cost and performance comparison between an oversized battery and a HESS requires further considerations as it is not available in recent literature.

References

[1] Wikipedia, “Lithium-ion battery,” Wikipedia, the Free Encyclopedia, 13 November 2022. [Online]. Available: https://en.wikipedia.org/wiki/Lithium-ion_battery. [Accessed 14 November 2022].

[2] Y. Chen, Y. Kang, Y. Zhao , L. Wnag, J. Liu, Y. Li, Z. Liang, X. He, X. Li, N. Tavajohi and B. Li, “A review of lithium-ion battery safety concerns: The issues, strategies, and testing standards,” *Journal of Energy Chemistry,* vol. 59, pp. 83-99, 2021. https://doi.org/10.1016/j.jechem.2020.10.017.

[3] International Energy Agency, “Global Electric Vehicle Outlook 2022,” IEA, 2022.

[4] BloombergNEF, “Electric vehicle outlook 2022,” BloombergNEF, 2022.

[5] J. Wiklund, “Electric Vehicles expected to comprise 31% of the global fleet by 2050,” Global Fleet Management, Bobit, 12 January 2022. [Online]. Available: https://www.globalfleetmanagement.com/10159371/electric-vehicles-expected-to-comprise-31-of-the-global-fleet-by-2050. [Accessed 2022 11 14].

[6] The Faraday Institution, “High-energy battery technologies,” 2020.

[7] J. Deng, C. Bae, A. Denlinger and T. Miller, “Electric vehicles batteries: Requirements and Challenges,” *Joule,* pp. 509-515, 18 March 2020. doi:https://doi.org/10.1016/j.joule.2020.01.013.

[8] M. Shuai, M. Jiang, P. Tao, C. Song, J. Wu, J. Wang and T. Deng, “Temperature effect and thermal impact in lithium-ion batteries: A review,” *Progress in Natural Science: Materials International,* vol. 28, 2018. doi:https://doi.org/10.1016/j.pnsc.2018.11.002.

[9] L. Kraft, T. Zund, D. Schreiner, R. Wilhelm, F. Gunter, G. Reinhart, H. Gasteiger and A. Jossen, “Comparative evaluation of LMR-NCM and NCA cathode active materials in multilayer lithium-ion pouch cells: Part II. Rate capability, long-term stability, and thermal behaviour,” *Journal of The Electrochemical Society,* vol. 168, 2021. doi:https://doi.org/10.1149/1945-7111/abe50c.

[10] R. Abdelhedi, A. C. Ammari, A. Lahyani, A. Sari and P. Venet, “Optimal power sharing between batteries and supercapacitors in electric vehicles,” in *7th International Conference on Sciences of Electronics, Technologies of Information and Telecommunications (SETIT),* 2016. https://doi.org/10.1109/SETIT.2016.7939849.

[11] S. Chen , F. Dai and M. Cai , “Opportunities and challenges of high-energy lithium metal batteries for electric vehicle applications,” *ACS Energy Letters,* vol. 5, pp. 3140-3151, 2020. doi:https://doi.org/10.1021/acsenergylett.0c01545.

[12] X. Liu, K. Li and X. Li, “The Electrochemical Performance and Applications of Several Popular Lithium-ion Batteries for Electric Vehicles - A Review,” in *Communications in Computer and Information Science (CCIS),* 2018. doi:DOI: 10.1007/978-981-13-2381-2_19.

[13] Z. Ahsan, B. Ding, Z. Cai, C. Wen, W. Yang, Y. Ma and S. Zhang, “Recent progress in capacity enhancement of LiFePo4 cathode for Li-Ion batteries,” *Journal of Electrochemical Energy Conversion and Storage,* 2020. doi:http://dx.doi.org/10.1115/1.4047222.

[14] A. Chakraborty, S. Kunnikuruvan, S. Kumar, B. Markovsky, D. Aurbach, M. Dixit and D. T. Major, “Layered cathode materials for lithium-ion batteries: Review of computational studies on LiNi(1-x-y)Co(x)Mn(y)O(2) and LiNi(1-x-y)Co(x)Al(y)O(2),” *Chemistry of Materials,* 2020. doi:https://doi.org/10.1021/acs.chemmater.9b04066.

[15] German Federal Ministry for the Environment, Nature Conservation and Nuclear Safety (BMU), “Status quo analysis of various segments of electric mobility and low carbon passenger road transport in India,” Deutsche Gesellschaft fur Internationale Zusammenarbeit (GIZ) GmbH, 2021.

[16] Wikipedia, “Lithium nickel manganese cobalt oxides,” 12 11 2022. [Online]. Available: https://en.wikipedia.org/wiki/Lithium_nickel_manganese_cobalt_oxides. [Accessed 12 1 2022].

[17] Adamas Intelligence, “State of charge: EVs, batteries and battery materials,” Adamas Intelligence, 2022.

[18] M. Kane, “Analysis: Tesla Model 3 Charges Faster At CCS2 Than Supercharger,” InsideEvs, 17 May 2021. [Online]. Available: https://insideevs.com/news/507489/tesla-model3-charging-faster-ccs2/. [Accessed 20 11 2022].

[19] R. Tian, S.-H. Park, P. King, G. Cunningham, J. Coelho, V. Nocolosi and J. Coleman, “Quantifying the factors limiting rate performance in battery electrodes,” *Nature Communications,* vol. 10, 2019. doi:https://www.nature.com/articles/s41467-019-09792-9.

[20] C. Heubner, M. Schneider and A. Michaelis, “Diffusion-Limited C-rate: A fundamental principle quantifying the intrinsic limits of li-ion batteries,” *Advanced Energy Materials,* vol. 10, no. 2, 2019. doi:https://doi.org/10.1002/aenm.201902523.

[21] M. Lain, J. Brandon and E. Kendrick, “Design strategies for high power vs. high energy lithium ion cells,” *Batteries,* vol. 5, no. 4, p. 64, 2019. doi:https://doi.org/10.3390/batteries5040064.

[22] Wikipedia, “Electric battery,” 27 June 2022. [Online]. Available: https://en.wikipedia.org/wiki/Electric_battery. [Accessed 7 July 2022].

[23] S. Rezvanizaniani, Z. Liu, Y. Chen and J. Lee, “Review and recent advances in battery health monitoring and prognosis technologies for electric vehicle (EV) safety and mobility,” *Journal of Power Sources,* vol. 256, 2014. doi:http://dx.doi.org/10.1016/j.jpowsour.2014.01.085.

[24] S. Ma, M. Jiang, P. Tao, C. Song, J. Wu, J. Wang, T. Deng and W. Shang, “Temperature effect and thermal impact in lithium-ion batteries: A review,” *Progress in Natural Science: Materials International,* vol. 28, 2018.

[25] P. Keil and A. Jossen, “Aging of lithium-ion batteries in electric vehicles: Impact of regenerative braking,” *World Electric Vehicle Journal,* vol. 7, no. 1, 2015. doi:https://doi.org/10.3390/wevj7010041.

[26] A. Tomaszewska, Z. Chu, X. Feng, S. O'Kane, X. Liu, J. Chen, C. Ji, E. Endler, R. Li, L. Liu, Y. Li and B. Wu, “Lithium-ion battery fast charging: A review,” *eTransportation,* vol. 1, 2019. doi:https://doi.org/10.1016/j.etran.2019.100011.

[27] T. Bryden, A. Holland, G. Hilton, B. Dimitrov, C. Albarran and A. Cruden, “Lithium-ion degradation at varying discharge rates,” in *3rd Annual Conference in Energy Storage and its Applications*, 2018. doi:https://doi.org/10.1016/j.egypro.2018.09.047.

[28] I. Buchmann, “BU-205: Types of Lithium-ion,” Battery University, 22 October 2021. [Online]. Available: https://batteryuniversity.com/article/bu-205-types-of-lithium-ion. [Accessed 14 November 2022].

[29] M. Al Sakka, H. Gualous, N. Omar and V. Joeri, “Batteries and supercapacitors for electric vehicles,” in *New Generation of Electric Vehicles*, Intech, 2012. DOI: 10.5772/53490

[30] S. S. Williamson, Energy management strategies for electric and plug-in hybrid electric vehicles, Springer, 2013.

[31] S. Mothilal Bhagavathy, H. Budnitz, T. Schwanen and M. McCulloch, “Impact of charging rates on electric vehicle battery life,” *Findings,* vol. March, 2021. doi:https://doi.org/10.32866/001c.21459.

[32] Q. Zhang, W. Deng, S. Zhang and J. Wu, “A rule based energy management system of experimental battery/supercapacitor hybrid energy storage system for electric vehicles,” *Journal of Control Science and Engineering,* vol. 2016, 2016. doi:https://doi.org/10.1155/2016/6828269.

[33] W. Zhuo , R. Li, C. Zhuo, Y. Li, J. Xia and J. Liu, “Battery-supercapacitor hybrid devices: Recent progress and future prospects,” *Advanced Science,* vol. 4, no. 7, p. 1600539, 2017. doi:https://doi.org/10.1002/advs.201600539.

[34] M. Horn, J. MacLeod, M. Liu and J. Webb, “Supercapacitors: A new source of power for electric cars?,” *Economic Analysis and Policy,* vol. 61, pp. 93-103, 2019. doi:https://doi.org/10.1016/j.eap.2018.08.003.

[35] A. Grama, T. Patarau, R. Etz and D. Petreus, “Simulink test bench for a hybrid battery-supercapacitor power system,” in *International Symposium for Design and Technology in Electronic Packaging*, 2014. doi:https://doi.org/10.1109/SIITME.2014.6967016.

[36] H. Kim and S. Jung, “Battery hybridization for achieving both high power and high energy densities,” *International Journal of Energy Research*, 2018. doi:https://doi.org/10.1002/er.4178.

[37] R. Wegmann, V. Doge and D. U. Sauer, “Assessing the potential of a hybrid battery system to reduce battery ageing in an electric vehicle by studying the cycle life of a graphite¦NCA high energy and a LTO¦metal oxide high power battery cell considering realistic test profiles,” *Applied Energy,* vol. 226, pp. 197-212, 2018. doi:https://doi.org/10.1016/j.apenergy.2018.05.104.

[38] A. Dutta, S. Mitra, M. Basak and T. Banerjee, “A comprehensive review on batteries and supercapacitors: Development and challenges since their inception,” *Energy Storage,* vol. e339, 2022. doi:https://doi.org/10.1002/est2.339.

[39] Eaton, “The major differences between supercapacitors and batteries,” 2022. [Online]. Available: https://www.eaton.com/content/dam/eaton/products/electronic-components/resources/brochure/eaton-supercapacitor-vs-batteries-white-paper-elx1150-en.pdf. [Accessed 14 November 2022].

[40] A. Mansour, C. M. Hedi and B. Faouzi, “Experimental study of a pack of supercapacitors used in electric vehicles,” *The Scientific World Journal,* vol. 2017, 2017. doi:https://doi.org/10.1155/2017/6702838.

[41] Wikipedia, “Supercapacitor,” 3 12 2022. [Online]. Available: https://en.wikipedia.org/wiki/Supercapacitor. [Accessed 5 12 2022].

[42] H. Razaei, S. Abdollahi, S. Abdollahi and S. Filizadeh, “Energy management strategies of battery-ultracapacitor hybrid storage systems for electric vehicles: Review, challenges, and future trends,” *Journal of Energy Storage,* vol. 53, 2022. doi:https://doi.org/10.1016/j.est.2022.105045.

[43] Y. Li and X. Jiao, “Energy management strategy for hybrid electric vehicles based on adaptive equivalent consumption minimization strategy and mode switching with variable thresholds,” *Science Progress,* vol. 103, no. 1, 2020. doi:https://doi.org/10.1177/0036850419874992.

[44] X. Luo, J. Barreras, C. Chambon, B. Wu and E. Batzelis, “Hybridizing lead-acid batteries with supercapacitors: A methodology,” *Energies,* vol. 14, no. 2, p. 507, 2021. doi:https://doi.org/10.3390/en14020507.

[45] O. Salari, K. H. Zaad, A. Bakhshai and P. Jain, “Filter design for energy management control of hybrid energy storage systems in electric vehicles,” in *9th IEEE International Symposium on Power Electronics for Distributed Generation Systems (PEDG),* Charlotte, 2018. doi:https://doi.org/10.1109/PEDG.2018.8447608.

[46] G. Cui, L. Jia and Z. Su, “SMES-Battery hybrid energy storage system integrated railway power conditioner for peak load shifting and power quality improvement in high-speed electrical railway,” in *International Conference on Electrical Machines and Systems*, 2021. doi:https://doi.org/10.23919/ICEMS52562.2021.9634287.

[47] S. Hussain, M. Ali, G.-S. Park, S. H. Nengroo, M. Khan and H.-J. Kim, “A real-time bi-adaptive controller-based energy management system for battery-supercapacitor hybrid electric vehicles,” *Energies,* vol. 12, 2019. doi:https://doi.org/10.3390/en12244662.

[48] S. Dusmez and A. Khaligh, “Wavelet-transform based energy and power decoupling strategy for a novel ultracapacitor-battery hybrid power split gear powertrain,” in *IEEE Transportation Electrification Conference and Expo (ITEC),* Detroit, 2013. doi:https://doi.org/10.1109/ITEC.2013.6573475.

[49] M. Ibrahim, J. Jemei, G. Wimmer and D. Hissel, “Nonlinear autoregressive neural network in an energy management strategy for battery/ultracapacitor hybrid electrical vehicles,” *Electric Power Systems Research,* vol. 136, pp. 262-269, 2016. doi:https://doi.org/10.1016/j.epsr.2016.03.005.

[50] J. Peng, R. Wang, L. Hongtao, Y. Zhou, H. Li, Y. Wu and Z. Huang, “A real-time layer-adaptive wavelet transform energy distribution strategy in a hybrid energy storage system of EVs,” *Energies,* vol. 12, no. 3, p. 440, 2019. doi:http://dx.doi.org/10.3390/en12030440.

[51] T. Zimmermann, P. Keil, M. Hofmann, M. Horsche, S. Pichlmaier and A. Jossen, “Review of system topologies for hybrid electrical energy storage systems,” *Journal of Energy Storage,* vol. 8, pp. 78-90, 2016. doi:https://doi.org/10.1016/j.est.2016.09.006.

[52] R. Sankarkumar and R. Natarajan, “Energy management techniques and topologies suitable for hybrid energy storage powered electric vehicles: An overview,” *International Transactions on Electrical Energy Systems,* vol. 31, no. 4, 2021. doi:DOI: 10.1002/2050-7038.12819.

[53] T. Babu, K. Vasudevan, V. Ramachandaramurthy, S. Sani, S. Chemud and R. Lajim, “A comprehensive review of hybrid energy storage systems: converter topologies, control strategies and future prospects,” *IEEE Access,* vol. 8. doi:https://doi.org/10.1109/ACCESS.2020.3015919

[54] D. Lemian and F. Bode, “Battery-supercapacitor energy storage systems for electrical vehicles: A review,” *Energies,* vol. 15, 2022. doi:https://doi.org/10.3390/en15155683.

[55] J. Awerbuch and C. Sullivan, “Filter-based power splitting in ultracapacitor-battery hybrids for vehicular applications,” in IEEE 12th Workshop on Control and Modelling for Power Electronics (COMPEL), Boulder, 2010. doi:https://doi.org/10.1109/COMPEL.2010.5562429.

[56] A. Baciu, G. Livint and G. Asachi, “Wavelet transform and neural network based control strategy for hybrid energy system,” in *International Conference on Electromechanical and Power Systems,* 2017. doi:https://doi.org/10.1109/SIELMEN.2017.8123293.

[57] J. Wang, J. Zhou and D. Xu, “A real-time predictive energy management strategy of fuel cell/battery/ultra-capacitor hybrid energy storage system in electric vehicle,” in

IEEE 2020 Chinese Automation Congress, 2020. doi:https://doi.org/10.1109/CAC51589.2020.9327653.

[58] S.-H. Noh, "Analysis of gradient vanishing of RNNs and performance comparison," *Information*, vol. 12, 2021. doi:https://doi.org/10.3390/info12110442.

[59] F. Chollet and & others, "Keras," 2015. [Online]. Available: https://github.com/fchollet/keras. [Accessed 2022].

[60] B. Wang, C. Wang, G. Ma and L. Zhang, "Power-split strategy based on average power method for semi-active hybrid energy storage system in small electric vehicles," in *10th International Conference on Applied Energy*, Hong Kong, 2018. doi:https://doi.org/10.1016/j.egypro.2019.01.970.

[61] Y. Zhang, S. Yang, S. Zhou and F. Chen, "Wavelet transform algorithm application in hybrid power system optimization of electric vehicles," in *Journal of Physics: Conference Series*, 2019. doi:10.1088/1742-6596/1302/4/042054.

[62] S. Zhang and N. Pan, "Supercapacitors performance evaluation," *Advanced Energy Materials*, vol. 5, no. 6, 2015. doi:https://doi.org/10.1002/aenm.201401401.

[63] Q. Zhang , L. Wang, G. Li and Y. Liu, "A real-time energy management control strategy for battery and supercapacitor hybrid energy storage systems of pure electric vehicles," *Journal of Energy Storage*, vol. 31, 2020.

[64] L. Trahey, F. Brushett, N. Balsara, G. Ceder, L. Cheng, Y.-M. Chiang, N. Hahn, B. Ingram, S. Minteer, J. Moore, K. Mueller, L. Nazar, K. Persson, D. Siegel, K. Xu, K. Zavadil, V. Shinivasan and G. Crabtree, "Energy storage emerging: A perspective from the joint center for energy storage research," *Applied Physical Sciences*, vol. 117, no. 23, 2020. doi:https://doi.org/10.1073/pnas.1821672117.

[65] L. Zhang , X. Hu, Z. Wang, J. Ruan, C. Ma and Z. Song, "Hybrid electrochemical energy storage systems: An overview for smart grid and electrified vehicle applications," *Renewable and Sustainable Energy Reviews*, Article in Press. doi:DOI: 10.1016/j.rser.2020.110581.

[66] N. Vukajlovic, D. Milicevic, B. Dumnic and B. Popadic, "Comparative analysis of the supercapacitor influence on lithium battery cycle life in electric vehicle energy storage," *Journal of Energy Storage*, vol. 31, 2020. doi:https://doi.org/10.1016/j.est.2020.101603.

[67] U.S. Department of Energy, "Energy storage technology and cost characterization report," 2019.

[68] lygte-info, “Samsung INR21700-50E 5000mAh (Cyan),” [Online]. Available: https://lygte-info.dk/review/batteries2012/Samsung%20INR21700-50E%205000mAh%20(Cyan)%20UK.html. [Accessed 22 06 2022].

[69] Tremondi, “Kokam SLPB compact cells -technical data,” 2018. [Online]. Available: http://www.tremondi.cz/wp-content/uploads/2018/03/Kokam_115.00_data-1.pdf. [Accessed 1 07 2022].

[70] Maxwell technologies, “3.0V 3400F Ultracapacitor Cell BCAP3400 P3000 K04/05,” 2018. [Online]. Available: https://maxwell.com/wp-content/uploads/2021/08/3V_3400F_datasheet.pdf. [Accessed 22 June 2022].

[71] J. Liu, Z. Dong, T. Jin and L. Liu, “Recent advance of hybrid energy storage systems for electrified vehicles,” in *14th IEEE/ASME International Conference on Mechatronic and Embedded Systems and Applications,* 2018. doi:https://doi.org/10.1109/MESA.2018.8449191.

[72] I. Oukkacha, M. B. Camara and B. Dakyo, “Energy management in electric vehicle based on frequency sharing approach, using fuel cells, lithium batteries and supercapacitors,” in *7th International Conference on Renewable Energy Research and Applications,* Paris, 2018. doi:https://doi.org/10.1109/ICRERA.2018.8566991.

[73] Z. Fu, Z. Li, P. Si and F. Tao, “A hierarchical energy management strategy for fuel cell/battery/supercapacitor hybrid electric vehicles,” *International Journal of Hydrogen Energy,* vol. 44, pp. 22146-22159, 2019. doi:https://doi.org/10.1016/j.ijhydene.2019.06.158.

[74] L. Sun, K. Feng, C. Chapman and N. Zhang, “An adaptive power-split strategy for battery-supercapacitor powertrain. Design, simulation, and experiment,” *IEEE Transactions on Power Electronics,* vol. 32, no. 12, 2017. doi:https://doi.org/10.1109/TPEL.2017.2653842.

[75] M. Ibrahim, S. Jemei, G. Wimmer, N. Steiner, C. Kokonendji and D. Hissel, “Selection of mother wavelet and decomposition level for energy management in electric vehicles including a fuel cell,” *International Journal of Hydrogen Energy,* vol. 40, pp. 15823-15833, 2015. doi:https://doi.org/10.1016/j.ijhydene.2015.06.055.

[76] Q. Zhang and W. Deng, “An adaptive energy management system for electric vehicles based on driving cycle identification and wavelet transform,” *Energies,* vol. 9, no. 5, p. 341, 2016.

[77] R. Madan, S. Singh and N. Jain, “Signal filtering using discrete wavelet transform,” *International Journal of Recent Trends in Engineering,* vol. 2, no. 3, 2009.

[78] S. Mallat, “A theory for multiresolution signal decomposition: The wavelet representation,” *IEEE Transactions on Pattern Analysis and Machine Intelligence,* vol. 11, no. 7, 1989. doi:https://doi.org/10.1109/34.192463.

[79] C. Wang, R. Xiong, H. He, Y. Zhang and W. Shen, “Comparison of decomposition levels for wavelet transform based energy management in a plug-in hybrid electric vehicle,” *Journal of Cleaner Production,* vol. 210, pp. 1085-1097, 2019. doi:https://doi.org/10.1016/j.jclepro.2018.11.082.

[80] K. Lei and Z. Chen, “Energy management strategy based on adaptive wavelet analysis for HESS,” in *IEEE 3rd International Electrical and Energy conference*, Beijing, 2019. doi:https://doi.org/10.1109/CIEEC47146.2019.CIEEC-2019342.

[81] Mathworks, “Choose a Wavelet,” 2022. [Online]. Available: https://uk.mathworks.com/help/wavelet/gs/choose-a-wavelet.html. [Accessed 05 07 2022].

[82] Wikipedia. The free encyclopedia, “Haar Wavelet,” 2022 05 2022. [Online]. Available: https://en.wikipedia.org/wiki/Haar_wavelet. [Accessed 05 07 2022].

[83] M. Yan, M. Li, H. He, P. Jiankun and C. Sun, “Rule-based energy management for dual-source electric buses extracted by wavelet transform,” *Journal of Cleaner Production,* vol. 189, pp. 116-127, 2018. doi:https://doi.org/10.1016/j.jclepro.2018.04.054.

[84] Q. Li, W. Chen, Z. Liu, M. Li and L. Ma, “Development of energy management system based on a power sharing strategy for a fuel cell-battery-supercapacitor hybrid tramway,” *Journal of Power Sources,* vol. 279, pp. 267-280, 2015.

[85] S. Bourdim , T. Azib, K. Hemsas and C. Larouci, “Efficient energy management strategy for fuel cell ultracapacitor hybrid system,” in *International Conference of Electrical Systems for Aircraft, Railway, Ship Propulsion and Road Vehicles & International Transportation Electrification Conference*, Toulouse, 2017.

[86] Y. Ates, O. Erdinc, M. Uzunoglu and B. Vural, “Energy management of an FC/UC hybrid vehicular power system using a combined neural network-wavelet transform based strategy,” *International Journal of Hydrogen Energy,* vol. 35, pp. 774-783, 2010.

[87] C. Zheng, H. Lian, T. Chen, Z. Cai and D. Fang, “A wavelet transform based power allocation strategy for lithium battery and ultracapacitor hybrid vehicular power systems,” in *31st Youth Academic Annual Conference of Chinese Association of Automation,* Wuhan, 2016.

[88] J. Pan, J. Yan, Q. Tu and C. Jiang, “Fuzzy control and wavelet transform based energy management strategy design of a hybrid bulldozer,” *Journal of Intelligent & Fuzzy Systems,* vol. 29, pp. 2564-2574, 2015.

[89] X. Zhang, C. Mi, A. Masrur and D. Daniszewski, “Wavelet transform-based power management of hybrid vehicles with multiple on-board energy sources including fuel cell, battery and ultracapacitor,” *Journal of Power Sources,* vol. 185, pp. 1533-1543, 2008.

[90] O. Erdinc, B. Vural and M. Uzunoglu, “A wavelet-fuzzy logic based energy management strategy for a fuel cell/battery/ultra-capacitor hybrid vehicular power system,” *Journal or Power Sources,* vol. 194, pp. 369-380, 2009.

[91] J. Hu, D. Liu, C. Du, F. Yan and C. Lv, “Intelligent energy management strategy of hybrid energy storage system for electric vehicle based on driving pattern recognition,” *Energy,* vol. 198, 2020. doi:https://doi.org/10.1016/j.energy.2020.117298.

[92] Y. Shen, X. Yang, J. Sun and P. Liu, “Symlet wavelet transform based power management of hybrid energy storage system,” in *4th IEEE Conference on Energy Internet and Energy Systems Integration,* 2020. doi:https://doi.org/10.1109/EI250167.2020.9347173.

[93] K. Song, H. Chen, P. Wen, T. Zhang, B. Zhang and T. Zhang, “A comprehensive evaluation framework to evaluate energy management strategies of fuel cell electric vehicles,” *Electrochimica Acta,* vol. 292, pp. 960-973, 2018. doi:https://doi.org/10.1016/j.electacta.2018.09.166.

[94] A. Kumar and Mamta, “Comparison of different types of IRR filters,” *International journal of advanced research in electronics and communication engineering,* vol. 5, no. 2, 2016. doi:http://dx.doi.org/10.13140/RG.2.1.4856.3605.

[95] Mathworks, “FIR Filter design,” 2022. [Online]. Available: https://uk.mathworks.com/help/signal/ug/fir-filter-design.html. [Accessed 14 07 2022].

[96] W. Enang and C. Bannister, “Modelling and control of hybrid electric vehicles (A comprehensive review),” *Renewable and Sustainable Energy Reviews,* vol. 74, pp. 1210-1239, 2017. doi:https://doi.org/10.1016/j.rser.2017.01.075.

[97] L. Nie, J. Guan, C. Lu, H. Zheng and Z. Yin, “Longitudinal speed control of autonomous vehicle based on a self-adaptive PID of radial basis function neural

network," *IET Intelligent Transport Systems,* vol. 12, no. 6, pp. 495-494, 2018. doi:https://doi.org/10.1049/iet-its.2016.0293.

[98] E. Schaltz, "Electrical Vehicle Design and Modelling," in *Electric Vehicles - Modelling and Simulations*, InTech, Available from: https://www.intechopen.com/books/electric-vehicles-modelling-and-simulations/electrical-vehicle-design-and-modeling, 2011. doi:DOI: 10.5772/20271.

[99] Wikipedia, "Nissan EM motor," 10 10 2022. [Online]. Available: https://en.wikipedia.org/wiki/Nissan_EM_motor. [Accessed 16 11 2022].

[100] Wikipedia contributors, "Transaxle," Wikipedia, The Free Encyclopedia, 16 April 2022. [Online]. Available: https://en.wikipedia.org/w/index.php?title=Transaxle&oldid=1083056114. [Accessed 22 June 2022].

[101] Marklines. Automotive Industry Portal, "Nissan LEAF teardown: Comparison of the GEN1 and new EV electric units (with photos)," Marklines , 14 August 2019. [Online]. Available: https://www.marklines.com/en/report/rep1899_201907. [Accessed 22 June 2022].

[102] R. Morales-Caporal, M. Leal-Lopez, J. d. J. Rangel-Magdaleno, O. Sandre-Hernandez and I. Cruz-Vega, "Direct torque control of a PMSM-drive for electric vehicle applications," in *International conference on electronics, communications and computers (CONIELECOMP)*, Cholula, Mexico, 2018. DOI: 10.1109/MASCON51689.2021.9563576.

[103] Mathworks, "Motor and Drive (system level)," 2022. [Online]. Available: https://uk.mathworks.com/help/physmod/sps/ref/motordrivesystemlevel.html. [Accessed 22 June 2022].

[104] M. Ehsani, Y. Gao, S. Gay and A. Emadi, Modern Electric, Hybrid Electric, and Fuel cell vehicles, Boca Raton: CRC Press, 2004.

[105] N. Campagna, V. Castiglia, R. Miceli, R. Mastromauro, C. Spataro, M. Trapanese and F. Viola, "Battery modles for battery powered applications: A comparative study," *Energies,* 2020. doi:http://dx.doi.org/10.3390/en13164085.

[106] O. Tremblay and L. Dessaint, "Experimental validation of a battery dynamic model for EV applications," *World Electric Vehicle Journal,* vol. 3, no. 2, pp. 289-298, 2009. doi:https://doi.org/10.3390/wevj3020289.

[107] E. Database, “Electric vehicle database,” 2022. [Online]. Available: https://ev-database.uk/cheatsheet/useable-battery-capacity-electric-car. [Accessed 28 11 2022].

[108] Bharti, A. Kumar, G. Ahmed, M. Gupta, P. Bocchetta, R. Adalati, R. Chandra and Y. Kumar, “Theories and models of supercapacitors,” *Nano Express,* vol. 2, 2021. doi:https://doi.org/10.1088/2632-959X/abf8c2.

[109] H. Miniguano, A. Barrado, C. Fernandez, P. Zumel and A. Lazaro, “A general parameter identification procedure used for comparative study of Supercapacitor models,” *Energies,* vol. 12, no. 9, p. 1776, 2019. doi:https://doi.org/10.3390/en12091776.

[110] E. Gongadze, S. Petersen, U. Beck and U. Van Rienen, “Classical models of the interface between an electrode and an electrolyte,” Milan, 2009.

[111] R. Pericet-Camara, “Interaction forces between surfaces coated with highly branched polyelectrolytes,” *Thesis,* 2006.

[112] Mathworks, “Supercapacitor,” 2022. [Online]. Available: https://uk.mathworks.com/help/physmod/sps/powersys/ref/supercapacitor.html. [Accessed 22 June 2022].

[113] M. Makar, L. Pravica and M. Kutija, “Supercapacitor-based energy storage in elevators to improve energy efficiency of buildings,” *Applied Sciences,* vol. 12, 2022. doi:https://doi.org/10.3390/app12147184.

[114] D. Pollock, “Filters and Wavelets for Dyadic Analysis,” 2007. [Online]. Available: https://www.le.ac.uk/users/dsgp1/ERC14/Chapter7.pdf. [Accessed 22 June 2022].

[115] S. Mallat, A wavelet tour of signal processing. The sparse way, Burlington: Elsevier Inc, 2009. doi:https://doi.org/10.1016/B978-0-12-374370-1.X0001-8.

[116] C. Wang, R. Yang and Q. Yu, “Wavelet transform based energy management strategies for plug-in hybrid electric vehicles considering temperature uncertainty,” *Applied Energy,* vol. 256, p. 113928, 2019. doi:https://doi.org/10.1016/j.apenergy.2019.113928.

[117] M. Schneiders, Wavelets in control engineering. Master's thesis, Eindhoven University of Technology, 2001.

[118] A. Taspinar, “A guide for using the wavelet transform in machine learning,” 21 12 2018. [Online]. Available: https://ataspinar.com/2018/12/21/a-guide-for-using-the-wavelet-transform-in-machine-learning/. [Accessed 25 11 2022].

[119] Mathworks, “Two channel analysis sub-band filter,” 2022. [Online]. Available: https://uk.mathworks.com/help/dsp/ref/twochannelanalysissubbandfilter.html. [Accessed 22 June 2022].

[120] S. Siami-Namini, N. Tavakoli and A. Siami Namin, “A comparison of ARIMA and LSTM in forecasting time series,” in *17th IEEE International conference on machine learning and applications*, Orlando, 2018. doi:https://doi.org/10.1109/ICMLA.2018.00227.

[121] S. Venna, A. Tavanaei, R. Gottumukkala, V. Raghavan, A. Maida and S. Nichols, “A novel data driven model for real time influenza forecasting,” *IEEE Access*, vol. 7, pp. 7691-7701, 2018. doi:https://doi.org/10.1109/ACCESS.2018.2888585.

[122] Wikipedia, “Sigmoid function,” 19 11 2022. [Online]. Available: https://en.wikipedia.org/wiki/Sigmoid_function. [Accessed 28 11 2022].

[123] J. Brownlee, Better Deep Learning. Train faster, reduce overfitting, and make better predictions, Machine Learning Mastery, 2020.

[124] J. Brownlee, “Train-Test split foe evaluating machine learning algorithms,” 24 7 2020. [Online]. Available: https://machinelearningmastery.com/train-test-split-for-evaluating-machine-learning-algorithms/. [Accessed 25 11 2022].

[125] Wikipedia, “DC-to-DC converter,” 27 10 2022. [Online]. Available: https://en.wikipedia.org/wiki/DC-to-DC_converter. [Accessed 20 11 2022].

[126] Skeleton, “SkelCap series-large supercapacitor cells,” 2022. [Online]. Available: https://www.skeletontech.com/en/skelcap-supercapacitors?hsLang=en. [Accessed 5 12 2022].

[127] Maxwell, “3.0V 3000F ultracapacitor cell BCAP3000 P300 K04/05,” 2022. [Online]. Available: https://maxwell.com/wp-content/uploads/2022/11/3003483-EN.0_DS_3V-3000F-Cell-BCAP3000-P300.pdf. [Accessed 5 12 2022].

[128] AliExpress, “Super Capacitors 3V 3400F Maxwell DuraBlue Series Capacitor BCAP3400P300K04 BCAP3400P300K05 Supercapacitor,” 2022. [Online]. Available: https://www.aliexpress.us/item/3256804712767791.html. [Accessed 7 12 2022].

[129] Amazon, “Maxwell 18V 500F Super Capacitor Car Start Battery 3.0V 3000F supercapacitor 6pcs/Set with OA Screw Type,” 2022. [Online]. Available:

https://www.amazon.com/Maxwell-Super-Capacitor-Battery-supercapacitor/dp/B09P71ZY1P/. [Accessed 7 12 2022].

[130] Made-in-China, “GTCAP High Power Ultracapacitor 5000F 2.7V Supercapacitor,” 2022. [Online]. Available: https://xiedenglang.en.made-in-china.com/product/mvFnBUhxJlpD/China-GTCAP-High-Power-Ultracapacitor-5000F-2-7V-Supercapacitor.html. [Accessed 7 12 2022].

[131] A. Florescu, S. Bacha, I. Munteanu and A. Bratcu, “Frequency-separation-based energy management control strategy of power flows within electric vehicles using ultracapacitors,” in *38th Annual conference on IEEE industrial electronics society*, Montreal, 2012.

[132] M. Masih-Tehrani, M. Ha'iri Yazdi, V. Esfahanian, M. Dahmardeh and H. Nehzati, “Wavelet based power management for hybrid energy storage system,” *Journal of modern power systems and clean energy*, vol. 7, pp. 779-790, 2019.

[133] Texas Instruments, “TMS320F28069M C2000 32 bit MCU with 90MHz, FPU, VCU, CLA, 256 KB flash, InstaSPIN-MOTION,” 2022. [Online]. Available: https://www.ti.com/product/TMS320F28069M. [Accessed 2 07 2022].

[134] Mathworks, “Hardware connections,” 2022. [Online]. Available: https://uk.mathworks.com/help/mcb/gs/hardware-connections.html. [Accessed 8 November 2022].

[135] Texas Instruments, “BOOSTXL-DRV8305EVM,” 2022. [Online]. Available: https://www.ti.com/tool/BOOSTXL-DRV8305EVM. [Accessed 12 07 2022].

[136] Semikron, “08753450_TDS - SEMITEACH - IGBT - SEMIKRON Online Shop,” 1 09 2015. [Online]. Available: https://www.semikron-shop.com/out/media/ds/SEMIKRON_DataSheet_SEMITEACH_IGBT_3M50GB123D_1M50GAL123D_P3_250F_08753450.pdf. [Accessed 13 July 2022].

[137] Maxwell Technologies, “BCAP1200 P270 K04 Maxwell Technologies-Mouser,” 2022. [Online]. Available: https://www.mouser.co.uk/datasheet/2/257/Maxwell_K2Series_DS_1015370-4-1179730.pdf. [Accessed 12 07 2022].

[138] Teknic, INC, “Hudson Brushless DC Servo Motors-Teknic,” 13 March 2020. [Online]. Available: https://www.teknic.com/files/downloads/Hudson%20User%20Manual.pdf. [Accessed 10 07 2022].

[139] N. Quang and J.-A. Dittrich, Vector control of three phase AC machines, Springer, 2015.

[140] Microchip, “Sensored (encoder-Based) Field Oriented Control of Three-Phase Permanent Magnet Synchronous Motor (PMSM) AN2757,” 2018. [Online]. Available: http://ww1.microchip.com/downloads/en/Appnotes/Sensored-Encoder-Based)-Field-Oriented-Control-of-Three-Phase-%20Permanent-%20Magnet-%20Synchronous-DS00002757A.pdf. [Accessed 10 07 2022].

[141] Mathworks, “Control PMSM Loaded with Dual Motor (Dyno) Using C2000 Processors,” 2022. [Online]. Available: https://uk.mathworks.com/help/supportpkg/texasinstrumentsc2000/ug/dual-motor-dyno-example.html. [Accessed 12 07 2022].

[142] Advanced Solutions Netherland B.V., “Classical IIR filter design: a practical guide,” [Online]. Available: https://www.advsolned.com/iir-filters-practical-guide/. [Accessed 10 07 2022].

[143] Wikipedia, “Bilinear Transform,” 2022. [Online]. Available: https://en.wikipedia.org/wiki/Bilinear_transform. [Accessed 14 07 2022].

[144] Mathworks, “Rate transition,” 2022. [Online]. Available: https://uk.mathworks.com/help/simulink/slref/ratetransition.html. [Accessed 15 11 2022].

[145] Mathworks, “Battery,” 2022. [Online]. Available: https://uk.mathworks.com/help/physmod/sps/powersys/ref/battery.html. [Accessed 22 June 2022].

Appendix A. Python programs

LSTM training python program

```
# -*- coding: utf-8 -*-
"""
Created on Mon Sep 23 13:25:29 2019

@author: Miguel Robayo
"""
import pandas as pd
#import numpy as np
from numpy import array
from keras.models import Sequential
from keras.layers import LSTM, Bidirectional
from keras.layers import Dense, Dropout
from keras.optimizers import Adam
from sklearn.model_selection import train_test_split
import matplotlib.pyplot as plt
ADAM=Adam(lr=0.001,beta_1=0.9,beta_2=0.999,amsgrad=False,)
data=pd.read_csv(r'C:\Users\mr597\Downloads\8dr10.csv')
seq=data.to_numpy()
x_train,x_test=train_test_split(seq,test_size=0.1,shuffle=False)
# split a univariate sequence into samples
def split_sequence(sequence, n_steps_in, n_steps_out):
        X, y = list(), list()
        for i in range(len(sequence)):
                # find the end of this pattern
                end_ix = i + n_steps_in
                out_end_ix = end_ix + n_steps_out
                # check if we are beyond the sequence
                if out_end_ix > len(sequence):
                        break
                # gather input and output parts of the pattern
                seq_x, seq_y = sequence[i:end_ix], sequence[end_ix:out_end_ix]
                X.append(seq_x)
                y.append(seq_y)
        return array(X), array(y)
def split_sequence1(sequence, n_steps_in):
        X= list()
        for i in range(len(sequence)):
                # find the end of this pattern
                end_ix = i + n_steps_in
```

```
            # check if we are beyond the sequence
            if end_ix > len(sequence)-1:
                break
            # gather input and output parts of the pattern
            seq_x= sequence[i:end_ix]
            X.append(seq_x)

    return array(X)
# define input sequence
n_steps_in, n_steps_out =8,8
# split into samples
X, y = split_sequence(x_train, n_steps_in, n_steps_out)
# reshape from [samples, timesteps] into [samples, timesteps, features]
n_features = 1
X = X.reshape((X.shape[0], X.shape[1], n_features))
y=y.reshape(y.shape[0],y.shape[1])
#define model
model = Sequential()
model.add(LSTM(50,return_sequences=True,activation='tanh',
input_shape=(n_steps_in, n_features)))
model.add(LSTM(50,return_sequences=False))
model.add(Dense(n_steps_out))
model.summary()
model.compile(optimizer=ADAM, loss='mse',metrics=['accuracy'])
#fit model
history=model.fit(X, y, epochs=170,verbose=1,validation_split=0.1)
plt.plot(history.history['loss'])
plt.plot(history.history['val_loss'])
plt.title('model train vs validation loss')
plt.ylabel('loss')
plt.xlabel('epoch')
plt.legend(['Train','validation'],loc='upper right')
plt.show()
fig1=plt.figure(figsize=(8,3),facecolor='white')
left,bottom,width,height=0.1,0.1,0.8,0.8
ax1=fig1.add_axes((left,bottom,width,height))
ax1.plot(history.history['acc'],color='blue',label='acc',linestyle='solid',alpha=0.8,linewidt
h=1)
ax1.plot(history.history['val_acc'],color='Red',label='val_acc',linestyle='dashed',alpha=0.
8,linewidth=1)
ax1.grid(color='darkgrey',which='both',linestyle=':',linewidth=0.5)
model.save(r'C:\Users\mr597\Downloads\2x50_170.h5')
```

```
#check prediction
x_input=split_sequence1(x_test,n_steps_in)
yhat = model.predict(x_input, verbose=2)
#print(yhat)
yhat0=yhat[:,0]
yhat1=yhat[:,1]
yhat2=yhat[:,2]
yhat3=yhat[:,3]
yhat4=yhat[:,4]
#plot ranges from l to r (seconds)
l=0
r=100
plt.figure(figsize=(12,5))
plt.plot(yhat0[l:r],'b',label='Predicted 1 step')
plt.plot(yhat1[l:r],'g',label='Predicted 2 step')
plt.plot(yhat2[l:r],'black',label='Predicted 3 step')
plt.plot(yhat3[l:r],'grey',label='Predicted 4 step')
plt.plot(yhat4[l:r],'yellow',label='Predicted 5 step')
plt.plot(x_test[l:r],'r',label='Real time data')
plt.title("Current Prediction 1 step in future")
plt.xlabel("time (seconds)")
plt.ylabel("Amperes (A)")
plt.legend()
plt.show()
```

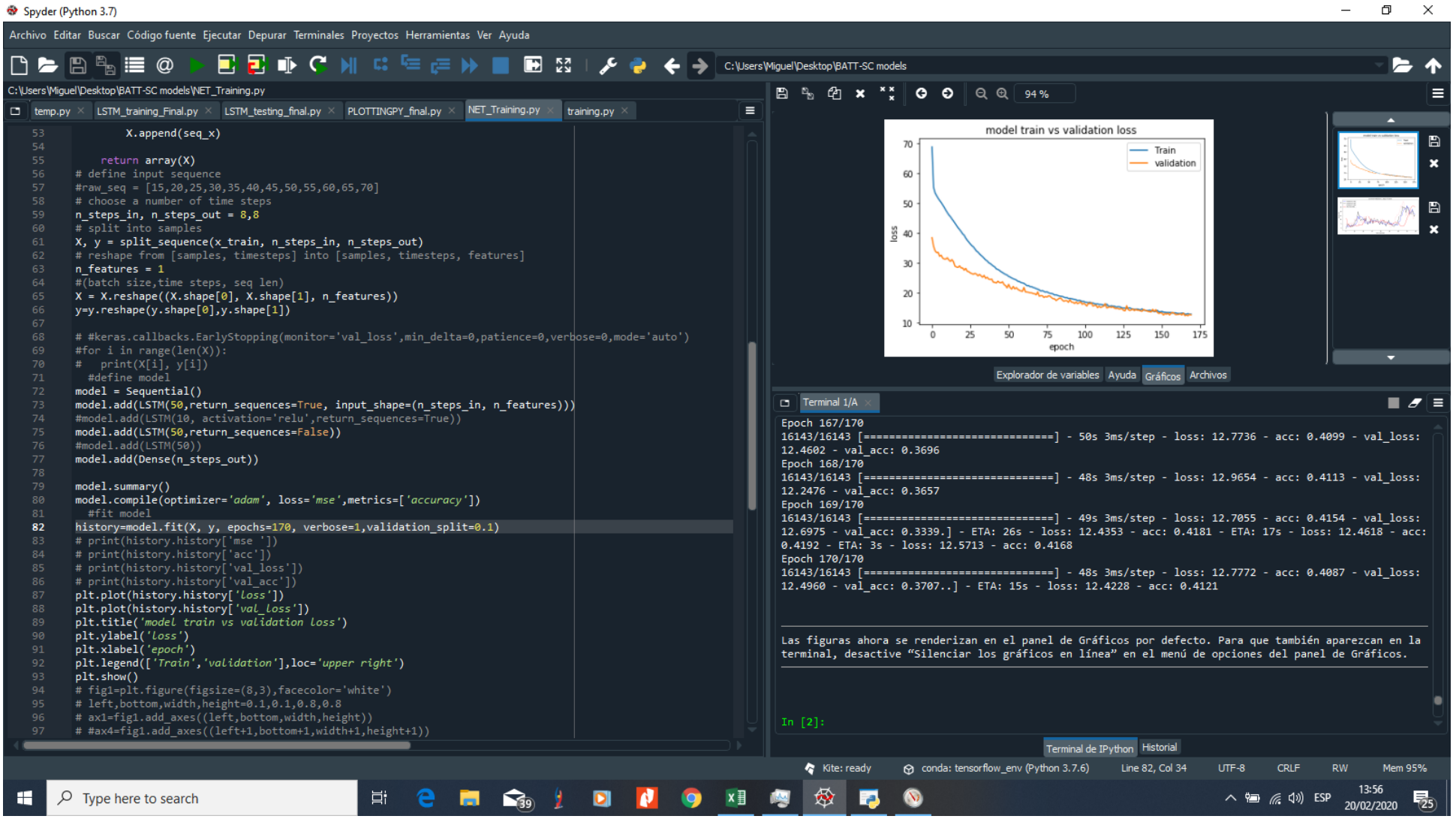
Spyder (Python 3.7)
Archivo Editar Buscar Código fuente Ejecutar Depurar Terminales Proyectos Herramientas Ver Ayuda
C:\Users\Miguel\Desktop\BATT-SC models\NET_Training.py
temp.py
LSTM_training_Final.py
LSTM_testing_final.py
PLOTTINGPY_final.py
NET_Training.py
training.py
X.append(seq_x)
return array(X)
define input sequence
#raw_seq = [15,20,25,30,35,40,45,50,55,60,65,70]
choose a number of time steps
n_steps_in, n_steps_out = 8,8
split into samples
X, y = split_sequence(x_train, n_steps_in, n_steps_out)
# reshape from [samples, timesteps] into [samples, timesteps, features]
n_features = 1
#(batch size,time steps, seq len)
X = X.reshape((X.shape[0], X.shape[1], n_features))
y=y.reshape(y.shape[0],y.shape[1])
# #keras.callbacks.EarlyStopping(monitor='val_loss',min_delta=0,patience=0,verbose=0,mode='auto')
#for i in range(len(X)):
print(X[i], y[i])
#define model
model = Sequential()
model.add(LSTM(50,return_sequences=True, input_shape=(n_steps_in, n_features)))
#model.add(LSTM(10, activation='relu',return_sequences=True))
model.add(LSTM(50,return_sequences=False))
#model.add(LSTM(50))
model.add(Dense(n_steps_out))
model.summary()
model.compile(optimizer='adam', loss='mse',metrics=['accuracy'])
#fit model
history=model.fit(X, y, epochs=170, verbose=1,validation_split=0.1)
# print(history.history['mse '])
# print(history.history['acc'])
# print(history.history['val_loss'])
# print(history.history['val_acc'])
plt.plot(history.history['loss'])
plt.plot(history.history['val_loss'])
plt.title('model train vs validation loss')
plt.ylabel('loss')
plt.xlabel('epoch')
plt.legend(['Train','validation'],loc='upper right')
plt.show()
# fig1=plt.figure(figsize=(8,3),facecolor='white')
# left,bottom,width,height=0.1,0.1,0.8,0.8
# ax1=fig1.add_axes((left,bottom,width,height))
# #ax4=fig1.add_axes((left+1,bottom+1,width+1,height+1))
C:\Users\Miguel\Desktop\BATT-SC models
94 %
model train vs validation loss
Train
validation
loss
epoch
Explorador de variables
Ayuda
Gráficos
Archivos
Terminal 1/A
Epoch 167/170
16143/16143 [==========] - 50s 3ms/step - loss: 12.7736 - acc: 0.4099 - val_loss: 12.4602 - val_acc: 0.3696
Epoch 168/170
16143/16143 [==========] - 48s 3ms/step - loss: 12.9654 - acc: 0.4113 - val_loss: 12.2476 - val_acc: 0.3657
Epoch 169/170
16143/16143 [==========] - 49s 3ms/step - loss: 12.7055 - acc: 0.4154 - val_loss: 12.6975 - val_acc: 0.3339.] - ETA: 26s - loss: 12.4353 - acc: 0.4181 - ETA: 17s - loss: 12.4618 - acc: 0.4192 - ETA: 3s - loss: 12.5713 - acc: 0.4168
Epoch 170/170
16143/16143 [==========] - 48s 3ms/step - loss: 12.7772 - acc: 0.4087 - val_loss: 12.4960 - val_acc: 0.3707..] - ETA: 15s - loss: 12.4228 - acc: 0.4121
Las figuras ahora se renderizan en el panel de Gráficos por defecto. Para que también aparezcan en la terminal, desactive "Silenciar los gráficos en línea" en el menú de opciones del panel de Gráficos.
In [2]:
Terminal de IPython
Historial
Kite: ready
conda: tensorflow_env (Python 3.7.6)
Line 82, Col 34
UTF-8
CRLF
RW
Mem 95%
Type here to search
ESP
13:56
20/02/2020

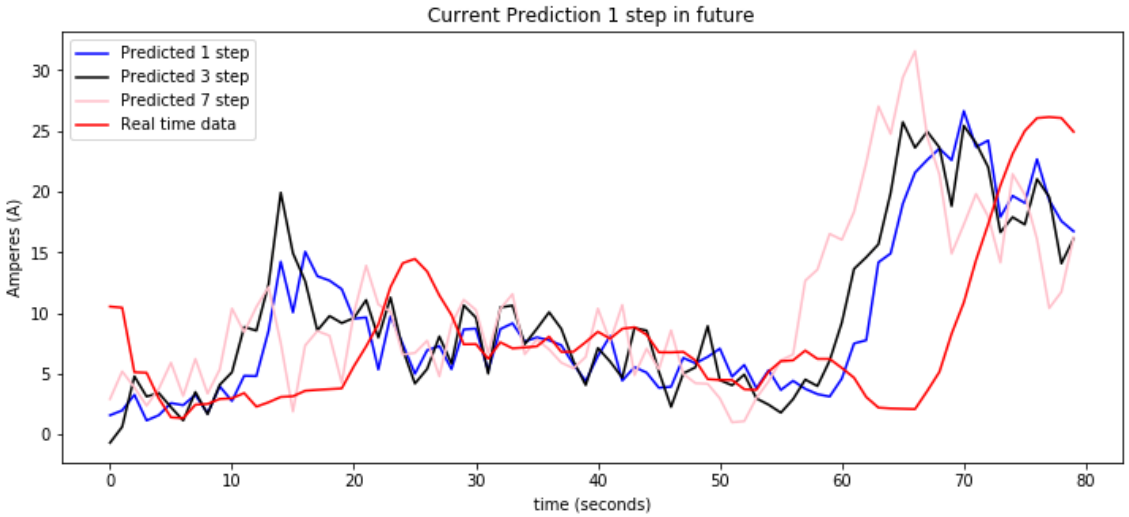

LSTM Testing program

```
# -*- coding: utf-8 -*-
"""
Created on Mon Oct  7 10:45:03 2019

@author: Miguel Robayo
"""
import time
import pandas as pd
import matplotlib.pyplot as plt
import numpy as np
```

```
from numpy import array
from keras.models import load_model
import h5py
print('h5py: %s' % h5py.__version__)
model=load_model(r'C:\Users\mr597\Downloads\2x50_170.h5')
t0=time.time()
t1=time.time()
total=t1-t0
print (total)
t2=time.time()
def split_sequence1(sequence, n_steps_in):
        X= list()
        for i in range(len(sequence)):

                # find the end of this pattern
                 end_ix=i+n_steps_in

                # check if we are beyond the sequence
                 if end_ix > len(sequence)-1:
                        break
                # gather input and output parts of the pattern
                 seq_x= sequence[i:end_ix]
                 X.append(seq_x)

        return array(X)
n_steps_in, n_steps_out = 8, 8
```

```
t3=time.time()
total1=t3-t2
t4=time.time()
print (t4)
testpd=pd.read_csv(r'C:\Users\mr665\Downloads\pdemand.csv')
test=testpd.to_numpy()
x_input=split_sequence1(test,n_steps_in)
yhat = model.predict(x_input, verbose=2)
yhat0=yhat[:,0]
yhat1=yhat[:,1]#
yhat2=yhat[:,2]#
yhat3=yhat[:,3]#
yhat4=yhat[:,4]#
plt.figure(figsize=(12,5))
plt.plot(yhat4[0:100],'grey',label='Predicted 4 step')
plt.plot(yhat4[0:100],'yellow',label='Predicted 5 step')
plt.plot(test[0:100],'r',label='Real time data')
```

Appendix B Experiment layout

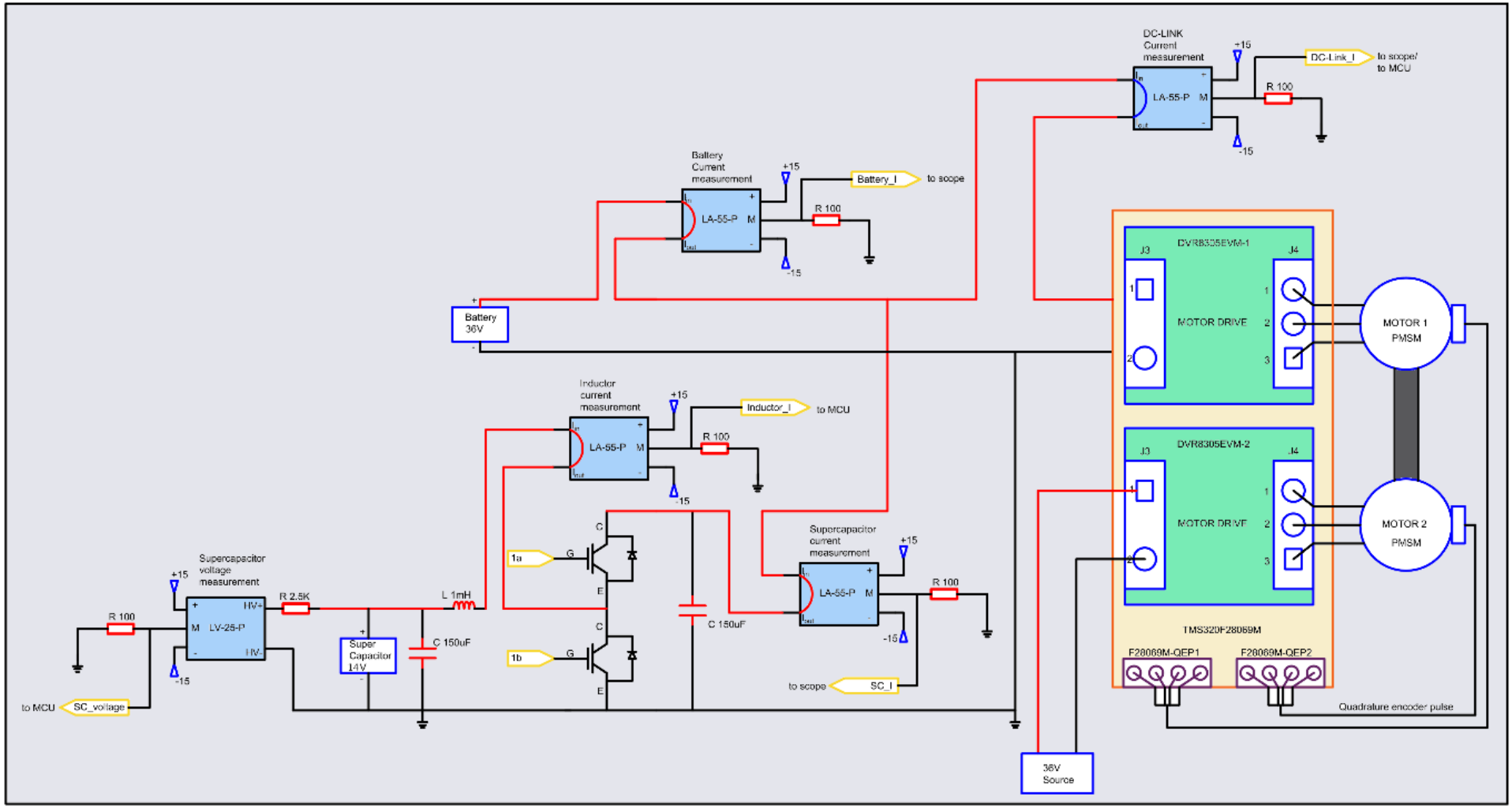

Signal conditioning and PWM

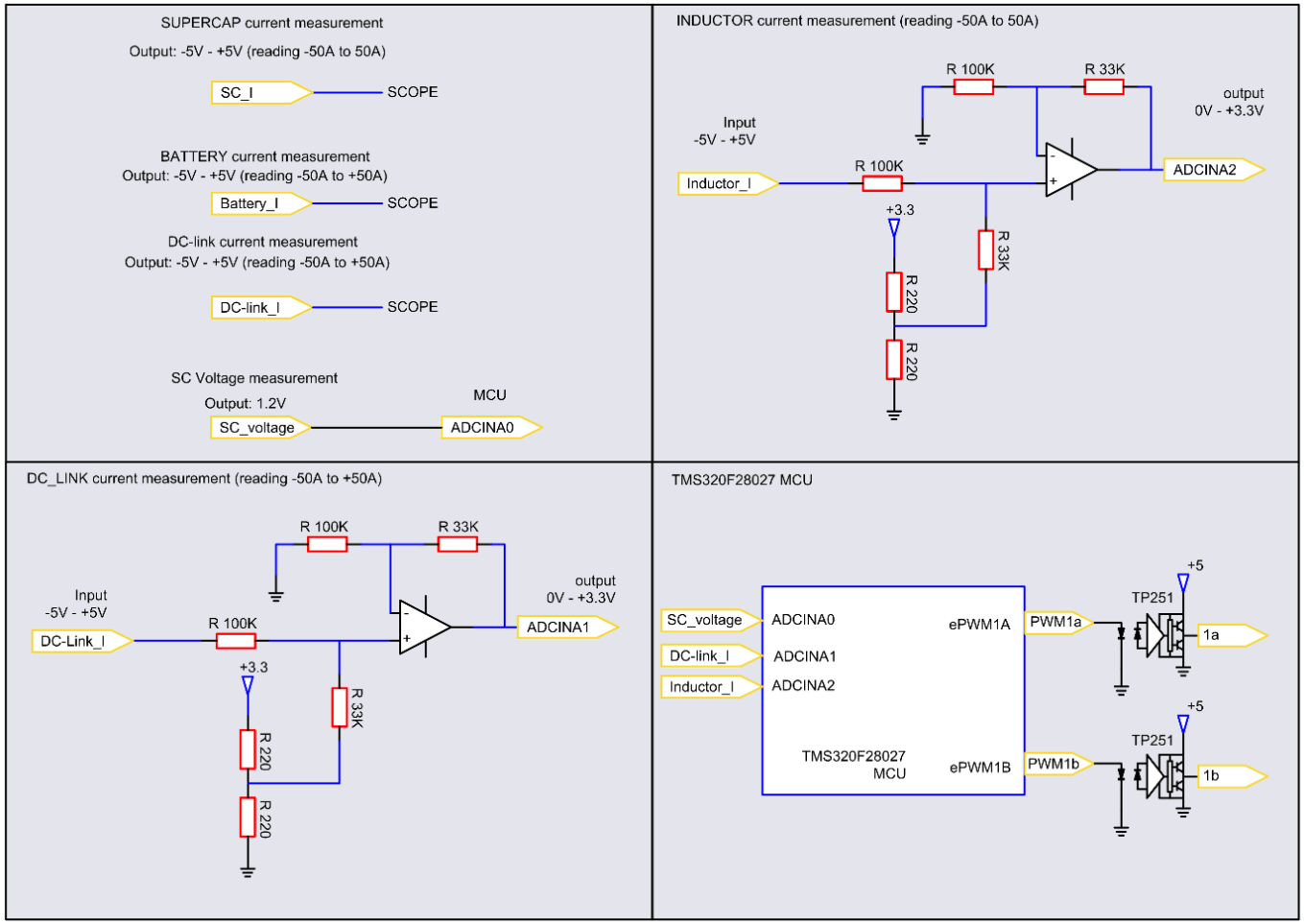

Microcontroller pin assignations.

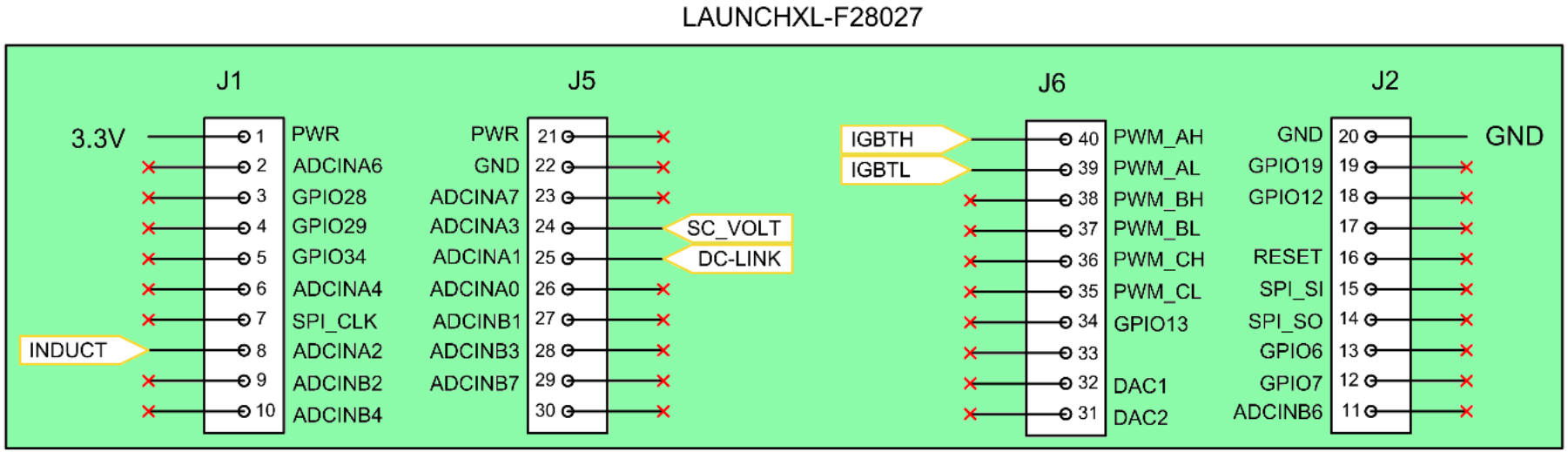

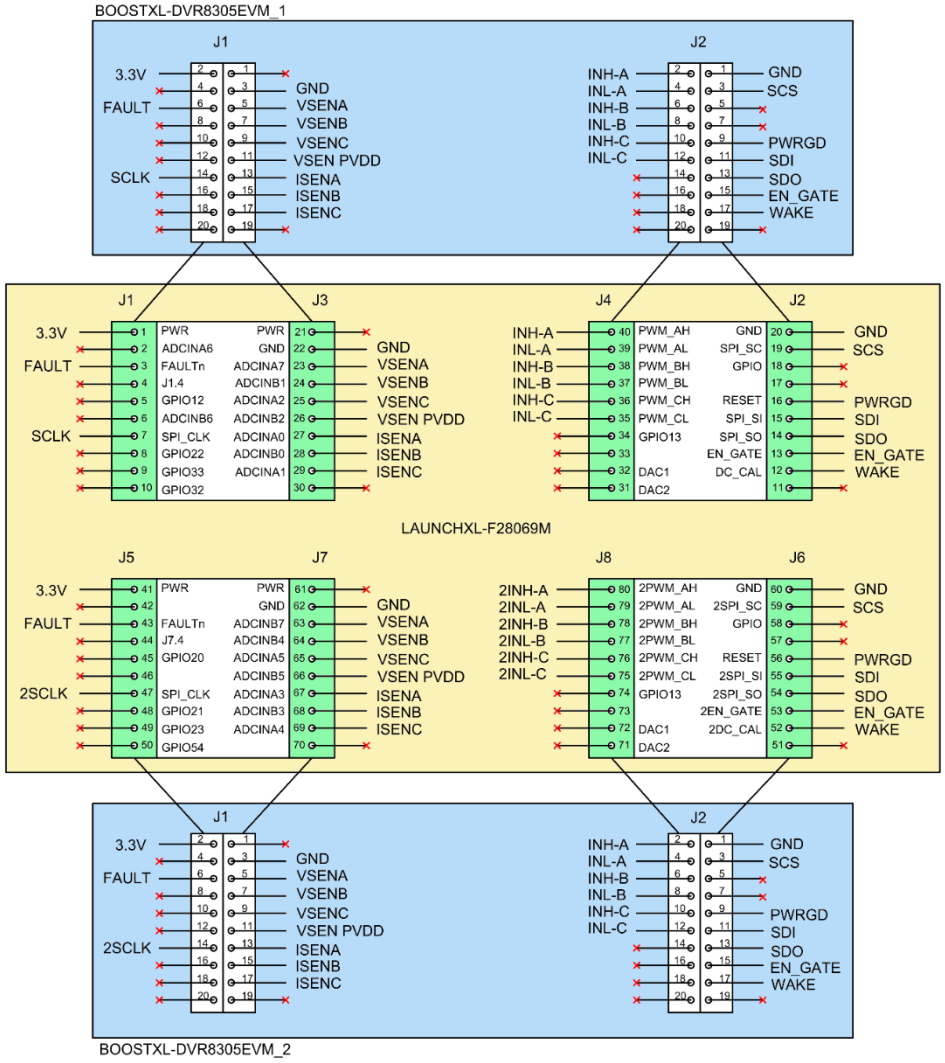
BOOSTXL-DVR8305EVM_1
J1
3.3V
FAULT
SCLK
GND
VSENA
VSENB
VSENC
VSEN PVDD
ISENA
ISENB
ISENC
J2
INH-A
INL-A
INH-B
INL-B
INH-C
INL-C
GND
SCS
PWRGD
SDI
SDO
EN_GATE
WAKE
J1
J3
J4
J2
PWR
ADCINA6
FAULTn
J1.4
GPIO12
ADCINB6
SPI_CLK
GPIO22
GPIO33
GPIO32
ADCINA7
ADCINB1
ADCINA2
ADCINB2
ADCINA0
ADCINB0
ADCINA1
PWM_AH
PWM_AL
PWM_BH
PWM_BL
PWM_CH
PWM_CL
GPIO13
DAC1
DAC2
SPI_SC
GPIO
RESET
SPI_SI
SPI_SO
EN_GATE
DC_CAL
LAUNCHXL-F28069M
J5
J7
J8
J6
2SCLK
2INH-A
2INL-A
2INH-B
2INL-B
2INH-C
2INL-C
ADCINB7
ADCINB4
ADCINA5
ADCINB5
ADCINA3
ADCINB3
ADCINA4
2PWM_AH
2PWM_AL
2PWM_BH
2PWM_BL
2PWM_CH
2PWM_CL
2SPI_SC
2SPI_SI
2SPI_SO
2EN_GATE
2DC_CAL
BOOSTXL-DVR8305EVM_2